An insight into nanostructures through coherent diffraction imaging

Sara Fernandez

Université Aix Marseille
ESRF - The European Synchrotron
Ecole Doctorale 352 PHYSIQUE ET SCIENCES DE LA MATIERE
UFR: SCIENCE
LABORATOIRE: IM2NP UMR7344 CNRS & Universités d'Aix-Marseille et de Toulon

Thèse présentée pour obtenir le grade universitaire de docteur

Discipline : PHYSIQUE
Spécialité : Matière Condensée et Nanosciences

Sara FERNANDEZ

An insight into nanostructures through coherent diffraction imaging

Soutenue le 01/12/2016 devant le jury :

Joel EYMERY	CEA - Grenoble	Rapporteur
Ullrich PIETSCH	University of Siegen	Rapporteur
Suzanne GIORGIO	CINAM - Marseille	Examinateur
Thomas SCHROEDER	IHP - Frankfurt (Oder)	Examinateur
Tobias SCHÜLLI	ESRF - Grenoble	Examinateur
Marie-Ingrid RICHARD	IM2NP - Université d'Aix-Marseille	Co-encadrant
Olivier THOMAS	IM2NP - Université d'Aix-Marseille	Directeur de thèse

Acknowledgments

Cette première ligne ne peut être que pour Marie-Ingrid Richard, qui a su me guider dans mon apprentissage et dans le monde de la recherche. Merci de me soutenir pendant toute la période de thèse. Merci pour tous les bons et mauvais moments et de partager avec moi autant d'heures d'expériences, autant d'allers et retours à Marseille… autant de discussions qui nous ont permis de nous entendre ! Merci pour tous les jours que tu es venu frapper la porte de mon bureau. Merci pour chaque dessin dans le tableau. Merci de partir dans tous les sens quand je voyais qu'une direction. Merci d'être la seule qui comprend que c'est facile d'exploser le dôme du minifour et de savoir comment c'est dur de trouver le bon hôtel à Marseille, quand ils ont tous le même nom. Merci parce que sans toi et ton infinie patience, cette thèse n'aurait jamais été possible.

Merci à Olivier Thomas. Pour ton suivi, pour tes connaissances. Pour m'accueillir dans ton équipe et m'avoir donnée l'opportunité d'évoluer aux niveaux personnel et professionnel. Merci de me faire confiance jusqu'au bout.

Merci à Tobias Schulli de m'avoir permis de participer dans ce grand projet qui est l'*upgrade* de ID01. Merci de faire possible cette bonne ambiance dans l'équipe et de faire de ID01 la meilleure ligne de lumière de l'ESRF (avec toutes mes excuses pour ceux qui pourraient apprendre cette vérité en lissant ce petit paragraphe).

Thanks to the members of the jury Joel Eymery, Ullrich Pietsch, Thomas Schroeder and Suzanne Giorgio for reading, criticising and evaluating my thesis.

I have to thank every member of ID01: those who are already gone (Genziana, Raphael, Marta, Jan, Rebeca, Dina) and those who are still there (Hamid, Steven, Tao, Vincent). Thanks for every lunch, for the nice work we do together, for the destruction and reconstruction of the beamline. Un remerciement spécial pour Gilbert Chahine. Pour tes conseils, pour les discussions pendant les nuits blanches. Pour l'encouragement. Merci de m'avoir fait confiance et de me laisser compter sur toi.

Merci aux marseillais, pour leur accueil, pour leur esprit. Merci de partager votre bonne humeur et votre savoir scientifique avec moi, pendant les manips, les séjours à Marseille, les congrès... Stephan, Thomas, Stephanie, Anton, Ren Zhe, Cédric. Mais aussi merci à Benjamin, Clara, Tassos, Manon… pour les soirées sur le port et au bord de la mer !

Roberto Felici, Olivier Balmes, Francesco Carla, Jakub Drnec, Maciej Jankowski. Thank you all for letting ID03 be my second beamline and suffer with me during the beamtimes. Thanks for your technical help and for sharing your knowledge about catalysis.

Merci à toutes les personnes qui ont fait possibles ce projet de recherche qui est ma thèse. Pascal Gentile pour les échantillons et Thomas David pour les mesures MEB et TEM, ainsi que pour les expériences sur ID01 et les discussions, que ce soit à Marseille, à Grenoble ou par mail. Merci à l'équipe de Lyon pour la préparation FIB et les mesures de tomographie électronique.

Thanks to Jan Philippe Hoffman and his group, for the samples and the beamtimes. Thanks for the nice collaboration that we have just started.

Thanks to the beamline staff of CRISTAL, BM32, ID13, ID16, BM02, ID10, CSAXS… for your help during and after the experiments and for the fruitful discussions. Thanks to Gunther Richter, David Floetotto and the MPI group, for the first year of my thesis. Thanks indeed to Sema, for being more than a colleague. We will keep our promise.

Y como no todo se limita a lo profesional, no podría no dar las gracias a mi familia. Por su apoyo incondicional, por su confianza, por escucharme llorar y reír en la distancia. *Ohana.*

Gracias mamá por tus nervios y alegría, por compartir conmigo tu entusiasmo. Gracias papá por tu saber, por tu escucha. Gracias a Inma y Marcial, por estar siempre ahí, por su apoyo y orgullo de sobrina que anima sin cesar a llegar al final. Gracias a Patricia por ser prima y amiga. Gracias a Alejandra (¡mi compañera de viajes, de meriendas de chocolate y mi mejor amiga!), Rocío (por demostrar que segundas oportunidades merecen más que la pena), Marta (por las nocheviejas, ¡y porque nuestra amistad ha sobrevivido a todas las peleas!) y Miri (porque toda física necesita una amiga psicóloga). Gracias a todas por hacer de Oviedo la ciudad a la que quiero volver.

Lucía dankon pro la reciproka terapioj, ĉar batalante kune akiris malsamajn aferojn. Gracias por ser tú, por ser mi ejemplo de cabeza loca ganadora.

A Paula, por las llamadas de las doce. 因为每天你做你想做多一点。

Thanks to Andrea and Federica. For being the ones that heard me to laugh and complain, complain, complain and complain even more. For the long hours in the office, the silence, and the countless coffees. Thank you for the day-to-day.

Gracias a Cris por los primeros meses aquí. Y a Berta, por los gordi-cafés. Porque los pocos meses que estuvisteis por aquí fueron suficientes para forjar una amistad.

Alex Vielen Dank für Ihre Persönlichkeit. Merci d'être toi. Je t'aime.

Per tutti gli italiani che hanno fatto Grenoble più di una semplice città di sci. Leoncino, Valeria, Niccolo, Luca, Ilaria, Arianna, Annalisa. Y a Marc, Irena y Jose Luis, porque os cuento ya casi como italianos. Merci également à Maxime Dupraz pour être collègue et ami. Merci Gwenael pour tes visites et ton amitié depuis Orsay. Merci Yijia pour nos petites rencontres à chaque occasion.

Mais aussi à toutes les personnes que je risque d'oublier, qui ont fait partie de ma vie et m'ont fait sourire ces trois dernières années.

Contents

Resumé de la thèse **10**

Introduction **10**

1 Strain and composition at nanometer scales **15**

1.1 Fundamental properties of crystals 16

1.1.1 Crystalline structure 16

1.1.2 Strain 17

1.1.3 Defects 19

1.2 One-dimensional crystals: nanowires 20

1.2.1 Ge/Si core/shell nanowires 22

1.2.1.1 State of the art 23

1.2.1.2 Intermixing in Si/Ge 26

1.3 Metallic nanoparticles 28

1.3.1 Strain in nano-particle based catalysts 31

1.4 CDI as a characterisation tool 33

1.5 Conclusions 36

2 Coherent X-ray diffraction **38**

2.1 Coherent X-ray sources 39

2.2 Coherent diffraction imaging methods 42

2.3 Bragg CDI 44

2.3.1 From X-ray Bragg Diffraction to Bragg Coherent Diffraction 44

2.3.2 Experimental requirements and data analysis 45

2.3.2.1 X-ray Bragg diffraction in the Fraunhofer regime 45

2.3.2.2 Oversampling . . . 47
2.3.2.3 Phase Retrieval algorithms . . . 48
2.3.2.3.1 Error reduction (ER) . . . 48
2.3.2.3.2 Hybrid Input-Output (HIO) Algorithm . . . 49
2.3.2.3.3 Charge flipping (CF) . . . 50
2.3.2.3.4 Shrink-wrap (SW) . . . 50
2.4 Experimental set-ups . . . 51
2.4.1 The ID01 beamline . . . 51
2.4.1.1 The upgraded ID01 optics hutch . . . 51
2.4.1.2 ID01 experimental hutch . . . 52
2.4.1.2.1 The diffractometer and the nano-positioning stage . . . 52
2.4.1.2.2 Focusing optics . . . 53
2.4.1.2.3 Sample environment . . . 54
2.5 Conclusion . . . 55

3 Interplay between strain and diffusion in core-shell Ge-Si nanowires 57

3.1 Introduction . . . 58
3.2 Residual strain in core-shell Ge-Si NWs: linear elastic model . . . 59
3.2.1 Strain in elastically isotropic materials . . . 60
3.2.2 Calculation of diffraction patterns: case of hexagonal wires . . . 61
3.3 Investigating the strain in single NWs . . . 65
3.3.1 Strain in as-grown nanowires and dependence on the core/shell ratio . . . 65
3.3.2 Investigating the strain field within single isolated NWs . . . 70
3.3.2.1 Combining CDI and TEM: homogeneity over the sample . . . 71
3.3.2.2 Retrieving the strain: measuring multiple reflections . . . 76
3.3.3 Discussion . . . 87
3.4 Intermixing in single core/shell nanowires . . . 89
3.4.1 Influence of the temperature in the strain field of single NWs . . . 89
3.4.2 Influence of the temperature in the morphology and composition of single NWs . . . 93
3.4.2.1 Measurements at room temperature . . . 93
3.4.2.2 *In situ* annealing experiments . . . 94

3.4.2.3 Discussion . . . 97
3.4.3 Correlating strain and diffusion . . . 99
3.5 Conclusions . . . 102

4 Investigating the strain within Pt catalysts under chemical reaction 104
4.1 Introduction . . . 105
4.2 Sample description and finite element modelling (FEM) simulations . . . 106
4.3 Study under ambient conditions . . . 109
4.3.1 Facet determination . . . 111
4.3.2 Phase retrieval . . . 114
4.4 *In situ* study at ID03 in controlled gas-phase environment . . . 119
4.5 *In situ* study at ID01 in controlled gas-phase environment . . . 126
4.6 Conclusions . . . 130

Conclusions and outlook 133
Bibliography . . . 137

List of figures 149

List of tables 158

Author's publications 160

Résumé de la thèse

La possibilité de manipuler les propriétés physiques des matériaux en les déformant élastiquement est l'objectif de l'ingénierie des contraintes, qui cherche ainsi à améliorer les performances des nouveaux dispositifs. Dans ce contexte, la déformation est entendue comme le déplacement des atomes par rapport à leurs positions d'équilibre dans un réseau cristallin parfait, qu'elle soit produite par l'épitaxie de deux cristaux ou bien par une différence de coefficient de dilatation, une contrainte résiduelle voire une force extérieure appliquée. Si à l'origine ce concept était utilisé pour améliorer la mobilité des porteurs de charge dans des transistors sur des systèmes consistant en une fine couche semi-conductrice épitaxiée sur un substrat, ce concept est étendu aujourd'hui à tout type de nanostructures. En effet, les nanostructures peuvent supporter des déformations élastiques considérables sans génération de défauts, contrairement à leurs analogues massifs. Comprendre l'influence des contraintes liées aux effets de taille, mais aussi aux interfaces ou à la morphologie des objets, permettrait de maîtriser les propriétés électroniques, optiques, magnétiques ou catalytiques des matériaux. La maîtrise des contraintes et donc, des propriétés physiques ou chimiques des objets, pourrait donc être exploitée dans une large variété de domaines.

La compréhension des effets des contraintes ne se limite pas pourtant à la croissance des nanostructures, puisque la fabrication et la fiabilité de nouveaux dispositifs doivent être également garantie. Il est ainsi impératif de caractériser les objets et de mesurer l'état de déformation dans les nanostructures, que ce soient des déformations intrinsèques (forme, interface...) ou la conséquences d'une force externe appliquée sur l'objet. De plus, des modèles théoriques et des calculs de type *ab initio* sont nécessaires pour bien comprendre le comportement des systèmes réels.

Ce travail de thèse utilise la diffraction cohérente des rayons X pour caractériser des nano objets uniques. Cette technique s'avère la plus adaptée pour étudier le champ de déformation dans les structures puisque aucune préparation des échantillons n'est nécessaire (ce qui pourrait modifier les caractéristiques intrinsèques des objets). Parmi les avantages de cette méthode, on peut mettre en avant la grande sensibilité aux déformations et sa nature non destructive, qui permettent d'effectuer des expériences *in situ*.

Ce travail de thèse résume les résultats d'étude des déformations sur deux types d'objets différents. Dans un premier temps, des effets d'interface dans des nanofils semiconducteurs de type cœur/coquille (Ge/Si) sont analysés, ainsi que leur évolution sous traitement thermique. Ensuite des particules métalliques (Pt) facettées et leur évolution physique sous réaction chimique sont examinées, comme compte tenu de leur morphologie, ce type de particules présente un grand intérêt pour la catalyse.

Introduction

The control of strain to tune the electronic properties of semiconductor materials in order to improve the devices performances has been an important research topic in materials science for the last two decades. In this context, strain refers to the elastic displacement of atoms in the crystal lattice with respect to their *ideal* positions due to the lattice mismatch of the epitaxied materials that form the heterostructure, originally a semiconductor overlayer grown on a thick substrate, or more generally caused by some internal stress brought by surrounding layers, temperature, mechanical loading etc. Thereby, the use of strained crystals has been proved to enhance the charge carrier mobility in transistor heterostructures and opened the field known as *strain engineering*. However this field has become much wider since then and extends now beyond semiconductors; any object whose size is reduced to the nanoscale can bear higher elastic strains compared to bulk as a consequence of its size. In this way, nano-objects will lead not only electronic advances, but also enhanced optical, magnetic, electrical or catalytic properties and if strain is carefully controlled, the use of nanostructures can be exploited in many fields.

The new physical and chemical challenges arising from miniaturisation must therefore be understood in order to be successfully applied. Furthermore tuning the properties through the control of strain is not simply a matter of growth or synthesis of nanostructures. Measuring the strain distribution within the objects, as well as the chemical and physical consequences of the strain field *e.g.* when a force is applied, are needed. Also *ab initio* modeling are necessary to understand expected and real behaviors. These are the pillars of strain engineering and they must all converge to achieve, step by step, relevant improvement in devices.

Therefore, complete characterisations of the intrinsic strain effects are needed, as well as studies about how they influence the properties of individual objects. As a matter of fact strain is not the only issue that need to be measured and understood; many other factors such as shape, defects, composition or surface relaxation must be taken into account. Hence, the evolution of strain engineering in nanostructures requires characterisation tools that can be used to quantify the structure and the actual strain in a sample, whether this strain is intrinsic or applied. In addition, strain within nanostructures is usually inhomogeneous so that tools able to resolve strain information with high precision and good spatial resolution are needed. In this regard, Bragg coherent X-ray diffraction imaging is a powerful technique because it allows to access simultaneously the electron density and the three-dimensional strain field within single crystals. Besides, this method has numerous advantages such as its non destructive nature, possibility of *in situ* experiments and the needless sample preparation (*i.e.* without any alteration of the original strain field).

In this PhD work, coherent diffraction imaging is used to investigate the strain field within two different systems, both of them being single individual objects. The first one, consists of Ge/Si core/shell nanowires, which are the building blocks for applications ranging from nano-electronics to biomedicine or photovoltaics, and the second, of Pt nanoparticles whose particular

shape would be the key for better catalysts. As mentioned above, not only the intrinsic strain is relevant but also its evolution under applied or external forces as it would be the case in future devices. Hence, the study of Ge/Si nanowires will focus on the pseudomorphic strain induced by the heteroepitaxy and the study will be completed with preliminary *in situ* experiments with interest in interdiffusion at high temperatures. On the other hand, after a careful study of the Pt nanoparticles at their *post growth* state, the catalytic activity during chemical reactions and the strain evolution of the particles have been investigated. This work has been performed within a collaboration between IM2NP (Aix Marseille Université and CNRS) and ESRF.

The manuscript is organised as follows:

In Chapter 1 the fundamental properties of crystals are revised, with focus on nanocrystals and in particular, on the systems investigated in this PhD work (*i.e.* semiconductor core-shell nanowires and metallic nanoparticles). The state of the art is summarised to highlight the motivations of the study presented here and how recently raised fundamental questions need to be answered. Then, I justify the choice of coherent X-ray imaging to carry out the experiments through comparison with other currently available characterisation techniques and recent examples from literature.

In Chapter 2 the basic principles of coherent lensless X-ray imaging techniques are explained, with details on Bragg coherent diffraction imaging: from important experimental requirements to record the data such as the oversampling criteria, to the data analysis through details on the phase retrieval algorithms necessary to determine the density and the phase of the measured sample. The development of these relatively recent techniques would not have been possible without the development of X-ray sources so that a brief description of the main ones is given, as well as the description of typical experimental set-ups such as the one at ID01 at the ESRF, where most experiments summarised in this report were performed.

In Chapter 3 I present several studies on Si/Ge core/shell nanowires. Using a coherent X-ray nano-focused beam, the investigation of single objects is carried out from the as grown samples (*i.e.* without any preparation) to measure the axial strain averaged over single nanowires. Then the study is performed for samples with different core/shell ratio and for individual wires from two of these samples. The isolation of the wires allowed to carry out coherent diffraction imaging experiments and retrieve the inhomogenous strain within single objects. The retrieved objects are analysed and the chapter ends with a discussion of the evolution of the nanostructure after annealing above room temperature.

Chapter 4 is dedicated to Pt nanoparticles for catalysis applications. The chapter is organised as follows: first, one nanoparticle is modeled by finite elements analysis and its corresponding diffraction pattern is calculated. Then, two methods to determine the facets orientation of the particles are presented, both of them using the three-dimensional reciprocal space maps recorded around a given Bragg peak of the object. The first of these methods is based on the stereographic projection of the intersection points of the rods with a sphere containing the streaked Bragg peak, similarly to the calculation of a conventional pole figure. The second one, consists in measuring the angle between the streaks, which is directly related to the crystallographic planes forming the crystal.
The methods are applied to experimental data, both under ambient conditions and in controlled-gas phase environment to observe morphology changes during chemical reaction.

Finally I give a short synthesis of the principal results obtained during this work and I discuss some interesting perspectives for future investigations.

CHAPTER 1

Strain and composition at nanometer scales

The aim of this work is to characterise individual nanometer-sized objects using coherent diffraction imaging (CDI). In this chapter, I will first overview the chemical and physical properties of a crystal and in particular, of the objects that are the purpose of this work, $i.e.$, of core-shell nanowires and metallic nanoparticles. I will discuss about their current and potential future applications, whose development requires a deeper understanding of fundamental relationships such as the one between morphology or chemical composition and strain. Important concepts such as atomic displacement or strain will be introduced.
Nowadays few investigations have been done on the strain effects due to thermal expansion mismatch in core/shell nanowires or to gas adsorption in metallic nanoparticles despite the interest that these subjects attract in a large number of communities. Most of these studies were performed on assemblies of nano objects even though their properties may vary from one single structure to another. The lack of knowledge in this field owes to the size of the individual objects and the need of adapted characterisation tools. I will show through examples from literature the matter of this study and how the continuous development of CDI can answer open questions.

1.1 Fundamental properties of crystals

1.1.1 Crystalline structure

A *perfect crystal* can be defined as the periodic repetition of a motif, this one being either a single or a group of atoms, along three non-coplanar directions $\vec{a}, \vec{b}$ and $\vec{c}$ that form the basis of the lattice. Therefore, the lattice can be defined as the set of vectors that satisfy:

$$\vec{r} = u\vec{a} + v\vec{b} + w\vec{c} \tag{1.1}$$

The three basis vectors $\vec{a}, \vec{b}$ and $\vec{c}$ are called primitive translation vectors of the lattice and they form a parallelepiped that is called the *unit cell*. If only one motif is contained in the unit cell, then it is called primitive one and the values of *u, v* and *w* are bound to be integers. The choice of the basis is not unique, as the lattice can be equally defined by any other set of translation vectors. In fact, it is sometimes more convenient to choose a set of vectors other than the primitive ones to describe the crystal, for symmetry reasons. So the different lattices can be classified with respect to symmetry and each unit cell (not necessarily primitive) defines a crystal lattice.
There are 14 different types of 3D lattices, called *the Bravais lattices*. Among the lattice types, we are concerned by the face centered cubic (FCC) lattice, the one of Pt, Si and Ge. The cubic unit cell contains 4 atoms and it is schematised in Fig. 1.1 a); the shortest distance between the atoms in the FCC structure is $a/\sqrt{2}$, where *a* is the lattice parameter. On the other hand, Silicon and Germanium both crystallise in a diamond crystal structure, which can be visualised as a lattice with a motif constitued of two atoms, positioned at (0, 0, 0) and (1/4, 1/4, 1/4). The cubic unit cell contains eight atoms.

Furthermore, the periodic arrangement of the lattice points allows to define the so called *crystallographic directions* and the *lattice planes* that form the crystal.

- Two lattice points define a lattice row $u\ \vec{a} + v\ \vec{b} + w\ \vec{c}$. Every lattice row defines a crystallographic direction, that is written $[u\ v\ w]$. The equivalent directions by symmetry are written $< u\ v\ w >$.
- Three lattice points define a lattice plane. The orientation of a lattice plane is characterised by the Miller indices (hkl) and the family of equivalent planes (thus parallel and equidistant) is written $\{hkl\}$. The distance between two subsequent planes is the *lattice spacing*, usually denoted d_{hkl}.

If we consider now a small object, $i.e.$, a finite crystal, we shall assume that the object contains a large number of unit cells. If $\rho_0(\vec{r})$ is the electron density inside a unit cell, then the density in the whole crystal will be written:

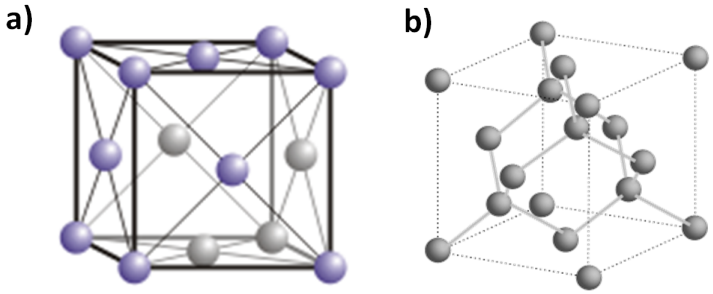

Figure 1.1: a) Face centered cubic structure of Pt. The minimum distance between the atoms is $a/\sqrt{2}$, with $a_{Pt} = 3.924$ Å. b) Diamond unit cell of Si or Ge. The side of the cube is $a_{Si} = 5.431$ Å and $a_{Ge} = 5.6575$ Å respectively.

$$\rho(\vec{r}) = z(\vec{r})[\rho_0(\vec{r}) * \delta(\vec{r} - \vec{R})] \tag{1.2}$$

where $z(\vec{r})$ is a function equal to unity inside the object and zero outside and $\vec{R}$ describes the position of the nodes in the Bravais lattice. This term will be useful in the following, as the amplitude diffracted by the object is proportional to the Fourier Transform (FT) of $\rho(\vec{r})$. Equivalently, the scattered amplitude of the unit cell is proportional to the FT of the electron density in the unit cell ($\rho_0(\vec{r})$): this is by definition the *structure factor*.

At this point, it is also important to note that crystals are anisotropic. Atomic planes with high Miller indices have lower atomic density than these with low index indices. Hence, the atomic planes of a crystal with high-index facets will be more separated and present different chemical properties, notably regarding adsorption and reactivity.

1.1.2 Strain

In real crystals, the periodicity is broken and imperfections must be considered. The shift of the atoms with respect to their ideal positions is described by *strain*.
The origin of strain can be either the presence of defects inside the crystal or an applied external force. In the particular case of nanocrystalline materials, due to their large surface-to-volume ratio, strain can strongly influence their properties, which is especially important for engineering and technological applications.

Let us stay in the context of crystals and consider any position in the ideal lattice, $\vec{r}$, as the origin of the system of coordinates. If the crystal is deformed, every point will be displaced to a new position, $\vec{r}\,'$. The difference $\vec{u} = \vec{r}\,' - \vec{r}$ is called the *displacement vector*. The coordinates of $\vec{r}\,'$ are a function of the ones before deformation ($\vec{r}$), and so are the ones of $\vec{u}$. Thus, if the displacement vector is known, the deformation of the body is entirely determined. Thereby, for an infinitesimal deformation, the strain can be defined as the symmetric part of the gradient of the displacement. If x_i and x_j are the components of $\vec{r}$, the strain tensor can be written:

$$\epsilon_{ij} = \frac{1}{2}\left(\frac{\partial u_i}{\partial x_j} + \frac{\partial u_j}{\partial x_i}\right) \tag{1.3}$$

This is a dimensionless quantity that is often expressed in percent. The strain is related to the stress tensor σ_{ij} by the equation:

$$\sigma_{ij} = C_{ijkl}\epsilon_{kl} \tag{1.4}$$

where C_{ijkl} are the elastic constants forming the *elasticity matrix*, and σ_{ij} are the components

of stress applied to the crystal, $i.e$, the applied force per unit area.

Strain is present at crystal surfaces and at interfaces between different materials. Also structural defects inside the crystal (such as dislocations, grain boundaries or stacking faults) are sources of strain that yield strain inhomogeneities within a single crystal (see Subsection 1.1.3). Besides, strain can be caused by an external force or influence, $e.g.$, by an electrical field (piezoelectricity), or it can be a consequence of temperature changes (thermal expansion). Because several studies on crystals under temperature changes have been performed during this work, let us quickly introduce the *thermal expansion* (ϵ_T) as the resulting deformation due to a temperature change as follows:

$$\epsilon_{T_{ij}} = \alpha_{ij} \Delta T \tag{1.5}$$

where ΔT is the temperature change supposed to take place uniformly throughout the crystal, and α_{ij} are constants called the *coefficients of thermal expansion*. In the case of cubic lattices, the coefficients are scalars and satisfy $\alpha_{ij} = \alpha \delta_{ij}$.

Measuring the strain in nanostructures is particularly important for their characterisation. As deformation at this scale can be very small, it is common to calculate the strain along a specific direction [hkl] in the crystal by considering that the strain inside the crystal is homogeneous, hence averaging the interplanar distances along this direction. In this way, one can define the strain as the variation of the interplanar distance d_{hkl} with respect to an ideal reference value, d_{ref}:

$$\epsilon_{hkl}\ (\%) = \frac{d_{hkl} - d_{ref}}{d_{ref}} \times 100 \tag{1.6}$$

This is the common equation of X-ray strain determination. X-ray techniques are the most widely used to measure the strain because of their accuracy; strains as low as 10^{-4} can be determined[1]. Traditionally measured on large or on assemblies of smaller crystals, there are nowadays few techniques allowing to determine the strain with nm spatial resolution -*i.e.*, to resolve inhomogeneous strain within single structures. The main ones are illustrated in Fig. 1.2; among them, transmission electron microscopy (TEM) and coherent diffraction imaging (CDI) are the ones used in this thesis.

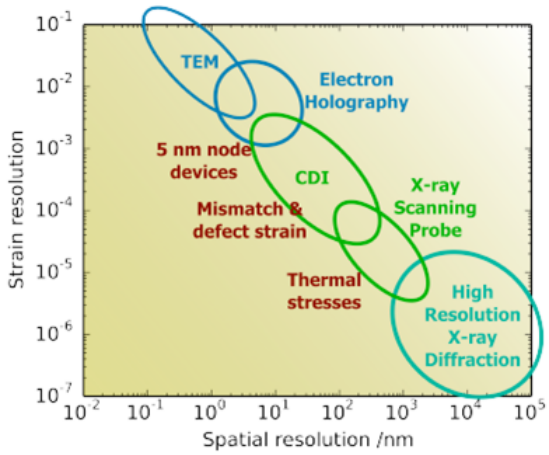

Figure 1.2: Comparison of the resolving power in strain and real space for electron microscopy and X-ray methods, from Ref.[2].

1.1.3 Defects

As previously stated, the arrangement of atoms in most crystalline materials is not perfect and the regular patterns are interrupted by crystallographic defects, which play an important role in the material intrinsic properties. There are different types of defects, often classified by dimensionality as follows:

- 0-dimensional or **point defects:** the symmetry is broken by a single lattice point (or very small set of points); its influence can propagate over the crystal. There are three major types of point defects, which are vacancies (abscence of one atom), interstitials (an additional atom set on a non-lattice point) and substitutional impurities (substitution of one atom by another one of different chemical species).
- 1-dimensional or **line defects: dislocations**. These are defects restricted to a row of lattice points that break the translation symmetry and introduce a strain field in the crystal. Any dislocation can be described by a combination of two types of dislocations:
  - Edge dislocations. They can be defined as the insertion (or removal) of an extra half plane of atoms in the crystal structure (see Figure 1.3 a)). The displacement caused by the dislocation is perpendicular to the defect line.
  - Screw dislocations. The displacement from the dislocation happens along the defect line (see Figure 1.3 b)).

  Edge and screw dislocations in a cubic crystalline structure are represented in Figure 1.3. In both cases it is possible to define the dislocation using the Burgers vector, which depicts the magnitude and direction of the lattice distortion. In real crystals, mixed dislocations are equally common; in this case, Burger vectors lie at an intermediate angle to the local direction of the dislocation line.
- 2-dimensional or **planar defects:** they involve an entire plane of lattice points in a crystal. This group includes surfaces, interfaces of two different crystals and also interfaces within a crystal such as stacking faults, grain or antiphase boundaries.
- 3-dimensional or **bulk defects:** such as voids or precipitates. These defects generally occur on a large scale and will not be further discussed in this thesis.

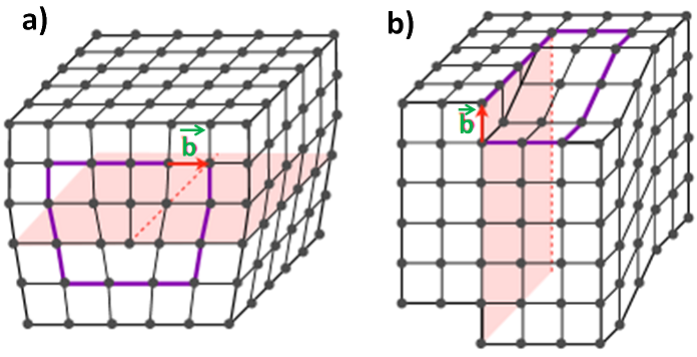

Figure 1.3: Schematic representation of an edge dislocation (a) and a screw dislocation (b) in a cubic crystalline material. The Burger vector, $\vec{b}$, represents the magnitude and direction of the lattice distortion. The shaded area represents the slipped plane, and the dashed line, the dislocation line.

Because of the importance which will be given to the 2-dimensional (2D) defects during this thesis, let us detail a bit more three types of defects belonging to this group.

According to the definition of crystal, any crystalline sample has to be considered as a *defective* or *deformed* crystal, because it is bounded by free surfaces. Thus, as they break the infinite periodicity, surfaces are classified as defects. However, surfaces reveal important information about the crystal, since their surface properties and shape depend on the crystal atomic structure and its orientation ($i.e.$, on the crystal plane that lies parallel to the surface). The preferred shape of a crystal is the one bounded by the surfaces that minimise the total surface free energy. Thereby, in the case of high-symmetry orientations, facets occur[3].

Of particular interest are the internal interfaces between two crystals, as they concern the growth of heterostructures. In these structures, atom layers of different compositions join to form a coherent interface, as illustrated in Figure 1.4 a) and b), where a layer is epitaxied on a substrate (with respective lattice parameters a_1 and a_2) . If the substrate is considered much thicker than the layer, the lattice parameter at the interface plane will satisfy $a = a_1 = a_2$, hence inducing strain in the layer. Note that the layer experiments strain also in the *out-of-plane* direction (perpendicular to the interface). It may happen however, that the two crystals do not fit perfectly, destroying the continuity at the interface or reducing the coherence, so that misfit dislocation arrays can occur (Figure 1.4 c)). It is the case for instance of large misfits (*e.g.*, Ge on Si), where elastic relaxation via 3D island growth is preferred over plastic relaxation. Calculations can be found in Ref.[4] and details in the case of core/shell semiconductor nanowires will be given in Subsection 1.2.1.

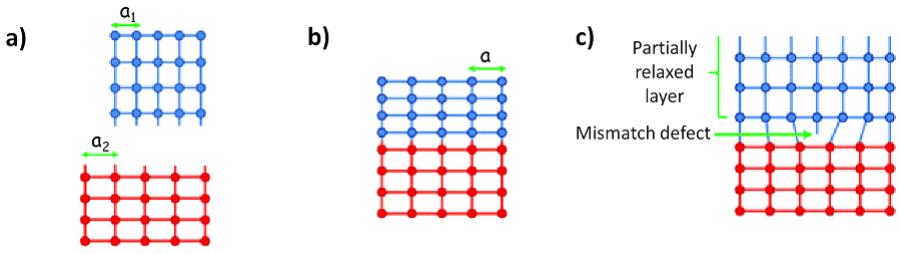

Figure 1.4: Illustration of the atomic structure of two layers before (a) and after epitaxy (b) and (c). In b) a perfect heteroepitaxy is represented, whereas in c) a mismatch defect at the interface induces relaxation in one of the layers.

The last type of 2D crystal defects that must be considered are the stacking faults, as they are widely observed in nanowires. A stacking fault occurs when a single layer takes a different position with respect to that required by the periodic sequence. In an unfaulted face cubic centered structure, the atomic layers are arranged following the pattern ABCABCABC, where A, B and C denote three subsequent layers. If one of the C planes is missing, $i.e.$, the pattern becomes ABCABABC then we are in presence of a stacking fault (see Fig. 1.5).
Other than the removal of one atomic layer, a partial plastic glide for example can give rise to a stacking fault.

Different defects can interact to yield new and singular properties associated to a given material. The way defects affect materials' behaviour constitutes a whole field of investigation.

1.2 One-dimensional crystals: nanowires

Nanowires (NWs) are solid rod-like materials whose diameter, of the order of nanometers (few nm up to few 100 nm), is much smaller than their (unconstrained) length. Their small size in one dimension, results in a large surface area and consequently, a broken symmetry of the

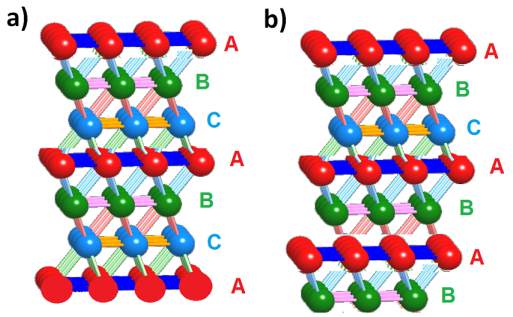

Figure 1.5: a) Perfect crystal with FCC structure b) Stacking fault in a FCC crystalline structure. Atom colors, labeled by different letters according to the text, represent different atomic layers.

crystal. Hence, NWs can present different properties than bulk or 3D materials. The possibility of tuning the composition, crystallinity and morphology has attracted a lot of attention because this comes together with changes in their electronic, optical, mechanical, thermal and chemical properties. To date, numerous studies have been carried out to explore NWs as new building blocks in applications ranging from electronic devices,[5] to batteries[6], solar cells[7] or biological sensors[8].

Nanowires can be “grown" or etched. The two synthesis modes are referred as *bottom-up* and *top-down* approach respectively.

- The top-down approach mainly consists in etching a bulk substrate, by lithography for instance, to remove material locally. Whereas this synthesis mode has strong advantages such as the precision in the location of the wires or in the homogeneity in terms of shape and composition, it is expensive and depending on the way the etching is performed, damage may be induced.

- In the bottom-up approach the structures are assembled from their sub-components exploiting their chemical properties. The initial phases of the materials involved in the growth are usually referred in the name of the process (PVD for physical vapor deposition, VLS for vapor liquid solid, VSS for vapor solid solid, *etc.*). The presence on the substrate of catalysts (metal droplets) or patterning (holes or defects in the substrate) favors the directional growth of the wire. This approach is suitable for the synthesis of heterostructures, because of their ability to get uniform coatings (for example in the case of core/shell NWs) and interfaces free of defects or dislocations.

In this manuscript, only nanowires synthesised by the bottom up approach were studied, so that only this method will be further discussed in the following. Comparison between both methods in the case of semiconductor NWs can be found in Ref.[9] and a detailed review of NWs growth can be found in Ref.[10].

A typical bottom-up growth is illustrated in Fig. 1.6. This is the Vapor-Liquid-Solid (VLS) mode. It starts from the dispersion of colloids on the substrate or the dewetting of a continuous film; then dissolution of gaseous reactants into metallic nanoparticles occur to form a metallic solution. Once the solution becomes supersaturated, a nucleus is produced. Then this nucleus grows and NWs form. Moreover, by changing the source reactants, one can form a heterostructure, as illustrated in the same Figure. Superlattice nanowires can also be achieved by the periodic introduction of different source reactants. Finally, axial and radial heterostructures can also be synthesised by choosing appropriate growth conditions.

Axial heterostructures consist of different material sections, with the same diameter, grown along the wire axis. Radial core/shell heterostructures are made by two coaxial cylinders of

different materials: the inner one forms the core, and the external one, is the shell. Both axial and radial heterostructures are of major interest; the latter are the purpose of this thesis. In literature, the temperature for successful growths of Ge NWs ranges between 260 and 500°C[11,12]; Si NWs need higher temperatures (400-500 °C)[13] and in the case of Ge-core, Si-shell NWs, the deposition of the shell is typically carried out at 600°C[14]. Growth details in our particular case will be given in Chapter 3. Indeed, the possibility of combining materials while manipulating the size forms the basis of new engineering strategies to build innovative materials and devices. Semiconductor NWs, and in particular SiGe NWs, have gained a lot of interest and are actively explored because they offer unique advantages and applications, as confirmed by the amount of literature devoted to these systems (see for instance the reviews of Amato *et al.*, Ref.[15] or the one from Hochbaum *et al.* for energy conversion applications, Ref.[16]). However, there are still important issues to be solved, such as the exact control of the NW position while producing sharp Si/Ge interfaces. But issues are not only at the growth level. Residual strains can have measurable effects on their electronic properties. Therefore, the level of strain at the interfaces must be carefully measured, controlled and understood in order to successfully obtain the desired properties. Si/Ge core shell nanowires are the subject of the next subsection.

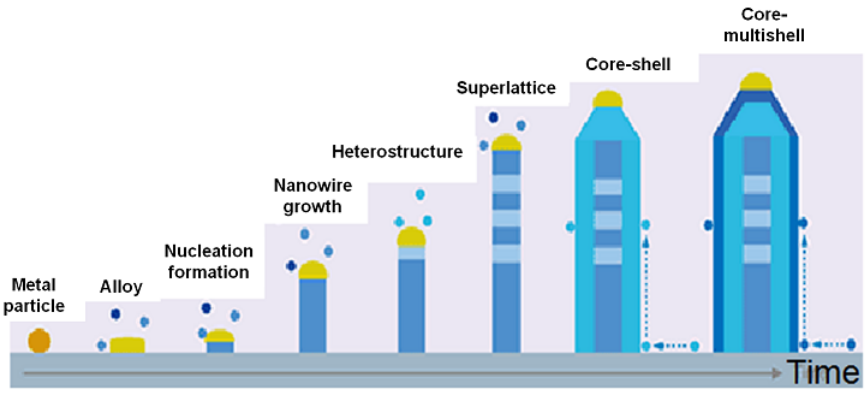

Figure 1.6: VLS growth mode from a metallic droplet and nanowires with multiaxial and radial heterostructures. Image taken from Reference[17].

1.2.1 Ge/Si core/shell nanowires

The concept of nanowire, the typical growth process and the types of NWs have been introduced here above. Now, I will give a general outlook of the particularities of Ge/Si core/shell NWs through a summary of the state of art of this system. I will also introduce the concept of intermixing in Ge/Si systems; the diffusion problem has been poorly studied in 1D materials so that this subject will be completed by numerical models and examples on 2D systems ($i.e.$, thin films).

In order to understand this particular system, let us briefly remind from the previous Section some properties of Si and Ge that will be useful in the following: Silicon and germanium have both the same crystalline structure (diamond cubic structure) and the lattice constant of Ge is larger than that of Si ($a_{Ge} = 5.658$ Å and $a_{Si} = 5.431$ Å respectively). They belong both to the IV group in the periodic table, hence they have four valence electrons and similar physical and chemical properties (such as self diffusivity, Young's modulus, Poisson ratio...). On the other hand, due to the different thermal expansion coefficients of Si and Ge ($\alpha_{Si} = 2.6 \times 10^{-6}\ °C^{-1}$ and $\alpha_{Ge} = 5.9 \times 10^{-6}\ °C^{-1}$) thermal stresses during thermal annealings may influence strain in Si/Ge heterostructures.

1.2.1.1 State of the art

Since the first demonstration of Ge/Si core/shell NWs growth by Lauhon *et al.* in 2002[14] many efforts have been dedicated to understand and control aspects of Ge-core, Si-shell NWs growth. Compared to pure Si or pure Ge NWs, core/shell structures present several advantages, such as a better conductance and a higher mobility of charge carries due to the conduction and valence band offsets between both materials[18,19].

When studying core/shell nanowires, there are two important factors to take into account: the size and the composition. Therefore, literature on characterisation of core/shell NWs can be divided in two groups:

- Studies as a function of the size effect, carried out by fixing the composition of the wire and varying the diameter.
- Studies as a function of the alloying effect, where the diameter is fixed and the composition is varied.

In the first group, numerical investigations have been done on the quantum confinement effect and the electronic properties of the wires depending on NWs' diameter. The density functional theory calculations works of Amato *et al.*[20] or the ones from Musin *et al.*[21] illustrate this group and how the Ge/Si core/shell are the most promising heterostructures among the possible Si/Ge geometries. Indeed, high-performance coaxially gated field-effect-transistors are advantageous in the development of NW-based devices, as the alignment of the energy band gaps at the interface can be manipulated, hence driving hole injection into either Ge core or shell regions. In a similar way, for the second group, the effect of alloying on the electronic properties has been discussed by Amato *et al.*[22] using numerical simulations. These studies concern pure Ge-core/pure Si-shell structures but also doped or $SiGe_x/Ge_{1-x}$ core/shell NWs.

There is nevertheless a third group to which the investigations on Si/Ge NWs reported in this thesis belongs: the effect of strain. As previously stated, strain can strongly influence the properties of nanostructures and in our case for example, the strain modulates the band gap of the NWs, *i.e.*, their electronic properties. Hence, strain could be used as a parameter in industry if the precise control of the strain level of the heteroepitaxy were managed[23,24,25,26].

In addition to extrinsic sources of strain like the presence of a substrate, the growth method or any applied deformation, Si/Ge core/shell NWs are intrinsically strained due to the large mismatch between the materials (which is about 4 %). The accommodation of large lattice mismatches can lead to interfacial defects or to a pseudomorphic strain.
The intrinsic strain distribution within semiconductor nanowires was theoretically studied[a] by Grönqvist *et al.* in 2009[27]. Their model, consisting in NWs with a diamond crystalline structure, was later extended to NWs with wurtzite structure and different morphologies by Ferrand *et al.*, who in addition, applied the model to NWs with different growth axis and multishell NWs[28]. Both studies are performed within the continuum elasticity framework and their results are in agreement in the case of cubic semiconductor NWs along the $< 111 >$ growth direction (Fig. 1.7). The most appealing result is perhaps the discontinuity at the core/shell interface with uniform axial strain (ϵ_{zz}) in the core and in the shell. As the lattice parameter of the core is larger than the one from the shell, the core presents an axial compression ($\epsilon_{zz} < 0$) whereas an axial tension can be observed in the shell ($\epsilon_{zz} > 0$). The inhomogeneities of the *in-plane* strain, ϵ_{xx} and ϵ_{yy} are attributed to the faceted shape of the wire, as these effects are not observed in cylindrical wires. Finally, small but non zero local shear strains (ϵ_{xz} and ϵ_{yz}) are observed. The authors explain this fact as a consequence of a warped cross section in the $xy-$plane. Hence, the *in-plane* compression of the core would lead, in addition to a radial compression of the shell, to

[a] This study focuses on NWs of large diameters, contrary to previous numerical investigations that concern only small diameters, *i.e.* up to 5 nm.

a non flat surface.
Their results apply to both infinite and finite NWs. As the core of the wire is radially compressed by the shell, in the case of finite wires, ϵ_{zz} would expand along the axial direction, whereas this expansion is prevented by the shell in the case of an infinite wire or far from its ends in the case of the finite one.

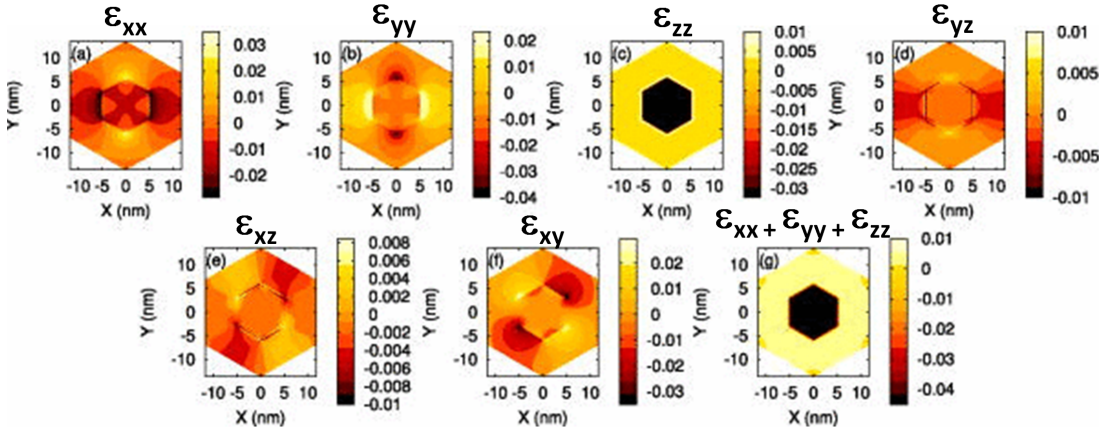

Figure 1.7: Strain fields of an infinite GaAs-core GaP- shell nanowire (lattice mismatch $\sim 3.6\%$), from Reference [27]. The hydrostatic strain evidences that the core is compressed while the shell is expanded.

The dependence of the strain with the diameter of the NW is also subject of investigation, as the distribution of strain within the wire compromises its stability. Continuum mechanics calculations predict a thickness limitation for coherent interfaces given that, in the case of a coherent interface, the thicker the shell, the more the Ge-core is compressed. In the case of cylindrical nanowires, calculations predict that there exists a critical core radius for which the strain relaxation is unfavourable for any shell thickness. In the same way, above this radius, relaxation of the shell increases towards the planar film values [29,30]. Beyond this coherence limit, defects form at the interface [31,32,33]. This can be observed in the equilibrium diagram shown in Fig. 1.8; the region at the left of each curve is the coherent region, and the region at the right is incoherent. Small diameters enable lateral relaxation so that large mismatch can be accomodated keeping a coherent interface. As the diameter increases, the critical radius decreases and it is sometimes more favorable to introduce misfit dislocations to reduce the mismatch strain[b]. This is $e.g.$ the case of Si/Ge NWs, where dislocations with larger Burger's vector $\vec{b}$ can be accomodated because of the large mismatch.

Despite the large amount of theoretical studies, few experimental characterisations of core/shell Ge/Si NWs can be found in literature. The intrinsic strain in these structures has been mainly studied by means of X-ray diffraction [19,36], Raman spectroscopy [37,38] and TEM [39,40].

The first strain measurements by X-ray diffraction were performed by Goldthorpe *et al.* on VLS-grown Ge-Si NWs [19]. They measured the axial and radial strain of NWs with different shell thicknesses: the Ge core was found to be compressed and not affected by the rough shell. Furthermore, the axial strain was found to decrease inversely with the increase of the shell thickness, hence loosing the coherence at the interface [32]. The axial relaxation regarding the theoretical predictions is justified by the formation of a periodic rough Si layer at the interface that favors the formation of dislocations, mostly extrinsic stacking faults (see Figure 1.9). Further investigations

[b] Note that the strain relief mechanism is not clear and some authors have stated that formation of islands at the interface is more favorable than the introduction of misfit dislocations [34]

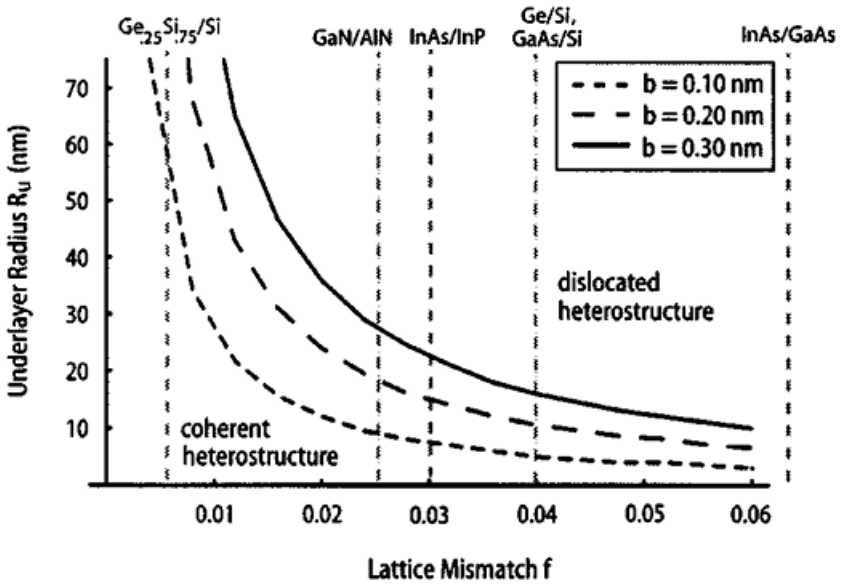

Figure 1.8: Critical NW radius versus lattice mismatch as a function of Burger's vector magnitude, calculated assuming isotropy and elasticity, from Ref.[35]. The critical radius decreases while increasing the lattice mismatch.

have shown that smooth Si surfaces, thus dislocations-free NWs, are achievable by changing the growth direction axis[14,36,41] or by deposition of a SiGe (Si-rich) shell instead of pure Si[36] in the presence of HCl during growth, which reduces gold diffusion from the catalyst. Note nevertheless that Si and Ge are elastically anisotropic, so that the strain and stress states depend on the growth axis. The Ge/Si core/shell NWs studied during this PhD thesis were grown along the $< 111 >$ direction on a Ge substrate (see Chapter 3).

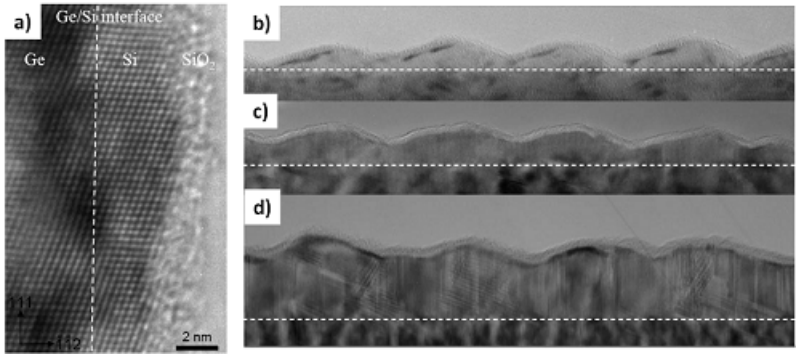

Figure 1.9: a) High-resolution TEM image of a 18 nm diameter Ge NW with a 2 nm Si shell. The shell is single crystalline and heteroepitaxial with the Ge core. TEM images b), c) and d) show the periodic modulation of the surfaces for a Ge core of 26 nm and shell thickness of 4.5, 6 and 17 nm respectively. From Ref.[19].

Despite Goldthorpe *et al.* showed the agreement of their measurements with Liang's theoretical model[32] of the maximum strain that a core/shell Ge/Si NW can accommodate (for a given diameter) before nucleation of defects, the first experimental measurement of the critical thicknesses for strain relief was performed by Dayeh *et al.* in 2012[39]. They first showed that a Si shell of 3 nm ensures smooth and crystalline shell for any core diameter (from 10 to 100

nm)[42] - proving at the same time theoretical predictions of the coherence limits[30]. Second, they showed that for a 16 nm diameter Ge core, the equilibrium critical thickness of the shell is 3 nm, accommodating a 3 % coherent strain. At this and smaller values, the epitaxied shell is perfectly coherent and there are no defects at the interface. For smaller core diameters, larger equilibrium critical shell thickness are expected. For shell thickness larger than this critical value, dislocation gliding along the inclined {111} planes were found to be responsible of the coherence loss.

1.2.1.2 Intermixing in Si/Ge

If the importance of avoiding misfit dislocations at the interface between the core and the shell in radial heterostuctures has been pointed out, it is equally important to obtain abrupt interfaces regarding future applications such as accurate band-gap engineering. The junction abruptness measures how fast the materials change across the heterojunction, and as growth is carried out at high temperatures, diffusion plays a key role in the composition gradient at the interface. The diffusion coefficient, D, depends on the temperature as follows:

$$D = D_0 e^{-\frac{Q}{k_B T}} \tag{1.7}$$

where D_0 is the diffusivity pre-factor related to the material, k_B is the Boltzman constant, Q the activation energy for diffusion, and T the temperature. Table 1.1 summarises these parameters for the materials involved in this study. Note that diffusion coefficients may vary if one takes into account defects in the crystalline layers such as the presence of Carbon or Oxygen[43], or defects such as dislocations.

	Diffusant	$D_0(\ cm^2/s)$	**Q (eV)**	**Temperature range (°C)**
Si	Au	2.4×10^{-4}	0.39	700-1300
	Ge	3.5×10^{-1}	3.92	855 - 1000
	Si	1.54×10^{-2}	4.65	855 - 1175
Ge	Au	2.25×10^{2}	2.5	600 - 900
	Si	2.4×10^{-1}	2.9	650 - 900
	Ge	2.48×10^{1}	3.14	549 - 891

Table 1.1: Diffusion data for the system Si-Ge, from Ref.[44].

Axial nanowire heterostructures typically exhibit finite concentration gradients across the interface, leading to a region with mixed composition ratios whose breath increases with the NW diameter[45,46] (see Fig. 1.10 a) and b)). These diffuse interfaces are due to the effect known as *reservoir effect*, which consists in the attribution of this composition gradient to the dissolution of growth species in the alloy seed particles. Progress has been made through growth alternative approaches to VLS or by using different catalysts[47,48]. By contrast, interface abruptness is not a problem in core/shell Ge/Si growth, as the two involved growth steps ($i.e.$, Ge NWs formation and Si deposition) are based on different synthesis methods (Ge NWs grown by catalysed VLS, then uncatalysed radial growth). Si and Ge precursors do not mix and sharp interfaces are obtained[14,49], as observed in Fig. 1.10 e). This can be understood by taking for instance the growth rates from Lauhon *et al.*[14] and the diffusion coefficient calculated from the values given in Table 1.1. In the case of radial growth of a 50 nm thickness *p*-doped Si shell (at 600° C after the growth of Ge wires at 380° C), interdiffusion along a length of 1 nm is expected, which is negligible for such a thick shell.

Whereas the diffusion during the growth of radial heterostructures is not a major issue, the case of axial heterostructures illustrates well the intermixing problem. Indeed, diffusion can happen not only at the interface because of the two materials, but it may also arise from the metal catalyst (generally gold). Gold contamination along pure Si wires has been shown to modify the strain[50,51], although the influence of gold in the electric properties of the wire is

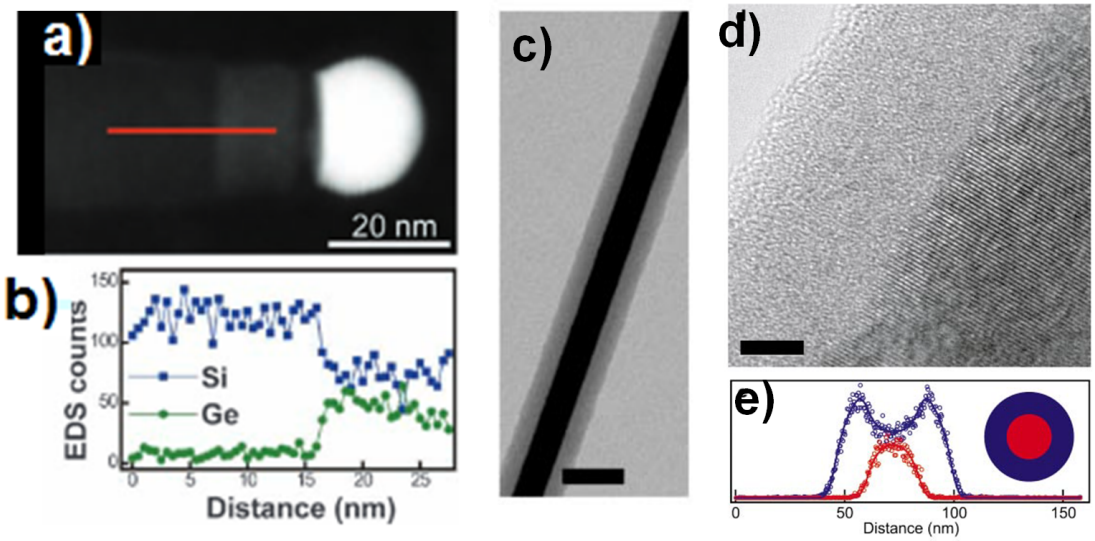

Figure 1.10: a) Scanning Transmission Electron Microscope (STEM) image of a $Si/Si_{1-x}Ge_x$ NW of 21 nm diameter. b) EDS line profile of Si and Ge through the $Si/Si_{1-x}Ge_x$ junction, as indicated in c). A sharp transition of less than 2 nm from Si to SiGe is observed. Both from Ref.[45]. c) TEM image of a Si-shell, Ge-core NW showing the core/shell structure. d) HRTEM image of a representative NW with a Si amorphous shell. e) EDS profile showing the abruptness of the interface. Scale bars are 5 nm. From Ref.[14]

negligeable[51]. In the case of pure Ge NWs, it was found that Au catalyst does not diffuse during growth[48]. Nevertheless, this is the reason why the catalyst is sometimes etched or removed before *in-situ* shell deposition in the case of radial heterostructures.
Note that the high surface area-to-volume ratios of nanostructures asks for additional factors to be taken into account and diffusion may become quite important at this scale. For instance, (in bulk) gold diffuses more slowly in silicon than in germanium (Table 1.1). However, in the case of gold diffusion in Ge NWs, the diffusion coefficient was found to be 3-4 orders of magnitude lower than in bulk, whereas the rate of gold diffusion into a Si NW is faster than in bulk (see experimental values in Table 1.2, from Ref.[52]).

Moreover, the diffusion constant *D*, not only depends on temperature but also on the Ge content (which may be important in the case of intermixing during the growth of heterostructures) and lattice strain. The asymmetric profile as a consequence of intermixing was carefully studied by Schorer *et al.* in short-period Si/Ge superlattices by means of phonon Raman spectroscopy[53]: Ge-rich regions rapidly intermix with Si whereas Si thin layers preserve a core of nearly pure Si (in temperature ranges between 430 and 780°C). In the same kind of structures, Si was observed to diffuse into Ge layers at temperatures as low as 450°C while being strongly dependent on the Si content and therefore varying during the interdiffusion process itself[54]. On the other hand, the influence of lattice strain on Si/Ge interdiffusion was observed not to be significant by Schorer *et al.*[53] whereas Cowern *et al.*[55] showed a decrease of diffusion under compressive strain. In the same way, Zaumseil *et al.*[56] observed a strong enhancement of the interdiffusion with the increase of relaxation in their studies of $Si_{1-x}Ge_x$ layers.
The curious asymmetry in the diffusion properties between Si and Ge and the difference of diffusivity behaviors at nanoscale with respect to bulk (*i.e.*, the discrepancies between classical theories and experimental results) raise fundamental questions and ask for a careful evaluation of interdiffusion, as well as studies on the consecutive strain[57] that may directly influence

electronic properties.

	D (cm^2/s)		Temperature ($^\circ C$)
	Nanowires	Bulk	
Au in Ge	10^{-16}	10^{-10}	700
	10^{-12}	10^{-8}	900
Au in Si	10^{-7}	10^{-8}	800
	10^{-6}	10^{-9}	900

Table 1.2: Diffusion coefficients of Au in Si and in Ge NWs for comparison with diffusivity in bulk, after [52].

Even though core/shell Ge/Si NWs seem to be stable against diffusion during growth, post-growth annealing experiments can give important insights into the properties of the materials. For example, an *in situ* annealing experiment performed on a GaAs NW revealed that a catalyst nanoparticle must be preferred in its solid state (rather than liquid) during growth[58]. Besides phase changes, post-growth annealing experiments allow to investigate the stability of the nanowires, in particular of the interface, and chemical intermixing at high temperature, therefore defining the limits towards industrial applications. For instance, stabilities and duration of solar cells based on nanowires or heterostructure must be improved to increase the efficiency and durability[59,60,61]. Moreover, theoretical studies predict morphological instabilities of core/shell NWs under high temperature due to mismatch strain, to the surface/interface diffusion and to volume diffusion[62]. The instabilities due to thermal stress for future operational devices have been recently reported for the particular case of core/shell Ge/Si NWs[63]. The authors calculated the thermal stress on thin NWs (10 nm diameter) with coherent interfaces and fixed ends, meaning clamped on a substrate or any other material as expected to be used in operational devices. They found that the critical length for the NW to be stable under axial compressive stress was function of the linear coefficient expansion, which decreases with the core diameter in the case of Ge-core/Si-shell NWs grown along the $< 111 >$ direction. The critical length of the NW (l_c) for a given upper bond of the temperature (ΔT_c) can be calculated as follows:

$$l_c^2 \Delta T_c = \frac{\pi^2 D^2}{4\alpha} \tag{1.8}$$

where α is the thermal expansion coefficient and *D*, the diameter of the NW - that is supposed to be cylindrical. Therefore, the geometrical parameters (length, diameter) can be chosen depending on the thermal mismatch effect between the substrate and the component. Interestingly, the bigger the core diameter, the shorter must be the NW to operate without risk of elastic structural failure at high temperatures. Above this limit, the temperature would induce a high thermal stress that would lead buckling instabilities.

To date, apart from the theoretical predictions, very little is known about how temperature affects core/shell Ge/Si NWs. Lauhon *et al.* mentioned in their pioneer work that at 600°C, a polycrystalline Si-shell would become crystalline, preserving the abrupt interface between both materials[14] but leading to a strain relaxed heterostructure. The possible intermixing after growth was studied by multiwavelength anomalous X-ray diffraction[64] on Si-core, Ge-shell NWs; results are summarised in Fig. 1.11. Surprisingly, intermixing occurs already at 400°C. The intermixing at high temperatures will be studied during this thesis work and some discrepancies will be shown, despite this is not understood so far.

1.3 Metallic nanoparticles

Nanoparticles (NPs) are defined as objects with sizes in the range of $10^{-9} - 10^{-7}$ m in the three dimensions. Because of their small size, NPs present optical, electronic, catalytic and magnetic

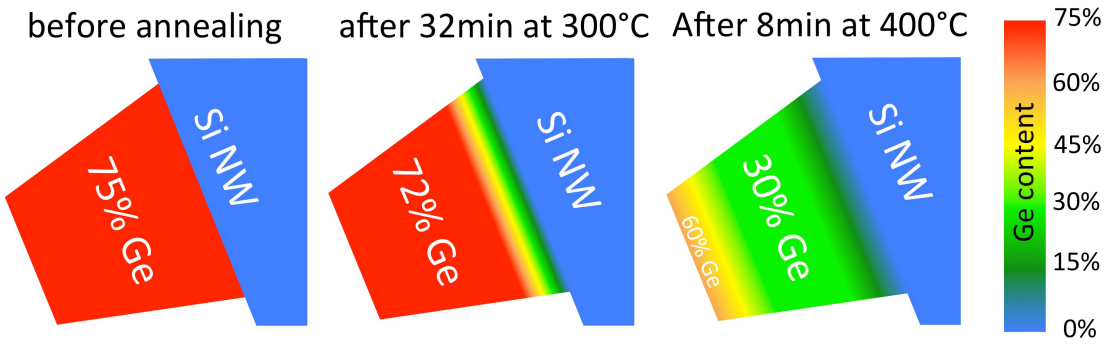

Figure 1.11: Effect of post growth annealing on Si-core, Ge-shell NWs, from Ref. [64]

properties that differ from the ones' of macroscopic objects and can be tuned for the development of new nanodevices [65,66].
As in the case of NWs, the main reasons why NPs' properties differ from those of the bulk are related to surface and quantum effects. Quantum effects (due to the electrons confinement that yields discontinuous energy levels) can be managed reducing the size of the particles. On the other hand, surface effects make materials chemically more reactive. Atoms at the surface of large crystals have much more neighbours than the atoms at the surface of particles, what can be equivalently explained in terms of the *coordination number, N*, which is defined as the number of nearest neighbours. NPs have lower coordination number, $i.e.$, they are more reactive.
Metallic NPs are therefore potential candidates for many fields but their synthesis and processing must be first managed, since size, shape, composition and structure are decisive in the NPs' properties. They must be grown in a controlled and reproducible way, and homogeneity over the sample is desirable, which is specially challenging in terms of reactivity and agglomeration for the available synthesis methods. Method synthesis of NPs are beyond the scope of this thesis but details can be found in Refs. [67,68].

One of the potential applications of metallic NPs is as catalysts. Catalysts are substances that accelerate chemical reactions without being consumed. In presence of a catalyst, the corresponding reaction requires less activation energy and as the catalyst is recovered in its original form, the chemical reaction can be seen as a cycle. In this way, a more efficient use of raw materials and a minimization of waste production is possible everyday in industry, where alternative catalytic routes are applied to accelerate reactions or make them happen at more convenient conditions (such as lower temperatures or pressures).

Depending on the way catalysts are present in the reaction, there are two types of catalysis:

- **Homogeneous catalysis:** both the catalyst and the reactants are in the same phase, $i.e.$ all are molecules in the gas or liquid phase.
- **Heterogeneous catalysis:** solids catalyse reactions of molecules in gas or solution. Catalytic reactions occur at the surface of the solid.

Chemical industry is largely based upon catalysis: roughly 85-90 % of all products are made in catalytic processes, playing an increasingly important role in fields ranging from energy, environment and agriculture to health care. Heterogeneous catalysis are the most commonly used in industrial processes. The use of nanometer-sized particles (with typical dimensions of between 1 and 10 nm) supported on an inert or porous structure as catalysts is generally chosen because of the cost reduction of the often expensive materials (e.g. platinum), but this is not the only advantage. As mentioned earlier in this Section, NPs have actually higher reactivity: the smaller

the particles, the faster the reaction (see Fig. 1.12a)). The size as the determinant factor of the activity of a metal nanocrystal was established in 1997 through the works of Haruta *et al.* [69], who showed for the first time the excellent catalytic properties of gold nanoparticles. Since then their use has been extended to an important group of reactions and numerous applications. However, size is not the only parameter influencing the reactivity of the NPs. Shape, structure, composition or even the type of support where the active nanoparticles sit[65,69] influence their catalytic activity.

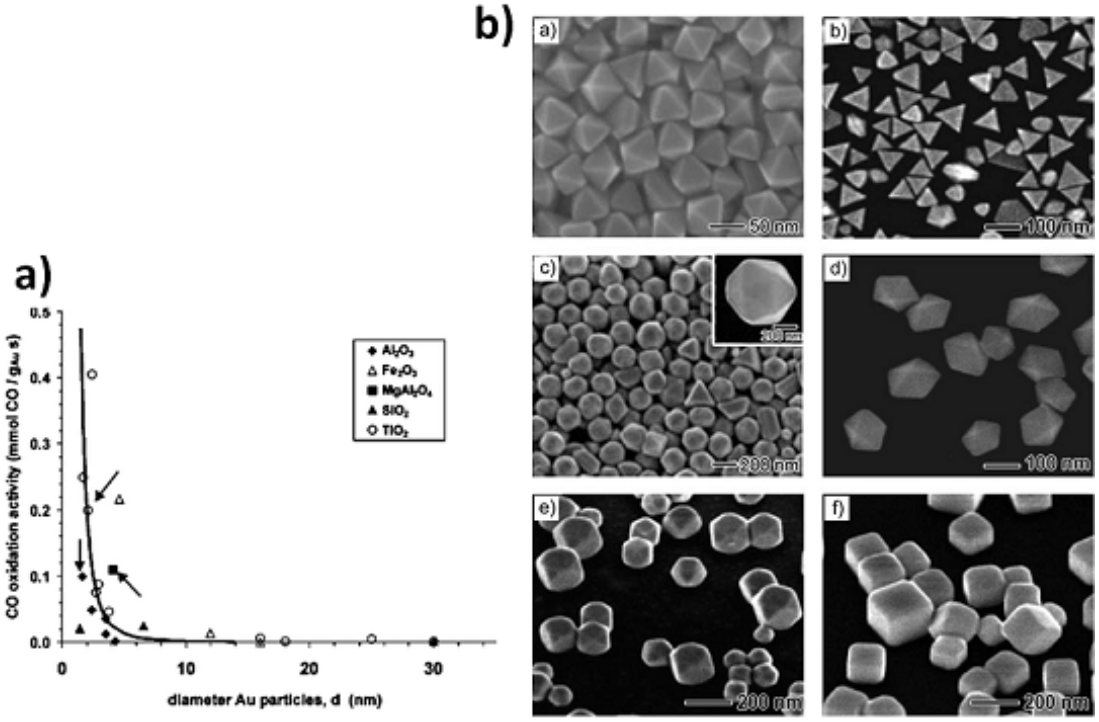

Figure 1.12: a) Measured activities for CO oxidation at 273 K as a function of the average particle size. The symbols are used to differentiate the support of the Au NPs. From Ref. [69]. b) Electron microscopy images of Au nanocrystals with different shapes, from Ref. [67]

The dependence of the particles shape and their recycling potential was very little explored until 2007, when it was finally demonstrated that the selectivity of the particles was more sensitive to the packing of atoms on the surface or the exposed facets of the crystals[70]. In this way, *e.g.*, the fact that platinum with {100} facets is more active for reactions involving H_2, whereas facets {210} are mostly active where CO is implicated[71] started to be used at the nanoscale level and the design of NPs with the convenient facets for each reaction or application began. Since then, much efforts have been dedicated to shape-controlled synthesis of metal nanoparticles and many different shapes have been reported, mostly for Au, Ag, Pd and Pt[67,72]. Figure 1.12 show some of the shapes obtainable for Au NPs, prepared by different synthesis methods. In spite of their complexity, solution-phase synthesis are generally preferred because of the versatility of obtained shapes, which differ from the Wulff polyhedrons with low-index facets obtained in inert gas or vacuum.

Catalysis is therefore one of the fields where metallic NPs play a key role because they are efficient, selective and recyclable. They can potentially reduce the energy consumption in the reactions activation, taking advantage of the fact that only surfaces or even particular orienta-

tions are active in a reaction, thereby saving material and responding to the requirements of the modern concept *green catalysis*. This is supported by the attribution of the Nobel prize to Gerhard Ertls in 2007 for his understanding of catalyst mechanisms and studies on the oxidation of carbon monoxide on platinum reaction. However, understanding the intimate chemistry of metallic NPs is a complicated task since factors like size and shape, but also composition or strain play key roles in the reactions and all of them have to be taken into account, and ideally, decoupled. The next subsection is dedicated to the particular properties of NP catalysts, with emphasis on the strain role in this field.

1.3.1 Strain in nano-particle based catalysts

The importance of size and shape of catalyst NPs has been introduced. Both factors may yield local changes in lattice parameter and strain distribution within nanoparticles, which can also affect their catalytic activity. Strain must therefore be considered in order to develop new successful synthesis methods. Understanding how all these properties are related to catalytic reactivity is possible if the process is followed on one single particle at a time, instead of on billion simultaneously reacting particles, since uniformity and reproducibility make part of the challenging issues in the synthesis of metal nano-particles.

Some strain effects are actually intrinsic to nanoparticle synthesis, since either expansion or compression of the crystal lattice can be originated by their own growth properties such as size, shape or composition[73]. Thus, the strain sources reported in the case of NWs can be extended to the three dimensional case to be mainly applied here. For instance, core-shell NPs lead intrinsic strain because of the lattice mismatch between different materials. Figure 1.13 illustrates different sources of strain in the case of metallic nanoparticles.
In Chapter 5, we will deal with the strain due to morphology since our study concerns regularly shaped platinum particles[72] whose facetted structure is far from the equilibrium shape classically given by Wulff construction. As stated in the introduction of this Section, shaping nanoparticles is promising for better stability and higher catalytic activity because the vertices and the edges contain under-coordinated surface metal atoms that make more favorable molecules adsorption[74]. Tian *et al.* succeeded to synthesise in a controlled way polyhedral shaped particles characterised by high-index Miller facets to take advantage of their selectivity properties[72], as shown in Fig. 1.14. For the interest that the CO oxidation reduction deserves, in this thesis the behavior of *tetrahexahedral* NPs, with preferred {210} facets, will be investigated.

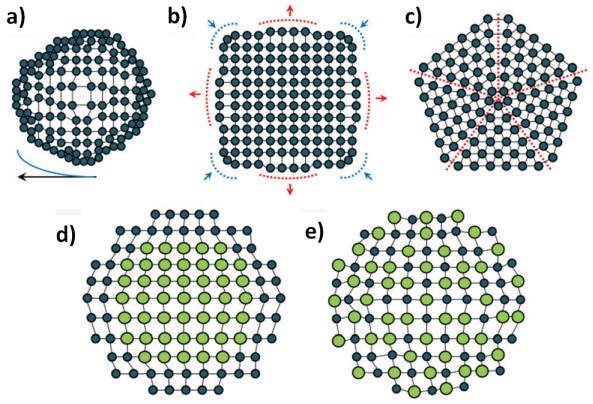

Figure 1.13: Sources of lattice strain in NPs, from Ref.[73]. a) Surface relaxation due to size. b) Anisotropic strain due to shape. c) Strain at grain boundaries due to twinning and unfilled volume. d) Strain from epitaxy in core-shell structures. e) Strain due to alloying.

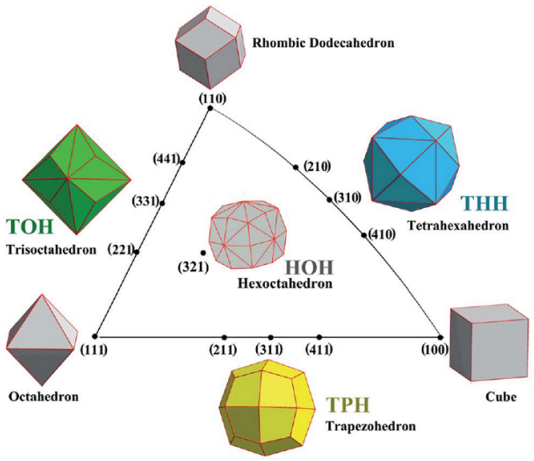

Figure 1.14: Illustration of the complex shapes of high-index faceted Pt NPs achieved by Tian *et al.* in 2007[72].

Whereas the morphology of the particles constitutes an advantage in catalysis, the displacement of atoms on surfaces may induce a strain gradient in the particles. The shape-strain relationship still needs to be understood. Indeed, multiple sources of strain can operate simultaneously in the same sample and their influence can not directly be decoupled. Very few techniques allow for a visualization of the strain distribution in individual particles, TEM being one of the mains[75,76], so that very little is known about the strain effects in catalytic reactions. As we will see in Section 1.4, CDI offers unique opportunities to analyse three-dimensional (3D) shape and strain *simultaneously* and *during* catalytic reactions.

State of the art for characterisation of catalyst nanoparticles combines high resolution TEM[75,76], synchrotron X-ray diffraction on assemblies of particles[77,78,79] molecular dynamics (MD) simulations[79] and recently, CDI. By means of CDI of crystal catalysts, some preliminary works have already been reported showing compressed or expanded atomic arrangements at the surfaces, edges or vertices in the crystals[80,81,82]. Note that CDI deals with big crystals compared with the ones used in real catalysis process; the feasibility of this technique is however limited by the coherent flux of the X-ray beam, hence CDI can only be successfully applied on crystals much bigger than the ones used in real catalyst process. The smallest crystalline size that can be measured is limited nowadays to 100 nm[83], but coherent properties of X-ray sources are expected to increase in the near future[c]. The difficult access to strain in so small particles justifies the study on a bunch of crystals with traditional X-ray methods.

Let us mention two works carried out *operando* and revealing interesting particles behavior in presence of gas, that evidence that NPs can even change in terms of size and shape during reaction. First, Hejral *et al.* measured assemblies of highly homogeneous particles using X-ray surface diffraction with different compositions. The samples, consisting of alloyed Pt and Pt-Rh alloys, were exposed to CO and O_2 with different mixing gas composition in successive steps towards higher activity conditions (see Fig. 1.15). Their results show that Pt-rich particles experimented the most remarkable shape changes, $i.e.$, facetting changes, with an increase in height[77].

The second example from literature, is the oscillatory behavior observed by Vendelbo *et al.* on Pt particles under the same reaction conditions, $i.e.$, during CO oxidation[76]. While they focus their study on the observation by TEM of a single particle during the reaction, the authors observe periodic facetting changes that follow the periodic CO changes (see Fig. 1.16).

Hence, evidence of shape changes during reactions, as well as preferential crystallographic

[c] http://www.esrf.eu/ebs

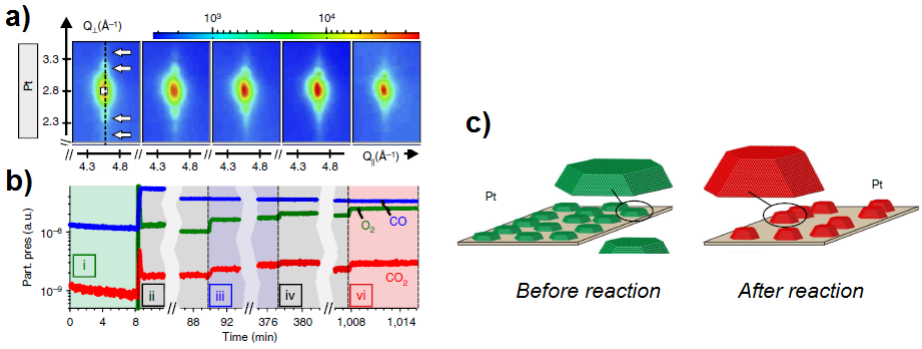

Figure 1.15: a) Reciprocal space maps of the averaged Pt NPs under different CO/O_2 mixtures. The thickness fringes are visible because of the shape homogeneity over the sample and they dissapear while increasing the O_2 flux in the reactor. b) Partial pressures at the different stages of the experiment. c) Average particles shapes and sample morphology before (green) and after (red) reaction. After[77]

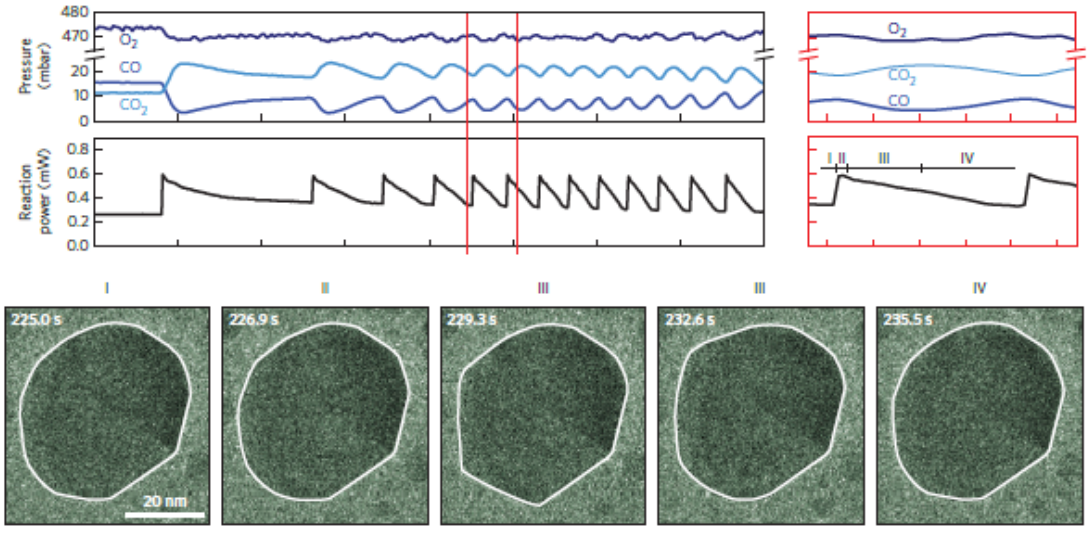

Figure 1.16: Correlation of oscillatory CO oxidation reaction with the morphology of a Pt NP. From Ref.[76]

facets orientation depending on the gas environment and reversibility[84] have been proved and by means of different methods. These findings can be crucial in the development of synthesis methods, since the knowledge and understanding of the behavior during reaction open pathways to design resistant and stable particles. However how these changes affect the strain within the crystals is still not well determined.

1.4 CDI as a characterisation tool

Imaging the structural properties of crystalline nanostructures and understanding their relationships with their physical properties is an actual need to develop and enhance the performance of current devices. The physical characterisation of such small objects with the adequate reso-

lution is currently achievable by few techniques. Atomic force microscopy (AFM) and scanning tunneling microscopy (STM) provide topography and morphology information respectively with atomic resolution. Scanning electron microscopy (SEM) generates 2D images with both topography and morphology information, in addition to elemental composition with Energy Dispersive X-Ray (EDX) analysis. 3D compositional imaging is possible at atomic resolution by tomographic atom probe (TAP), though the field of view is limited (at best, volumes of 100 nm diameter by 500 nm long can be analysed[85]). However, none of these techniques give information about the displacement fields or strain within the crystals. Apart from spectroscopic methods (Raman, X-ray photoelectron spectroscopy (XPCS), *etc.*), that provide only intra- and inter-particle averaged data, X-ray conventional techniques provide strain information on large samples or assemblies of nanostructures. But as it has been highlighted in this chapter, it is needed to map strain and composition locally and within individual objects. Hence, transmission electron microscopy (TEM) and X-ray lensless imaging methods are the most suitable methods to this aim, as they seem to respond to the main requirements: high strain sensitivity, good spatial resolution and compatibility with *in situ* experiments. TEM has been proved to be a powerful technique achieving even sub-ånstrong resolution. However, the higher the resolution, the smaller is the imaged zone. Also, in some cases sample thickness is a limitation since samples have to be carefully prepared and the strong electron-matter interaction may damage or destroy the sample.
X-ray microscopy techniques have seen a great development in the past few decades, and in particular, X-ray lensless imaging methods overcome problems such as lenses aberrations[86]. Hence, lensless imaging techniques seem to be the most promising ones to look below the surface of the samples. Some of these techniques (Bragg coherent diffraction imaging, holography and ptychography) will be further discussed in the next chapter, but let us close this one with some relevant examples of Coherent Diffraction Imaging (CDI) through last years to illustrate the continuous developing capabilities of this technique.

The first demonstration of lensless microscopy consisted in the inversion of a two-dimensional diffraction pattern, measured in small angle geometry, of gold nanospheres dispersed on a membrane[87]. The success of the reconstruction with the adequate algorithms was followed by the reconstruction of crystals from diffraction patterns measured in Bragg geometry[88] and later by the determination of the inhomogeneous strain field within the object[89]. The complete 3D displacement field was demonstrated afterwards by Bragg CDI measuring several Bragg reflections of a single ZnO nanorod[90]. At the beginning limited to weakly strained crystalline samples, the method was fast applied to many different systems: from nanowires[91,83] to polycrystalline thin films[92], achieving typical resolutions of a few nanometers and a strain sensitivity better than 10^{-3}.

The promising capability of measuring crystal properties *in situ* or *operando* has been also demonstrated. *In situ* CDI experiments have been successfully carried out at high pressure[93,23], high temperature[92,94,95] or during hydration[96], for which the relative simplicity of the experimental set-up is remarkable, consisting of a Kapton film wrapping the sample with the solution container close to it. Nevertheless it is worth to note the feasibility of CDI experiments in multiple environments (aqueous[97], reactive[98,99], ultra high vacuum chambers[100]...). The development of particular sample environments have allowed diffusion studies (see e.g. the results of Xiong *et al.* in Fig. 1.17, where the atomic displacement during Cu diffusion in a Au nanocrystal has been investigated[100,101]) and it has been also possible to measure the phase change of Pd nanoparticles during catalytic reactions[102] or the behavior of dislocations in cathode nanoparticles during electrical measurements[103].

The case of highly strained crystals is more difficult because one of the assumptions of CDI is the homogeneity of the initial guess of the reconstructed object. Nevertheless, more adapted algorithms with additional constraints taking into account inhomogeneities in the density and phase have been developed[104,105], and some successful studies have been already reported[106,107,108], which are often supported by simulations that allow to adjust the initial guess and prevent knowledge about the expected strain field. In order to extend the method to strained

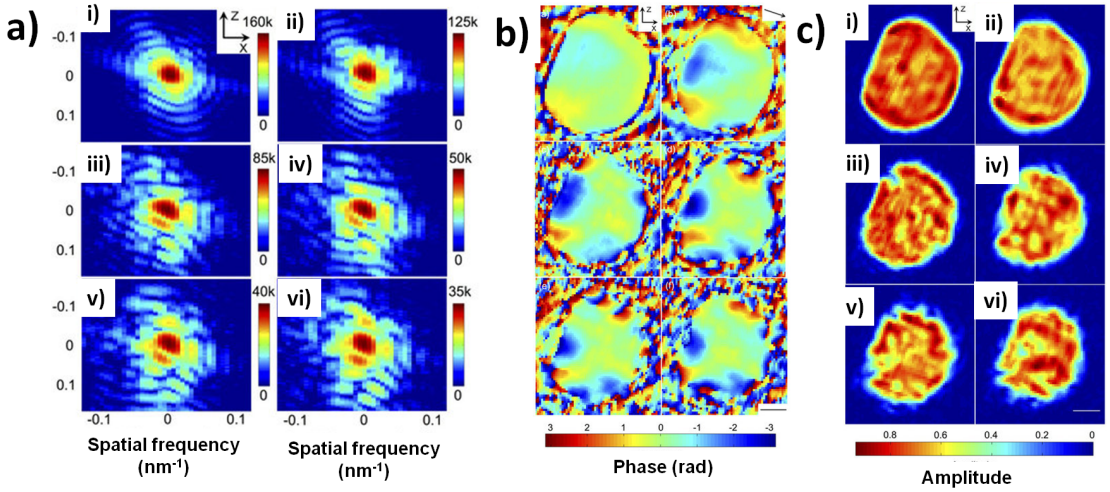

Figure 1.17: a) Evolution of the diffraction pattern of a Au nanocrystal during Cu diffusion (from i) to vi)) and the corresponding reconstructions. In b), the projections of the atomic displacement and in c) the reconstructed amplitude. From Ref. [100].

objects, some works have been dedicated to analyse the signature of different kinds of defects on the coherent diffraction patterns [109,110]. Also, CDI has been carried out successfully on objects with single defects such as stacking faults [107], inversion domain boundaries [111], twin domains [112] or dislocations [113,114,115]. These studies give insight in the crystal structure associated to the growth of the materials. For instance, Harder *et al.* showed the systematic formation of single dislocation loops in calcite crystals with a preferred position in the object. The formation of these defects would explain the strain relief while growing layers on organic substrates [115] (see Fig. 1.18).

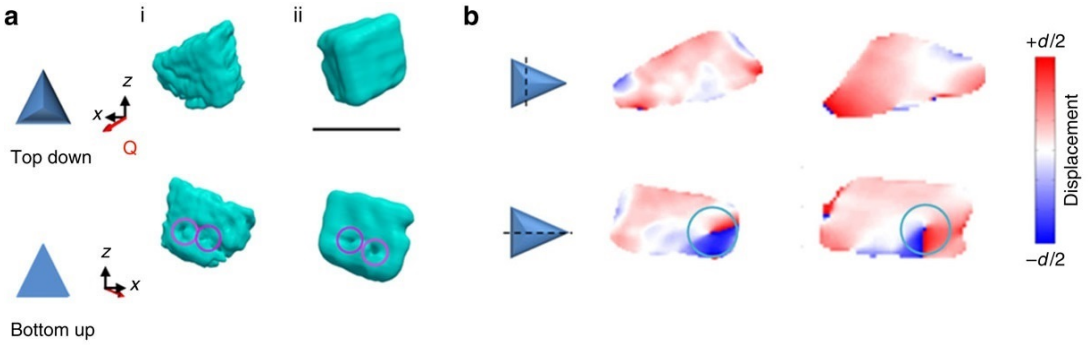

Figure 1.18: a) Reconstructions of the density of two different calcite crystals (i) and (ii). b) 2D cuts at the positions indicated by the dashed lines showing the projected atomic displacement. The magenta circles show the strained region around the defects in the crystals. From Ref. [115]

1.5 Conclusions

In this chapter, I have reviewed the fundamental properties of crystals and the different possible sources of strain in NCs. Details in the case of core/shell semiconductor NWs and catalyst NPs have been given, as the characterisation of both types of nanostructures makes the purpose of this work. A summary of the state of art and the potential applications of both systems motivate us to respond fundamental questions such as the relationships betweens shape and strain. Finally, I have given examples of the current capabilities of CDI, which support the choice of this technique as a powerful tool to investigate strain in nanostructures.

CHAPTER 2

Coherent X-ray diffraction

In this chapter, I first introduce the main coherent X-ray sources and their properties, focusing on third generation synchrotrons. The development and progress of these sources allowed the progress of relatively new imaging methods that take advantage of the enhanced coherence of their X-ray beams. Among these techniques, coherent diffraction imaging is the one used in this work. The technique is detailed in Section 2.3. Then, I will overview the basics of kinematical diffraction and the interest of coherent diffraction. The experimental requirements are later explained, in the case of crystalline samples. In the last section, the experimental set-up used for CDI experiments at the ID01 beamline at the ESRF is described.

2.1 Coherent X-ray sources

Before starting to describe and compare X-ray sources the notion of brilliance must be introduced, since it allows to quantify the quality of an X-ray source in the context of coherent X-ray optics. The brilliance is a function of a given photon energy E, generally chosen within a 0.1% bandwidth. It takes into account the source area (in mm^2), the divergence of the beam (in $mrad^2$) and the X-ray flux (in photons per second). If $B(E)$ denotes the brillance (or spectral brightness), it can be defined as follows[116]:

$$B(E) = \frac{Number\ of\ photons\ per\ second}{Divergence \cdot Source\ size} \tag{2.1}$$

Therefore, the brilliance is maximized by decreasing as much as possible the source size and beam divergence, and increasing the photon flux. The brilliance is generally expressed in $ph/s/mm^2/mrad^2/0.1\%\ bandwidth$.

Two categories of X-ray generators can be distinguished: laboratory sources and large instruments, such as X-ray free electron lasers (XFELs) and synchrotron sources. According to Equation (2.1), the last ones produce much brighter X-rays (and more coherent beams) than laboratory sources, because of the small size of the source and their high flux. The called *fourth generation sources*, based on FELs, produce very short coherent light pulses of very high peak intensity and brightness. Indeed, thanks to the rapid and continuous evolution of third and fourth generation sources in the last years (see for instance Refs.[117,118]), now it is possible to get enough coherent flux to do coherent diffraction experiments within a reasonable timescale. Figure 2.1 shows the evolution of X-ray sources over the last decades and give rough values of the spectral brightness for each of them.

In third generation synchrotron sources and X-FELs, photons are generated by the acceleration of electrons. The main difference in the generation of radiation is the way they accelerate the electrons: the e-beam follows a circular trajectory in the case of synchrotron radiation, while in a X-FEL they are accelerated in Linear Accelerators (LINAC). Details about X-ray sources operation can be found for instance in References[119,120].

It is worthy to mention that the brilliance of a source is an intrinsic property of the source, and it cannot be increased with optic elements. High brilliance is therefore crucial for obtaining a coherent beam. Nevertheless, an X-ray beam must be considered as the result of the interference of waves emitted by different emission points, which are intrinsically subjected to irregular temporal fluctuations in amplitude and phase. Moreover, this emission points have in reality a certain extension. Thus, any source is naturally incoherent: one would rather talk about beams with a high degree of coherence than about coherent beams. In order to characterise the degree of coherence of an X-ray beam, two parameters must be introduced: the temporal and spatial coherences.

- **Spatial or transverse coherence**

  Let us consider the Young interferometer (sketched in Figure 2.2) to introduce the notion of spatial coherence. The experimental set-up consists of a finite extended and quasi-monochromatic line source S, of length σ, cut in two by an optic axis z and a screen (see

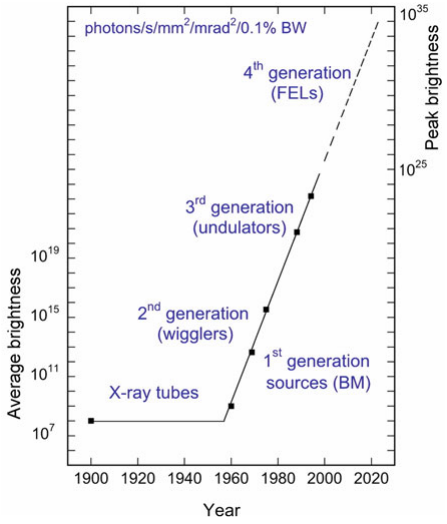

Figure 2.1: Average brilliance of X-ray sources and their evolution over the decades (from Ref. [119])

Figure 2.2). Two slits are inserted between the source and the illuminated screen, at a distance R from the source and symmetrically positioned with respect to the optic axis z. Given the extended nature of the source, the field emitted by any point of the source will be independent of the one emitted by the others. Provided that the slit apertures are small enough, the pattern observed on the screen will consist of a series of fringes, alternatively bright or dark, corresponding to the sum of the intensities produced by two different source points. If the distance R between the source and the slits is large, the emitted waves will be approximately parallel and the path length will be $dsin(\theta)$, with θ being the scattering angle and d the distance between the two slits. Therefore, denoting λ the wavelenth, the intensity on the screen will be maximum when:

$$dsin(\theta) = m\lambda \tag{2.2}$$

and minimal when:

$$dsin(\theta) = (m + 1/2)\lambda \tag{2.3}$$

with $m = 0, 1, 2, 3...$

Thus, there exists a distance d for which the maximum and minimum, coming from two different points of the sources will superimpose, yielding to a uniform intensity pattern. This upper limit of the distance is the definition of the transverse coherence length ξ_T:

$$d = \frac{\lambda \cdot R}{\sigma} \equiv \xi_T \tag{2.4}$$

The expression is valid in the small-angle approximation. Equation (2.4) shows that small sources and large distances between the source and the sample (*i.e.* the diffracting object) are necessary to perform X-ray experiments that need coherent beams.

In addition, equation (2.4) sets the condition of fringe visibility: the sample, of diameter a, must be smaller than the transverse coherence length $\xi_T > a$. On the other hand, from equations (2.2) and (2.3), one can determine the distance between two consecutive fringes:

$$l = \frac{\lambda}{a} \tag{2.5}$$

where *a* is the diameter of the sample. This formula allows to calculate the distance of the detector during the experiments in order to optimise the resolution, as it will be seen in Section 2.3.2

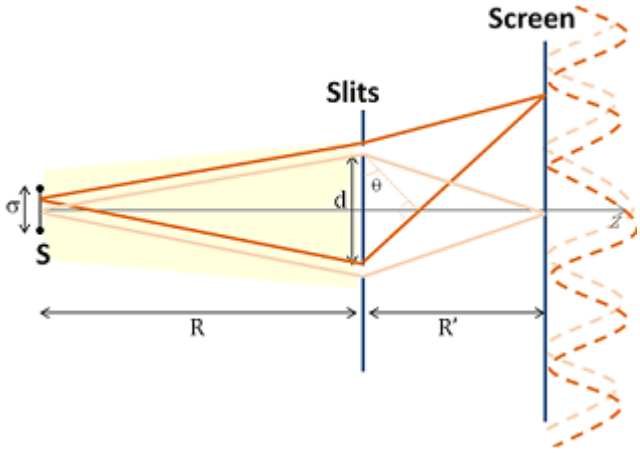

Figure 2.2: Scheme of Young's interferometer. The beam is represented in yellow. Two independent waves and their corresponding fringes are represented in orange, the wave coming from one point in the upper side of the source and in flesh tone, the one coming from one point in the optical axis.

- **Temporal or longitudinal coherence**

  In order to explain the concept of spatial coherence, the fringes produced by the superposition of radiation from two spatially separated points have been considered. If now the same point in space but at different times is considered, the notion of temporal coherence can be easily understood . This parameter must be introduced due to the non-monochromacity of real sources.

  Let us consider the Michelson interferometer, sketched in Figure 2.3. This experimental set-up consists of a quasi-monochromatic source, two perpendicular mirrors (M_1 and M_2) and a beam splitter. The main beam is split in two so that every frequency component produces on the detector a signal consisting in a succession of maxima and minima (note that only the case of plane waves is considered). The positions of the maxima and minima depend on the delay between the two beam paths ($L_2 - L_1$), so that they are slightly different for two wavefronts with different wavelengths, arriving to the detector at different times. The measured intensity on the detector will be the sum of the intensities produced by each component. Therefore, as the time increases, the visibility of the fringes is reduced. Similarly to the spatial coherence, the temporal coherence is the delay at which the fringes become invisible, $i.e.$ the two previously considered wavefronts are in antiphase. It can be shown[121] that this distance, *i.e.* the longitudinal coherence, corresponds to:

$$\xi_L = \frac{<\lambda>^2}{2\Delta\lambda} \tag{2.6}$$

where $<\lambda>$ is the average wavelength emitted by the source, and $\Delta\lambda$ is the difference in wavelengths between the shortest and longest emitted waves.

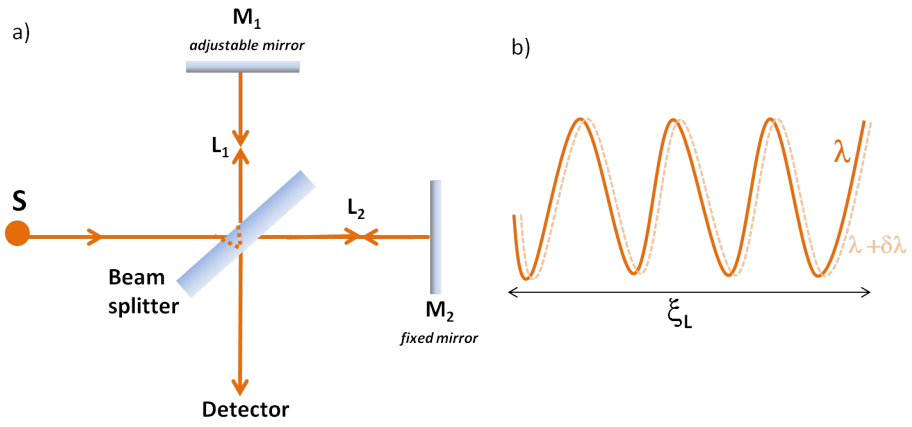

Figure 2.3: a) Schematic of a Michelson's interferometer. S represents a non monochromatic source. b) Intensity fringes produced by waves of different wavelengths (λ and $\lambda + \delta\lambda$ (dashed line)).

The description of spatial and temporal coherence properties of X-ray beams can be applied to evaluate the coherence of X-ray sources. The number of photons going through a coherent surface (meaning an area of which dimensions are equal to the transverse lengths of coherence) is the coherent flux, F_{coh}, defined as:

$$F_{coh} = B\lambda^2 \frac{\Delta\lambda}{\lambda} \tag{2.7}$$

The dependence of the flux on the brilliance of the source allows us to classify X-ray tubes and rotating anode sources as the less coherent, with transverse coherence lengths ξ_T of a few hundred nanometers and coherent fluxes of at best, $300\ photons/s$ for $\lambda = 1.54$ Å(8 keV). In third generation synchrotron X-ray sources, high values of ξ_T are obtained by geometrical configurations (small source size, long beamlines...), and longitudinal coherence ξ_L is not a big issue to study nanostructures: with a regular Si 111 monochromator of bandwidth $\delta\lambda/\lambda = 10^{-4}$, $\xi_L \leq 0.7\,\mu\text{m}$ [122]. However, only a small part of the total radiation is coherent (about 0.1% of total). The coherent flux can be increased up to $10^{11} photons/s$ by taking only the coherent part of the beam placing some slits close to the sample, as it will be seen in Section 2.3.2.

Recently emerged XFEL sources have extremely large coherence lengths, because of the way the photons are produced [123].The peak brightness of the XFEL pulse is 10^9 times higher than that of the most powerful third generation source, and the degree of lateral coherence of an X-ray beam generated by this type of source would be 100 %. Details on the coherent properties of XFEL sources can be found in Reference [124].

2.2 Coherent diffraction imaging methods

X-ray microscopy methods have the advantage over optical or electronic microscopes of penetrating deeper into matter, being able to image the internal structure of the samples with nanometer resolution and without specific sample preparation. Nevertheless the resolution is limited by the imperfections of X-ray lenses, such as low efficiency, strong aberrations or low numerical aperture. Coherent diffractive imaging (CDI) techniques aim to solve this problem by combination of highly coherent beams and computational algorithms, without any optics inserted between the sample and the detector. This is why CDI methods are often referred to as "lensless" techniques.

However because of the high frequency and small wavelength of X-rays, current X-ray de-

tectors are only sensitive to the time-averaged intensity, $i.e.$ to the number of detected photons. A diffracted wave being function of both the amplitude and phase of the scattering object, the phase is lost. This is known as the "phase problem"; its mathematical demonstration in the context of crystallography can be found in Ref.[125]. The phase problem can be solved by selecting *the coherent fraction* of the total flux, assuming that the phase depends on the exact departure time of the photons.

There exists several approaches that allow to recover the lost phase. One possibility is to encode the phase, as it is done in holographic imaging. This method[126] consists of the illumination of the sample with a reference wave and the recovery of the intensity using a planar imaging device, as the differential filter shown in Figure 2.4. The recorded intensity is thus the interference between the reference wave, that has not been disturbed, and the one scattered from the object. If both waves are coherent, the knowledge of the phase of the reference allows one to reconstruct the entire wave field scattered from the object. A comprehensive review on the X-ray holographic techniques is given in Ref.[127]. As examples of holography achievements, let us cite the first 3D reconstruction of a crystal in the Fourier holography configuration[128] or the works from Eisebitt *et al.*[129], that succeeded in imaging the magnetic domain structure in a thin film. The spatial resolution typically obtained is of $30 - 50$ nm, although a resolution of 16 nm has recently been obtained with a XFEL generated beam[130].

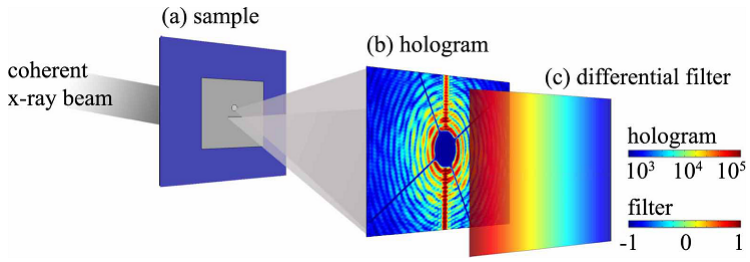

Figure 2.4: Set-up for Fourier holography[131] a) The object and reference slit are illuminated by the coherent X-ray beam. b) Hologram c) Linear differential filter.

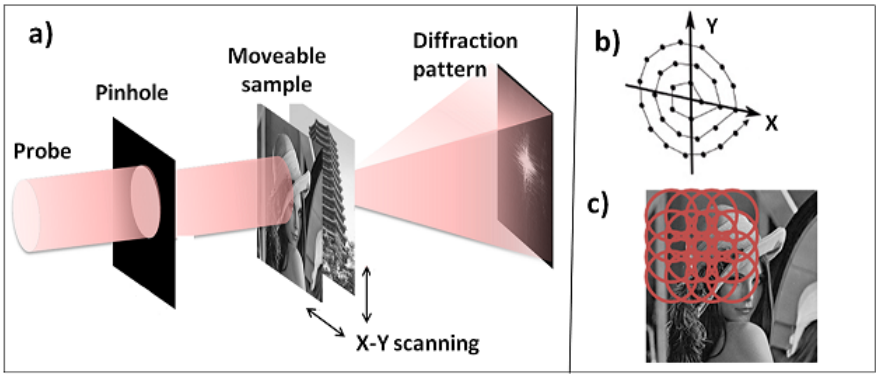

Figure 2.5: a) Experimental set-up used for ptychography, from[132] b) Example of trajectory followed by the sample while recording the diffraction patterns. The "spiral" trajectory is often chosen to avoid periodicity artifacts. Each point on the spiral corresponds to a detector image. c) Circles represents the position of the beam while scanning the sample, showing the overlapping.

Another possibility is to recover the phase by ensuring that the sample is isolated and its far-field pattern is sampled finely enough. A tilt series of diffraction patterns is acquired over various sample orientations that yield a 3D image. The object can be retrieved applying a series

of numerical algorithms on the 3D diffraction data without a priori knowledge about the sample, as shown experimentally for the first time by Miao *et al* in 1999[87]. This is the basis of CDI, that can be applied in both small angle and Bragg diffraction geometry. As Bragg CDI is the main technique used in this works, it is further discussed in section 2.3.

A third approach consists of illuminating the sample with a known probe, and measuring the diffraction patterns for multiple positions of the sample with respect to the illumination. Ensuring an overlap of the illumination between different acquisitions, a computer algorithm allows to retrieve the sample and the incident wavefront[133,134,135]. The algorithms are more robust to stagnation, noise and ambiguities, than the ones used for traditional X-ray microscopy or other CDI techniques because of the redundancy on the data due to overlapping. This method, called ptychography, offers the possibility of imaging extended and non-isolated objects[136] and allows to image the displacement field of periodic crystals with sub-beam resolution. For these reasons, ptychography has gained continuous interest since the first sucessful demonstration[137] and it has been applied in many fields (from computer chips[138] to biological samples (see for instance[139]).

Any of these techniques promises 3D resolution limited only by radiation damage, wavelength, the collected solid angle and the number of x-rays or electrons collected. Attractive resolution values of about 2-4 nm in material sciences should be possible at a modern synchrotron, and atomic resolution could be accomplished using x-rays pulses[140].

2.3 Bragg CDI

2.3.1 From X-ray Bragg Diffraction to Bragg Coherent Diffraction

Diffraction can be defined here as the change of direction of an X-ray monochromatic beam when it impinges on a crystal while conserving the kinetic energy, hence, conserving its wavelength $\lambda, (\lambda = \frac{hc}{E}$, where h is the Planck constant and c the speed of light). Given the short wavelength of X-rays (from 0.01 to 100 nm), the atoms scatter the incident electromagnetic wave through the atoms' electrons. The direction that a single photon follows after hitting a given atom depends on the position of the atom in the crystal. Therefore, the whole diffraction pattern -recorded in the far field- will consist of the interference of the scattered waves. The condition for two scattered waves to be constructive, $i.e.$ to yield a bright spot or Bragg peak, is that their path-length-difference has to be a multiple of the wavelength λ of the incoming beam. This is stated by the Bragg law:

$$2dsin\theta = \lambda, \tag{2.8}$$

This equation can be easily understood looking at the representation in Figure 2.6, where the blue points represent the atoms in the crystal, regularly spaced and distributed in three parallel atomic planes. Every plane is separated from the others by a distance d.

Therefore, as in a crystal the atoms are arranged in a highly periodic structure, the analysis of a single Bragg peak contains information about the atomic level structure of the material. In particular, one can access the lattice parameter *a* of the crystal by looking at the $d - spacing$ between atomic planes which is actually dependent on the crystal structure. In the case of simple cubic crystals, this dependence is given by:

$$d = \frac{a}{\sqrt{h^2 + k^2 + l^2}} \tag{2.9}$$

where *(hkl)* are the *Miller indices* that characterise the orientation of a lattice plane with respect to a given crystallographic axis.

Experimentally, it is convenient to define the momentum transfer vector ($\vec{q} = \vec{k_f} - \vec{k_i}$). As diffraction is an elastic process, $|\vec{k_i}| = |\vec{k_f}|$ and the Bragg law can be written as follows:

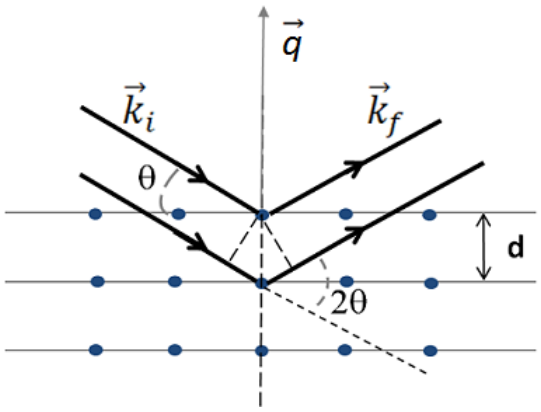

Figure 2.6: Bragg condition for diffraction in crystals. The incident beam of propagation vector $|\vec{k_i}| = \frac{2\pi}{\lambda}$ impinges on the crystal with an incident angle θ. Only the waves exiting in a specific direction $\vec{k_f}$ will interfere in a constructive way to yield a measurable intensity.

$$|\vec{q}| = \frac{2\pi}{d} \tag{2.10}$$

Consequently X-ray diffraction allows to access different $\vec{q}$ - hence to different crystalllographic planes - by changing the incident angle θ. In other words, by rotating the sample (or alternatively changing the wavelength of the incident radiation) one can in principle probe the full Fourier space. Nevertheless, this approach is valid only for in-phase incident waves, meaning that only the waves that have equal phase will interfere constructively. If the sample dimensions exceed the spatial coherence, which is usually the case in classical X-ray diffraction, small scale local structures are averaged. The interest of coherent X-ray diffraction consists in the increase of the coherence length of the incident wavefront in order to resolve individual structures with higher resolution, answering new needs of characterization for the recent developments in fields as micro and nano-technologies.

2.3.2 Experimental requirements and data analysis

In the previous section I have shown the possibility of getting information on the atomic structure of a crystal by classical X-ray diffraction. Nevertheless if one aims to characterise single nanostructures or retrieve local information with high resolution, chromatic and parallel incoming waves are required. Hence, the need for coherent X-ray beams (see section 2.1) are needed. In order to increase the coherence lengths of the beam, experimental set-up and conditions while performing experiments are decisive. In this section I briefly discuss experimental conditions allowing to take advantage of the spatial coherence length of synchrotron radiation. As it will be seen in Section 2.4, source size is decisive but it is helpful to include focusing optics in the experimental set-up.

2.3.2.1 X-ray Bragg diffraction in the Fraunhofer regime

As it has been seen in section 2.1, the crystal subject to study must be placed far from the source to get a good transverse coherence length. Nevertheless, in a synchtrotron X-ray experiment slits and focusing optics are placed between the source and the sample (see section 2.4) so that aberrations are introduced[141]. Hence, the slits close to the sample position are coherently illuminated producing a diffraction pattern in which the fringes are visible, but the intensity arising from the actual sample has to be recorded far from the object[142]. This distance *D* between

the sample and the detector has to be such that $D > a^2/\lambda$, where a is the size of the sample and λ the wavelength of the incoming beam. This defines the *far field* or *Fraunhofer regime*.

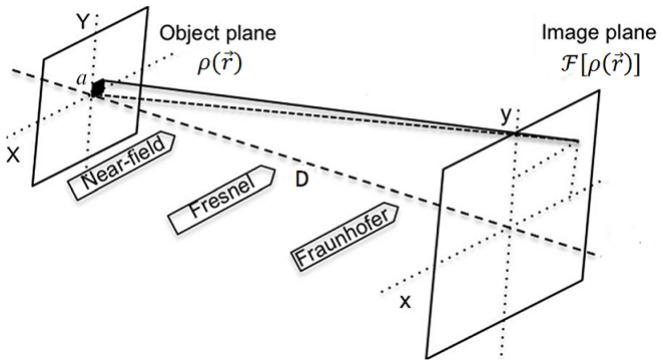

Figure 2.7: Sketch of three-different regimes in CDI, from [143]. CDI experiments are performed with the detector in the Fraunhofer regime and the sample in the Fresnel regime, considering the slits as second source.

Moreover, one can calculate the distance required to better resolve the fringes according to the size of the sample. From equation (2.5) and considering two incident plane waves, separated on the detector by a small angle $\alpha \simeq l/D$, it follows:

$$\frac{l}{D} = \frac{\lambda}{a} \tag{2.11}$$

where $l = number of pixels \times pixel size$. In this way, the minimum resolution (1 bright fringe on 1 pixel, separated from another by one dark pixel) corresponds to 2 pixels. This formula allows to take into account the oversampling (see section 2.3.2.2) and defines the resolution in reciprocal space:

$$\delta q = \frac{2\pi}{\lambda} \frac{pixel\ size}{detector\ distance} \tag{2.12}$$

In the case of 300 nm diameter nanowires as considered in this thesis this implies that at an energy of 8 keV, to see 4 pixels per fringe the detector must be placed at about 66 cm from the sample (for a pixel size of 55 μm).

Whereas the intensity is recorded with the detector in the far field, the sample has to be placed in the Fresnel regime (see Fig. 2.7) [a] so that one can still consider the incident wavefront as plane waves. Measuring in this configuration, and in the kinematic approximation, the diffracted amplitude is simply the Fourier transform of the exiting wave from the sample:

$$\tilde{A}(\vec{q}) = \int \tilde{\rho}(\vec{r}) e^{i\vec{q}\cdot\vec{r}} d^3r = \mathscr{F}[\tilde{\rho}(\vec{r})] \tag{2.13}$$

The exit wave $\tilde{A}(\vec{q})$ contains information about the sample (electron density and phase) and in principle, one should be able to retrieve this information by performing the inverse Fourier transform of the diffracted wave. However, as introduced in section 2.2, only intensities are measured, hence the modulus square of the amplitude:

$$I = |\tilde{A}(\vec{q})|^2 = \mathscr{F}[\tilde{\rho}(\vec{r})] \tag{2.14}$$

[a] The Fresnel regime occurs when the deterctor is placed at a distance $D < a^2/\lambda$

Note that the Inverse Fourier Transform (IFT) of the measured intensity provides the autocorrelation function of the electron density. This is, by definition, the Patterson function, which can be equivalently defined as the autocorrelation of the electronic density $\mathscr{F}^{-}[I] = \rho(\vec{r}) * \rho(-\vec{r})$ of the object.
The so-called *phase retrieval algorithms* have been proposed as solution to the phase problem. Here below I describe the basis of these algorithms and explain the difference and improvements between some of them.

2.3.2.2 Oversampling

When a big crystal is illuminated by an X-ray beam, the diffraction pattern in the far field consists of distinct Bragg peaks of finite size due to constructive interference of the incoming waves. These Bragg peaks are at the Nyquist frequency[b] corresponding to a unit cell. Between the Bragg peaks, there is practically no intensity.
Let us consider an infinite periodic 1D density funcion $\rho(x)$ with period L in real space. Here $\rho(x)$ is the unit cell density distribution and it is zero outside the interval $[-L/2, L/2]$. Thus, due to the bounded support of $\rho(x)$ with diameter L in real space, the associated diffraction pattern is characterised by smallest features of size $2\pi/L$ called *speckles*. This is illustrated in Figure2.8 a).
The sampling theorem [144] quantifies the smallest sampling period allowing to encode all information in the case of non-periodic samples whose diffraction patterns are continuous: a sampling period of π/L is sufficient to encode all information. If the full complex field at the detector could be measured, the Nyquist sampling period would be increased by a factor of two to $2\pi/L$, as the density itself is limited to the interval $[-L/2, L/2]$ in real space. As S is equal to the Bragg peak distances and the size of the speckles, a minimum oversampling factor of $\sigma \geq 2$ in the 1D problem and by extension $\sigma \geq 2^{1/2}$ and $\sigma \geq 2^{1/3}$ in two and three dimensions are necessary to encode the information of the sampled crystal [144,145]. Actually, sampling a small crystal at the Nyquist frequency by a factor of $\sigma = 2$ in each direction yields to the phase information independently of the dimensionality of the problem [146].

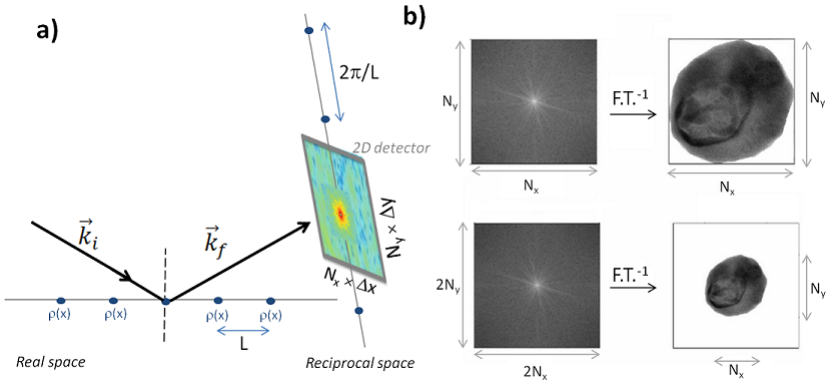

Figure 2.8: a) When a coherent X-ray beam impinges onto a crystal, its reciprocal space is made by a set of sharp points called speckles. As experimentally it is impossible to measure the continuous diffraction pattern, the crystal has to be *oversampled* on a finer grid. The sampling distance in real space Δx is given by [147] $\Delta x = \frac{\lambda L}{Np}$, where p is the pixel size. b) Same diffraction pattern sampled at the Nyquist frequency (above) and at twice the Nyquist frequency (below) and their corresponding reconstructions (from [148]). Oversampling with a ratio $\sigma \geq 2$ confines the object in a region (*"support"*) surrounded by zeros.

[b] The Nyquist frequency f_{N_y} is defined with regards to the sample size a as $f_{N_y} = 2\pi/a$.

Experimentally, this means that the measurement has to be performed with a Fourier space resolution δq smaller at least by a factor two than the Nyquist frequency. Hence, how well the diffraction pattern is sampled depends on the pixel size and the distance from the sample to the detector (see equation (2.12)). In the case of sampling a specimen at twice the Nyquist frequency ($\sigma = 2$) with a two-dimensional (2D) detector of $N = N_x \times N_y$ pixels, the fast fourier transform (FFT) of the diffracted pattern will be a $2N$ array in which the object is bordered by a no-density region. The object is thus confined in a region that is called the *support*[145] (Figure 2.8 b). The oversampling ratio can be defined in real space as follows:

$$\sigma = \frac{Total\ number\ of\ pixels}{Number\ of\ pixels\ in\ the\ support} \tag{2.15}$$

2.3.2.3 Phase Retrieval algorithms

As it has been introduced before, the measured amplitude in the Fraunhofer regime and in the kinematical approximation is the Fourier Transform (F.T.) of the electron density of the illuminated crystal (Equation (2.14)). Oversampling an object during a CDI experiment ensures, in principle, the phase retrieval of the set of phases, however there is still an ambiguity of the solution: there is not a unique phase that satisfies Equation (2.14). For instance, it is impossible to distinguish the FT of a given real density function $\rho(\vec{r})$ from its conjugate $\rho^*(\vec{r})$, or from one shifted in position $\rho(\vec{r} + \delta\vec{r})$. Indeed, because of the zeros surrounding the support, the number of independent equations to solve is higher than the number of pixels to reconstruct. This is commonly referred to as the *"uniqueness problem*".
The phase problem can be solved by imposing constraints in the computation routine. These routines, or mathematical algorithms, are inspired by the so-called Gerchberg-Saxton algorithm[149], and they mainly consist of:

1. Simulating an initial object $g(\vec{r})$ taking the measured amplitude and a random phase.
2. Calculating the FT of this first guess of the object, $\mathscr{F}[g(\vec{r})]$. This yields a diffraction pattern that differs from the measured one.
3. Imposing constraints in reciprocal space, $i.e.$ replace the new amplitude for the experimental one ("modulus constraint"). Retaining the new phase, calculate the inverse Fourier Transform ($\mathscr{F}^{-1}$) of the object.
4. Iterating until convergence. The convergence is measured by means of the error metric (see equation (2.18)).

In the last step, a new estimate $g'(\vec{r})$ is obtained replacing the modulus in real space with the corresponding measured amplitude.

Although this idea is the basis of the phase retrieval procedure, GS algorithm converges slowly (a very large number of iterations is necessary) and noise in experimental data easily yields local minima. That is why other similar algorithms have been developed and it is suitable to combine them during a cycle. Here below I describe the main differences between the algorithms employed (together) in the data analysis of this report. An interesting review with mathematical details in terms of projections and comparison of these and other algorithms can be found in Reference[150].

2.3.2.3.1 Error reduction (ER)

The original goal of GS algorithm was to solve the phase problem in microscopy, from two intensity measurements[149]. The generalization of the algorithm (outlined in figure 2.9) that relates two different domains (hence real and reciprocal space) by imposing partial constraints in both domains is nowadays referred to as error reduction (ER)[151]. In the context of CDI,

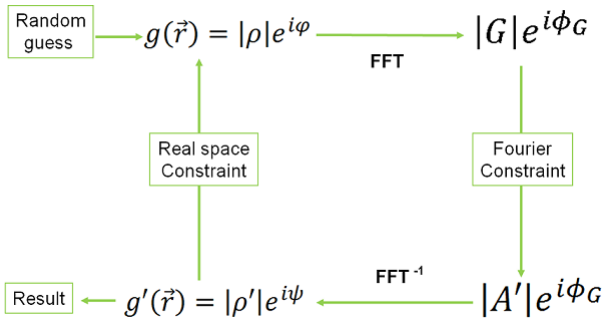

Figure 2.9: Representation of the iterative phase retrieval algorithm. Here, according to the text, $|A| = \sqrt{I}$ and $|A| = \mathscr{F}[\rho(\vec{r})]$. φ is a random value of the phase to initiate the algorithm.

the oversampling condition imposes a constraint in real space ("support constraint") so that the sample is supposed to be isolated and confined in a well-defined region. The support constraint implies to have some knowledge about the sample, despite some information can be derived from the Patterson function of the scattering object (see Section 2.3.2). The Patterson function is twice as big as the original object[152]. A tight support efficiently improves the convergence of the algorithm. Following the notation used in section 2.3.2.3, one can write the support constraint as follows:

$$g_{n+1}(\vec{r}) = \begin{cases} g'_n(\vec{r}) \;\; if \;\; \vec{r} \in S \\ 0(\vec{r}) \;\; if \;\; \vec{r} \notin S \end{cases} \tag{2.16}$$

so that the electron density is forced to be zero outside the support S at each iteration. The suffix n refers to the iteration number. The reciprocal space condition consists in replacing the computed amplitude with the measured one; the Fourier constraint can be written:

$$|A'_n| = \frac{A_n(\vec{q})}{|A_n(\vec{q})|}\sqrt{I} \tag{2.17}$$

The cycle is repeated until convergence is achieved, so that constraints in real and reciprocal space are both satisfied. The *error metric function* allows to monitor the progress at each iteration *n*:

$$R_n = \frac{\sum_{i=1}^{N}(|G_{n,i}| - \sqrt{I})^2}{\sum_{i=1}^{N} I_i} \tag{2.18}$$

where *i* is the pixel number on the camera and *N* the total number of pixels. The metric error decreases at each iteration or stays the same[151] and when $|G_{n,i}|$ is the true amplitude, $R = 0$. In practice the cycle is rather interrupted when R becomes smaller than a threshold linked to the noise level.

2.3.2.3.2 Hybrid Input-Output (HIO) Algorithm

This algorithm aims to solve the problem of stagnation in the local minima of ER[151]. The principle remains the same, but modifications in real space constraints are introduced: instead of setting to zero the pixels outside the support, they "are driven" to zero as follows:

$$g_{n+1}(\vec{r}) = \begin{cases} g'_n(\vec{r}) \;\; if \;\; \vec{r} \in S \\ g_n(\vec{r}) - \beta g'_n(\vec{r})(\vec{r}) \;\; if \;\; \vec{r} \notin S \end{cases} \tag{2.19}$$

where β is a feedback constant set between 0.5 and 1. Hence, the pixels outside the support in the output object depend on the previous and current iterations and they gradually decrease to zero. The convergence of HIO is much faster and many variations have been developed [153,154]. This algorithm is widely used in the imaging reconstruction field [154].

2.3.2.3.3 Charge flipping (CF)

CF algorithm has been developed by Oszlanyi & Suto in 2004 while thinking about the small information content in the pixels where density is close to zero [155]. Their idea was later modified and used for the first time on X-ray experimental data by Wu *et al.*. The difference with respect to ER is once more on the real space constraint, which consists here on reversing ("flipping") the sign of the density in the pixels outside the support:

$$g_{n+1}(\vec{r}) = \begin{cases} g'_n(\vec{r}) \;\; if \;\; \vec{r} \in S \\ -g'_n(\vec{r}) \;\; if \;\; \vec{r} \notin S \end{cases} \tag{2.20}$$

Thus, the density is not forced to be zero outside the support, but negative, confining the values in a narrow band bordering the object. As crystal structures occupy only a small fraction of space with high density, the dimensionality of the problem is reduced.

A series of HIO followed by CF allows to refine the object, although HIO is more efficient.

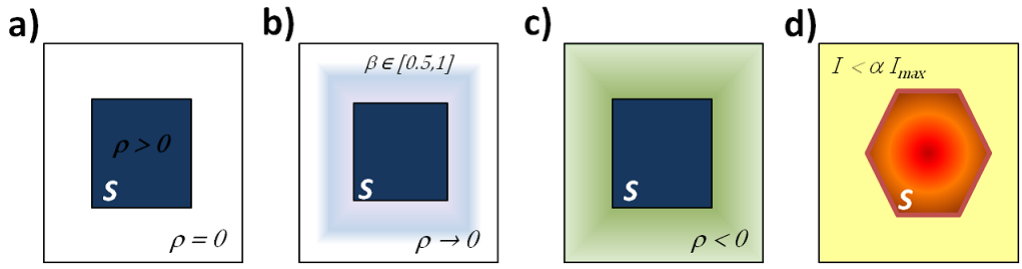

Figure 2.10: Schema of the different *real space constraints* for the algorithms explained in the text. a) ER b) HIO c) CF d) SW, α represents the threshold and β is the feedback parameter.

2.3.2.3.4 Shrink-wrap (SW)

The approach of the shrink-wrap [152] is different from the previous ones because knowledge about the specimen before retrieval is not needed. The object support function is determined together with the object itself.

The idea is to take the autocorrelation function as initial support and update it by thresholding the intensity of the current estimate. HIO has to be applied in combination with SW in order to preserve the symmetry of the Fourier transformed object after some iterations. After about 20 iterates, the reconstructed image is convolved with a Gaussian, so that a new threshold can be defined. Provided that the object is well isolated, the strong contrast between noise and signal guarantees the stability and convergence of the algorithm that always converges to the correct shape, for any random value of the initial phase.

A slightly different approach of Marchesini's SW has been used for the reconstructions shown in this thesis. First, instead of taking the autocorrelation function as initial guess of the support, a symmetric support is chosen (a square for 2D-phase retrieval or a cube in the 3D case) with a size a bit larger than the one determined by the fringes of the diffraction pattern. The updating of the support during the iterations consists in taking the pixels at the support edges and applying an intensity threshold to keep them or not. In this way, the algorithm finds the real object shape typically after 30-50 iterations.

2.4 Experimental set-ups

2.4.1 The ID01 beamline

Most of the experiments contained in this thesis were performed at the European Synchtrotron (ESRF), which is a first 3^{rd} generation high energy X-ray source and currently one of the most brilliants in the world. The ID01 beamline is dedicated to the characterization of single nanostructures and the study of local properties of 3D structures by coherent x-ray diffraction methods or nanodiffraction.

Since the Upgrade Phase I of the ESRF, which was completed at the end of 2014, ID01 is a long beamline (endstation at 118 m from the source) with a high flux coherent beam that can be focused down to 300×150 nm. The source size being of about $130\ \mu m\ (horizontal) \times 20\ \mu m\ (vertical)$, and according to equations (2.4), the transverse coherence length of the upgraded ID01 is estimated to be $200\ \mu m(V) \times 48\ \mu m(H)$ for an X-ray wavelength of $\lambda = 1$ Å. This supposes an enormous gain of coherent flux with respect to the beamline before the upgrade (transverse coherence length of $60\ \mu m\ (V) \times 20\ \mu m\ (H)$, Ref.[156]). In addition, the beam is much more stable and less sensitive to vibrations.

Although it is also possible to perform small-angle X-ray scattering (SAXS), grazing-incidence diffraction (GID) and grazing-incidence small angle x-ray scattering (GISAXS) experiments at ID01, the description of the beamline hereafter focuses on the experimental set-up dedicated to Bragg CDI experiments.

2.4.1.1 The upgraded ID01 optics hutch

Before reaching the optics hutch, the electron beam passes through three undulators in series, one 35 mm period undulators (U35) and two 27 mm undulators (U27), so that the energy range of the beamline can be tuned between 5 and 60 keV. The desired photon energy can be selected by changing the gap between the magnets of the undulators (insertion devices) and choosing one of its harmonics. For coherent diffraction experiments low energies are suitable and it is mandatory to use a very well-defined bandwidth (Equations (2.4) and (2.6)). The best regime for nanofocusing and CDI at ID01 beamline is between 7 and 12 keV, and optimised for the current focusing optics at 8 keV. This range of energy is obtained usually with only two undulators.

Before arriving to the experimental hutch (EH), the beam passes through three optics hutches (OH). An overview of the first (OH1) and second (OH2) hutches can be seen in Figure 2.11. The first reflective element in the optics hutch is a white beam mirror assembly, which intends to reduce the horizontal divergence of the non-focused incoming beam on the monochromator, placed just after the mirror.
The Si(111) monochromator is used to produce a beam of radiation with a narrow wavelength distribution, obtaining typically an energy resolution of $\frac{\Delta E}{E} = 10^{-4}$. The ID01 monochromator can be used in both double crystal or channel cut geometries. Whereas the double crystal monochromator consists of two different Si-111 crystals which move independently, the channel-cut configuration uses only one crystal and tilt one surface with respect to the other around an average fixed Bragg angle. Because of the way it mechanically works the double crystal is very susceptible to vibrations, which can drastically change the coherence properties of the beam. Therefore the double crystal is preferred for high-flux experiments and it turns out be stable enough and it is more flexible and easier to align, so this is the one used in most of the experiments presented here.

In OH2, a transfocator composed by 58 Be lenses focuses the beam vertically and increases the flux density. Fluorescent screens, cameras and attenuators are also present along the beam path.

In the third optics hutch (OH3), a photon beam position monitor (XBPM) allows to watch the variations in the position of the beam. Then, two front-end shutters ("fast shutters") separate

the optics and the experimental hutches. The fast shutter is a rapid closing valve that stops an air inrush in case of a fast vacum-to-air leak.

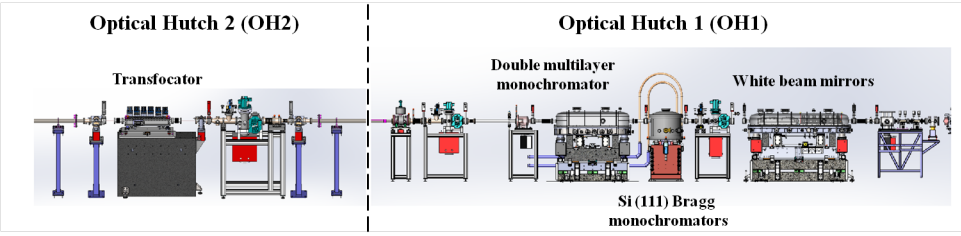

Figure 2.11: Overview of OH1 and OH2. The beam comes from the right to the left (*i.e.* from OH1 to OH2). Si (111) Bragg monochromators (double crystal geometry/channel cut geometry)

2.4.1.2 ID01 experimental hutch

2.4.1.2.1 The diffractometer and the nano-positioning stage

Coherent diffraction experiments are performed on a 3+2-circles diffractometer, so that the sample and detector support are mechanically decoupled to prevent sample vibrations due to the detector arm movements. Sample rotations are called θ, μ, ϕ while δ and ν are the motors name of vertical and horizontal detector movements respectively, as sketched in Figure 2.12.

The detector is a 2D MAXIPIX that consists of four chips in a 2×2 arrangement with $516 \times 516\ pixels$ in total, the pixel size being of $55\ \mu m^2$ [157]. It is placed on the detector arm and it can be moved according to the experiment needs. It is also possible to work in *accumulation mode* so that long exposures to the scattered photons are replaced by a sequence of short exposures in order to avoid pixel saturation. A high resolution detector (Andor camera) for full-field imaging is available and a new Eiger detector will be soon available as well.

The sample stage consists of a hexapod that allows translations of the sample along the beam (X), perpendicular to it (Y) and in the vertical plane (Z) for alignments within a range of $\pm 5\ mm$ and an accuracy of 100 nm. A piezo-electric stage (PI) mounted on the hexapod allows more precise and fast movements, within a range of $200\ \mu m$ and a resolution of 20 nm. In order to align the sample, there is a microscope that rotates together with the θ angle and that allows to localize nanostructures on a sample or focus in a region of interest for any kind of sample. Also, given the importance of staying in the center of rotation of the diffractometer to perform the rocking scans - so that the beam stays on the nanostructure during the measurement - a telescope is mounted on the marble (see Figure 2.12). The center of rotation is in general determined before carrying out any CDI experiment by using a Cu pin of approximately $20\ \mu m$ on the top, or a Si wedge.

Although the microscope is really helpful to align and localize the structures, it is often not suitable to determine the position of the beam on the sample, an issue when working with nm-beams and objects of the same scale. In order to solve this problem a new technique based on Scanning X-ray diffraction (SXD) [158] has been developed at ID01 beamline. This technique has been called *quick MAPping (K-map)* [159]. It consists in scanning the sample with a nanofocused beam while recording 3D reciprocal space maps, *i.e.* rocking curves around a given Bragg position, besides obtaining real space maps with a sub-micrometer resolution. The real space maps being correlated with the diffraction images, the novelty consists in the enormous gain of time: for example, a 2D real space map of $100 \times 100 \mu m$ making 500 nm spatial intervals and with an exposure time of 10 ms, would take with k-map less than 7 minutes, to be compared with the 11.2 h in classical step mode. The fast localization of nanostructures allows to systematically search specimens all over a sample, for instance to measure pre-selected ones, or identify the

ones being measured to combine the results with any other technique for complementary studies. In addition, K-map allows to access to the strain and crystallographic tilts of samples in the micro-scale with practically no dead time[159].

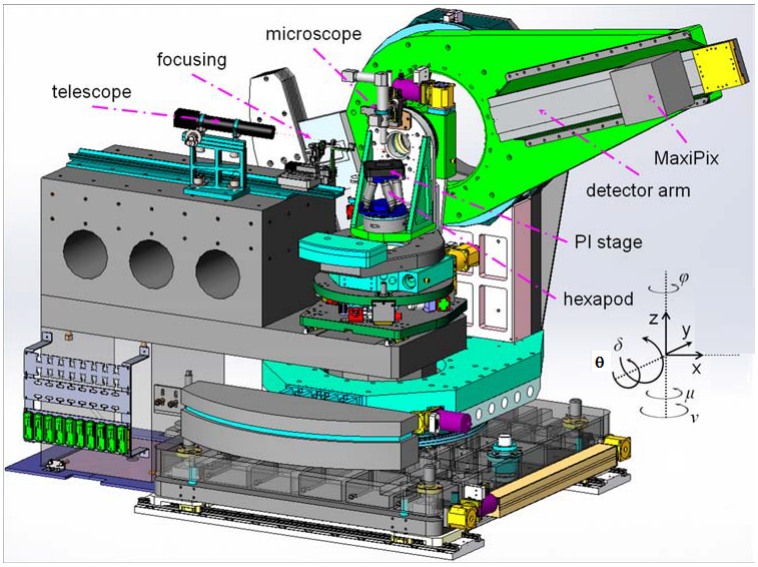

Figure 2.12: The 3+2-circles diffractometer

2.4.1.2.2 Focusing optics

When it arrives to the sample position, the size of the X-ray beam is bigger than its coherence length. In order to avoid measuring the scattered intensity with a classical diffraction contribution, it is necessary to select only the coherent part of the beam. To do this, horizontal and vertical slits are placed just before the sample and closed to smaller values than the theoretical transverse coherence length, typically to $60(horizontal) \times 300(vertical)\mu m^2$ when working at $8keV$. In this way a coherent beam is obtained, but still larger than the sample. In order to enhance the flux focused on the sample, optical devices have to be used. Among the focusing optics devices for X-rays, the most used are Fresnel Zone Plates (FZP), Kirkpatrick-Baez mirrors (KB-mirrors) and Be compound refractive lenses (CRLs). The choice of the optical element depends on the main concern of the experiment, since one has to make a compromise between conserving incoming flux, spatial and angular resolution or coherence.

At ID01, the beam is focused using a Fresnel Zone Plate that gives a minimum focal size of $100(V) \times 150(H)\ nm^2$ (when it is fully illuminated). This is a diffractive optic that consists of an arrangement of concentric rings (zones) of alternating refractive indices. The zone width gradually decreases as the zone radius gets larger, so that the optical path difference of scattered waves from the rings with respect to the directly propagating incident plane wave is an integer multiple m of $\lambda/2$. This corresponds to the beam from the center of the zone plate to the focal point f (see figure 2.13):

$$r_m^2 + f^2 = \left(f + \frac{m\lambda}{2}\right)^2 \tag{2.21}$$

which can be written as (by neglecting the λ^2 term):

$$r_m = \sqrt{m\lambda f} \tag{2.22}$$

Therefore a FZP is designed for a given energy, 8-9 keV in the case of the FZPs used at ID01. Whereas a FZP produces several diffraction orders, (as illustrated in Figure 2.13) one is actually interested only in the first one ($m = 1$), because the flux concentrated in the focal spot is much higher. A beam-stop blocks the zeroth order whereas higher harmonics ($m > 1$) are blocked by placing an order selection aperture (OSA) in the experimental set-up, which is very close to the sample. The outermost zone width of ID01 FZP is 70 nm for all the lenses and the diameter is $300\ \mu m$. The diameter of the OSA is of about $50\ \mu m$. FZPs make little scattering background (because of their low thickness) and they are easy to align. For these reasons and due to the efficiency, FZPs are the most reasonable choice for hard X-rays, in terms of focal spot sizes and focusing: at 8 keV, the theoretical efficiency can be as high as 32 %. Further details on FZP can be found in Refs.[116,156].
The focusing elements are mounted on a rail close to the sample, as illustrated on Figure 2.12 so that they can be translated depending on the energy.
The commissioning of a new KB mirror for ID01 is expected for December 2016. The achromaticity of KB mirrors will allow anomalous nano-diffraction imaging: as they are based on reflection, the focused spot does not suffer modifications if the incident X-ray beam energy changes.

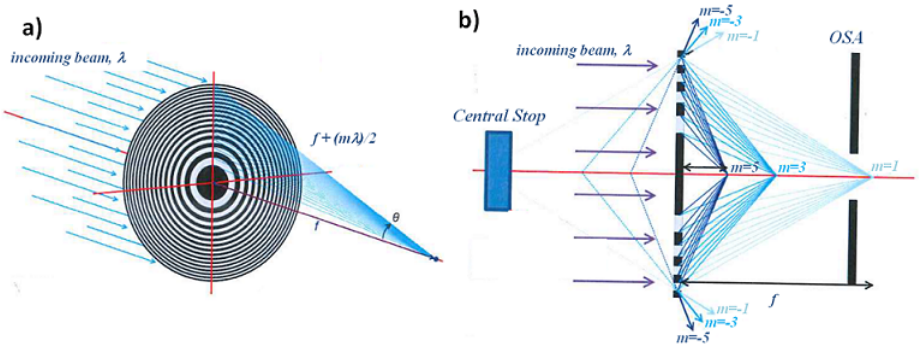

Figure 2.13: a) Optical path shift from different zones of a FZP. b) Schematic of the propagation of the wavefield produced by an illuminated FZP. A central stop and a collimating aperture placed close to the focal point are used to isolate the first order from the others.

2.4.1.2.3 Sample environment

Several sample environments are available at ID01 beamline in order to perform *in situ* experiments. The environments I present here have been developed dealing with the constraints of the piezo positioner (weight, size) and the limited space between the sample and the focusing optics, in addition to stability and movement precision issues. The experiments performed in this PhD work used a small furnace and a catalysis reactor. The last one has been developed during my PhD thesis.

The furnace consists on a compact high vacuum chamber that can heat the sample up to $1200°C$ with domes made of several materials (Be, PEEK, polycarbonate and polystyrene). When choosing a dome for an experiment, absorption is one of the most important parameters to take into account (see table 2.1). Nevertheless one can choose the dome regarding the experimental requirements. For instance, the transparent dome (poly-carbonate) allows to "see" the sample with the microscope and the one in polystyrene cannot be used when heating up at high temperature.

The temperature can be controlled automatically thanks to a well-tuned PID controller (*Eurotherm 2408*). Details on the mini-furnace can be found in Ref.[160].

On the other hand, a mini-reactor has been developed to perform the catalysis experiments presented in chapter 5. It is similar to the UHV chamber but some changes have been made for

Dome material	Number of photons on the detector	Transmission
Be	$2.09 \cdot 10^6$	64 %
Polystyrene	$2.24 \cdot 10^6$	70 %
PEEK	$1.706 \cdot 10^6$	53 %
Polycarbonate	$1.713 \cdot 10^6$	53 %

Table 2.1: Transmission test with the available domes at ID01. The number of photons in air being $3.252 \cdot 10^6$, the polystyrene dome is the preferred one

gas compatibility (*i.e.*, with thermocouples type S, not in stainless steel in order to avoid reactions with the gases in the chamber). The base of the reactor consists of an octagonal aluminium plate with eight mounting openings for the PI stage. The base is an aluminum reactor of hexagonal shape, which sides are used for gas inlet, gas outlet and heater connection (see photo in Figure 2.14). The connections to the reactor consist of Teflon gas lines, which are in principle flexible enough to prevent vibrations at atmospheric pressure. Any of the domes described above can be mounted, nevertheless it is suitable to improve the catalytic chamber by decreasing the volume of the reactor for upcoming experiments. Outside the experimental hutch, in the control room, a gas rig with mass flow controllers can also be installed.

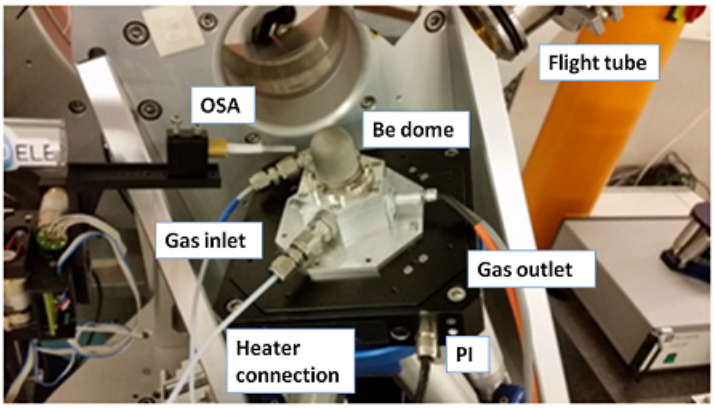

Figure 2.14: Photograph of the reactor installed onto the PI of the beamline. Note that the OSA is very close to the Be dome.

2.5 Conclusion

In summary, I have introduced several lensless imaging techniques and detailed coherent diffraction imaging as this is the main technique used during my PhD thesis. The experimental conditions to perform CDI experiments in Bragg geometry and the algorithms used during the data analysis have been introduced. The need of coherent X-rays, *i.e.* of synchrotron radiation, has been thus justified. Then I have discussed about the experimental set-up of ID01 beamline, which has been upgraded to deal with important factors during CDI experiments such as obtaining larger coherent lengths or improve stability during the measurements. Also, I have highlighted the possibility of performing *in situ* experiments describing the different sample environments available at ID01 beamline, where most of experiments reported in this manuscript were carried out.

CHAPTER 3

Interplay between strain and diffusion in core-shell Ge-Si nanowires

In this chapter, I report the study of strain and composition in individual Ge-Si core-shell nanowires (NWs) by means of Coherent Diffraction Imaging (CDI) and Transmission Electron Microscopy (TEM). First, I will introduce the samples giving details on the growth parameters and I will give information about prior knowledge about the as-grown NWs. An analysis of the elastic strain in the NWs is then described, together with the predicted diffraction patterns for the modeled structures. After that, a first X-ray diffraction study will be presented, which aims to determine the strain along the growth axis direction of the as-grown samples and its dependence on the core/shell ratio. As a consequence of the strained shell, the study will motivate a more careful analysis of the strain field within the Ge core, which only can be successfully retrieved if the NW is completely isolated. Hence, sample preparation is crucial and two different ways of isolating NWs for CDI experiments will be explained. The first one, scratching the NWs on membranes, allows to combine TEM studies with CDI experiments, whereas the second method needs a FIB manipulator but gives access to different components of the strain tensor.

Once strain and composition fields at room temperature are determined, one can investigate the temperature effects on the nanostructures. Interdiffusion at the core/shell interface will be investigated by *in situ* CDI and environmental TEM. The combination of both methods will bring us to preliminary conclusions about the intermixing in core/shell nanowires.

3.1 Introduction

All the samples investigated in this chapter consist of Ge/Si core/shell NWs grown by chemical vapor deposition through the vapor-liquid-solid (VLS) mechanism[161]. Samples are grown by Pascal Gentile at CEA-Grenoble. Colloidal gold particles are used as catalysts for the nanowire growth, which is initiated at 410°C with GeH_4 as a precursor (partial pressure of 10 Torr). HCl is introduced during the growth in order to reduce tapering, to work at high temperature and to keep the colloid diameter. An epitaxial growth of the Ge core is ensured by the choice of the substrate orientation: a Ge(111) substrate guarantees a mostly vertical and monocrystalline Ge-core, since the (111) crystal plane has the lowest surface energy of all crystallographic orientations[162]. By choosing this substrate, Ge NWs get a faceted hexagonal shape, free of dislocations and stacking faults[36,162]. During the Ge wires growth, the gold catalyst is encapsulated by stopping the HCl flow while keeping the gaseous Ge precursor injection. Then the Si is deposited at 600°C and pressures between 3 and 6 Torr under a low flow of HCl, that avoids radial growth and reduce gold diffusion. The high temperature during Si deposition is required to get a crystalline shell. An example of so grown samples is shown in Figure 3.1 a).
It is worth to note that the use of HCl during the growth of the Ge core is expected to reduce gold migration from the catalyst as it has been observed in Si NWs[36,163,164] and to yield smooth facets as can be clearly observed in Fig. 3.1 b).

Nominal diameters of the NWs given hereafter are estimated from the Au catalyst size, while the length can be controlled through growth parameters such as partial pressures of the gas precursors, temperature and deposition time. Moreover, the NWs present a conical shape ("tapering"), with a diameter varying up to 25 % over the length.

Preliminary STEM studies performed by Thomas David at IM2NP-Marseille show that as-grown NWs are fully relaxed but some discrepancies will be seen in the following. Furthermore, chemical analysis performed by energy dispersive X-ray spectrometry (EDX) evidences a very well defined core-shell structure, meaning a total absence of Ge in the shell and an abrupt interface (see Figure 3.2). The abruptness of the interface between the core and the shell is easily obtained because of the different types of growth (catalysed for the Ge NW and not catalysed for the Si shell) and Si and Ge precursors do not mix[49]. However, given the large lattice mismatch between Si and Ge ($\sim 4.01\%$), defects at the interface can be expected - theoretical models predict that only under restrictive conditions Si/Ge coaxial heterostructures are able to accommodate the full mismatch without the creation of dislocations[166,31], smooth and defect-free interface are a major challenge. On the other hand, it has been observed that the Si shell

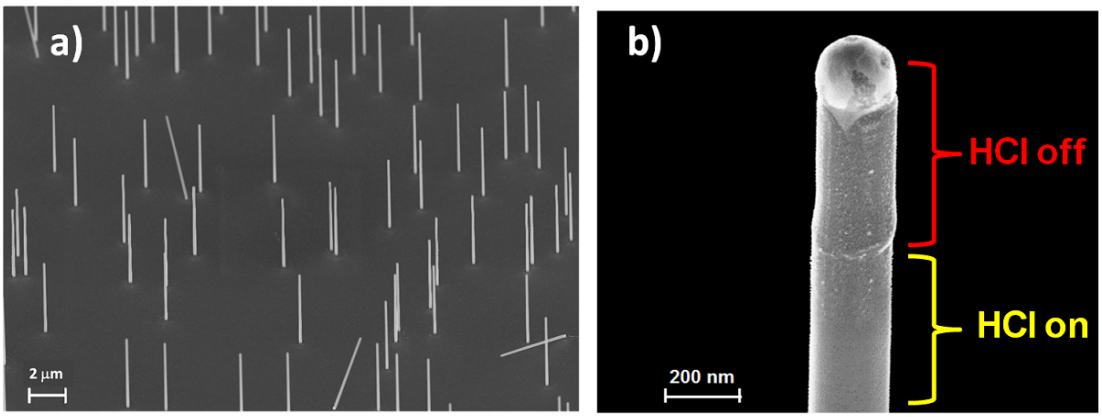

Figure 3.1: a) SEM image of an assembly of Ge/Si core/shell NW measured at ID01 beamline. NWs grow along the $< 111 >$ directions. b) Tip of a Si NW showing the sidewalls in presence and abscence of HCl flow. The segment where the HCl flow is off (top part) is much rougher and small gold droplets diffusing down from the Au catalyst can be observed. From Ref. [165]

roughness increases with the Ge core diameter before dislocations form at the interface[19]. The determination of the axial and radial strains are the subject of the present study.

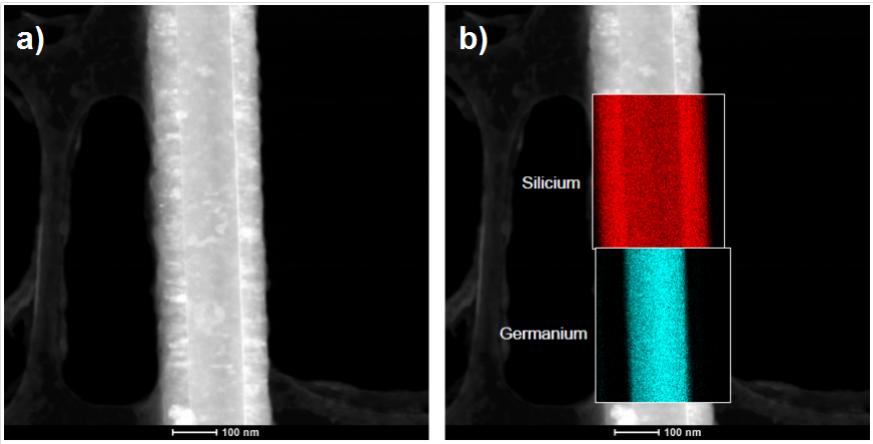

Figure 3.2: STEM image of a Ge/Si core/shell NW (a) and its corresponding EDX map (b).

Most CDI experiments presented here were carried out at ID01 beamline. Only the experiment presented in Subsection 3.3.2.1 was performed at the CRISTAL beamline in the synchrotron SOLEIL (France); set-up and experimental details will be given in the corresponding section.

3.2 Residual strain in core-shell Ge-Si NWs: linear elastic model

In Chapter 1 it has been evidenced that as a result of the epitaxy between two materials such as the ones forming the core and the shell of the here studied NWs, there exists a residual strain in the nanostructures that can be used as an adjustable parameter. Theoretical studies in the case of semiconductor NWs has been explained in Section 1.2.1.1, but a more precise analytical

description is necessary to understand the particular case of Si and Ge, given that the different values of the stiffness constants may lead different distributions of local strain.

In this section, I will apply the model developed by Liang *et al.*[32] for SiGe core-shell films and small pillars to the core/shell NWs case. First, the isotropic case will be discussed: the cylindrical geometry makes easier the understanding of the evolution of the theoretical elastic epitaxial strain with the diameters of the core and shell. Secondly, the case of hexagonal Ge-Si core shell NWs will be analysed. As this is a closer approach to the real system, the expected diffraction patterns of single NWs deduced from the calculated strain will be shown. These simulations will allow to compare the ideal case of pseudomorphous epitaxy with the one of incoherent interfaces.

3.2.1 Strain in elastically isotropic materials

A schematic diagram of the cylindrical Ge-Si system is shown in Fig. 3.3, where a is the outer shell radius and c is the inner-core radius. The $z-$direction corresponds to the nanowire growth direction, whereas (r, θ) or (x, y) denote the in-plane coordinates in the NW crystal frame. Both materials, Si and Ge, exhibit cubic elastic symmetry and have the same orientation, with different values of the lattice constants a_{Ge} and a_{Si} (Table 3.1). The growth is assumed to be coherent, with no misfit defect at the interface, so that the lattice mismatch $\epsilon^{\text{misfit}} = (a_{Si} - a_{Ge})/a_{Ge} = -4.01\%$ is fully accommodated by elastic strain.

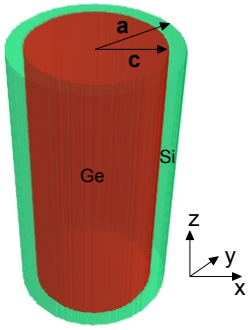

Figure 3.3: Schematic diagram of the cylindrical Ge-Si nanowire. The $z-$axis denotes the NW growth direction.

		Si	Ge
a_0 (Å)		5.43	5.658
Elastic constants (GPa)	C_{11}	165.8	128.5
	C_{12}	63.9	48.3
	C_{44}	79.6	66.8

Table 3.1: Lattice parameters and elastic constants used in the analytic model[167].

A good starting point to determine the strain components is to assume that Si and Ge have the same elastic constants (which are summarised in Table 3.1). Analytical expressions to determine the strain at any point r have been demonstrated by Liang *et al.*[32], which are the following:

$$\epsilon_{zz}^{\text{shell}} = -\frac{c^2}{a^2}\epsilon^{\text{misfit}}, \tag{3.1}$$

$$\epsilon_{zz}^{\text{core}} = (1 - \frac{c^2}{a^2})\epsilon^{\text{misfit}}, \tag{3.2}$$

$$\epsilon_{rr}^{\text{shell}} = \frac{-c^2\epsilon^{\text{misfit}}(1+\nu)}{2a^2(1-\nu)}(1 - \frac{a^2}{r^2}), \tag{3.3}$$

$$\epsilon_{\theta\theta}^{\text{shell}} = \frac{-c^2\epsilon^{\text{misfit}}(1+\nu)}{2a^2(1-\nu)}(1 + \frac{a^2}{r^2}), \tag{3.4}$$

$$\epsilon_{rr}^{\text{core}} = \frac{a^2-c^2}{2a^2}\epsilon^{\text{misfit}}\frac{1-3\nu}{1-\nu}, \tag{3.5}$$

$$\epsilon_{\theta\theta}^{\text{core}} = \epsilon_{rr}^{\text{core}}, \tag{3.6}$$

where ν is the Poisson's ratio ($\nu = 0.27$). The strain components are given with respect to Ge bulk lattice parameter in the core and with respect to Si lattice parameter in the shell ($i.e$ with respect to the bulk lattice parameter of the element/material associated to the given region). ϵ_{xx} and ϵ_{yy} can then be deduced by applying the following formula:

$$\epsilon_{xx} = \epsilon_{rr}cos^2(\theta) + \epsilon_{\theta\theta}sin^2(\theta), \tag{3.7}$$

$$\epsilon_{yy} = \epsilon_{rr}sin^2(\theta) + \epsilon_{\theta\theta}cos^2(\theta). \tag{3.8}$$

The principal strain components (ϵ_{zz}, ϵ_{xx} and ϵ_{yy}) for a 100 nm nanowire, calculated using the here above equations, are displayed in Fig. 3.4. These results evidence an induced stress in the whole system due to the epitaxial growth of Si around the Ge NW. Furthermore, as the inner Ge core has a larger lattice parameter than the surrounding Si shell, it tends to contract. Therefore the outer Si shell tends to expand when the core and the shell are linked together.

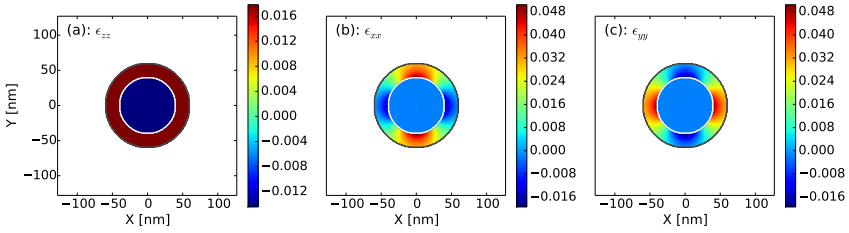

Figure 3.4: Theoretical elastic epitaxial strain components in a Ge-Si core-shell nanowire at its center in the z-direction: a) ϵ_{zz}, b) ϵ_{xx} and c) ϵ_{yy}.

The longitudinal strain ϵ_{zz} results from the lattice mismatch in the direction of the nanowire axis, which is shared between the core and the shell with a weight inversely proportional to their area. Equations 3.1 and 3.2 allow to calculate the expected axial strain (ϵ_{zz}) in the core and in the shell for different core/shell radius. The so calculated ϵ_{zz} for a series of core diameter ranging from 50 to 200 nm is displayed in Figure 3.5. The thinner the core, the smaller the out-of-plane strain in the shell and the higher its out-of-plane strain ($\epsilon_{zz}^{\text{core}}$). A narrow core is fully strained to the thick shell and equivalently, as it is a thin shell to a wide core. Indeed, for a given shell thickness, smaller diameter cores are strained more than the larger ones.

3.2.2 Calculation of diffraction patterns: case of hexagonal wires

Once the strain inside the NWs is known, the diffraction patterns from the objects can be calculated. In the case of hexagonal NWs, small deviations in the strain field within the NW exist from the cylindrical model. These differences are further discussed in Ref.[28]. However, to simplify the model, the strain is supposed to be isotropic in the calculations of the diffraction patterns presented here. As discussed in Chapter 1, the local deformation, in the vicinity of a point $\vec{r}$, is fully

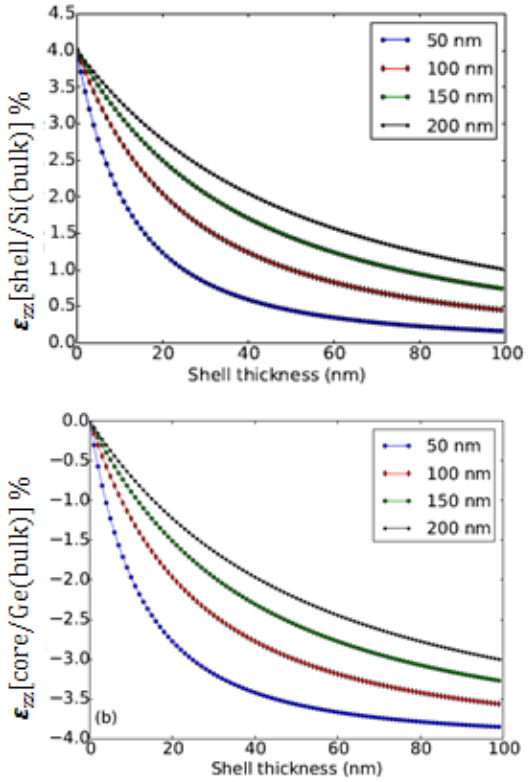

Figure 3.5: Theoretical elastic epitaxial out-of-plane strain in the shell (a) and in the core (b) of Ge-Si core-shell nanowires as a function of shell thickness for a cylindrical geometry. The diameter of the Ge core is indicated in the legend.

described by the atomic displacement, hence the tensor of the derivatives of u($\vec{r}$), $\partial u_i/\partial x_j$; the symmetric part is the strain tensor $\epsilon_{ij} = 1/2(\partial u_i/\partial x_j + \partial u_j/\partial x_i)$. Thus the displacement field u($\vec{r}$) relates the position of any point $\vec{r}$ in the strained material to its value in the mismatched, unstrained system.

For the calculation of the diffraction patterns, the reference lattice parameter is the unstrained lattice parameter of bulk Ge ($a_{Ge_0} = 0.5658$ nm). According to Ref.[168], the diffracted intensity $I(\vec{q})$ is proportional to the squared modulus of the Fourier Transform of the complex-valued real-space object $\tilde{\Omega}(\vec{r_0})$, which fulfills:

$$\tilde{\Omega}(\vec{r_0}) = [c_{Ge}(\vec{r_0})\tilde{F}_{Ge}(\vec{q_0}) + c_{Si}(\vec{r_0})\tilde{F}_{Si}(\vec{q_0})]e^{i\vec{q_0}\vec{u}(\vec{r_0})}, \tag{3.9}$$

where $\vec{q_0}$ is the reciprocal space lattice vector, $\tilde{F}_{Ge}$ ($\tilde{F}_{Si}$) is the structure factor of Ge (Si), and c_{Ge} (c_{Si}) is the fractional concentration of Ge (Si) respectively ($c_{Ge} + c_{Si} = 1$). The Ge/Si NWs studied during this work, grow along the [111] crystallographic direction so that $q_{0z} = \frac{2\pi}{d_{111}^{Ge\ bulk}} = 1.923$ Å^{-1}.

Figures 3.6(b-c) and 3.7 display the calculated diffraction patterns of the **111** Bragg reflection of the Ge-Si core-shell nanowire displayed in Fig. 3.6(a). Two cases are shown: either a coherent (b) or an incoherent (c) Ge-Si interface. In the case of a coherent interface only one peak is observed in the (Q_x-Q_z) plane because the lattice spacings from both materials accommodate to match in the interface plane. This is why the Bragg peak is positioned at $Q_z \sim 1.95$ Å^{-1}, which corresponds to a lattice parameter of 5.581 Å. In the case of the incoherent interface, the Ge core

and the Si shell diffract at the Q_z position of their bulk lattice parameter: *i.e.* Q_z = 1.923 Å^{-1} for Ge and Q_z = 2.004 Å^{-1} for Si. In addition, six streaks in the $Q_x - Q_y$ plane are observed. They correspond to the six crystalline facets forming the hexagonal cross-section of the NW, and this is observed at two different positions along Q_z in the case of an incoherent interface (Fig. 3.6 c) and Fig. 3.7c) and d)). The two streaked peaks are due to the different lattice parameters of the Si shell and Ge core, both of them supposed to have smooth and well defined facets. Thickness fringes owing to the finite size of the wire are also observed along the streaks, and in the case of a coherent interface (Fig. 3.6b) and Fig. 3.7a) and b)), beat frequencies from the interferences between the core and shell thickness are visible.

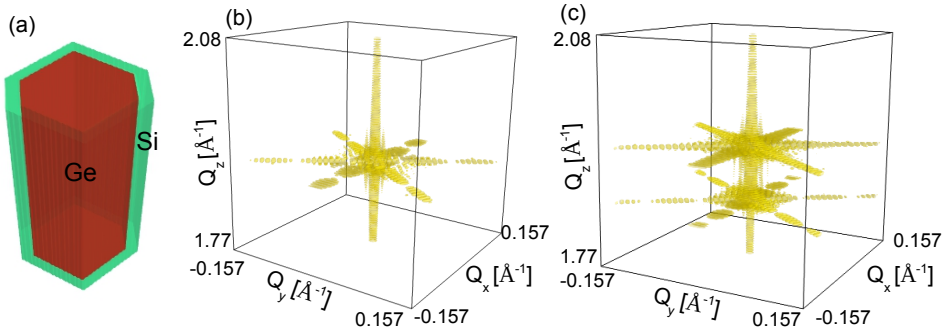

Figure 3.6: (a) Schematic view of the hexagonal Ge-Si core-shell nanowire. (b)-(c) Three-dimensional diffraction patterns of the **111** Bragg reflection in the case of a coherent (b) or incoherent (c) Ge-Si interface.

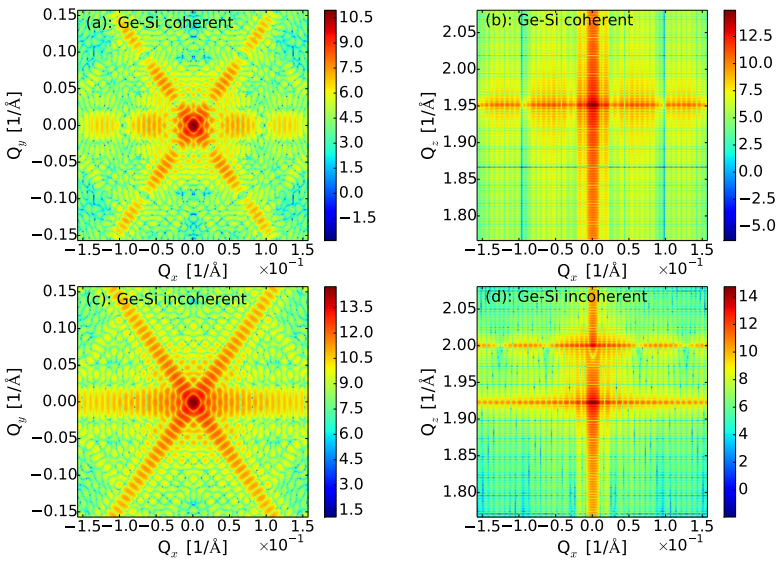

Figure 3.7: Diffraction patterns of the **111** Bragg reflection of an hexagonal Ge-Si core-shell nanowire displayed in the Q_x-Q_y (at the Q_z position of the scattering from the Ge core) and Q_x-Q_z planes in the case of a coherent (a-b) or incoherent (c-d) Ge-Si interface.

Calculating an in-plane reflection is also possible from the strain values calculated in the

previous Subsection. Let us show the diffraction patterns obtained for the $\mathbf{22\bar{4}}$ reflection, the x-axis being assumed along the in-plane $[22\bar{4}]$ direction, so that $q_{0x} = \frac{2\pi}{d^{Ge\ bulk}_{22\bar{4}}} = 5.44$ Å^{-1}. Compared to an incoherent interface, in the case of a coherent interface the signal from the Si shell is closer to the one of the Ge core, as it can be observed in Figure 3.8.

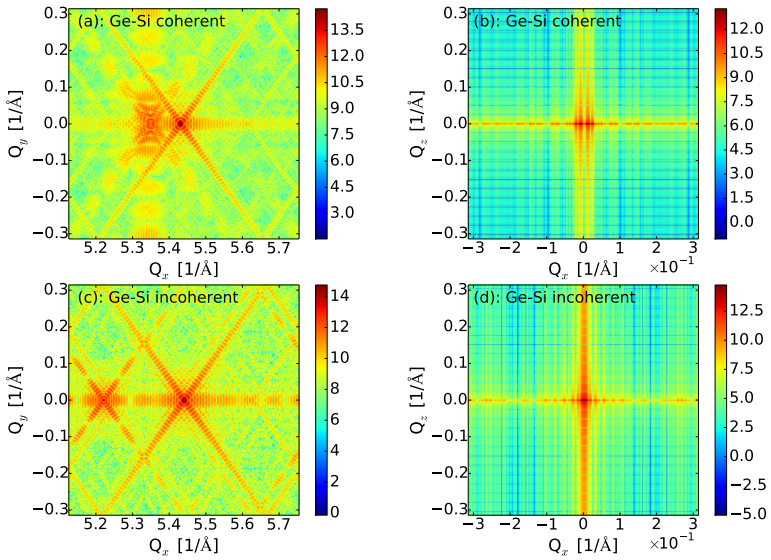

Figure 3.8: Diffraction patterns of the $\mathbf{22\bar{4}}$ Bragg reflection of an hexagonal Ge-Si core-shell nanowire displayed in the Q_x-Q_y and Q_x-Q_z planes in the case of a coherent (a-b) or incoherent (c-d) Ge-Si interface.

The interest of calculating the here above diffraction patterns is their comparison to the experimental data that will be shown and analysed in the following. Indeed, from single recorded diffraction patterns, important qualitative information such as the coherence (or not) of the interface of the wire can be determined.

3.3 Investigating the strain in single NWs

3.3.1 Strain in as-grown nanowires and dependence on the core/shell ratio

As stated in the introduction, we have started the characterisation of core/shell Ge/Si NWs by studying a single wire in its state after growth, *i.e.* without any manipulation and on its original substrate. The use of a nano-focused beam for diffraction experiments, with a size of the order of the NWs diameter, allows to select and analyse one single nanowire. In addition, probing the strain locally gives insights in single structures, such as crystalline structure changes[169] or localised defects, often at the bottom of the wires as a result of the epitaxy with the substrate[111]. However, the arrangement of the wires on the substrate is critical: the wide footprint of the X-ray on the sample can yield parasitic signal from surrounding wires or islands on the substrate, or even average properties if several wires fulfilling the same Bragg conditions are close to each other. In the experiment here reported, we study three different samples grown as explained in Section 3.1, so that the majority of the wires grow vertically from the substrate surface and the others are aligned along one of the other three $< 111 >$ directions, *i.e.*, they are tilted at 70.5° from the substrate normal. A scanning electron microscopy (SEM) image of one of the studied samples showing the NWs distribution and their orientation can be seen in Fig. 3.1 a).

The three samples consist of Ge-core wires with a 50 nm Si-shell. Also NWs with a 100 nm Ge-core and a 20 nm Si-shell were measured. The characteristics of the NWs are summarised in Table 3.2. The length of the wires is about 5 μm and they exhibit an hexagonal cross-section formed by {112} side facets. The decrease of the Ge NW core radius leads to an increase of the density of wires on the sample.

Sample number	**Core diameter**	**Shell diameter**	γ
1	50	50	1
2	100	50	0.5
3	200	50	0.25
4	100	20	0.2

Table 3.2: Summary of the characteristics of the samples measured at ID01; $\gamma =$ Ratio shell/core. Note that the diameters correspond to the nominal values of the diameter of the gold colloids and are smaller than the ones observed in the SEM images.

The nanodiffraction experiment was carried out at ID01 beamline; the X-ray beam was focused using a Fresnel Zone Plate placed at the focal distance in front of the center of rotation of the diffractometer, together with a central beam stop and an order-sorting aperture that blocks all except the first diffraction order. A more detailed description of the set-up at ID01 can be found in Chapter 2. The typical photon energy for this experiment and the ones that will be reported here above is 8 keV, and the exact focal length was optimised for each experiment, obtaining typical spot sizes of 150 (V) $\times$ 400 (H) nm^2.
The described experimental set-up is illustrated in Figure 3.9 a), a focal size of $130 \times 380\ nm^2$ (vertical $\times$ horizontal) was obtained with the Fresnel Zone Plate in the case of this particular experiment. The intensity distribution around the symmetric **111** reflections was measured in a coplanar diffraction geometry, with the sample surface mounted horizontally. At the working energy of 8 keV, **111** Ge and Si Bragg reflections are accessible at a scattering angle of $2\theta_{Bragg} = 27.44°$ and $28.63°$ respectively. Owing to this geometry for the incident Bragg angle, the footprint of the X-ray beam on the sample surface was about 540 nm along the X-ray beam propagation. The detector recording the diffracted intensity was placed at 0.97 m from the sample, in order to well observe the thickness fringes of individual wires.

In order to study one single nanowire, the samples were first aligned at the **111** Ge Bragg

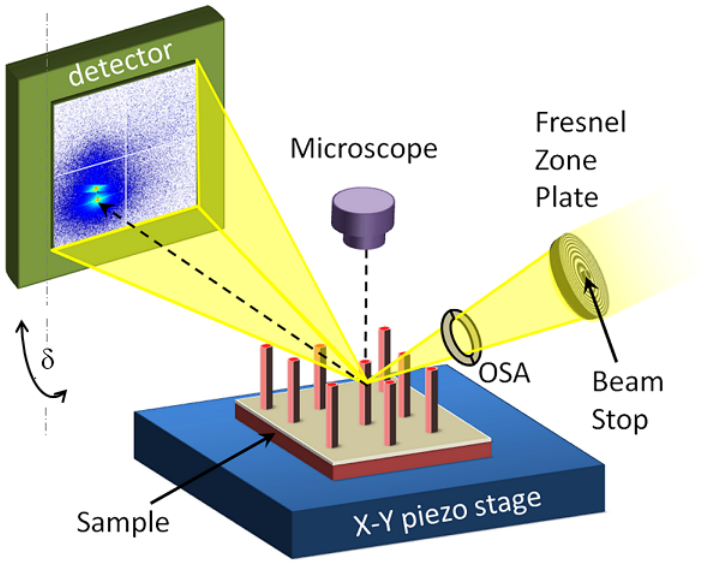

Figure 3.9: a) Experimental set-up at ID01 for CDI experiments on an assembly of NWs. Recording the scattered intensity from the Ge core of an isolated NW, also the diffracting shell yields to a Bragg peak on the 2D detector. The *out-of-plane* angular distance between the Bragg peaks on the detector depends on the lattice mismatch; radial scans moving the detector along the vertical direction (δ) allows to determine the axial strain of the NW.

reflection to map out the intensity distribution in the x and y directions of the sample using the quicK-Mapping technique[159] explained in Chapter 2. Once the NWs were identified in the real space (x,y) maps, the X-ray beam was focused on an isolated one in the explored region. Then symmetric reciprocal space maps (RSMs) were collected around the **111** Bragg reflection of different single nanowires with different core/shell ratio. Reciprocal space maps for three different wires corresponding to samples 1, 2 and 3 (as labeled in Table 3.2) with Ge-core nominal sizes of 50, 100 and 200 nm, together with a measurement of sample 4 (different shell thickness), were recorded and will be analysed in the following.

Figure 3.10 shows the RSMs recorded for the two samples with 100 nm Ge-core. Figs. 3.10 a) and b) correspond to the diffracted intensity from a single wire of 20 nm shell thickness and 50 nm respectively. The RSMs consist of a sharp and intense Bragg peak from the Ge substrate, superimposed by a vertical streak corresponding to the crystal truncation rod (CTR) originated from the **111** Ge substrate surface. The inclined streak is caused by the saturation of the pixel detector when the rocking curve crosses the bright Ge substrate Bragg peak. The elongated signal at $Q_z = 1.9234$ Å^{-1} corresponds to the Ge core of the NW in both cases (circled in Fig. 3.10). A two-dimensional (2D) cut at this position of the rocking curve, yields to the high-resolution RSMs shown in Fig. 3.11 a) and b) for the NWs of 20 nm and 50 nm thickness shell respectively. While the scattered intensity from the thicker NW (Fig. 3.11 b)) exhibits six intensity modulated streaks, the thinner one yields a rounded Bragg peak. The thickness fringes allow to estimate the diameter of the Ge core to 220 and 157 nm respectively, in contrast with the expected diameter from the colloid size (100 nm). Therefore, both nanowires have larger diameters. There are two possible explanations for the size difference: one would be due to the melting of the colloid during growth, which would lead to hemispherical droplets on the substrate surface with larger diameters as a consequence of volume conservation. Another possibility would be the coalescence of gold colloids before the NW growth. On the other hand, the difference of size between both NWs could be related to the tapering: NWs have larger diameters at the bottom and there is not guarantee that the measurements were taken at the same position of the NW.

The shape differences (faceted and circular) may be related to the variation of at least one parameter during the growth, such as the HCl flow during the shell deposition or the use of sligtly different temperatures. Indeed, any of these parameters could change the radial growth speed which may directly influence the faceting of the wires[170].

Let us go back to Figure 3.10. The shown 3D RSMs have been recorded by performing a rocking curve, hence by rotating the selected NW around the **111** Ge Bragg reflection of a total angular range of 1.6°. The use of the MAXIPIX (2D detector) allows the collection of 2D slices of reciprocal space at each scan step. As Si and Ge have different lattice parameters, they yield peaks at different Q_z values (see Figure 3.9): their positions depend on the scattering angle and the rocking angle of the sample. From the position of the Ge and Si **111** Bragg reflection from the NW, which are positioned close to the **111** Ge substrate's reflection, the lattice parameters (of core and shell) perpendicular to the substrate surface can be determined. Indeed, the experimental lattice mismatch between both materials is determined by the distance between the Bragg peaks positions on the detector, since one expects a compression at the interface of the nanostructure as a result of the epitaxy. Hence, the relative strain can be retrieved by measuring the shift of the peaks with respect to the substrate diffraction peak. However, the rocking curves are performed with the detector fixed at the $2\theta_{Bragg}$ angle position and far from the sample to increase the resolution in reciprocal space. As consequence of the large distance, the detector only covers one or two degrees and one can miss a relaxed Si Bragg peak. In order to explore a wider range around the Ge Bragg peak, *radial scans* have also been performed, meaning moving the detector along the vertical direction ($i.e.$ along the δ angle at ID01 beamline).

In the experimental data (Fig. 3.10), apart from the intense peak around Ge position, a less intense signal can be observed around $Q_z = 2.0038$ Å^{-1}, the expected position of the Si bulk Bragg peak. Since the surface of the substrate must diffract at the Ge bulk position, one can take its position on the detector as reference to calculate the variation of the lattice parameter of the signals expected to correspond to Ge core and the Si shell of the nanowire:

$$\epsilon\ (\%) = \frac{a - a_{ref}}{a_{ref}} \times 100 \tag{3.10}$$

where a and a_{ref} are the experimental lattice parameters and the reference one respectively, here the bulk Ge (see Chapter 1). Therefore, if a completely relaxed Si shell is grown around the Ge NW core, the smaller (111) lattice plane spacing of Si, leads to a scattering signal located at higher Q_z compared to the Ge core ($d_{Ge_{111}} = 3.279$ Å$> d_{Si_{111}} = 3.136$ Å). If the Si shell is subjected to tensile strain along the wire axis (with respect to Si bulk), the scattered signal will be displaced along Q_z towards the Ge Bragg peak position.

The fit of the experimental peaks from Fig. 3.10 b) - *Sample 2* -, yields the intensity profile shown in Fig. 3.11 c), where the dashed lines correspond to the bulk expected positions. The fit was performed for the four samples, and for different NWs when possible - isolating wires in high density samples was extremely challenging -. For all core radii, the scattered signal consists of two maxima: one elongated horizontal signal coming from the Ge NW core (positioned at the bulk Ge Bragg peak) and a second one displaced towards larger Q_z, $i.e.$ smaller lattice parameters, which corresponds to the Si shell. Results show that the Ge core is completely relaxed (its corresponding signal was found systematically at the bulk Ge Bragg peak) for any core/shell ratio, whereas the Si shell was found to be dependent on the core diameter and tensile along the wire axis with respect to Si bulk. Results from the fits are summarised in Table 3.3; for the thicker sample (Ge core diameter of 200 nm) the shell is completely relaxed. The shell of NWs with the same core diameter (100 nm) are higher strained than the thinnest one (50 nm core, 50 nm shell). The strain differences between NWs from the same sample can be explained by the local strain variations because of the diameter variation along each wire. On the other hand, strain in samples 2 and 4 (same core diameter) are not really comparable since the growth conditions have been different, as evidenced by the shape differences discussed here above (see Figs. 3.10 a) and b)).

For clarity, the experimental results presented in Table 3.3 have been plotted in Fig. 3.13, together with the theoretical predictions of strain accommodation in the case of fully coherent nanowires calculated using the model proposed by Liang *et al.*[32] (see Section 3.2.1 for further details). In their model the lattice mismatch is supposed to be fully accommodated and the absence of misfit defects is assumed. In such a case, larger diameter cores induce more strained shells (*i.e.* higher axial strains $\epsilon_{Si_{shell}/Si_{bulk}}$). As observed in Fig. 3.13, the experimental results found in this study do not follow the elastic epitaxial strain expected for a coherent shell; strain relaxation may occur by formation of misfit defects at the interface for the measured nanowires.

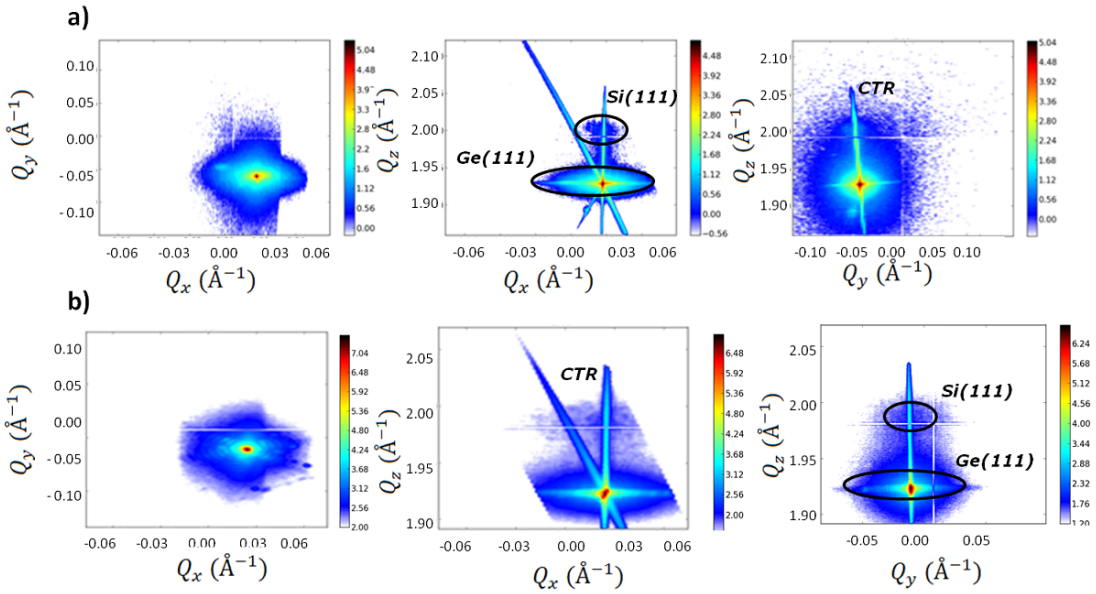

Figure 3.10: Intensity distribution as a function of the x, y and z coordinates of the reciprocal space vector $\vec{Q} = \vec{k_f} - \vec{k_i}$ of two NWs with the same core diameter (100 nm), but different shell thickness: a) 20 nm and b) 50 nm. The signal arising from the NW has been circled. The intense vertical and inclined streaks are due to the substrate CTR and the detector saturation respectively.

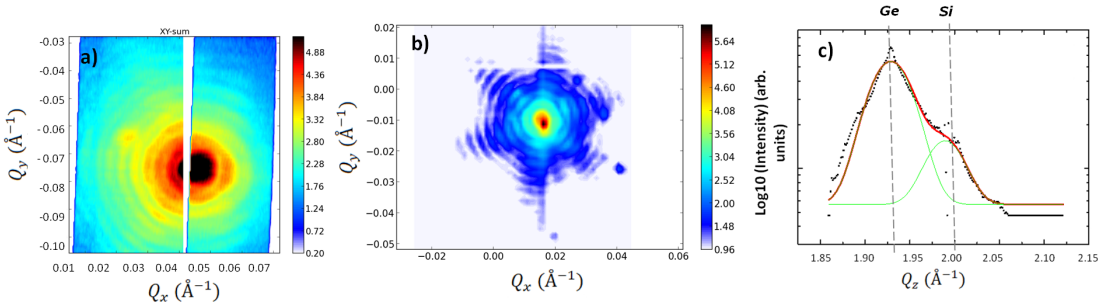

Figure 3.11: 2D diffraction patterns of single nanowires from samples 2 (a) and 4 (b). The facets are evidenced in the thicker NW. The missing data are due to the strong CTR from Ge substrate c) Intensity profile from Fig. 3.10) b) and fit of the Ge and Si peaks allowing to calculate the axial strain. Dashed gray lines indicate the **111** Ge and Si bulk Bragg positions.

Figure 3.12 shows the $Q_z - Q_y$ cuts of the NWs of 50 nm and 200 nm core respectively. In

Sample number	NWs diameter (nm)	γ	Nanowire	$\epsilon_{Si_{shell}/Si_{bulk}} \pm \Delta\epsilon_{Si_{shell}/Si_{bulk}}(\%)$
1	$d_c = 50, d_s = 50$	1	1	0.37 ± 0.03
2	$d_c = 100, d_s = 50$	0.5	1	0.83 ± 0.02
			2	0.88 ± 0.03
			3	0.81 ± 0.02
			4	0.91 ± 0.03
3	$d_c = 200, d_s = 50$	0.25	1	0.01 ± 0.06
			2	0.01 ± 0.06
			3	0.03 ± 0.04
4	$d_c = 100, d_s = 20$	0.2	1	0.695 ± 0.08
			2	0.393 ± 0.07

Table 3.3: Measured strain in the shell of single NWs with different ratio $\gamma = \frac{shell\ diameter}{core\ diameter} = \frac{d_s}{d_c}$.

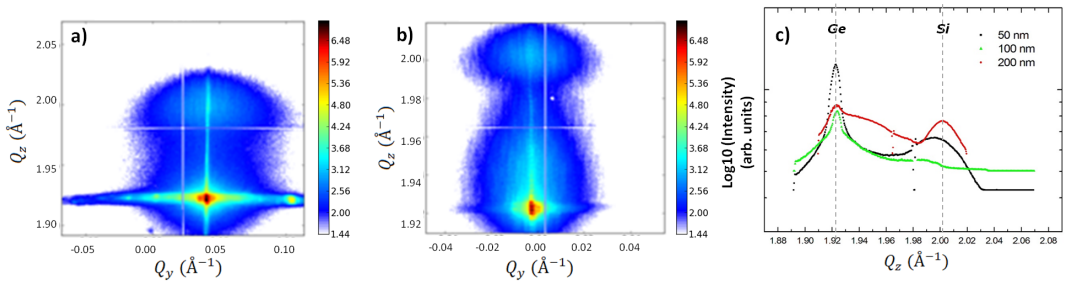

Figure 3.12: 2D RSMs of a) Sample 1 ($\gamma = 1$) and b) Sample 4 ($\gamma = 0.25$). c) Experimental curves of three different NWs, representatives of each sample of different core diameters.

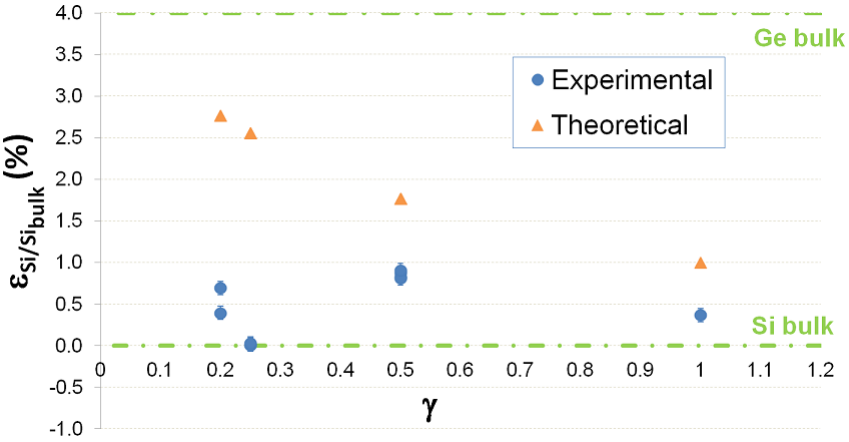

Figure 3.13: Measured strain in the Si shell with respect to Si bulk for the samples with different radius $\gamma = \frac{d_s}{d_c}$. The theoretical predictions[32] in the elastic epitaxial case are also plotted.

these cases, the signal is much blurrier than for the 100 nm core (Fig. 3.10), where the cross sections at the maximum of intensity of the rocking curve evidenced the NW shape. The recorded RSM from sample 1 is believed to be the average of more than one NW, given the high density of NWs on the sample and the parasitic spots in the diffraction pattern. In the case of the thicker wires, $\gamma = 0.2$, the Bragg peak can be actually fitted by three gaussians (see Fig. 3.12 c) 3.3).

The first one is attributed to the Ge core, then the one at the Si bulk position ($Q_z = 2.00$ Å^{-1}) may come from a relaxed shell. The third one at $Q_z = 1.94$ Å^{-1} is attributed to Si deposited on the substrate during the growth or other surrounding NWs or islands, diffracting as a result of the large X-ray beam footprint in this geometry. The attribution of the relaxed peak to the shell is supported by *in situ* growth experiments of core-Si shell-Ge NWs on Si(111) substrates[64]. The cited study showed by X-ray diffraction that during the injection of the shell gas precursor on two samples prepared under identical conditions except the catalyst amount, strained Ge islands formed at the surface either in presence or not of Si NWs.

Results from this Section can be summarised as follows: first, the axial strain Ge core is zero, and second, the shell is weakly strained and depends on the Ge core diameter. Despite the real diameter of the NWs is unknown, as from the diffraction patterns only the core diameters can be determined from the thickness fringes, the measurements evidence a relaxed shell that does not follow the expected behavior of fully epitaxial nanowires. A non coherent interface may explain the relaxation of the shell, via defects formation, morphology changes or misfit dislocations (see Chapter 1). Further investigations are hence necessary to figure out the reason why Ge core is completely relaxed and understand the actual influence of the shell. Knowledge of the strain field within the Ge core could provide information about the formation of defects at the interface for instance. In order to retrieve this information, CDI is used in the next Section. Single NWs from sample 2 will be investigated in Subsections 3.3.2.1 and 3.4.1. Then one NW from sample 3 will be studied in Section 3.3.2.2.

3.3.2 Investigating the strain field within single isolated NWs

The results presented in the previous Section (Section 3.3.1) motivate the preparation of low number density or strictly isolated nanowires for CDI experiments. Whereas it takes longer during the beamtime to find the object in a so-prepared sample, this ensures that the whole recorded intensity is originated by the nanostructure.

The nanowires can be detached from the substrate in two different ways:

1. Directly scratching a second surface over the sample or using an ultrasonic bath. The surface where the NWs will be dispersed can be chosen regarding the experiment requirements and this is the easiest and fastest way. However, in this way as the wires break, defects can be induced in the NWs by the manipulation process itself. Also, after deposition, NWs are randomly distributed over the substrate/membrane and they can be located very close to each other. Therefore, it can be very time consuming to find a good location on the sample during an experiment, even if microscopy allows to localise separated wires, because even in SEM images, crystalline defects are not observed. Different substrates were tested during the first experiments of this PhD work: first, sapphire (Al_2O_3) and micro-trenches patterned Si substrates (see Fig. 3.14a)), and second, Si_3N_4 and Copper TEM compatible membranes. Examples of the so dispersed NWs and a diffraction pattern of a single NW on an Al_2O_3 substrates is shown in Fig. 3.14. The rounded $\bar{2}\bar{2}4$ Ge Bragg peak in Fig. 3.14 b), evidences a complex strain field inside the NW that hides the characteristic streaked shape caused by the faceted structure. Experience shows that wires deposited on such surfaces are more prone to induced defects than the ones on membranes. Let us worthily mention that NWs over the sample exhibit different strain states and the one here shown is just representative. On the other hand, membranes have the advantage of being compatible with posterior TEM studies, but localising the X-ray studied NWs can be challenging. An added difficulty is the orientation of the deposited NWs. Micro-Laue diffraction analysis shows that most Ge/Si wires lie on one of their {112} facets but they can be slightly rotated or differently oriented, in contrast with metallic NWs[171,172]. NWs dispersed on membranes will be studied hereafter (Section 3.3.2.1).

2. Using a micro SEM/FIB manipulator (see Fig. 3.14 c)). This method consists in transferring a single NW from the original growth substrate to a holder such as a tomography tip or

a TEM lift-out grid. The NW is cut from its root then glued with Carbon in the upright position. The samples were prepared in this way by our collaborators in *CMTC-Grenoble* and in the *Institut Lumiére Matière, Lyon*. Sections 3.3.2.2 and 3.4.1 are dedicated to single structures isolated using this preparation technique.

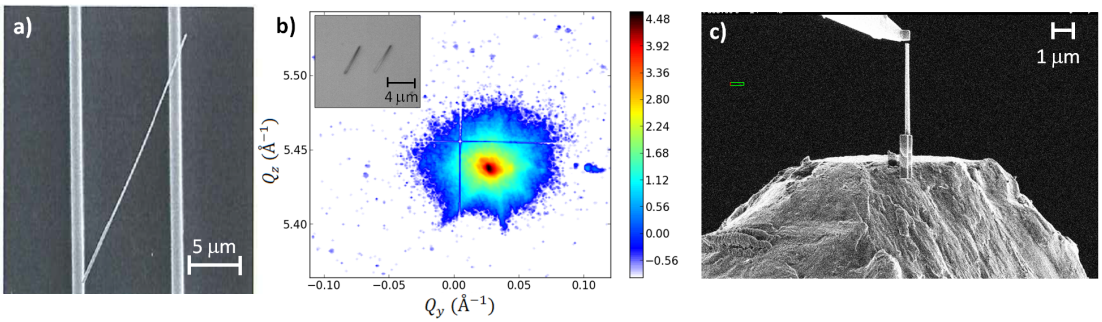

Figure 3.14: Summary of different systems of isolated NWs. a) NW deposited on a bridge between two Si trenches. b) Diffraction pattern around the $\bar{2}\bar{2}4$ Ge Bragg reflection of a Ge/Si core shell NW lying on a sapphire substrate. The RSM corresponds to the NW on the right of the inset image. c) SEM image showing the transfer of the NW using a FIB manipulator.

3.3.2.1 Combining CDI and TEM: homogeneity over the sample

In this section I will present the results obtained during an experiment carried out at the CRISTAL beamline, at the synchrotron SOLEIL (France). Therefore, the properties of the source, $i.e.$ the coherence lengths of the X-ray beam, differ from the ones given in Chapter 2 for the ID01 beamline at the ESRF.

At the experimental hutch of CRISTAL, the X-ray beam is delivered by a single undulator (U20) that allows to work in an energy range between 4 and 30 keV. For CDI experiments, energy is set between 6 and 12 keV. Although it is possible to use other techniques such as time-resolved diffraction or high angular resolution diffraction on this beamline, here we focus on the experimental set-up used for the coherent X-ray diffraction experiments.

The monochromatic beam is obtained using a Si(111) monochromator. The larger source size at SOLEIL and the closer position of the sample with respect to it ($\sim$ 40 m), yield a much shorter coherence vertical length compared to the one from ID01. The theoretical vertical transverse coherence length at CRISTAL beamline is estimated to $\xi_T = 80\ \mu m$ for a wavelength $\lambda = 1$ Å.

A 6-circle diffractometer is installed in the experimental hutch of CRISTAL. Similarly to ID01's diffractometer, the detector arm allows to move a MAXIPIX 2D detector[173] in both horizontal (γ) and vertical (δ) direction, and there are four motors allowing to rotate the sample. Motors movements are described in Fig. 3.15 a); further details on the beamline can be found in Ref.[174,142].

The working energy during this experiment was 8.5 keV. Pre-sample slits were closed to $80 \times 20\ \mu m^2$ (V $\times$ H) to be in coherent conditions during the measurements. The coherent beam was focused using a FZP, which typically yields a spot of about 2 $\times$ 0.5 μm^2 (H) $\times$ (V) on the sample.

The Ge/Si core shell nanowires were deposited on a Cu TEM-grid as explained earlier in this Section. In order to save time during the X-ray experiment, it is convenient to select the less dense regions of the samples just after preparation -as the NWs are long enough this can be easily done using an optical microscope. Thanks to this first overview of the sample, and the features of the TEM grid (such as the asymmetric mark in the center or the edges), a first zone to be probed can be prepared when fixing the sample on the holder, $i.e.$, paying attention to the

orientation of the grid with respect to the incoming beam. An example of the NWs distribution over the sample is shown in Fig. 3.15 b).

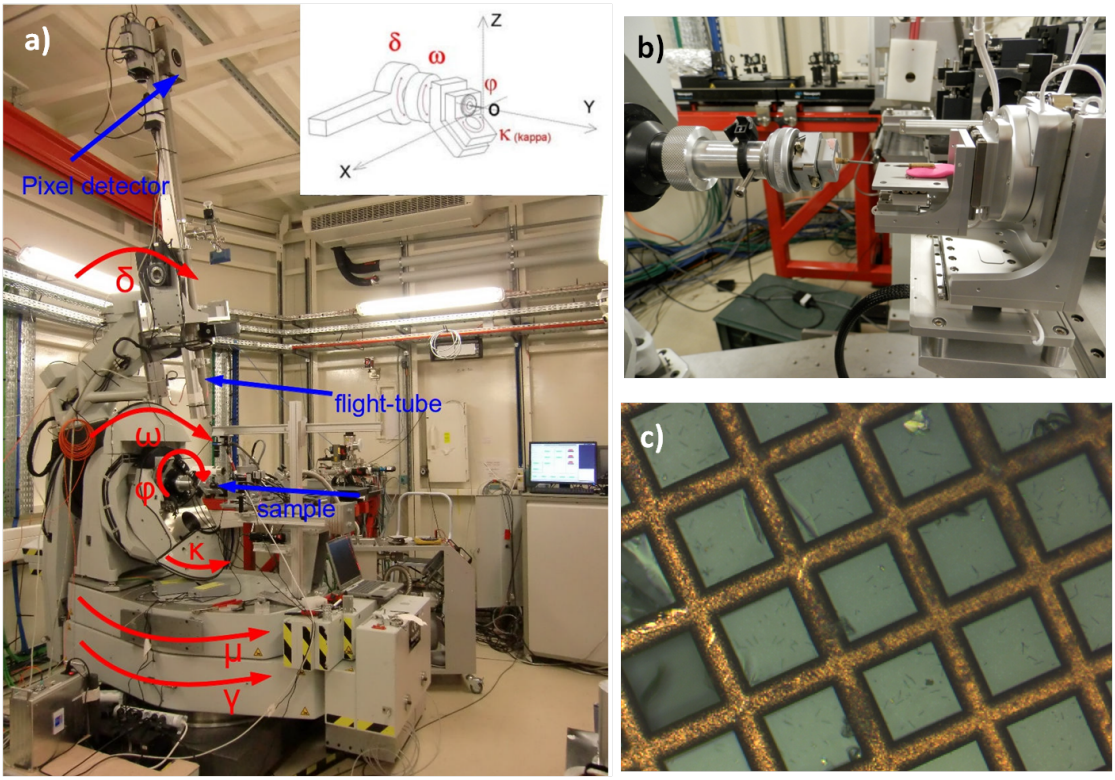

Figure 3.15: a) 6-circles diffractometer and b) mini-goniometer at CRISTAL beamline, from Ref.[175]. c) Image of the measured sample taken with an optical microscope to localise the NWs before the CDI experiment. The NWs were deposited on the TEM grid by the scratching method, which explains the broken areas.

The TEM grid was mounted on the sample holder of the diffractometer using a Carbon tab, so that the X-ray beam direction was parallel to the grid surface. An optical microscope installed above the sample surface gives a first localisation of the illuminated region, then one can move the sample using the piezoelectric translation motors to more precisely explore the suitable part of the sample. In addition, the knowledge of the localisation on the sample allows to combine CDI of individual objects with other *ex situ* techniques such as TEM.
As it has been previously mentioned, Si/Ge NWs lie on their {112} facets but they can be slightly rotated or misaligned, and as they are low-scattering objects, it is helpful to start the experiment by aligning the sample at the Cu diffraction conditions (*e.g.*, at the **2$\bar{2}$0** Bragg reflection, as the $2\theta_{Bragg}$ angle is close to the $\bar{2}\bar{2}4$ Ge one's). Furthermore, in these conditions X-ray maps can be performed to localise the beam, helped by the grid frames, thus to ensure that the image given by the microscope corresponds to the illuminated region.

Then the scattering angle was fixed at the expected **224** Ge Bragg position ($\omega \approx 39.164°, \delta = 78.328°$) and the sample was scanned along the x and y directions to find (224) *in -plane* oriented NWs. While scanning in two dimensions at the Bragg angle, an increase of intensity is expected at NWs positions. Once the NWs were localised, the X-ray beam was focused on the corresponding positions (the most intense ones) to map the reciprocal space around this reflection. In total, RSMs of eight different NWs were recorded; three of them are shown in Fig. 3.16. The thickness

fringes allow to estimate the size of the measured NWs, ranging all of them between 207 and 249 nm. The Bragg peaks consist of six streaks corresponding to the six expected {112} crystalline facets and the 3D intensity is mainly contained in a 2D plane. Some parasitic spots arising from NWs located close to the measured one and with the same orientation are visible in the RSMs, notably in (a) and (c). Besides, there are two features that appear systematically in the measurements: first, the center of the Bragg peak is surrounded by intense spots symmetrically distributed, and second, two additional streaks (circled in black in Fig. 3.16) are observed in the same directions for all the NWs. The origin of these features is unknown, it may be due to the scratching method in the samples preparation or induced by the Si shell -whose scattered intensity has not been observed. Nevertheless, the reproducibility of the measurements, meaning that the RSMs of different wires are similar, implies that the NWs of one sample (*i.e.*, grown in the same conditions) are homogeneous in terms of shape and strain.

An *ex situ* TEM analysis was then performed on this sample, as the measured NWs could be identified by using the beamline's microscope. Large view TEM images of the sample showed that lots of NWs were actually located around the measured ones, meaning that not all of them lie on their {112} facets, so they were not visible during the X-ray diffraction experiment. First individual TEM images of the NWs evidenced their conical shape (see Fig. 3.17), with slight variations of the diameter between the top and the bottom (and particularly evidenced at the top). The diameter of all the measured NWs was about 200-350 nm, in agreement with CDI measurements from the evaluations of the thickness fringes (note that in CDI likely we are only sensitive to the Ge-core).

The composition and morphology profiles of individual NWs can be determined by EDX analysis (Fig. 3.18). The intensity profile when the electron beam goes through the entire core-shell structure shows a core-shell structure comparable to the one obtained by Varahramyan *et al.* [176] on similar core/shell Ge/Si_xGe_{1-x} heterostructures: the interface is very well defined, with a large signal of Ge that decays when the beam moves to the NW edges and a less intense Si signal that presents two maxima at the NW edges. However, in contrast with Varahramyan group's result, the Ge profile presents a dissymmetry. A simple modeling of the morphology of the core by a truncated triangular shape ($i.e.$, supposing an hexagonal cross-section) can explain the dissymmetry of the Ge core (as shown by the fit in Fig. 3.18). On the other hand, the Si shell thickness is estimated from this profile to 10 nm and it remains constant as a function of the cross section. Therefore the apparent conical shape must be related to the core morphology. The model has been confirmed by the High Resolution TEM (HRTEM) measurements here below.

The thickness of the NWs and a so-prepared sample, limits TEM resolution. However, based on the CDI results concerning the homogeneity of the NWs around the sample, single NWs grown in the same conditions may all have the same properties. NWs from the original Ge substrate were then prepared for a further study. NWs lying on the Ge substrate can be picked up on a lamellae using a FIB manipulator in such a way that the thickness is uniform and cross-sections can be better resolved. Hence, HRTEM can be achieved. Results are shown in Figure 3.19 (a-c). Owing to the different atomic number Z of Si and Ge, a contrast is evidenced at the interface of the heterostructure in the NW section. It is in this region that larger strain is expected, so that several HRTEM around the interface were taken. Results show a rough Si-shell of about 10-12 nm and a quite well faceted core that confirm the previous EDX results. Also, {111} planes are observed to be partially coherent at the Ge-Si interface, meaning that the shell is crystalline and it is oriented like the core (see Fig. 3.19 b)). Furthermore, these images give access to local quantitative information about the in plane strain in the imaged region by the method known as *Geometrical Phase Analysis* [177] (GPA). GPA employs Fourier Transform based algorithms to measure the variations in the lattice spacings - so that absolute values of lattice parameters are not measured, but local displacements relative to a given reference. The analysis resulted in a 4 % lattice mismatch between the core and the shell in both ϵ_{xx} and ϵ_{yy} directions (see Figure 3.19), meaning that both materials would be fully relaxed at its bulk lattice parameter.

Furthermore the diffraction patterns are comparable to the ones alculated in Section 3.2.1. In

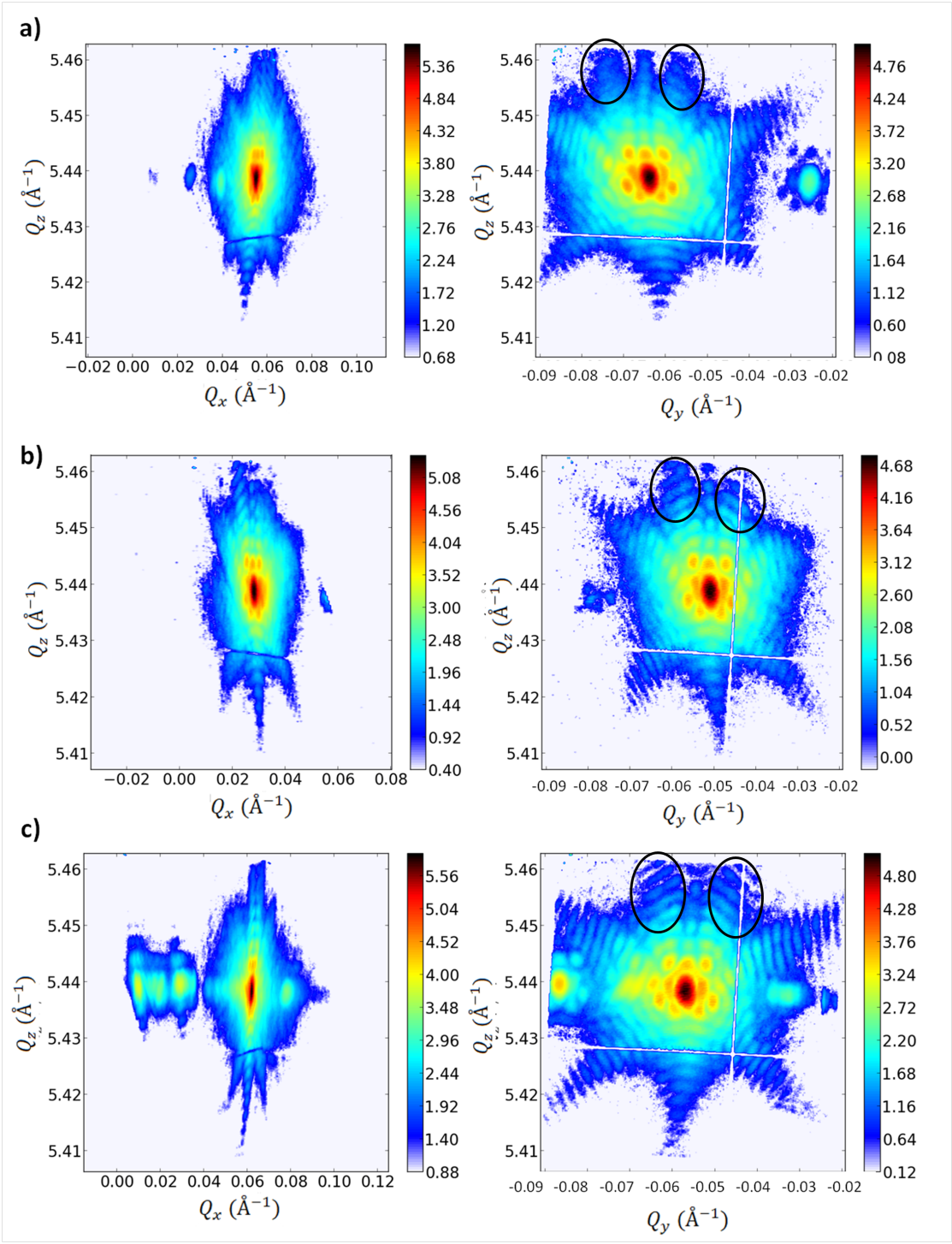

Figure 3.16: RSMs around the $\bar{2}\bar{2}4$ Bragg reflection of three different NWs deposited on a TEM grid. The additional streak observed in the 3 imaged NWs has been circled.

both cases the diffraction patterns exhibit six streaks modulated in intensity (in agreement with

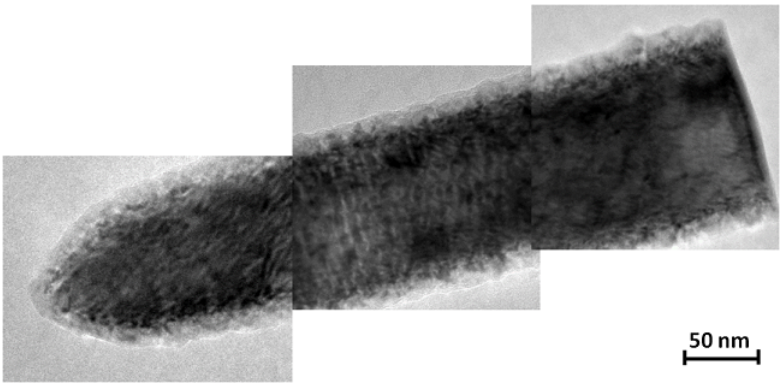

Figure 3.17: TEM micrograph of a core/shell NW showing diameter variations along the length.

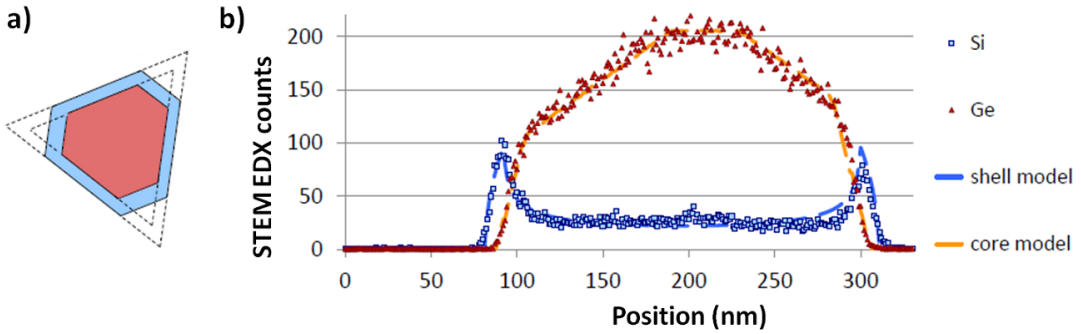

Figure 3.18: a) Model of the NW cross section that best fit the EDX line scans b) Example of an EDX line scan and fit to the truncated triangle configuration model.

the finite diameter of the wire), but there are no similarities with the intensity heterogeneities observed in the experimental refraction patterns, either for a not coherent shell or a partially coherent one. Thus the origin of the observed features can not be attributed to the shell.

To conclude, we have proved the shape and strain homogeneity of the NWs grown by CVD and dispersed over a Cu membrane. The Si shell is partially epitaxied to a faceted Ge core, both materials being mostly relaxed in the plane directions. The observed shell thickness is much smaller than the nominal one, while the NW exhibits a conical shape with a varying diameter along the length (see Fig. 3.17). The flat and well defined facets of the core yield coherent diffraction patterns of single wires that present similar characteristics. The experimental features (spotty central peak and additional streaks) could arise either from the very thin and partial epitaxied shell or defects due to the scratching process to prepare the wires. On the other hand, the rough shell has defects and maybe misoriented grains that, added to the small amount of Si, might not contribute to the measured diffracted intensity. The *in-plane* strain was determined using GPA. However strain measurements were performed supposing an unstrained Ge core so that only relative values could be calculated. In addition, the accuracy and reliability of the measurements strongly depend on the non-zero displacement position chosen as reference, thickness changes (that induce defocus) and noise in the images. These measurements have been used to simulate the diffraction patterns of the imaged nanostructures. The experimental features are not reproducible in the simulations so that, in principle, they are not related to the morphology of the nanowires.

The results shown up to now will be combined with additional CDI measurements in the next

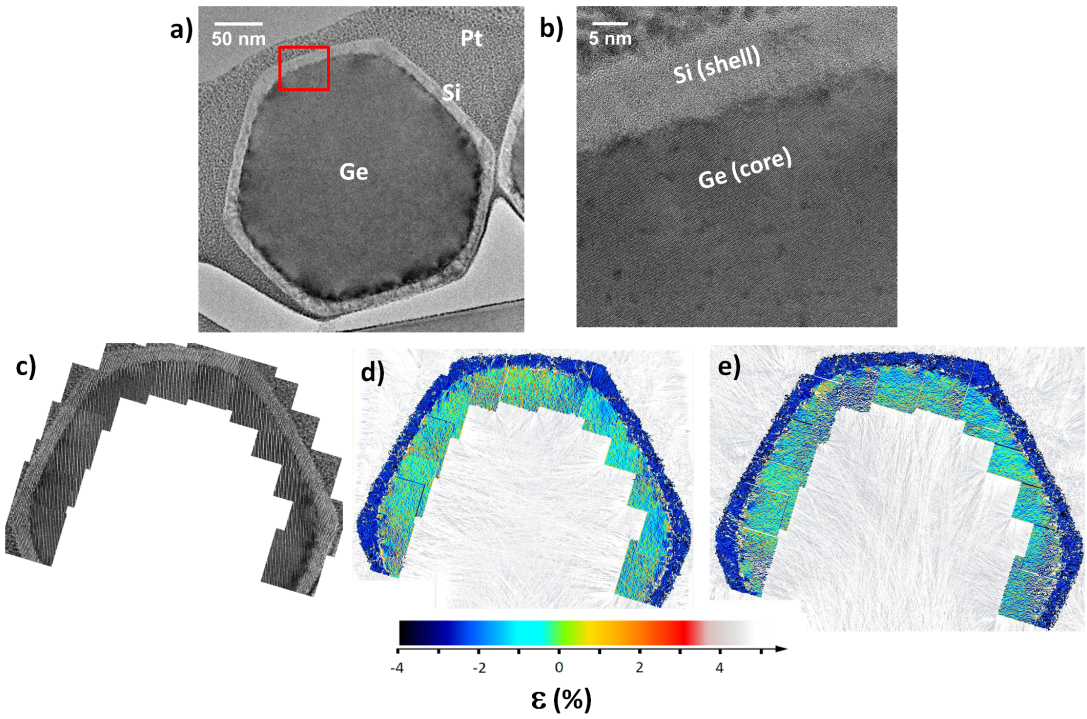

Figure 3.19: a) TEM image showing the cross-section of a Ge/Si core/shell NW. The Pt layer protects the NWs during the TEM preparation. The red square shows the region where the high-resolution micrograph shown in b) has been taken. c) Series of TEM micrographs employed to apply the GPA method to determine the strain in the x and y directions: ϵ_{xx} (d) and ϵ_{yy} in (e).

section. In contrast with TEM, CDI has no thickness limitations and the whole three-dimensional (3D) strain tensor is in principle accessible by measuring three different non coplanar Bragg reflections of the same nanostructure[90].

3.3.2.2 Retrieving the strain: measuring multiple reflections

In the previous Subsection the coherent diffraction patterns of core/shell Ge/Si NWs have been analysed and the results have been combined with TEM analysis. In order to completely determine the strain distribution within a single nanostructure, several Bragg reflections (at least three non coplanar[90]) must be recorded.

If one aims to study the 3D strain field in a selected nanostructure, it is necessary to guarantee that all the measurements are performed on the same object. Thus, the previous sample preparation is not suitable as it does not ensure staying on the same nanowire when changing the Bragg reflection, *i.e.* when the sample is rotated and the experimental geometry eventually changed. Besides, surrounding signal can systematically interfere with the studied nanostructure making the phase retrieval specially challenging or even impossible (as the real space constraint is not completely satisfied).

In order to completely isolate a nanowire, so that phase retrieval and therefore strain distribution determination within the object are possible, the sample of the experiment presented hereafter was prepared using a SEM/FIB manipulator as explained earlier in this Section. The

NW is glued vertically on a Cu pin commonly used for tomography measurements, as shown in the SEM image (Fig. 3.20). In such a system, one is sure that the recorded intensity strictly arises from the scattering NW. The nominal diameter of the core was 200 nm, whereas the shell thickness was kept to 50 nm.

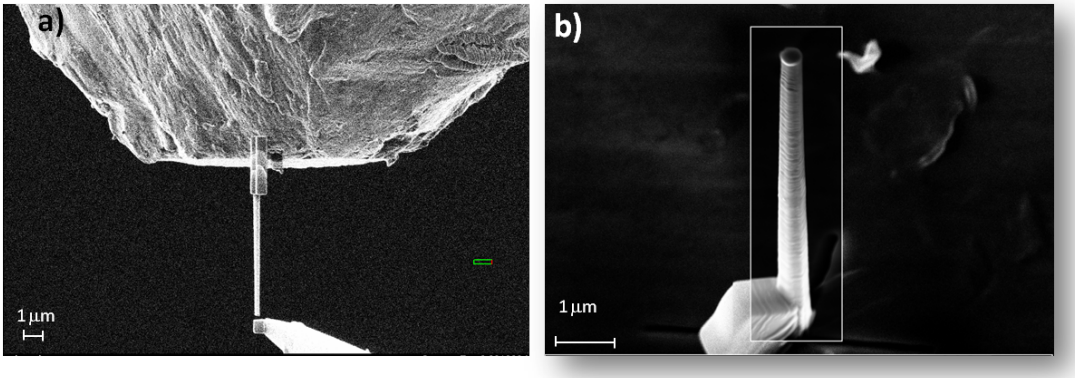

Figure 3.20: a) SEM image showing the preparation of the NW using a coupled Focused-Ion-Beam/SEM manipulator. b) SEM image showing the studied NW once glued on the Cu tip. The conical shape is evidenced, exhibiting a diameter difference of 220 nm between the top and the bottom. The roughness of the shell and the Au catalyst (in the top of the wire) are also visible.

The experiment was carried out at ID01 beamline at a working energy of 9 keV. Before starting the experiment, it is very important to determine the center of rotation of the diffractometer and bring the X-ray beam to this position in order to avoid shifts during the measurements, meaning that the beam has to stay on the sample during the data acquisition. Whereas the position of the center of rotation is important for all nanofocusing experiments in order to determine the illuminated structure or region in a sample, it is crucial here since the low scattering signal of the nanowire at different reflections may be highly time consuming and it can only be faster if the exact position is known and it remains there with goniometer rotations. Indeed, if the crystal is well aligned with the beam in the center of rotation, it will not move during data acquisition and aligning successive Bragg reflections may require only fine alignments. The center of rotation is generally estimated at ID01 using a Si reference sample which has a triangular shape or with a tip as the one holding the NW. The alignment procedure is based on the visualisation of the tip or one of the edges of the wedge using the microscope and a telescope (for rough vertical alignments); two screens in the control cabin allow to see how the reference behaves when one rotates the sample (θ, ϕ). Thus, the accuracy of the center of rotation is limited by the tip diameter but also by the sphere of confusion of the diffractometer. Other strategies can be used during the experiment to redefine the position - parameters such as temperature gradients may cause drifts.

As the NW is a low-scattering object it is convenient to start the experiment by locating the Cu tip and ensure that it is in the beam's path. The followed strategy in the experiment consisted in the use of the *k-map* technique[159] on the holder at the **001** Cu Bragg reflection. The choice of this Cu Bragg reflection is motivated by the proximity of the Bragg angle to the **111** Ge one' s, which is the NW known orientation. The real space map of the Cu tip is shown in Figure 3.21 b). Then one can compare the tip's profile with the SEM images (Fig. 3.21 a) and place the beam in the expected location of the NW. As the wire stands perpendicular to the tip and the growth direction is known ($i.e.$ $< 111 >$), it is easier to start the experiment by looking for the **111**

Ge reflection as previously done in the experiment reported in Section 3.3.1. In this geometry, only two axes of the diffractometer are needed to study the **111** reflection, $i.e.$ $\theta = 12.178°$ and $\delta = 24.346°$ at the working energy. Notice that misalignments can occur because of the FIB manipulation or if for instance, the pin has not been fixed exactly parallel with the silver paste. Therefore finding the NW can be time consuming depending on the tilt.

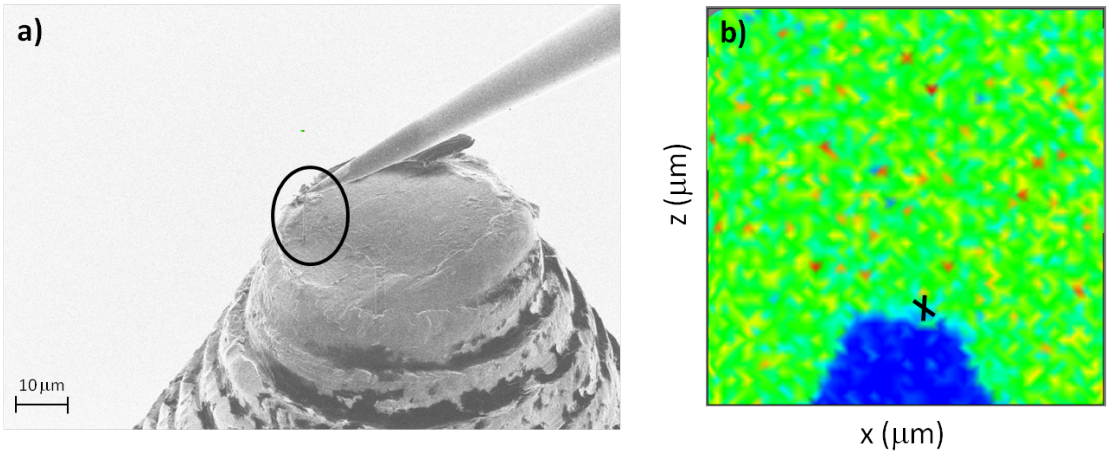

Figure 3.21: Comparison of the SEM image showing the position of the NW on the tip (a) and the quicK map during the CDI experiment (b). The features of the tip allow to identify a lower part of the tip where the NW is located. As the NW is barely visible, it has been circled in (a), and the cross points the approximative expected position in b).

After a precise alignment at the **111** Bragg reflection of the NW, the three-dimensional (3D) intensity has to be recorded. The use of a 2D detector makes possible to record the 2D frames at a given θ angle, hence a 2D slice in reciprocal space with a resolution that mainly depends on the distance between the sample and the detector. Here, with the detector placed at about 1.10 m from the sample, the reciprocal space resolution in the detector plane is about $\delta q = 2.28 \times 10^{-4}$ Å^{-1}. But to record the 3D intensity, the sample has to be rotated to record subsequent 2D frames at the consecutive θ angles[178]. In order to ensure oversampling and to be able to reconstruct the object (meaning to retrieve the amplitude and the phase of the object using the phase retrieval algorithms), the diffracted intensity has to be sampled with at least two points per fringe (see Chapter 2). In the detector directions, the sampling ratio ($\sigma = \frac{2\pi}{\delta q L}$, where L is the NW diameter) is $\sigma = 7.87$, hence we get an oversampling higher than necessary. Then the step size in the rocking curve and the angular range have to be carefully chosen to get enough resolution also in the detector plane, the resolution in this direction being defined as $\delta q_\omega = \frac{2\pi}{d_{hkl}} \delta\omega$ (where ω is the Bragg angle). A step size of $\Delta\omega = 0.002°$ is generally chosen. This yields again an oversampling ratio larger than necessary ($\sigma = 4.72$). As proof of the oversampling criterium, the finite size of the wire will induce fringes normal to the crystallographic directions of its facets, as already observed in the previous Sections. By oversampling the diffraction pattern, the recovery of the phase using the *phase retrieval algorithms* (see Chapter 2) is possible, as it will be explained in the following.

In Figure 3.22 a), the integrated intensity along the three directions is shown. In the $Q_x - Q_y$ plane, the six streaks separated of about 60° are expected to arise from the 6 facets observed by TEM ($i.e.$ the cross-section of the core has an almost regular hexagonal shape). The thickness fringes are very well defined proving that the oversampling condition has been satisfied during the measurement. The symmetry of the Bragg peak characterises the strain-free core of the NW. However, two intense spots close to the peak center (indicated by arrows in the Figure) whose

nature is unknown are also visible, and make think about another streak poorly defined. In the Q_z-direction the elongated peak is quite large, and seems to be "double" in this direction. No signal was detected at the Si bulk position.

The second reflection subject to study was the **333** Ge. The studied planes are hence parallel to the previous ones but as $|\vec{Q}|$ is larger, one is more sensitive to the atomic displacement u_z. In addition, it is an easy access reflection and redundancy in the data set is useful to increase the reliability of the corresponding component of the atomic displacement. The larger length of the scattering vector (or equivalently the larger scattering angle $2\theta_{Bragg} = 78.49°$) leads to a higher sensitivity to defects and strain in the crystal. The 3D intensity distribution from the nanowire around the Ge **333** Bragg reflection is shown in Figure 3.22 b) and, interestingly, similar features to the ones observed around the **111** can be observed.

Then two more reflections were recorded: the **2$\bar{2}$0** and the **331**. As the orientation of the reciprocal lattice with respect to the diffractometer has been determined through the **111** reflection, and given that the NW is formed by 6 {112} facets, one can orientate the crystal in such a way that the {220} planes diffract by rotating the sample around the $z-axis$ (ϕ) and placing the detector at the $2\theta_{Bragg} = 40.2868°$ in the horizontal direction ($i.e., \delta = 0°, \nu = 2\theta_{Bragg}$). One **220** reflection will be found every $120°$. On the other hand, the **331** atomic planes are inclined by an angle Φ with respect to the surface ($\alpha_{<111><331>} = 22°$) so that this is an *asymmetric* Bragg reflection. Therefore, the Bragg condition for these planes will be satisfied for angles of incidence of either $\theta_{Bragg} + \Phi$ or $\theta_{Bragg} - \Phi$.

Even if the measured reflections are coplanar, they allow to retrieve different components of the strain tensor.

The RSMs around these reflections are displayed in Figure 3.22 c) and d) respectively. In both RSMs the streaks modulated in intensity in the $Q_x - Q_y$ plane are visible, and the symmetry around the center of the peak is conserved. These features make us think about a low strained crystal, supporting the previous deduction. The discontinuous streak, indicated by arrows, is observed in all the reflections. Its nature is unknown but it is thought to arise from Ge misoriented grains around the core due to the FIB preparation of the sample that would damage the sample. They can also be due to the bending of the nanowire, as it will be discussed later. The symmetry of the Bragg peak is only slightly broken in the **2$\bar{2}$0** Bragg peak, where a splitting of the peak in the Q_z direction can be observed. This double peak is probably a fingerprint of crystal defects in the nanowire and it reminds notably the stacking faults in III-V NWs found by Favre-Nicolin et *al.*[107]. It is worth to note that some reflections are more sensitive to defects than the others[110].

From the measured diffraction patterns, the nanowire was reconstructed using the phasing algorithms explained in Chapter 2. In the following I detail the procedure for the reconstruction from the **111** Ge Bragg reflection. The recovery of the phase from every reflection is possible by combining the algorithms in the same way or changing parameters such as the feedback, number of iterations of a given algorithm or adjusting the support size.

The streaks in the measured diffraction pattern contain approximately 9 pixels per fringe (so that the oversampling criteria is satisfied), and the finite support size can be chosen according to this expected size. A support slightly larger that the wire speeds up the convergence of the algorithm; here (for the **111** reflection) a rectangular prism of $44 \times 56 \times 120$ pixels was chosen. The size along the z direction can be estimated from the beam size.

Once the data are othonormalised, the input intensity of the algorithms needs some additional preparation, notably:

1. The intensity has to be cropped to a size array whose dimensions are 2^n ($n \in \mathbb{N}$ for faster computation of the Fast Fourier Transform package (see Chapter 2). For the **111** reflection, the cropped array resulted to an array of $256 \times 512 \times 512$ pixels.

2. The maximum of intensity, *i.e* the center of the Bragg peak, has to be centered in the array for the Fourier Transform to function correctly. By doing this and applying the *Fast Fourier shift function*, the zero frequency component is moved to the center of the array and

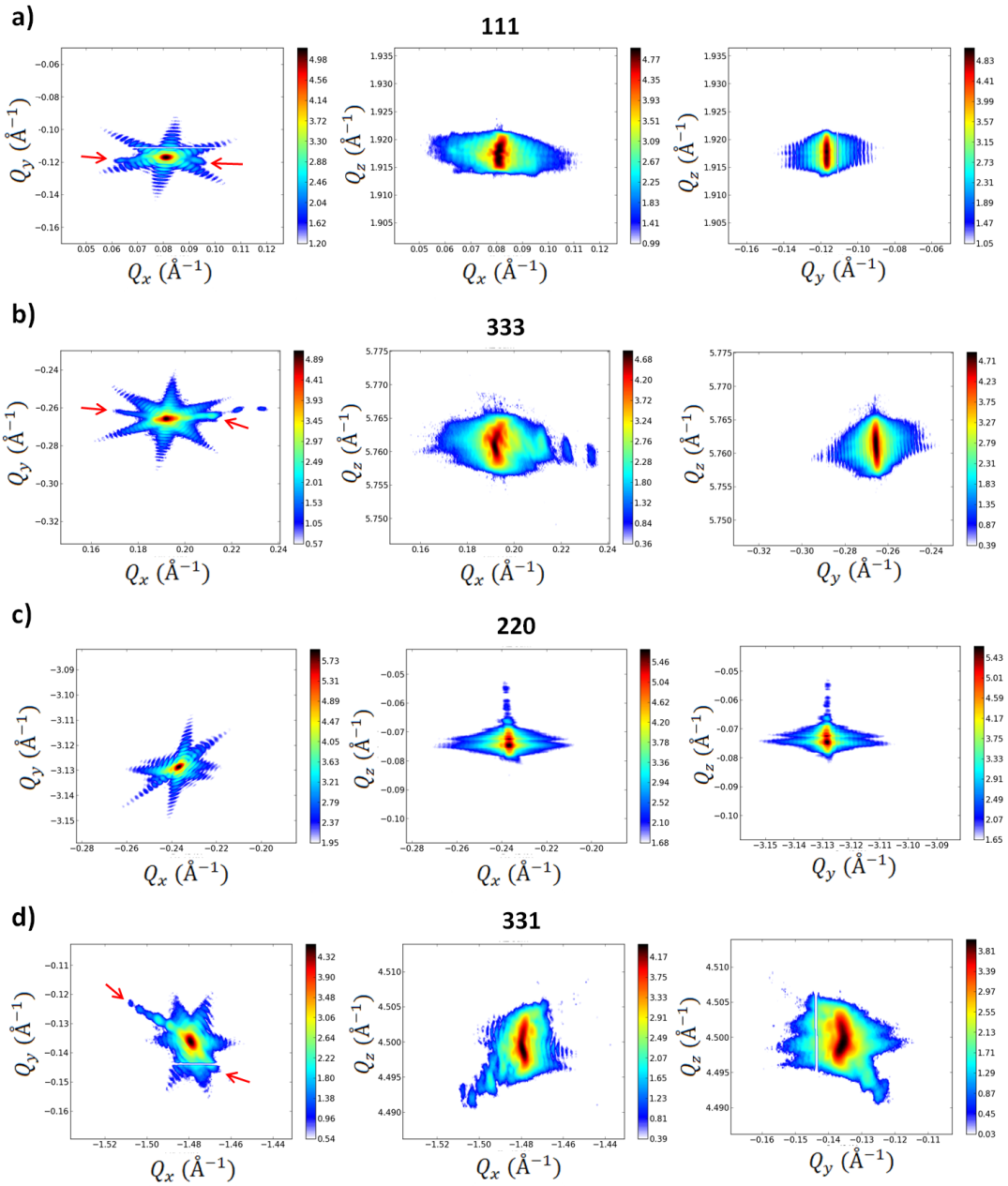

Figure 3.22: RSMs around the a) **111**, b) **333**, c) **2$\bar{2}$0** and **331** Bragg reflections of a Ge/Si core/shell NW.

the central pixels move to the edges. If this step is skipped, the asymmetry of the Bragg peak will lead to a gradient in the reconstructed phase. However, subpixel resolution cannot be achieved and it is sometimes necessary to remove a residual linear ramp after reconstruction.

The as-prepared intensity array and the preliminary support are introduced in the algorithms together with a mask to hide the detector cross and eventually hot pixels. Then 3 cycles of 50

Error Reduction (ER) followed by 80 Hybrid Input-Output (HIO) algorithms are used before applying 10 times the shrink wrap (SW) procedure (details of the algorithms can be found in Chapter 2). This was repeated 110 times and with 10 different random seeds to get a curve as the one shown in FIg. 3.23, where the number of remaining pixels in the support is displayed as a function of the number of iterations. A convergence is observed for all the random guesses: at about 40 iterations the number of pixels in the support decreases very slowly, meaning that the suitable shape (hexagonal cross section shown in Fig. 3.23) has been found but consecutive solutions are not physical. Therefore, the SW must be stopped.

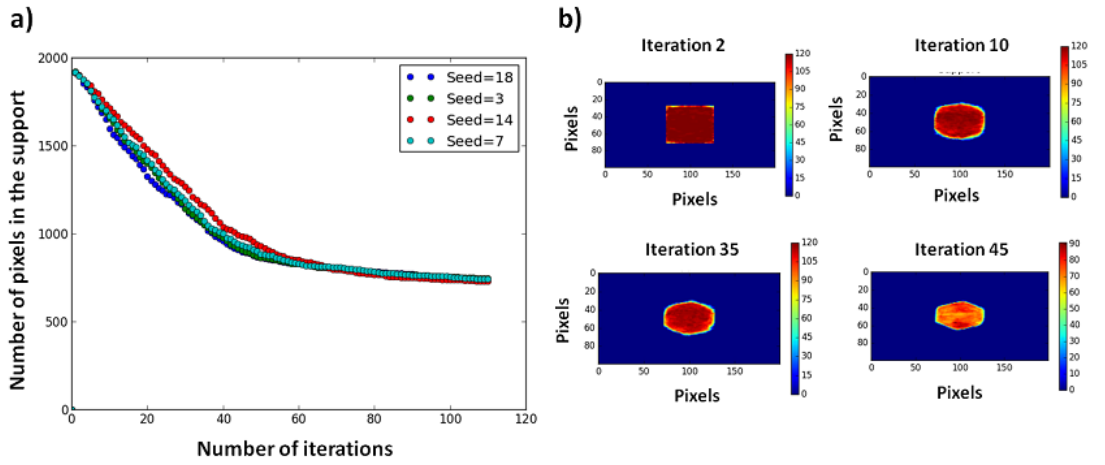

Figure 3.23: a) Number of pixels contained in the support as a function of the iterations during the SW procedure for 4 different initial random values. b) Evolution of the support through the iterations. Note that the support is flat (only ones in the prism) but here the sum of the pixels along the $z - axis$ is represented.

Afterwards fourteen independent runs consisting of 30 cycles of 50 ER + 100 HIO were performed. Each run had a different starting phase and they were performed for 5 different supports. Then two criteria were used to select the good solution:

- The lowest metric error, $i.e.$, the reconstructed amplitudes (Fourier transform of the retrieved object) that better match the experimental one. The metric error of the final solutions are of the order of 10^{-2}.
- The standard deviation of the modulus maps, $i.e.$, the solutions whose density is more homogeneous along the NW axis are selected. As one expects the diffraction signal to come mostly from the Ge core and the Si contribution, if there is, must be very small, only the core of the NW can be in principle reconstructed.

Once the solution is determined, the remaining phase ramp must be removed and the phase must be corrected from the refraction effects, as it will be further explained in Chapter 4 (where the influence is more important because of the bigger size of the particles). The resolution of the reconstruction can be estimated from the decay of intensity in the detector as: $\frac{2\pi}{\Delta q_{max}}$, thus resolution can be increased by longer exposure times while recording every frame in the rocking curve. In the case studied here, this corresponds to a spatial resolution of 11 nm.

The 3D reconstruction of the Ge core of the NW is shown in Figure 3.24. The size of the retrieved object is found to be $275 \times 300 \times 600\ nm^3$, with a voxel size of $7.3 \times 5.4 \times 5.3\ nm^3$, in agreement with previous estimations (nominal diameter 250 nm). Also the six facets, as

observed in TEM studies, are evidenced. In Figure 3.24 b) and c) the measured amplitude and the reconstructed one are shown for comparison, the metric error being around 2×10^{-2}.

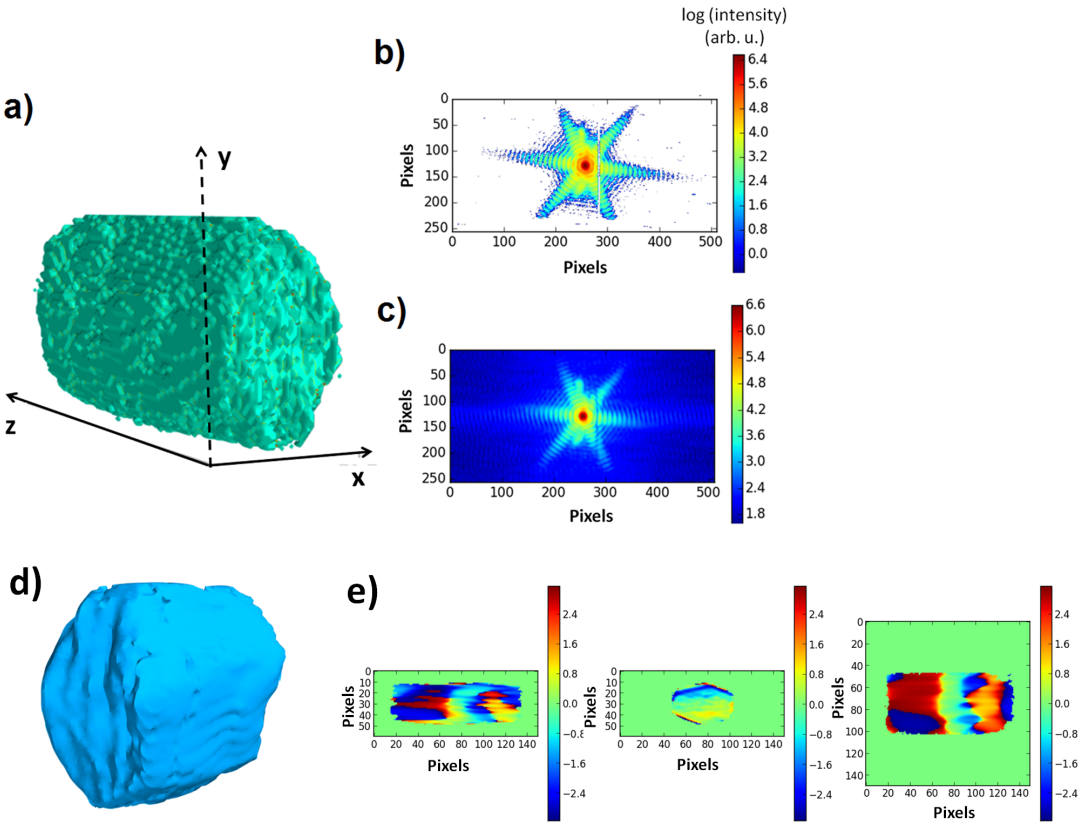

Figure 3.24: a) View of the isosurfaces of the retrieved nanowire from the **111** Bragg reflection. The support size is $275 \times 300 \times 600$ nm^3. b) Raw experimental amplitude. c) Reconstructed amplitude from the retrieved object. d) Isocontour of the reconstructed density. e) Wrapped slices of the retrieved phase at the center of the NW, as found by the algorithms.

Figure 3.24 d) shows a view of the reconstructed density represented as an iso-surface. The density was observed not to be homogeneous over the crystal, which is one of the known and intriguing problems of CDI. Density discontinuities have been sometimes attributed to a partial coherence of the beam [179,180], but it can also be due to the phase influence in the case of highly strained objects [181]. Therefore the reliability of the solution is contained in the phase of the object, which is much more accurate and encloses real information about the sample.
The retrieved phase (see Figure 3.24 e)) needs however some treatment, as some artifacts may be introduced by the phasing algorithms. First, the refraction effects have to be corrected in the case of larger objects (see Chapter 4), and second, the phase must be unwrapped. Phase wraps are visible in the phase between the red and blue regions (which corresponds to a phase of π and $-\pi$ respectively). The wrapped phase is a common artifact introduced by any inversion algorithm because they assume that the reconstructed phase is constrained to the interval $[-\pi, \pi]$; the non physical 2π jumps have to be removed to get a continuous phase (see Figure 3.25). Recovering the original phase values is one of the most difficult steps in CDI data analysis, specially in the three-dimensional case. As phase unwrapping is a problem found in many other signal processing techniques, algorithms have been developed with this purpose (see for instance

Refs.[182,183] for the 1D, 2D and 3D case respectively).
Given the wrapped phase $\psi = \mathscr{W}(\phi)$, where ψ is the wrapped phase and ϕ the real one, the basic unwrapping process consists in calculating the phase difference (discrete gradient) between two neighbouring pixels: $|\psi_i - \psi_{i-1}|$ (where the subindex i labels a given pixel), and then add an integer number of cycles of 2π to minimise the phase gradient. This is only true in the case $|\psi_i - \psi_{i-1}| < \pi$, but as long as the Nyquist condition is satisfied the true continuous phase can be in this way recovered, and the 2π jumps removed.

Nevertheless, the unwrapping problem is more complex in 2D and 3D because in these cases the solution is path-dependent. The problem of wrapped phases can be addressed in many elaborated ways and it is beyond the purpose of this thesis; details can be found in Reference[184]. In the presented study, the problem was solved using the unwrapping function of the *Skimage* package of Python[185].

As mentioned in the data preparation Section, a third artifact that can appear is the phase ramp due to a not well centered Bragg peak in the input array of the algorithm. Moreover, in order to retrieve the 3D object, not only a single detector image is taken but a set of diffraction patterns that are stacked to form the 3D Bragg peak. Therefore, the peak is centered looking at the sum of intensity of the images, but the independent frames might be recorded at slightly shifted positions during the experiment. In order to remove the phase gradient in the retrieved object, one can center the Bragg peak using the center of mass of the Bragg peak $|A(\vec{q})|^2$.

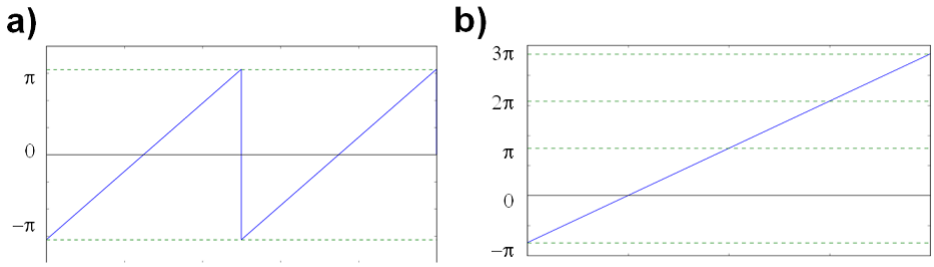

Figure 3.25: Illustration of the 1D unwrapping problem. a) Original wrapped phase profile presenting phase jumps. b) Continuous phase after unwrapping.

2D slices of the corrected phase are displayed in Figure 3.26 a), b) and c). Surprisingly the phase is not homogeneous, it presents continuous variations that are more pronounced along the length of the nanowire ($z - direction$). A plot of the phase values along this direction is shown in Fig. 3.26 e): an average phase jump of $\Delta\phi = 5.6$ radians separates two parts in the NW. A region that extends over almost 100 nm (in yellow) separates a constant zero-phase region from a second one where the phase decreases linearly towards the top of the wire. The phase jump corresponds to an atomic displacement $\Delta u_{111} = 2.911$ Å along the projection of the scattering vector Q_{111}. This would explain the broad Bragg peak in the $z - direction$, Δu_{111} being smaller than one (111) lattice spacing of Ge. On the other hand, in the $x - y$ plane the phase is mostly homogeneous. Heterogeneities in this plane are mainly observed at the intersection with the yz and xz-planes at the middle of the NW, where the phase jump is observed (see Fig. 3.26).

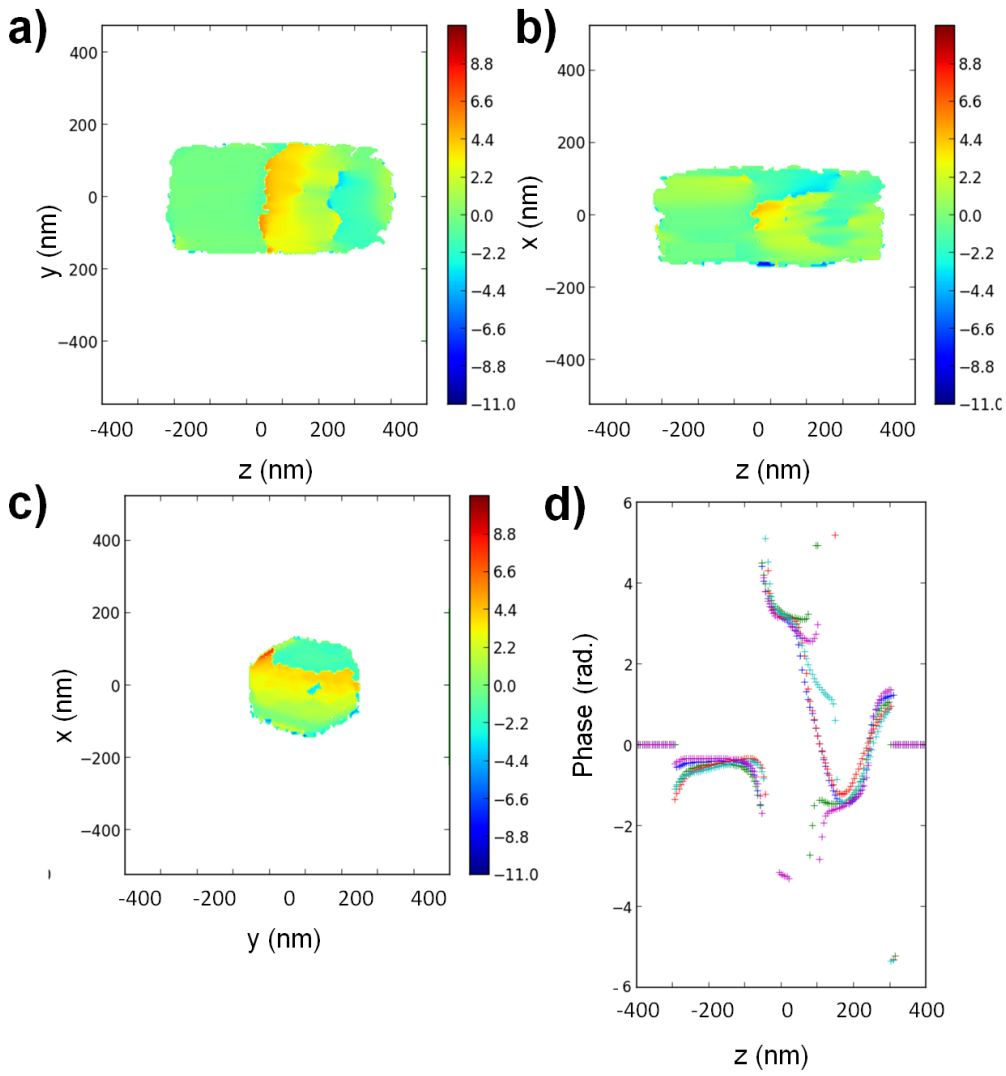

Figure 3.26: 2D slices of the corrected phase at the center of the NW in the yz (a), xz (b) and xy(c) planes. d) Plot of the phase as a function of the length showing the phase jump for several cuts at $y = 0, y = 70$ and $y = -70$ nm.

The retrieved phase allows to calculate the strain within the crystal, which is shown in Figure 3.27. The almost flat phase of the $x - y$ planes yields to a relatively unstrained nanowire in its cross section direction. The higher and smaller phase values observed previously along the length can be identified in the strain maps at different z values.

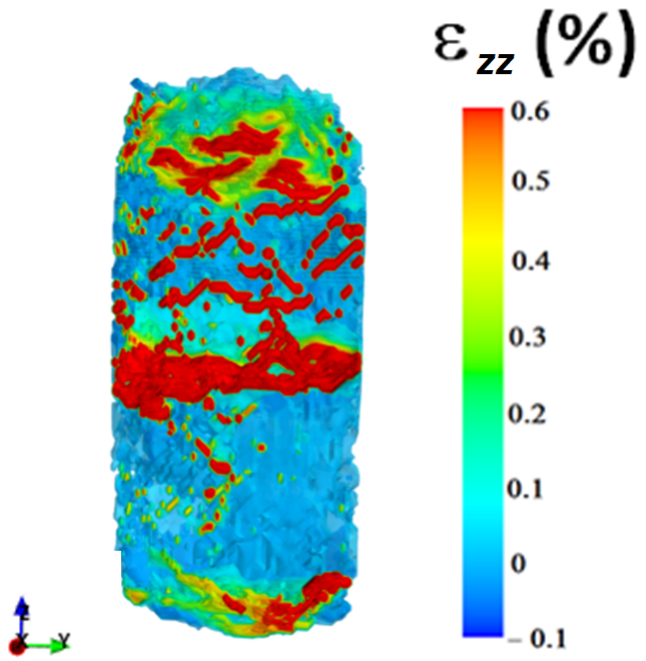

Figure 3.27: Isosurfaces of the calculated strain from the **111** reflection.

Fig. 3.24 d) shows the reconstructed density as an isosurface. Because of the maximum value of the phase, much greater than $\pi/2$, the amplitude is not well reconstructed and effects of the phase can be observed in the retrieved density[181]. Still, strong variations in the standard deviation of the modulus map were observed for different solutions, while all of them had similar metric errors. The homogeneity along the wire, except in the jump phase region, is thus a reliable criteria to determine the solution.

To justify that the phase is the real one despite the non physical amplitude and be sure that the phase jump is not an artifact from the unwrapping algorithm, the diffraction pattern of a Ge/Si core/shell NW with a phase jump of 5 radians in the middle was simulated (see Fig. 3.28) and compared with the one from a non defective NW ($i.e.$, one with a flat phase all along the wire). The simulated diffraction patterns are identical in the $Q_x - Q_y$ plane, but the Bragg peak is broader in the Q_z direction, as evidenced in the plot along this direction (Fig. 3.28e)). The introduced phase of 5 radians in a small region of 24 nm in the NW yield an increase of the FWHM of $\sim 68\%$. To go further and evidence the effect in the RSMs, the phase shift was extended to a bigger region of 560 nm (for a total length of 2 μm): in this case the same influence is obvious in the diffraction pattern, illustrated in Fig. 3.29 a). The peak is much broader whereas the centrosymmetry of the peak is conserved and there is still no evidence of strain in the cross-section. Finally, the case of a stacking fault (SF) in the middle of the NW was simulated. It is known that in presence of a stacking fault at this position, a jump phase of $2\pi/3$ is introduced[110,181]. A splitting of the Bragg peak is visible in the calculated diffraction pattern, in agreement with studies of SF in NWs reported in literature[83].

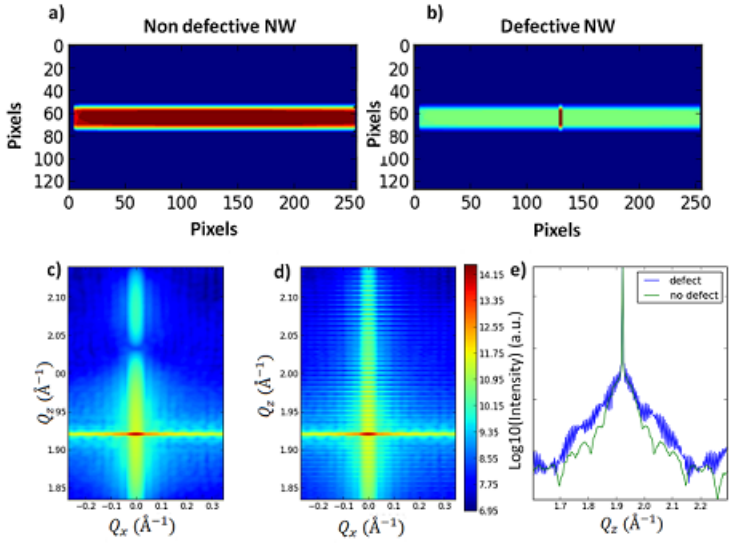

Figure 3.28: a) Sum of the density along the $x-$axis of an hexagonal core/shell NW. b) Illustration of the zone of the NW where a 5 radians phase shift was inserted. c) and d) Simulated diffraction patterns corresponding to the objects in a) and b) respectively. The colorbar corresponds to the logarithmic intensity. e) Intensity profiles along the Q_z direction, showing the effect of the insertion in the width of the Bragg peak.

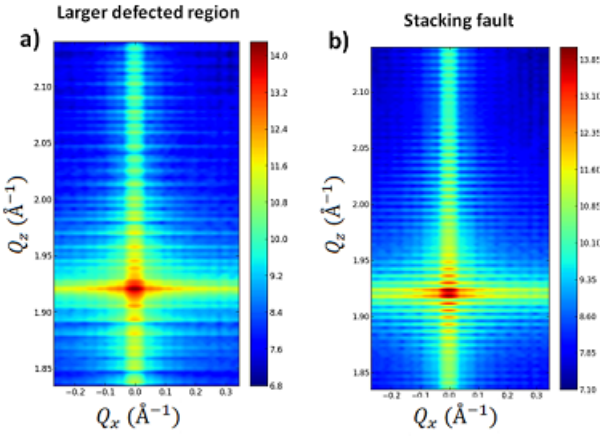

Figure 3.29: Simulation of the diffraction patterns of a core/shell NW with a phase shift of 5 radians in a larger region (a) and of one with a stacking fault in the middle (b).

The studied NW was reconstructed for each reflection yielding a reproducible hexagonal cross-section of smaller diameter, meaning that measurements have been done in the upper part of the NW. The unwrapped phases for each reflection are shown in Fig. 3.30, together with 3D views of the calculated strain. The 2D slices are taken close to the center of the NW. The **333** and **331** reflections (Fig. 3.30 a)) yield reconstructed heterogeneous phase. In the case of the **333**, there are different regions separated by phase jumps similarly to the results from the **111** reflection. A low amount of residual tensile strain localised at the edges and different positions along the $z-$direction is observed for both reflections.

The reconstructed phase from the **2$\bar{2}$0** Bragg reflection yields a phase jump of $\Delta\phi = 5.3$

radians at the position indicated by the arrows and heterogeneities notably along the length; the reconstructed NW exhibits strong tensile strain ($\epsilon_{xx} > 0.005$) that extend along the $y-$direction.

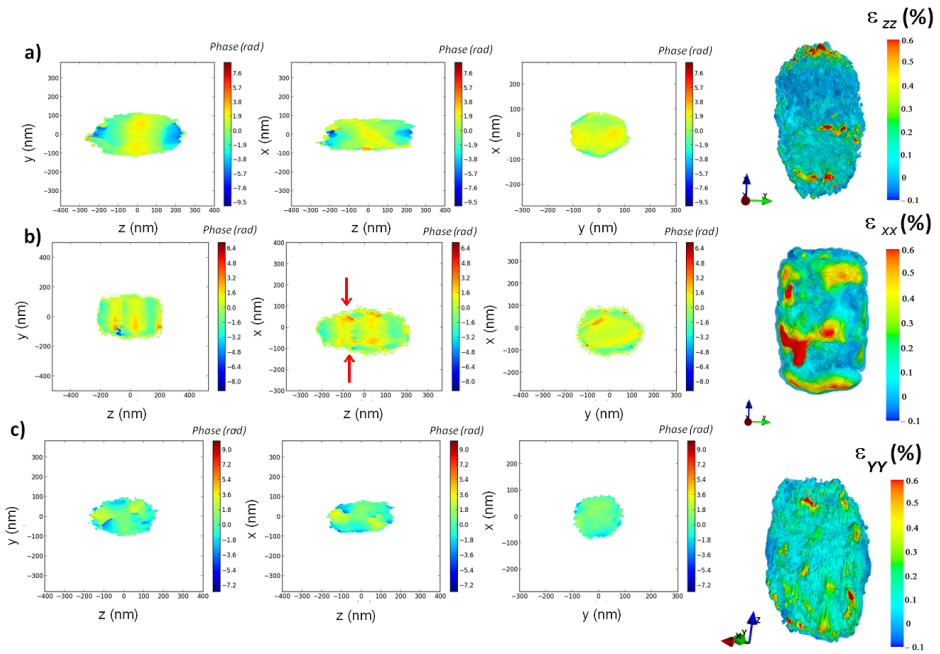

Figure 3.30: Phase maps cutting through the crystal at the middle of the reconstructed NW from the a) **333**, b) **2$\bar{2}$0** and c) **331** Ge Bragg reflections.

Therefore, the Ge NW seems to be strained mostly in the $z-$direction, maybe due to the conical shape or defects introduced by the FIB treatment to prepare the samples. Neither in the diffraction patterns nor in the retrieved objects there is clear signature of the Si shell, which should induce strain at the edges of the wire. As the Si was observed to be fully relaxed at its bulk lattice parameter for this core diameter in Section 3.3.1, the Si shell is probably too thin to be observed in the diffraction patterns or perhaps, since it is fully relaxed, the shell might not contribute at all to the recorded signal at the Ge position. Another possibility could be polycrystalline shell as observed for other samples (Section 3.1).

3.3.3 Discussion

In this Section the strain field in core/shell single NWs at room temperature has been investigated, first in the as-grown sample and then after manipulation for CDI experiments. The main results concern the strain in the Ge core: it is found to be relaxed at its bulk lattice parameter along the wire direction, and this, for any diameter. If the NWs are isolated, whether by scratching the original sample or using a nanomanipulator, the strain within the Ge core can be determined. However, it is important to know if a single NW is representative of the ensemble, as physical properties of nanostructures may vary depending on the morphology or strain states of single objects and many applications need assemblies of wires. Therefore the first result from CDI experiments is the homogeneity of the NWs in terms of shape and strain when the NWs are grown in the same conditions, as the diffraction patterns are similar. The homogeneity of the wires is also useful to extract information of single structures using other techniques, such as

chemical composition or, in the case presented here, get information about the shell. Apart from the partial epitaxy found for the NWs of 100 nm core (nominal size), TEM allowed to study the *in plane* strain of the nanowires by means of GPA. This analysis showed a relaxed core and a relaxed shell, with respect to Ge and Si bulk respectively, but with an ordered interface presenting certain periodicity.

From the samples studied as-grown in a first stage, a single NW from the thickest one (nominally 200 nm diameter core and 50 nm diameter shell) was prepared to retrieve as many components as possible of the strain tensor during one beamtime. Four Bragg peak reflections were successfully recorded, then the strain components $\epsilon_{xx}, \epsilon_{yy}$ and ϵ_{zz} were calculated using the phase retrieval algorithms. The main challenge of the phase retrieval is to find the *good support*, meaning the shape that corresponds to the real morphology of the NW - or the core of the NW. The shrink wrap algorithm may drive wrong solutions since features in the diffraction patterns such as the “spotty" signal found in every reflection can be retrieved as additional facets in the resulting object. This spotty streak is thought to arise from other parts of the NW illuminated by the wings of the beam, but it could be also due to the preparation process.
The solutions of 3D phase retrieval could be not accurate as the NWs are known to be tapered and the phasing algorithms assume homogeneity along the $z-$direction. It is in this direction that a jump phase is found, the phase being quite homogeneous in the cross-section direction. The presence of defects is supported by the asymmetry of the diffraction patterns and the splitting of the Bragg peak of the $\mathbf{2\bar{2}0}$ reflection, but the origin is unknown. If the preparation of the wire is not responsible of the defect(s) yielding the jump phase, then it could be an intrinsic defect related to the thick diameter of the wire.

Phase retrieval reconstructions have two difficulties in the case of the Ge/Si core shell NWs, which are related to the lack of knowledge about the interface. To distinguish the CDI signature of the wires on the diffraction patterns, more experiments in the same and similar conditions should be performed ($e.g.$, deposition of the wires on different kinds of membranes or use the manipulator to prepare much longer wires to avoid measuring the damaged part of the wire). Additional measurements to get information about the interface would lead the understanding of the structures: misfit dislocations, 3D islands at the interface, or small compositional gradients may lead the observed strain.

The observed strain in the shell of the as-grown nanowires could not be related to the epitaxy (or partial epitaxy) of the shell, since the core is not compressed. The residual measured strain in the shell is therefore not really understood, as the shell is not observed during the study of individual wires. Thicker shells could help in this sens, to increase the scattering volume. This strain could be the impact of temperature changes during the growth, given the difference of coefficients of thermal expansion between Si ($\alpha_{Si} = 2.6 \times 10^{-6}$ K^{-1}) and Ge ($\alpha_{Si} = 6.1 \times 10^{-6}$ K^{-1}).

3.4 Intermixing in single core/shell nanowires

In this Section I report two *in situ* annealing experiments performed on Si/Ge NWs, one by means of CDI and the other one using TEM (Subsections 3.4.1 and 3.4.2 respectively). The motivation of the annealing experiments raises from the technological importance of understanding the Si-Ge interdiffusion behaviors and build accurate Si-Ge interdiffusivity models. By combination of CDI and electron tomography the complete mechanism of interdiffusion can be understood: strain evolution and composition at atomic resolution of core/shell NWs can be determined under high temperature. TEM allows to resolve local composition and directly visualise the diffusion process at the interface between the materials forming the core and the shell, whereas CDI may answer fundamental questions such as the relationship between strain and diffusion.

3.4.1 Influence of the temperature in the strain field of single NWs

The CDI experiment was performed at the ID01 beamline at a working energy of 8 keV. The furnace described in Chapter 2 was installed on the hexapod, so that the temperature could be monitored from the experimental hutch and it was possible to work under a vacuum of the order of 10^{-2}. The study was performed on a core/shell NW from one of the samples characterised in Sections 3.3.1 and 3.3.2.1. Preparation of the sample using a FIB manipulator was carried out at the Institut Lumière Matière (Lyon, France) using a similar design of the tomography pin as the previous one ($i.e.$, similar dimensions and shape), the main difference laying in the material of the tip. Cu diffuses at high temperature so that a holder made of this material would influence the measurements and blur conclusions about diffusion in the NW itself. Hence, nano-tomography tips were fabricated in stainless steel to glue isolated wires. The glued NW was picked up from Sample 2 as denoted in Section 3.3.1, $i.e.$, NWs with a nominal core diameter of 100 nm and a shell thickness of 50 nm. A SEM image of the prepared nanowire can be seen in Fig. 3.31, from which the actual diameter is estimated to be 250 nm, and the length of about 7 μm.

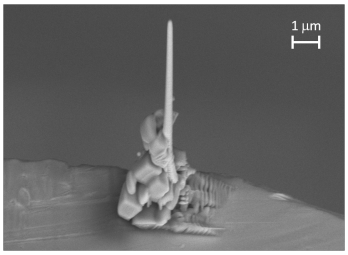

Figure 3.31: SEM image of the NW prepared using a FIB micro-manipulator. A large amount of carbon surrounds the bottom of the wire, which was used to glue the NW on the tomography tip.

The flexibility of the set-up being good enough to work in high-angle diffraction geometry, the strategy to locate and measure the NW once in the beamline was the same than the one explained in Subsection 3.3.2.2, looking at the **111** Ge Bragg reflection of the NW. However, as this time the tip was not of Cu, the comparison between the *k-maps*[159] cartographies and the SEM images to localise the wire was done from measurements in forward scattering instead of in diffraction conditions.

The detector was placed at 1 m from the sample, yielding a reciprocal space resolution of about $\delta q = 2.23 \times 10^{-4}$ Å^{-1}. Rocking curves were performed around the **111** Ge Bragg reflection with a step size of $\Delta\theta = 0.005^{\circ}$ over a range of 1.6°, which is enough to get an oversampled diffraction pattern as evidenced by the fringes visible in the recorded intensity maps. The latter are displayed in Fig. 3.32 a). The centrosymmetry of the diffraction patterns may correspond to

a free or weakly strained NW, except for some parasitic spots in the $Q_x - Q_y$ plane. The thickness fringes allow to estimate the diameter of the NW to 221 nm.

From the diffusivity values and considerations of Chapter 1 for bulk crystals, Si diffuses in Ge faster than Ge in Si. At $650°C$, with the tabulated values, the diffusion coefficient of Si in Ge is $D = 3.53 \times 10^{-17} cm^2/s$. Staying at this temperature for one hour, the mean diffusion length $d = \sqrt{D\Delta t}$ is estimated to 3.6 nm (where $\Delta t = 1$ hour). Thus, this could be already significant *e.g.* for a shell of 10 nm as the one of the wire studied here, according to the general TEM measurements performed on this sample (Subsection 3.3.2.1). In addition, the presence of defects in the wire may speed up the diffusion.
For technical reasons the NW was only heated up to $450°$C (temperature read by the thermocouple). The increase of temperature was done in steps of $100°$C. The recorded diffraction patterns at $91°$ C, $253°$ C and at room temperature (RT) after reaching the $450°$C are shown in Fig. 3.32 b), c) and d) respectively. The NW was observed to be unstable at high temperature and recording high quality measurements was difficult because of residual contamination of the Be dome of the furnace - some grains in the dome diffracted disturbing the NW signal. These observations were verified by rotating the dome and by comparison of the diffraction patterns at room temperature with the dome and without it. In addition, a spotty signal is superposed to one of the streaks at these temperatures, making difficult the phase retrieval treatment. At the final stage, $i.e.$ at room temperature after being heated (Fig. 3.32 d)), the peak has slightly lost the symmetry but *a priori* there are no strong changes in shape or strain.

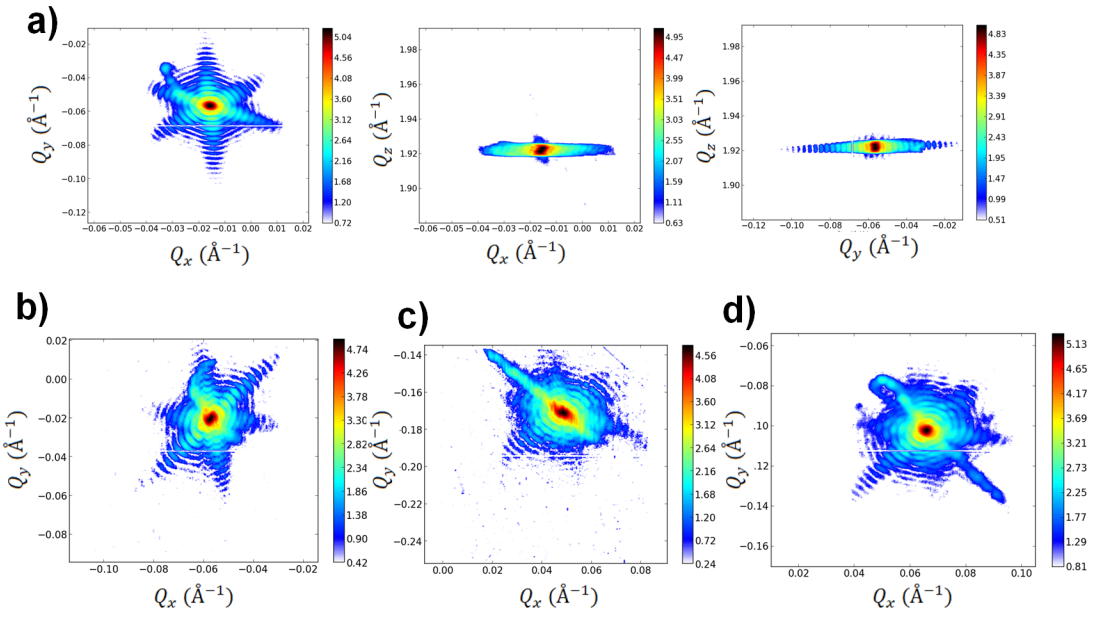

Figure 3.32: Coherent X-ray diffraction measurements around the **111** Ge Bragg reflection of a single core/shell Ge/Si NW at RT (a), 91 ° C (b), 253 ° C (c) and after cooling down, at 24 ° C (d).

3D reciprocal space maps were recorded at different positions of the NW at RT before and after heating (see Figs. 3.33 a) and b)). Some differences can be observed in the recorded diffraction patterns depending on the positions of the X-ray beam, meaning that there may be different local strain states in the NW; note *e.g.* the centrosymmetry differences and the remarkable extension of an additional streak, pointed out by the red arrows in Figs. 3.33b) i) and ii). From these measurements and taking advantage of the fact that the beam size is smaller than the

length of the NW, it is possible to calculate the average strain information along the wire with respect to a fixed position ($e.g.$ the top or the bottom of the NW) as previously done in Section 3.3.1, using the Formula 3.10. In addition, if one defines the orientation of the atomic planes at this reference position (top/bottom) as “normal orientation", the angular deviation at the other positions along the length of the wire with respect to this reference can be extracted. The difference in tilt of the crystallographic planes α, usually referred as *lattice tilt*, can be determined as follows:

$$\alpha = \arccos\left(\frac{\vec{Q_0}\cdot\vec{Q_1}}{\left\|\vec{Q_0}\right\|\left\|\vec{Q_1}\right\|}\right) \tag{3.11}$$

where $\vec{Q_0}$ and $\vec{Q_1}$ are the scattering vectors at the reference and investigated position respectively. Taking the reference at the higher position indicated by the crosses along the NW in the real space map of Fig. 3.33 a), where $z = 0$, the average strain and tilt at several positions along the NW have been plotted in Figure 3.33. In Figs. 3.33 c) and d), $i.e.$ before and after annealing, an increase of the tilt is observed along the NW. The lattice tilt, of about $0.4°$ over 4 μm in the beginning, is much higher after cooling down, becoming as high as $2.1°$ over 4 μm. The maximal strain along the wire has increased as well, of about $|\Delta\epsilon_{zz}| \sim 0.03\%$, maybe because of the NW bending.

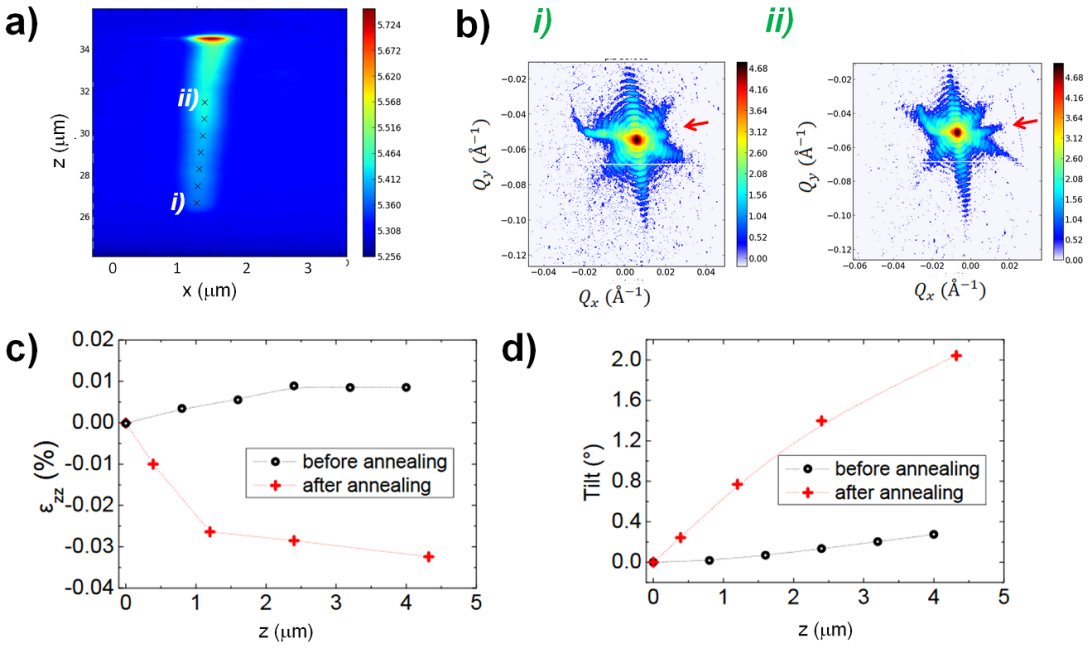

Figure 3.33: a) 2D real-space map (step of 0.8 μm) of the integrated intensity at different incident angles with respect to the **111** Ge Bragg reflection. The crosses along the NW indicate the positions where the rocking curves used to calculate the tilt and strain at RT before heating were performed. b) Sum of the 3D recorded raw intensity at the higher and lower positions along the wire (labelled *i)* and *ii)* in a)) with the Be dome. c) *Out-of-plane* strain and d) lattice tilt as a function of position of the beam on the NW at RT before and after annealing the sample. The reference is taken at the top of the NW, where $z = 0$ has been defined by convenience.

A SEM image of the NW after the X-ray experiment is shown in Fig. 3.34. In this image it

is clearly observed that the NW is bent and some carbon seems to be sticked upper in the wire because of the annealing.

The parasitic signal appearing in all diffraction patterns (Fig. 3.32) could arise from diffraction from parts of the wire illuminated by the wings of the beam, as it was already suspected from the measurements at room temperature. Moreover, looking at the evolution of the diffraction patterns and the lattice tilt evolution, one may conclude that the more important the tilt becomes, the more the parasitic signal interferes with the streaked Bragg peak. As a matter of fact, this strong interference makes extremely difficult the inversion of the diffraction patterns recorded during and after annealing the sample. In order to understand if the asymmetry observed in the final diffraction pattern (Fig. 3.32 d)) is due to the tilt, instabilities or to the temperature (which would influence morphology or strain), environmental TEM is helpful. In particular, electron tomography would allow to access chemical composition at high temperature and determine the evolution of the interface during the annealing process.

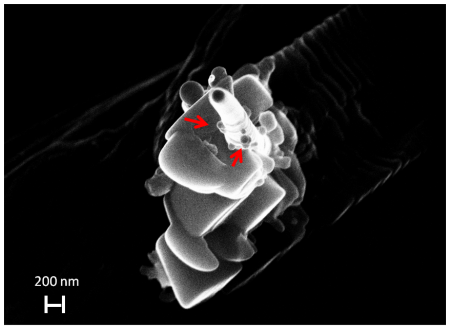

Figure 3.34: SEM image of the NW after annealing during the CDI experiment. It can be observed that the NW is bent, as well as carbon clusters on the surface (some of them are pointed out by the red arrows).

3.4.2 Influence of the temperature in the morphology and composition of single NWs

Studying the composition of core/shell NWs with high resolution is possible by electron tomography. The experiment was performed at the CLYM platform in Lyon, which proposes the access to FIB and is fully equipped for conventional TEM and/or STEM tomography in a TITAN microscope (FEI TITAN 300 keV). This instrument presents the great advantage to be environmental and equipped with heating holders that allow to perform preliminary annealing experiments up to 1300°C to observe intermixing and melting. The heating holder from DENSsolutions® consists of a nano-chip metal heater encapsulated between a Silicon Nitride support film (20 nm thick) (Fig. 3.35). The temperature ranges between room temperature and 1300°C. A closed-loop temperature feedback system offers a major advantage for image stability, temperature response times and reliability.

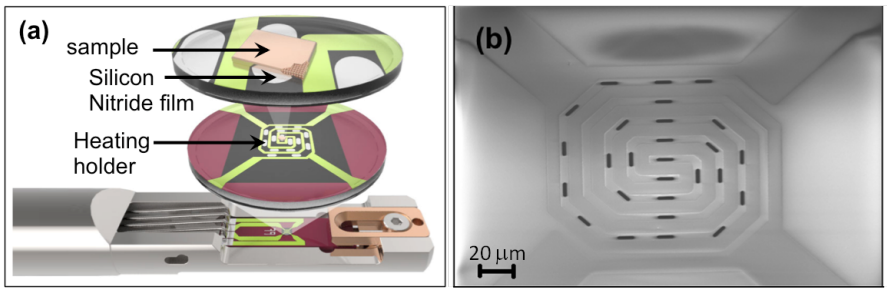

Figure 3.35: (a) Nano-chip sample carrier for temperature accuracy and sample stability. (b) Core of the nano-chip.

3.4.2.1 Measurements at room temperature

Given the thickness limitations of TEM and because high-resolution is desirable to observe the interdiffusion at the interface, new samples (*i.e.*, NWs with smaller diameters than the ones studied by CDI) were prepared to perform the experiment. The preparation of the NWs for the experiment consisted in transfering them from their native substrate to one of the membranes (see Fig. 3.35) through an ultrasonic bath as explained in Subsection 3.3.2. By chance, some of the NWs laid quasi-parallel to the rotation axis for tomography. A plasma cleaner was used to remove the carbon contamination from the samples. Typical high resolution and high angle annular dark field (HAADF) measurements at RT are shown in Figs. 3.36 a) and b). These measurements allow to estimate the shell thickness to 22 nm and the core diameter to 100 nm, meaning a core significantly larger than the nominal one but a much smaller shell (a gold colloid of 50 nm was used, and a shell of 40 nm was expected). Figure 3.36(b) shows a TEM image of a nanowire whose core has possibly two different crystallographic orientations, which are indicated by the numbers 1 and 2. This may be caused by a defect inside the core of the nanowire. Interestingly, most of the HAADF measurements of the nanowires exhibit Moiré fringes, as can be observed in Fig. 3.36 c). Moiré fringes are artifacts in TEM images generally caused by the superposition of crystals with different lattice parameters, but sometimes very difficult to interpret owing to the nature of the images (which are actually 2D projections of the sample, so that many atomic layers can be superposed in a single projection). The observed Moiré-like patterns have several possible origins:

1. Changes of thickness or composition, since the contrast in HAADF STEM depends on the atomic number Z. In this way, for instance, heavy elements ($e.g.$ gold) can be easily distinguished from lighter ones ($e.g.$ silicon or germanium).

2. As a consequence of the tilt of one of the lattices that overlay at the same position or if for example, different grains due to crystallographic defects superpose in the image.

3. As a result of different lattice constants that overlap. Moiré fringes have been observed in literature in core/shell nanostructures on the positions where the crystal lattices from the two materials (the one from the core and the one from the shell) overlap[186,187,188]. The spacing of the Moiré fringes allows to determine the relaxation mechanisms of the misfit strain[186] and map stress effects[187].

The 3D tomographic mapping should explain the origin of these Moiré fringes: either orientation or lattice parameter differences, composition or thickness variations may explain the artifacts. Data analysis is in progress.

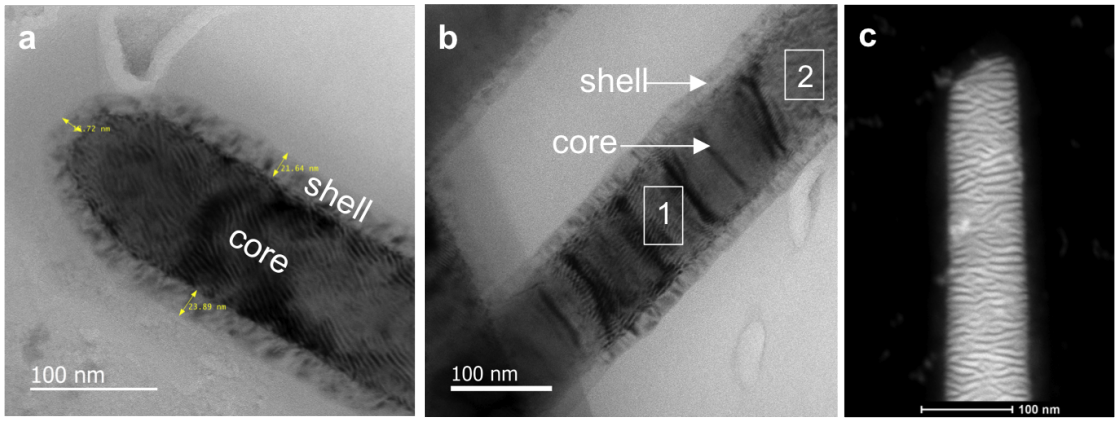

Figure 3.36: (a-b) TEM and (c) HAADF measurements of one of the NWs deposited on the Silicon Nitride membrane for *in situ* experiments. In (c) a Moiré-like pattern along the NW is observed.

Before starting the annealing experiment, two-dimensional EDX spectra were acquired on a single NW (see Fig. 3.37) to confirm the Ge-Si core-shell geometry. As expected and in agreement with previous EDX analysis on similar samples, the germanium was detected only in the core of the wire (Fig. 3.37 b)) but surprisingly, also gold was detected, possibly in the core region (see Fig. 3.37(d)). As explained in Chapter 1 and in the Introduction of this Chapter (Section 3.1), a gold catalyst is used to grow the Ge NWs as a first step in the core/shell growth process, which may induce gold diffusion on the sidewalls of the Ge core during the growth. In order to block this phenomena and avoid the tapering of the wire as a consequence of the constant loss of catalyst material, all the samples studied in this manuscript were grown with the addition of HCl. HCl etching inhibits in principle gold surface diffusion[189,190] but the one-dimensional EDX profiles of Ge, Si and Au shown in Figs. 3.37 a)-c) evidence remaining catalyst residues. As it will be discussed hereafter, the presence of gold atoms in the NW volume is an important factor to take into account when studying interdiffusion in Si or Ge structures, since it is a strong contaminant able to diffuse through the NW and it might contaminate the entire structure in few minutes.

3.4.2.2 *In situ* annealing experiments

The intermixing study becomes therefore more complex since not only Si in Ge and Ge in Si diffusivities must be considered, but also the Au one (in both Si and Ge). In addition, Au diffusivity is expected to be much more important than the Si or Ge ones, according to the tabulated values presented in Chapter 1, so that Au diffusion in the Si shell can be quite important at

temperatures above 700°C (see Table 1.3.). Interdiffusion between the three materials may lead crucial problems regarding devices applications, since the abruptness of the band offset at the Si-Ge interface would be likely influenced.
The diffusion coefficient of Ge in Si is lower than 10^{-18} cm^2 s^{-1} whereas the one of Si in Ge is in the order of 10^{-15} to 10^{-16} cm^2 s^{-1} at 700 °C[43,191,192]. At this temperature, the diffusion of Ge atoms into Si is virtually zero, whereas Si atoms can diffuse in Ge as far as 10 nm at in 15 min. At 850°C, the diffusivity for Si in Ge is then 5×10^{-14}, meaning that Si atoms can diffuse as far as 300 nm in 15 min at this temperature [a]. These estimations indicate that the intermixing problem of Si and Ge has to be studied at temperatures above 600°C. Therefore time-resolved *in situ* STEM-EDX was performed in a larger range of temperatures with respect to CDI experiments: TEM measurements were performed from 20°C to 1200°C to probe diffusion in the Ge-Si core shell nanowires.

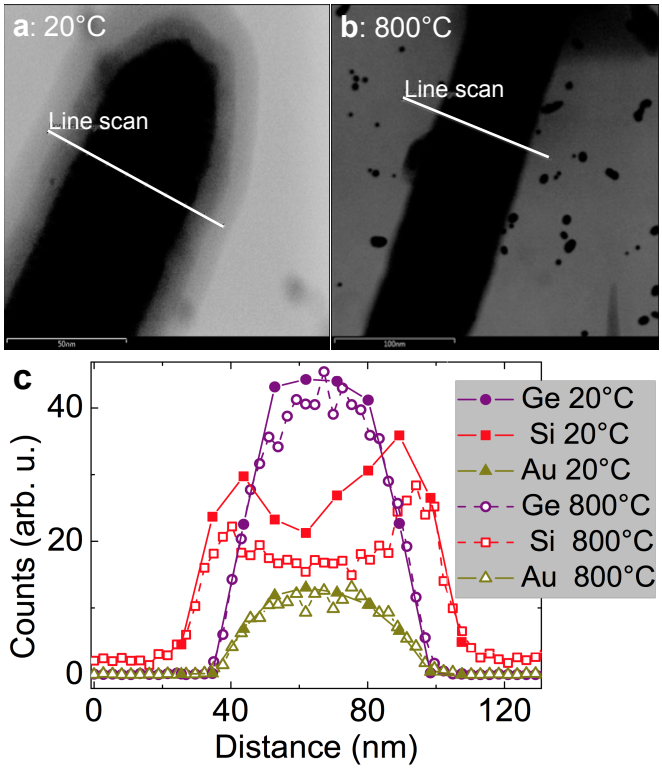

Figure 3.37: One dimensional EDX profiles (c) at 20°C (a) and 800°C (b) on two different parts of the same nanowire (a-b).

Figure 3.38 displays STEM images of a Ge-Si core-shell nanowire as a function of temperature and annealing time. It appears that no significant changes like interdiffusion signature occur until 900°C. A sharp core-shell interface is still observed at 900°C and after 45 minutes of annealing. A one-dimensional EDX profile was performed at 800°C and is shown in Fig. 3.37, which demonstrates that no intermixing occurs up to this temperature. Curiously, even Au atoms are not observed to diffuse - the Au EDX profiles at 20°C and 800°C are similar (Fig. 3.37). At 800°C, the diffusion coefficient of Au in bulk Ge is $\sim 2\times10^{-13}$ m^2/s[193], meaning that Au atoms diffuse, as far as 2 µm in 1 second at this temperature.

Changes happen from 1200°C as observed in Figs. 3.39 (a-b). Table 3.4 indicates the melting

[a] These values are in agreement with the ones calculated from the prefactor and the activation energy values given in Chapter 1.

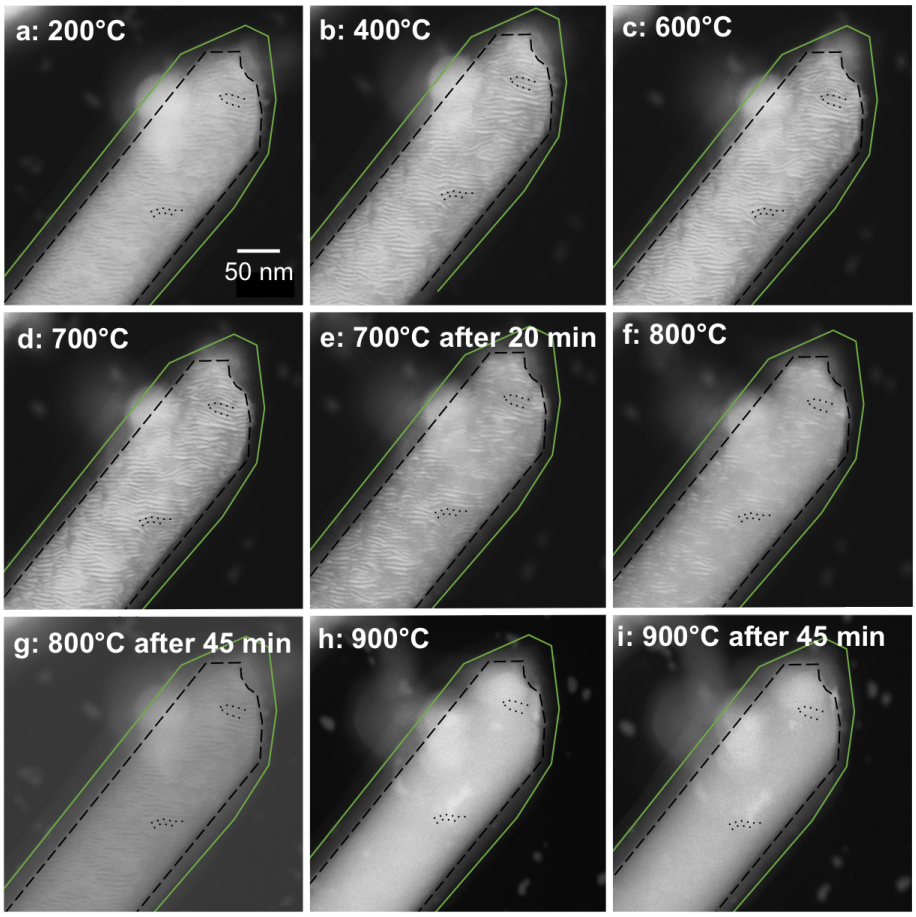

Figure 3.38: STEM imaging of a Ge-Si core-shell nanowire as a function of temperature and annealing time. A black dashed and green full lines are guide for the eyes and indicate the core-shell and shell-air interfaces, respectively. The dashed lines inside the Ge core highlight some fringes on the Moiré pattern. One pixel corresponds to 0.178 nm.

point of the different elements: 1200°C is then higher than the melting point of Ge and Au. The STEM image shows that Ge becomes liquid and its diffusion starts at 1200°C. The solid/liquid interfaces can be clearly observed in Figs. 3.39 (a-b) due to the contrast difference. The melting temperature was identified by the loss of the diffraction pattern in the parts of the NW separated by dark regions (indicated by the arrows in the Figure). The melting process was observed to take place at different times depending on the location of the NWs on the membrane, probably due to the temperature gradient of the sample holder. In the same way, diffusion of Ge in NWs laying directly on the membrane took place before than in the ones superposed forming clusters of wires. Interestingly, the diffusion process led to the formation of Si (or possibly SiC) nanotubes by Ge or Au-Ge diffusion. Indeed, as observed in Fig. 3.40, only Si and C atoms remained to form a nanotube. Some traces of Ge, O and Au were weakly observed at the final stage of the wire (see Figs. 3.40 and 3.41). The carbon shell around the NW is probably due to the long exposure of the wire to the electron beam, the thickness of which has maybe increased with temperature[194].

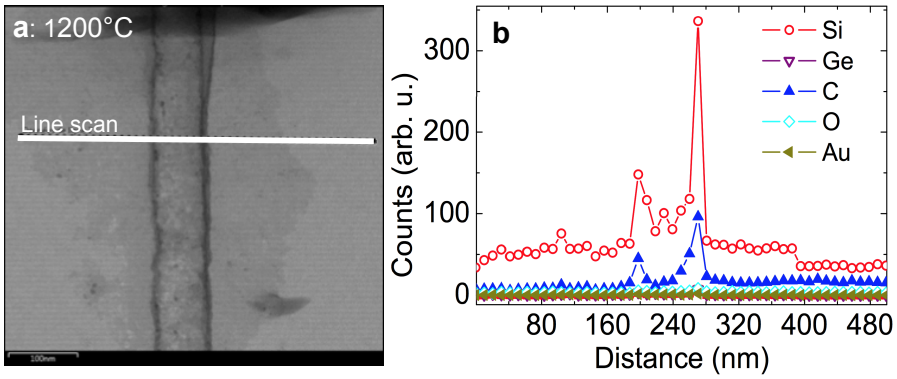

Figure 3.39: a) TEM micrograph of the NW at 1200°C showing the position at which the EDX profile in b) was performed. b) One dimensional EDX profile at RT after the annealing of the wire at 1200°C, at the position indicated by the black line in a).

Table 3.4: Melting points of the elements involved in the study

Element	Melting point (°C)
Ge	938.2
Si	1414
Au	1064

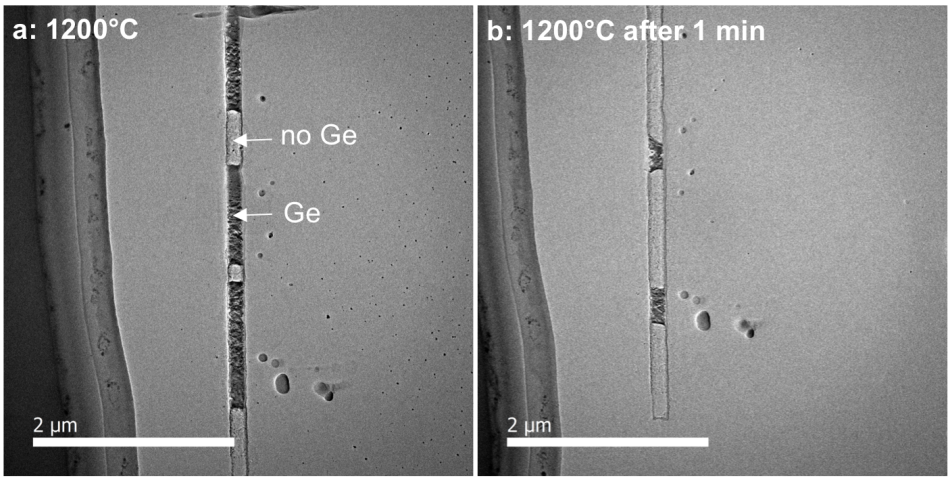

Figure 3.40: STEM imaging of a Ge-Si core-shell nanowire at 1200°C (a) and after 1 min of annealing at 1200°C (b).

3.4.2.3 Discussion

There are several results from the *in situ* TEM study that it is worth to highlight and relate with intermixing studies reported in literature by means of electron microscopy.
Firstly, the absence of gold diffusion towards either the core or the shell of the NW has been observed, contrary to which should happen at the bulk scale. Our results are in agreement with the detailed study of Holmberg[52] about gold diffusion from the catalyst towards pure Si and Ge NWs. In his works, Holmberg showed that Au atoms diffuse in Ge NWs extremely slowly whereas no gold atoms from the catalyst were observed to diffuse in Silicon NWs. Only when a

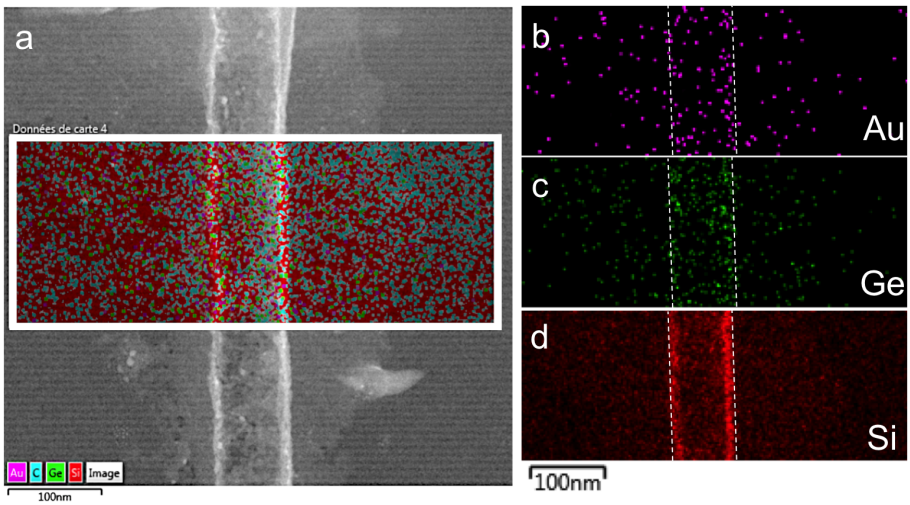

Figure 3.41: Elemental mapping of a single nanowire 1200°C. (a) The region mapped during EDX is shown by a white square. Ge (b), Au (c) and Si (d) elemental mapping. The dashed white lines are guide for the eyes and indicate the total size of the nanotube.

large source of gold was in contact with Si NWs interdiffusion was observed, being in this case 1-2 orders of magnitude faster than in bulk. In this case diffusion of Au atoms in Si would be mediated by interstitial impurities[b]. Hence, according to these findings, the remaining atoms of Au in the Ge core (likely located at the surface) would not diffuse far enough to be visible, if they actually do.

The other interesting result is the total absence of intermixing between the core and the shell and the melting of Ge yielding SiC tubes. The melting temperature of Ge wires was studied through *in situ* TEM by Wu and co-workers[195]. These authors studied Ge NWs encapsulated within carbon nanotubes and interestingly found a size-dependent melting temperature, with a considerable melting point reduction with respect to bulk for thinner wires. In their investigations, they found that 55 nm diameter wires started to melt at $650°$C and fully melted at $848°$C. The melting point reduction gets more important as the diameter decreases: a 25 % reduction is found for NWs of 30 nm diameter. In the experiment reported here the whole wire melts when the temperature at the membrane where the wires lay is $1200°$C. It makes sense to think that this is not the melting temperature of the Ge cores, because of the temperature gradient over the membrane, but also because the Ge core is not directly in contact with the membrane because of the relatively thick Si shell (*i.e.*, comparing to theirs). Other than the melting temperature, which is not exactly known, the melting process is not gradual in the case of Ge/Si core shell nanowires since the Ge did not start to melt at lower temperatures than the mentioned one. A possible explanation is that the Si-shell slows down the formation of the Si-C nanotubes, or maybe it is due to the length of the wires. Indeed, Wu et Yang[195] mentioned that larger lengths leaded to melting temperatures closer to the bulk's one, despite this is not further discussed in their reported work and their investigations concerns lengths up to $1\ \mu m$.

The complete absence of intermixing between Si and Ge is still intriguing, as Si and Ge are known to be miscible. A possible explanation would be the presence of a passivation layer of SiO_2 layer between the core and the shell, but after the EDX profiles (Fig. 3.39), the presence of O_2 is not significant. Another possible barrier could be the HCl used during the growth (see Section 3.1). In this case, Cl atoms would stay at the interface and inhibit diffusion. Answering this question is the purpose of next Section.

[b]Note that for many applications, the properties and composition of semiconductor nanowires are modified by adding impurities

3.4.3 Correlating strain and diffusion

The goal of this Section is to investigate the reason why Si and Ge forming the shell and the core of the nanowires do not intermix. As stated before, HCl could be the responsible of the inhibition of interdiffusion between these materials. HCl is used during growth to reduce tapering, get smooth facets and inhibit gold migration to the NW surface[164,170,196] (see Section 3.1).

Two samples were prepared in the same conditions than the previous ones, meaning Ge/Si core/shell NWs on a Ge(111) substrate, with the only difference that HCl was not used during the growth. Au colloids of 100 nm were employed, and a 10 nm shell was deposited *in situ* just after Ge NWs of about 2 μm were grown. Then one of the samples was annealed at 700°C. SEM images of both samples are shown in Fig. 3.42. Gold clusters are in particular visible in Fig. 3.42, on the Si surface. The tapering effect is evidenced in these images, $e.g.$, the centered NW imaged in Fig. 3.42 b) exhibits a diameter difference of about 170 nm between the top and the bottom.

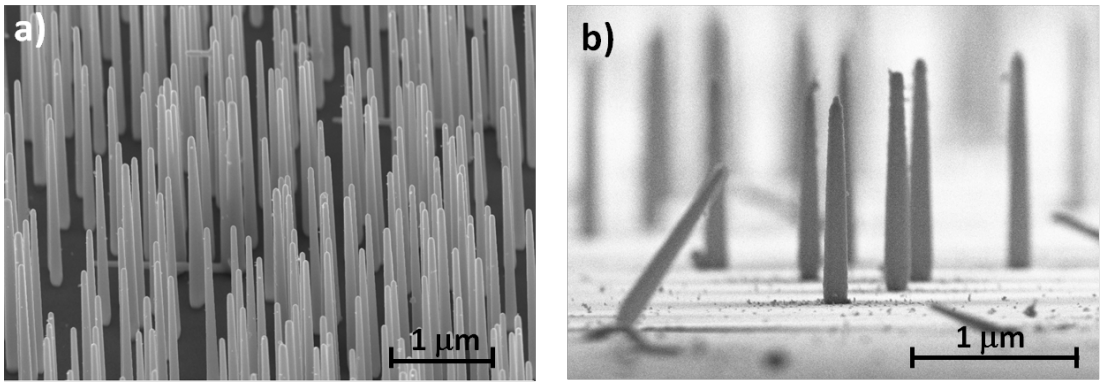

Figure 3.42: a) SEM image of an assembly of NWs grown on a (111)Ge substrate without HCl. b) Sample grown in the same conditions than a), with subsequent annealing at 700°C during 1 hour.

The samples were then measured “as grown" at the ID01 beamline, at a working energy of 8 keV and following the procedure described in Section 3.3.1. The recorded **111** Ge Bragg reflection of one NW from the first sample as-grown is shown in Fig. 3.43 a), which is comparable to the RSM analysed in Section 3.3.1. The analogous RSM of a NW from the sample annealed at 700° is displayed in Fig. 3.43 b). Before annealing, the elongated signal of the Ge core is observed around the Ge bulk position $|\vec{Q}_{111}|_{Ge} = 1.923$ Å^{-1}, and the **111** Si reflection from the shell is positioned at the Si bulk one, $|\vec{Q}_{111}|_{Si} = 2.004$ Å^{-1}. After annealing, the signal remains at the same position within an incertitude in the position lower than $\Delta Q_{111} < 0.001$ Å^{-1} owing to the fitting and small fluctuations during the measurements. Indeed, no signal is observed in between these peaks. Hence, Si and Ge have not interdiffused on the annealed sample and HCl would not be the responsible of the absence of intermixing between Si and Ge. Or maybe higher temperatures are needed to promote the intermixing.

Still looking for the reason of interdiffusion lack, two more samples were measured, consisting of samples grown in exactly the same conditions ($i.e.$, same growth temperature, pressure, gold colloid size and in abscence of HCl) but using a (111)Si substrate. Such a choice of substrate complicate the CDI experiment because NWs are not oriented, as it can be observed in Fig. 3.44, but finding vertical NWs is possible using the *k-map* technique[159].
Measurements on single wires were performed around the **111** Ge Bragg reflection of core/shell NWs as grown, then on annealed NWs. The recorded RSMs are displayed in Fig. 3.45; they are comparable to the ones grown on the Ge substrate (Fig. 3.43). The CTR is now visible in the

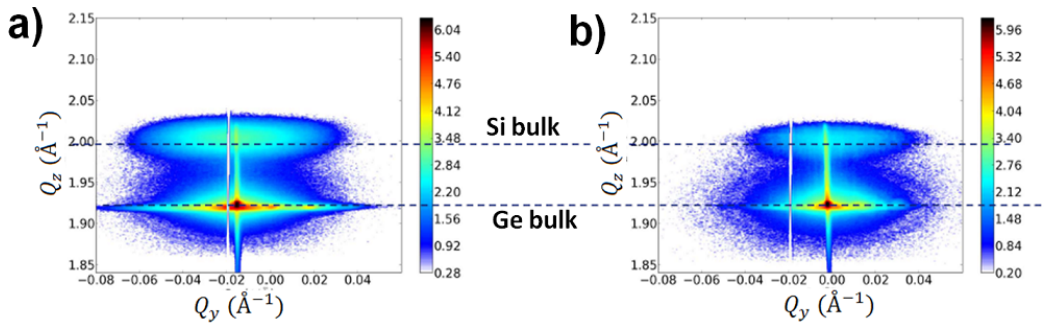

Figure 3.43: $Q_y - Q_z$ RSMs of single NWs grown on a (111)Ge substrate without HCl, as grown (a) and after annealing at 700°C. Dashed lines at the Ge and Si bulk position are guidelines to compare the diffracting signals before and after annealing. The colorbar corresponds to the logarithmic intensity.

upper part of the detector, superposed to the Si shell as expected given the substrate orientation. Besides the Bragg peaks of Si and Ge from the NWs, alloyed structures are diffracting in between ($Q_z = 1.94$ Å^{-1}); these structures (clusters or maybe islands) are visible in the SEM image (Fig. 3.44. It is worth to note that, on the substrate, there is a much larger number of clusters than in the case of growth performed on Ge.

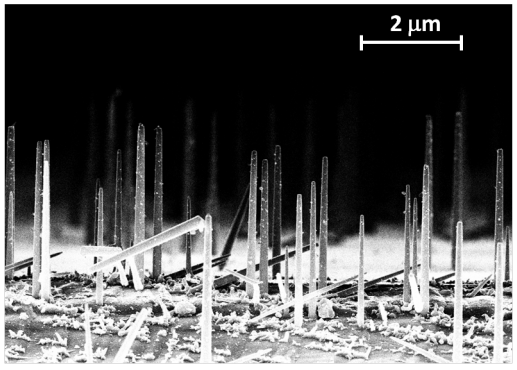

Figure 3.44: a) SEM image of an assembly of NWs grown on a (111)Si substrate without HCl.

In the RSM of the as grown sample, (Fig. 3.45 a)), core and shell diffract at the Ge and Si bulk positions respectively, meaning that the substrate does not influence the coherence at the interface of the wires. The same result is obtained after the RSM from the annealed sample (Fig. 3.45 b)). Nevertheless, interdiffusion has occurred in the alloyed islands. The composition of these nanostructures is likely different from the one of the NWs, as it could be their interface, because they are formed in absence of gold.
Another interesting fact from the experimental results rises from the faceting of the NWs core; a 2D cut in the $Q_x - Q_y$ plane elucidates a refaceting after the annealing. This is shown in Figure 3.46: a rounded Bragg peak becomes streaked after the annealing at 700°C. The mentioned behavior was observed for several wires over the samples. The shape change does not happen in the NWs grown on the Ge substrate, that exhibit an hexagonal shape from the growth and keep this morphology through the annealing.

The explanation for the absence of intermixing between Ge and Si shell is possibly not the use of HCl during the growth but it could be related to the strain relaxation of the core and the

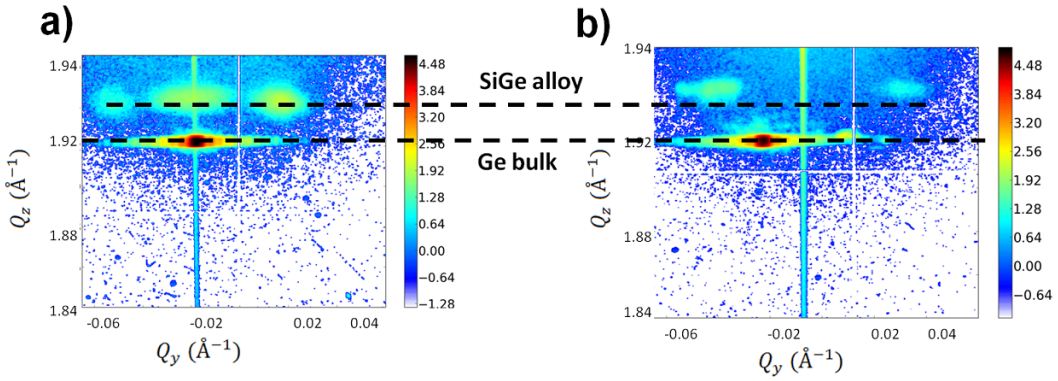

Figure 3.45: $Q_y - Q_z$ RSMs of single NWs grown on a (111)Si substrate without HCl, as grown (a) and after annealing at 700°C. Dashed lines at the Ge and Si bulk position are guidelines to compare the diffracting signals before and after annealing. Alloyed islands on the substrate have interdiffused. The colorbar corresponds to the logarithmic intensity.

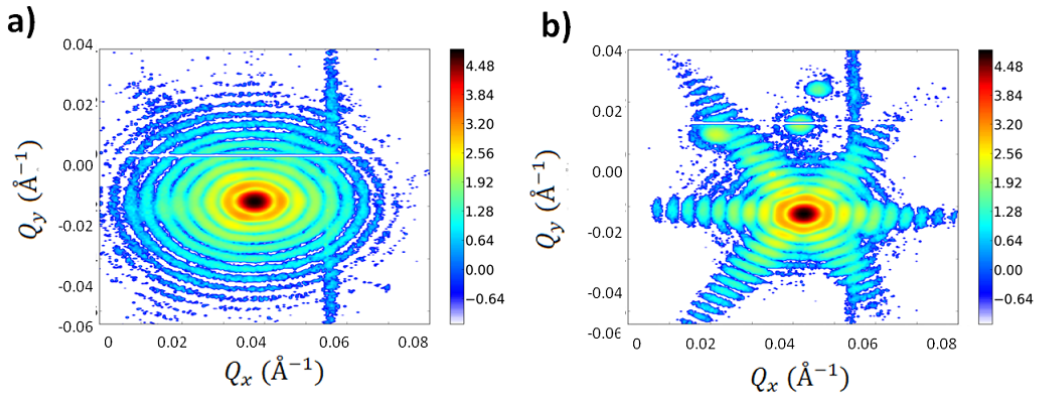

Figure 3.46: $Q_x - Q_y$ RSMs of single NWs grown on a (111)Si substrate without HCl, as grown (a) and after annealing at 700°C during 1 hour. A change of faceting is evidenced due to the annealing. The colorbar corresponds to the logarithmic intensity.

shell. Diffusion in Si (or Ge) of Ge (or Si) occurs by interstitially or vacancy mechanisms. The presence of strain, arising from the core/shell interface, alters the equilibrium concentration of intrinsic defects at high temperatures and yield the enhancement of interdiffusion in the case of strained heterostructures[197]. It is possible that, in absence of strain and misfit defects, these equilibrium concentrations may be preserved, thus inhibiting diffusion. Further investigations are nevertheless needed to understand this behavior, notably a complete characterisation of the interface since misfit defects are suspected. The amount of gold and its distribution over the wire might also influence the intermixing between Si and Ge.

On the other hand, the choice of the substrate does not modify neither the coherence at the interface nor the chemical intermixing between the core and the shell. However, shape differences were observed: the substrate orientation governs the epitaxy of the Ge NWs to the single-crystal substrate[198] and strongly influences the nucleation and initial stages of growth[199]. As a matter of fact, NWs grown on the Ge substrate are more tapered than the ones on the Si one. This is still proved by the larger length of the latter ones (see Figs. 3.42 and 3.44). The different

radial growth speeds owing to the tapering may explain the shape variations of the Ge cores rising from the homoepitaxy/heteroepitaxy to the substrate[196]. The evolution of the Ge NWs towards an hexagonal shape is not understood so far and further investigations are necessary.

3.5 Conclusions

In this chapter single core/shell Ge/Si NWs from different samples have been characterised. A theoretical model was first employed to understand the epitaxial strain induced in the NWs by the large mismatch between the core and the shell lattice parameters. Diffraction patterns in the case of coherent and incoherent interfaces were simulated, for a better comprehension of the X-ray experiments results.
The first analysis on this system resulted in a relaxed Ge-core and a very little strained Si-shell in the axial direction of the NW. The tensile strain of the shell with respect to the Si bulk lattice parameter was shown to vary with the core diameter, but not to follow the theoretical predictions within the elastic epitaxial model, perhaps because of misfit dislocations at the Ge-Si interface.
The *in-plane* strain was investigated by means of GPA: core and shell were shown relaxed in the radial direction as well. High resolution measurements showed however a partial epitaxy between the core and the shell, the later being rough and containing defects though.

The investigation of strain in the NWs was then focused on the Ge cores. For this, individual wires were prepared to perform Bragg CDI measurements and carry out phase retrieval. In particular, a NW with 200 nm core was found to present strained regions along its length; reconstructions were performed from RSMs around four different reflections which presented very weak distortions from strain-free NWs. However, results are not conclusive since defects along the wire whose origin is not known are observed. They could be extrinsic defects created by the manipulation process to isolate the NW.

In situ annealing experiments were afterwards performed to investigate the interdiffusion within single NWs and the influence of the interface between the core and the shell intermixing. CDI measurements revealed an important lattice tilt of the (111) crystallographic planes, *i.e.*, along the growth axis of the NW, that increased after annealing. A significant lattice tilt of 2°C over 4 μm was found after cooling down the sample. However, carrying out CDI experiments in the furnace installed at the beamline turned out to be very difficult because of the dome contamination and the decrease of coherent flux. Indeed, when high resolution is required longer counting times are needed and stability of the sample is crucial. Understanding the changes of the diffraction patterns during the thermal treatment brought us to perform *in situ* TEM measurements. The NWs were observed to be stable and diffusion was not observed. Ge melting started at 1200°C (reference temperature at the center of the grid) leading the formation of Si(C) nanotubes. The inhibition of intermixing may be explained by the presence of a passivation layer at the interface between the Ge-core and the Si-shell or the abscence of vacancies in the NWs.
The surprising evolution of the faceted shape of the Ge-core of the NWs with temperature deserves investigation as well, CDI being the most suitable tool to perform this study owing to its non destructive nature. Measuring the NWs grown on a Si substrate at different temperatures could give insights into the growth dynamics.

There are still many questions rising from the study here presented. First, the reason of strain relief in the NWs should be determined. TEM tomography and HRTEM at the interface may give some answers. Then careful studies must be performed in order to investigate the actual coupling between stress and diffusion. A study of the interface is mandatory, to confirm the presence of misfit dislocations or an inhibiting SiO_x diffusion barrier, for instance. If so, an iterative study of Ge core/SiGe shell NWs with different SiGe concentrations could be performed in order to determine whether strain influences diffusion. Disentangle strain and chemical composition is still a grand challenge.

CHAPTER 4

Investigating the strain within Pt catalysts under chemical reaction

4.1 Introduction

The physical and chemical properties of Platinum nanoparticles (NPs) make them suitable for many industrial applications, such as fuel cells[200], automobile exhaust purification[201] or bio sensors[202]. While the demand increases, the reserves are limited and expensive, hence it is necessary to synthesise more stable particles and improve their catalytic performance. In the case for instance of the automobile industry, Pt catalysts are used to remove CO: the presence of Pt in the oxidation of CO ($2\ CO + O_2 \rightarrow 2\ CO_2$) reduces the activation energy of the reaction by adsorption of the reactants on the catalyst surface, hence increasing the rate of the chemical reaction. The mechanism of the reaction is illustrated in Figure 4.1. The efficiency of the catalyst is enhanced by increasing the Pt exposed surface but also by modifying the shape of the NPs. Indeed, the crystallographic surfaces of the particles have different reactivity and they may change during reaction. The study of the CO oxidation reaction in presence of Pt NPs is the purpose of this chapter.

In particular, I report the application of Bragg CDI on model Pt particles with tetrahexahedral (THH) shape, whose high-index facets have been proved to exhibit higher catalytic reactivity and stability[72,203]. The morphology and strain distributions within individual particles are determined by phase retrieval routines. I explain how it is possible to determine the Miller indices of the facets by analysing the reciprocal space raw data.

Since tuning their shape is an actual possibility to enhance the catalytic activity of the particles - because this determines the surface atomic arrangement, composition and strain - finite element analysis of the sample is briefly discussed in Section 4.2, together with a new technique based on the calculation of the pole figure from a coherent diffraction pattern that allows to index the facets of single crystals.

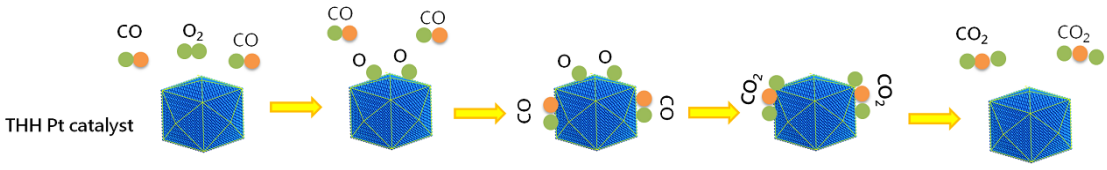

Figure 4.1: Representation of the different steps in the oxidation of carbon monoxide: $2\ CO + O_2 \rightarrow 2\ CO_2$. The oxygen molecules dissociate into two separate atoms of oxygen that are then adsorbed by the surface of the catalyst. CO molecules are adsorbed as well, then combined with each of the oxygen atoms to form a CO_2 molecule. Finally, the carbon dioxide molecules are desorbed from the surface of the catalyst.

Furthermore, as evoked previously, changes of shape, size and atomic structure of the surface of the particles can occur during reaction. These structural changes may result in activation or deactivation phenomena[204]. To understand possible structure-activity relationships, *operando* studies have been performed. The real time characterisation under catalysis operating conditions needs an appropriate *in situ* cell, allowing to track parameters such as temperature or gas composition in the cell at every stage of the reaction. For this reason, two *in situ* experiments are presented in this chapter: one at ID03 beamline, then a second one at ID01 using the new reactor described in Chapter 2.

4.2 Sample description and finite element modelling (FEM) simulations

The sample consists of high-crystalline Pt NPs randomly oriented on a glassy carbon substrate, as shown in Figure 4.2 a). The glassy carbon substrate is actually a well polished rod of 0.5-1 cm length that acts as electrode during the particles deposition. Nucleation of Pt nanospheres occurs after applying the electrochemical procedure explained in Ref.[72] at room temperature. The size of the spheres, from $100\ nm$ to $1\ \mu m$, can be controlled by varying the growth time. Then the applied potential is changed to induce the formation of $24\ \{hk0\}$ facets and consequently the characteristic tetrahexahedral (THH) shape of this sample. The THH shape can be described as a cube whose faces are capped by square-based pyramids, as shown in Figure 4.2 b). The size distribution is relatively narrow with relative standard deviation ranging from 10 % to 15 %, and the density of particles over the sample depends on the considered region: some clusters of 3-10 particles can be found in selected areas, while other NPs are well isolated (separated by several μm from the others). This can be observed in Figure 4.2 a).

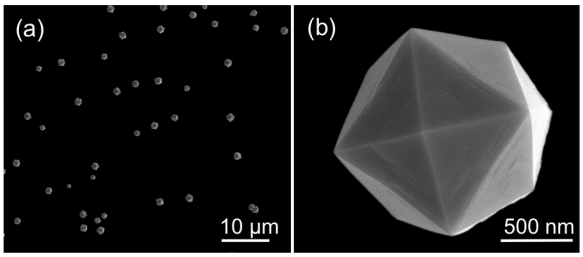

Figure 4.2: a) Scanning electron microscope image (SEM) of a typical sample after growth. b) Magnified image of one of the NPs, illustrating the THH shape.

The surface structure of the as-prepared THH Pt NPs has been studied previously by high-resolution transmission electron microscopy and selected-area electron diffraction[72,203,205]. The analysis concluded that most particles are bounded by $\{730\}$ facets, though $\{210\}$, $\{520\}$ and $\{310\}$ surface facets can be found as well. It was also shown that (730) facets correspond to periodic arrangements of two (210) and one (310) microfacets.
Since the morphology of the particles is suspected to lead an intrinsic strain in the sample and given the high sensitivity of CDI to small strain fields, an estimation of the residual strain within the particles is necessary to calculate the expected diffraction patterns from these objects. Hence, finite element analysis was used to determine the strain afterwards used in the diffraction patterns calculation. A single particle was modeled using COMSOL MULTIPHYSICS®. The knowledge of the atomic displacement of all unit cells in the sample provided by COMSOL®allows to retrieve the phase of the measured object. The geometrical shape considerations of the modeled NP were based on previous SEM analysis and the relationship between the Miller indices {hk0} and the geometric parameters that follow:

$$\frac{m}{n} = \frac{k}{2h} \tag{4.1}$$

where *m* is the height of the square pyramid and *n* the side length of the cube. To get the best fit with the experimental data, $\{210\}$ facets ($m/n = 1/4$) were chosen for simulations and a small size of 100 nm, for faster computation. A scheme of the single particle as simulated can be found in Figure 4.3 a). Note that here the bottom facet is flat, in agreement with the particle that was measured by CDI (see Section 4.3) and with posterior SEM studies. As shown in the same sketch, a particle whose (001) planes are parallel to the surface of the substrate was simulated.

Finite Element Modeling (FEM) was then performed to calculate the strain distribution in

the sample. The complete displacement field of the atoms in the NP was calculated taking into account the elastic anisotropy of Pt and constraining the bottom part of the particle to the substrate (*i.e.*, $\vec{u}(\vec{r}) = 0$ for the whole surface in contact with the glassy carbon). The elastic constants C_{11} = 359.5 GPa, C_{12} = 245.6 GPa and C_{44} = 85.8 GPa, from Ref.[206] were used. Initial additional strain was simulated by thermal expansion, changing temperature by 300° C in the displacement calculation in order to create significant residual strain.

The out-of-plane atomic displacement $\vec{u}_z(\vec{r})$ in the total particle ranges from -0.3 Å at the bottom of the particle to 3.7 Å at the upper vertex, as shown in Fig. 4.3 a). It can be observed in the two-dimensional cuts (Figs. 4.3 b) and c)) that smaller atomic displacements values take place in the edges, possibly arising from the faceting. The derived strain from the calculations is shown in Figure 4.4.

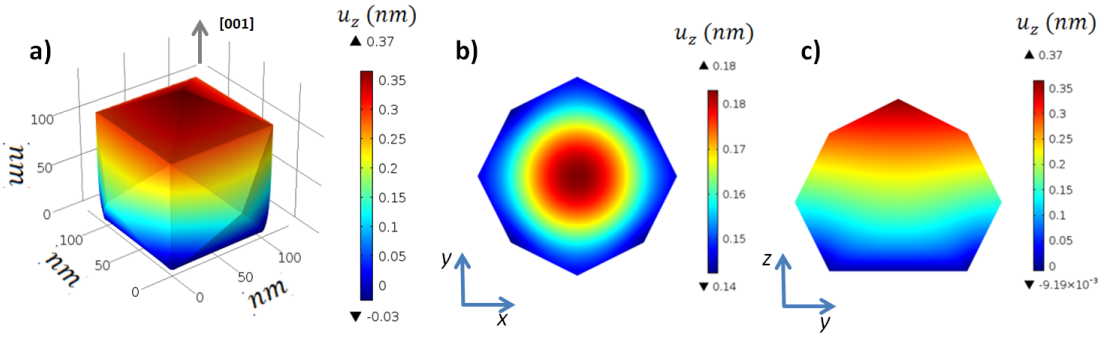

Figure 4.3: a) The THH shape consists in a cube whose faces are bounded by equal pyramids. As the NPs do not have a preferential orientation, the crystallographic orientation is simulated as found for the particles measured during the CDI experiments. The colormap corresponds to the $z-component$ of the atomic displacement $\vec{u}_z(\vec{r})$. b) xy cut of $\vec{u}_z(\vec{r})$ in the middle of the particle, *i.e.*, at $z = 50$ nm c) xy cut of $\vec{u}_z(\vec{r})$ at $x = 50$ nm.

Experimentally, only the intensity around the **002** Pt Bragg reflection was measured (see Sections 4.3 and 4.4), so that only the atomic displacement in the $z-direction$ can be accessed. Following the notation of Chapter 2:

$$I = |\tilde{A}(\vec{q})|^2 = \mathscr{F}[\rho(\vec{r})e^{iq_{002}\cdot u_{\vec{002}}(\vec{r})}]^2 = \mathscr{F}[\rho(\vec{r})e^{iq_{002}\cdot u_z(\vec{r})}]^2 \tag{4.2}$$

The phase of the complex-valued object ($g(\vec{r}) = \rho(\vec{r})e^{iq_{002}\cdot u_z(\vec{r})}$) can be written:

$$\varphi = q_{002}\cdot u_z(\vec{r}) = \frac{4\pi}{a_{Pt}}u_z(\vec{r}) \tag{4.3}$$

where a_{Pt} is the lattice parameter of Pt ($a_{Pt} = 3.9242$ Å).

The values of the atomic displacement at the nodes which form the crystal lattice were exported from COMSOL. They were interpolated over a regular grid. Then, the scattered intensity around the **002** Pt Bragg reflection was calculated by performing the Fast Fourier Transform (FFT) of the object, according to Equation 4.2. Results are shown in Figure 4.5. The Bragg peak is centered at $|\vec{Q}| = 3.20$ Å^{-1} for an energy of E=8 keV and it is almost symmetric, as corresponding to a weakly strained) nanocrystal. Indeed, strain-free particles yield to the same diffraction patterns.

In the case of faceted crystals, when the scattering signal is measured close to the Bragg peak, reciprocal lattice points transform into shape functions consisting of truncation rods or streaks from each facets. Therefore, the calculated 3D Bragg peak consists of 24 flares, each one arising from one of the facets of the particle, *i.e.*, each streak being perpendicular to each facet. The

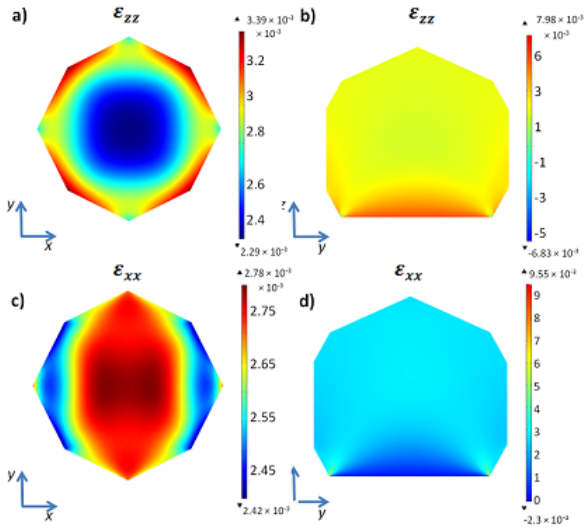

Figure 4.4: Strain fields calculated in the parallel direction to the scattering vector ϵ_{zz} (a) and (b), and the in-plane component ϵ_{xx} (c) an (d). 2D cuts are taken at the same position as in Figure 4.3).

streaks are modulated in intensity due to the finite dimensions of the particle, their periodicity being inversely proportional to the diameter of the NP.

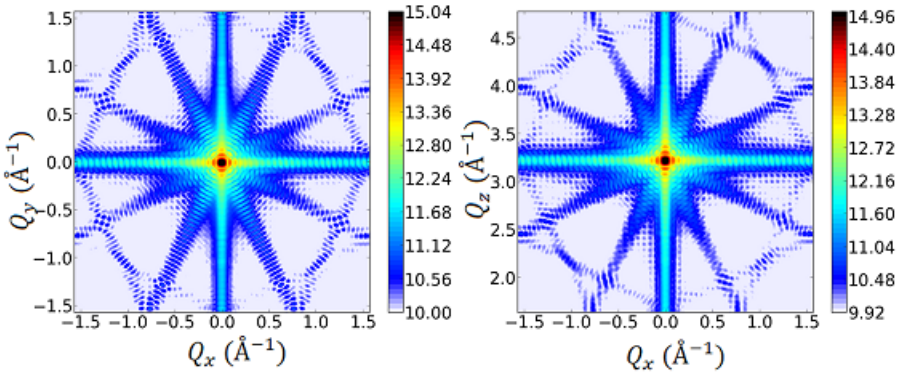

Figure 4.5: Scattered intensity calculated from FEM atomic displacement. The 2D cuts show a symmetric Bragg peak centered at $|\vec{Q}| = 3.20$ Å^{-1}. Aliasing artifacts can be observed due to the employed FFT algorithm.

The sharp and well-defined directions of the streaks suggest the possibility of indexing the Miller indices of the facets. Let us define a sphere around the 3D Bragg peak whose center is the center of mass of the peak ($Q_{COM} = \frac{\sum_i Q_i \cdot I_i}{I_{total}}$ where the sum runs over all the reciprocal space points Q_i), as shown in Figure 4.6. The directions of the streaks correspond to the normals of the nanocrystal facets, thus one can take the known [001] direction and define the normal plane (001) containing the point Q_{COM} as the equator of the sphere. The intersection of the normal defining the equator plane with the sphere defines the North (N) and South (S) poles (Fig. 4.6).

Consider now only the upper hemisphere (l or $|\vec{Q}_z \geq 0$). The intersection points of every streak with the hemisphere ("poles") can be projected on a reference plane, *i.e.* on the equator of

the sphere. The stereographic projection of the hemisphere on the equator plane is called "pole figure" and it consists in our case of sharp peaks whose symmetry and positions are related to the particular centered cubic structure of Pt. Every peak arises from a specified crystallographic axis, that can be in this way labeled with the corresponding (hkl) Miller indices of the facets. The pole figure resulting from the projection of the simulated scattered intensity is shown in Figure 4.7. Hence this method applied to experimental data allows indexing the facets of a single nanocrystal.

4.3 Study under ambient conditions

A first study of the sample described in Section 4.2 has been performed at ID01 beamline under ambient conditions, *i.e.*, at room temperature and atmospheric pressure. The sample studied during this experiment consisted of THH NPs with an average size of 300-700 nm, as observed by SEM analysis prior to the experiment (see Fig. 4.2). During this preliminary study it has been observed that some of the particles did not show a THH shape or had been deformed/strained during the electro-deposition process.

The experimental set-up used for the CDI experiments has been already described in Chapter 2 of this manuscript. Before measuring the THH NPs, a characterisation of the beam has been done using a 2D ptychography approach and a test sample. Measurements in forward geometry and with the detector placed at a distance of about 2 m from the sample were performed. The test sample was a Siemens star, a patterned object whose periodicity makes easier the reconstruction and gives an idea about the focal spot characteristics during the experiment. Object and probe were reconstructed using the 2D ptychography code of the PyNX package[207] with a resolution of 25 nm (reconstructed pixel size). Figure 4.8 shows the reconstructed complex wave field and the beam profile in both horizontal (H) and vertical (V) directions. The reconstructed probe shows a full-width-at-half-maximum (FWHM) peak size of $400\ (H) \times 100\ (V)\ nm^2$. The asymmetry of the focal spot (especially evidenced in the horizontal direction) might be introduced by FZP. imperfections[23] or by diffraction effects from the vertical slits placed just before the FZP[208,141].

In figure 4.9 the schematics of the coplanar scattering geometry used during the experiment is illustrated. The sample surface was mounted horizontally and the intensity distribution around the **002** Pt reflection of single particles was measured. For this, the incident angle was set to $\theta_{Bragg} \approx 20.55^\circ$ and the detector was positioned at a distance of 1.26 m from the sample, at the scattering angle $2\theta_{Bragg} \approx 41.15^\circ$. As the orientation of the particles on the substrate is random, *k-maps*[159] on different regions of the sample were used to localise (002)-oriented Pt particles.

The incoming X-ray beam (at E=9 keV) was then focused on the identified single particles using a FZP and an order sorting aperture (OSA). Once a particle is illuminated, the 3D diffraction patterns can be recorded using rocking scans around the Bragg angle: the 2θ angle is fixed, while the sample is rotated over a few degrees with respect to the direction of the incoming beam. A 2D diffraction image is taken at each angle-step. Here, small steps of $\Delta\theta = 0.005^\circ$ were chosen to ensure oversampling, and a short counting time of 1 second, to get good resolution while preserving the stability of the particles. In Fig. 4.10 the sum of the measured intensity along the $y-$ and $z-$ components (*i.e.*, in the $Q_y - Q_z$ plane) of the **002** Pt scattering vector after orthonormalisation of the data using the *xrayutilities* package[209] of four different single isolated Pt NPs is shown. The NPs have been labeled from 1 to 4 in the black circles on the diffraction patterns. The center of mass of the Bragg peak of the 4 measured particles are in the range of 3.202 ± 0.008 Å and consequently, the particles are relaxed to their intrinsic cubic lattice constant (no out-of-plane strain with respect to the bulk lattice parameter of Pt taken as reference).

Thickness fringes are visible in all the coherent patterns, so that (supposing no or weak strain effects) an estimation of the average size can be done along the Q_y-direction: 355, 220, 185 and 380 nm for particles 1 to 4 respectively. As the NPs are quite homogeneous in shape (according to SEM images of the same sample) and given the assymmetry of the Bragg peaks, the differences between the diffraction patterns must arise from different strain states. Particle 1 is the most

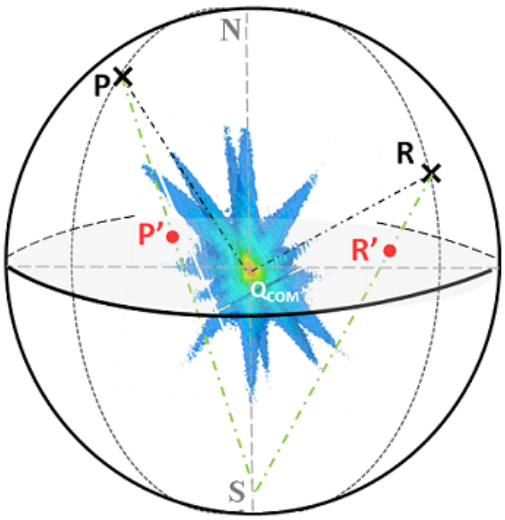

Figure 4.6: Illustration of the stereographic projection of two poles (P and R) on the equator plane (shaded). The projected poles (P' and R') are the intersection of the line joining the South pole with the corresponding pole. The direction of the streaks defining the poles and the radius of the sphere have been extended for clarity.

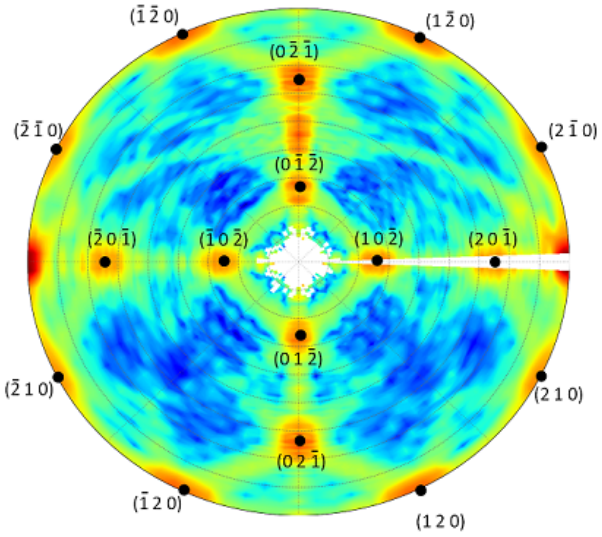

Figure 4.7: Stereographic projection of the simulated data (from Fig. 4.5) for $l \leq 0$. This **002** pole figure is equivalent to the projected poles on the reference plane (see Fig. 4.6). The simulated facets of type {210} yield 16 peaks whose (hkl) indices are indexed. Additional peaks and high intensity regions arise from aliasing in the calculation and from extra small facets created during the modelling of the particle.

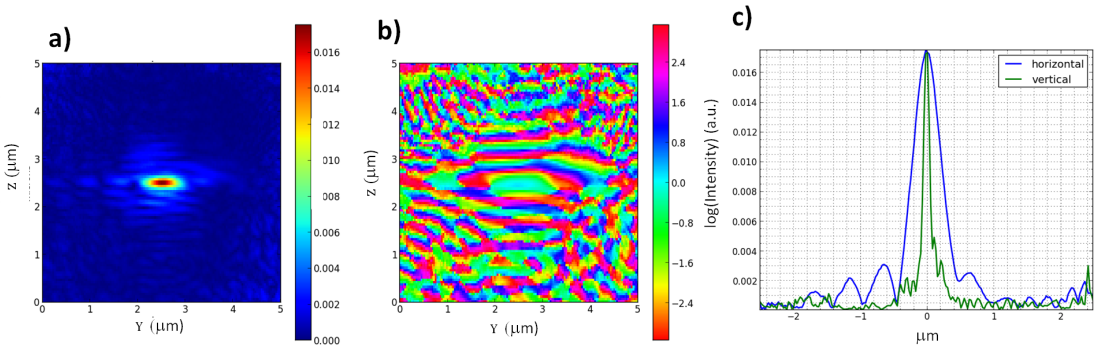

Figure 4.8: Ptychographic reconstruction of the x-ray wave field amplitude (a) and phase (b) and line profiles (c) of the horizontal and vertical focus intensities yielding a spot size of 100 (V) × 400 (H) nm^2.

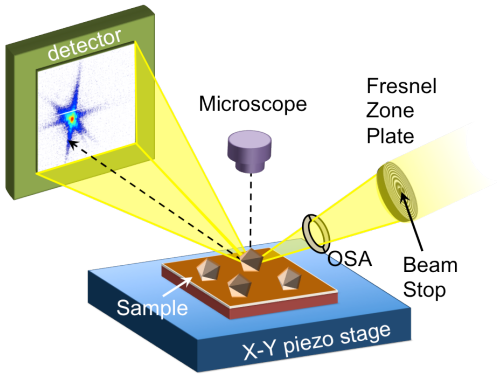

Figure 4.9: Schematic overview of the experimental setup in co-planar diffraction geometry at ID01 beamline.

similar to the simulated one: the 24 streaks corresponding to the 24 well crystalline facets of the THH shape are visible in the 3D Bragg peak. Some streaks are also well defined in the case of particles 2 and 4, rough facets may explain the absence of the other streaks. Furthermore, the streaks are different from each other: either broad and sharp streaks can be observed. Broad flares arise from small facets, so NPs 2 and 4 must be formed by facets with different sizes. These differences in size of the facets could explain imperfection at vertices observed in SEM images. In addition, the center of the Bragg peak of particle 4 is split. This is a sign of the presence of defects in the nanocrystal. Finally, very little information can be deduced from the diffraction pattern of particle 3: symmetry has been lost, the particle is probably highly-strained.

4.3.1 Facet determination

In the following, I focus the study on particle 1. Its centrosymmetric diffraction pattern signal implies that its strain field is weaker compared to the other deformed particles and the well-defined [hkl] direction of the streaks due to its high-crystalline quality can be used to determine the (hkl) Miller indices of the facets.

Here, I analyze the crystallographic facets by rotating the orthonormalised 3D Bragg peak and analyzing the projections (see Fig. 4.11). Streaks in [001], [010] and [100] directions can be easily identified so that the angle between these directions and the streaks can be measured.

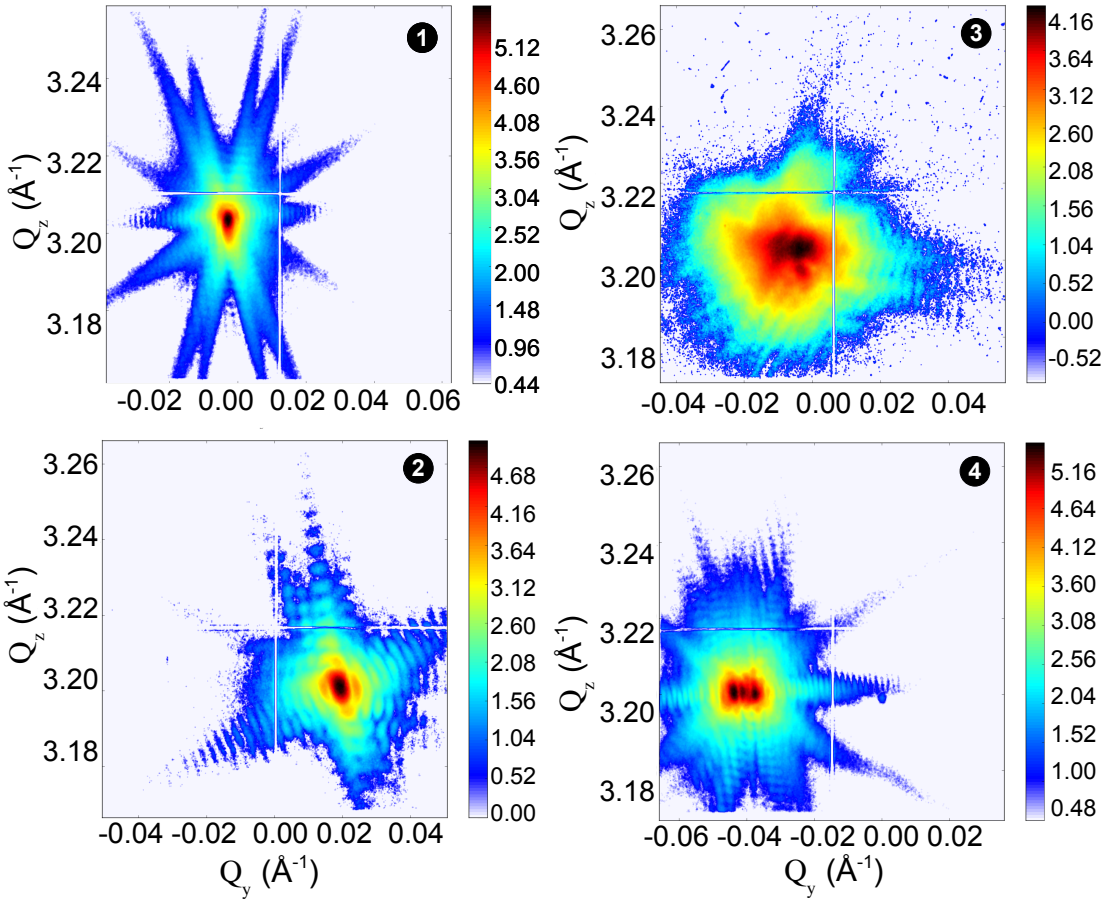

Figure 4.10: X-ray reciprocal space maps around the **002** Pt reflection for four different THH NPs. The sum of the measured intensity (logarithmic scale) is displayed as a function of Q_y and Q_z.

The angle α between two {hkl} planes in a cubic lattice is given by:

$$cos(\alpha) = \frac{h_1 \cdot h_2 + k_1 \cdot k_2 + l_1 \cdot l_2}{\sqrt{h_1^2 + k_1^2 + l_1^2}\sqrt{h_2^2 + k_2^2 + l_2^2}} \tag{4.4}$$

The measured angles were then compared with the theoretical values for the most common facets observed in literature[72,203,205], which are shown in Table 4.1. Results after fitting are shown in Fig. 4.11: the particle is bounded by 24 facets of high-index {210} planes, as an angle of $(63 \pm 1)^\circ$ or $(26 \pm 1)^\circ$ is measured between the streaks and the [100], [010] or [001] direction. An extra $(\bar{1}30)$ facet is observed in Figure 4.11.

In Section 4.2 I have introduced a method allowing to determine the {hkl} Miller indices of the facets using the reciprocal data. This technique can be applied to particle 1 as well. The radius of the sphere is chosen in order to intersect all the rods of the 3D diffraction pattern; the stereographic projection of the intersection points between this sphere and the streaks is shown in Fig. 4.12. Since experimental streaks are broader than the theoretical ones, they yield wider peaks but the 4 fold symmetry corresponding to a cubic-face-centered crystalline structure can still be recognised. The position of some peaks can easily be fit with the theoretical positions

plane 1 (hkl)	theoretical angle between (001) and plane 1 (°)	theoretical angle between (100) and plane 1 (°)
(110)	90	45
(201)	63.43	26.56
(301)	71.57	18.43
(502)	68.20	21.80
(703)	66.80	23.20

Table 4.1: Theoretical angles between planes.

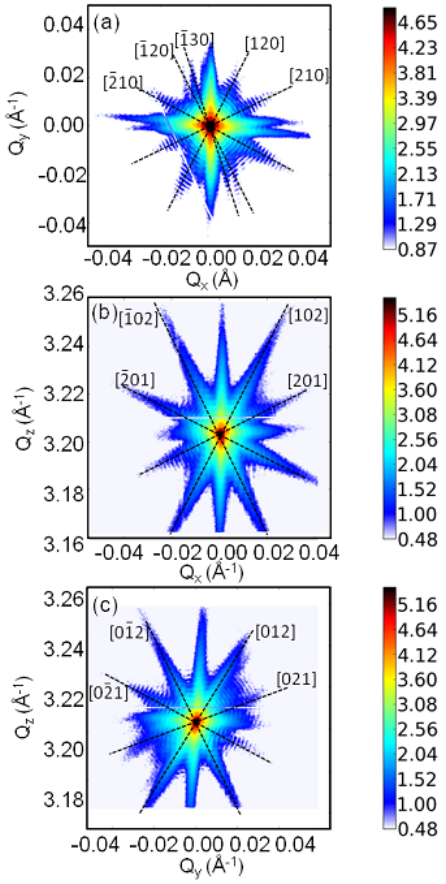

Figure 4.11: X-ray reciprocal space maps around the **002** Pt reflection for particle 1: sum of the measured intensity (logarithmic scale) displayed as a function of (a) Q_x and Q_y, (b) Q_x and Q_z (c) Q_y and Q_z.

(black points) of the {210} planes, but a slight rotation with respect to the [002] direction (defining the center of the pole figure) can be observed, meaning that the (002) atomic planes of the particle could be slightly misoriented, *i.e.* not perfectly horizontal. This can be for instance observed when looking at the position of the peaks at $\phi = 0°$. Also, an asymmetry of few degrees is evidenced when looking at the upper/lower part of the figure ($\phi = 90°$).

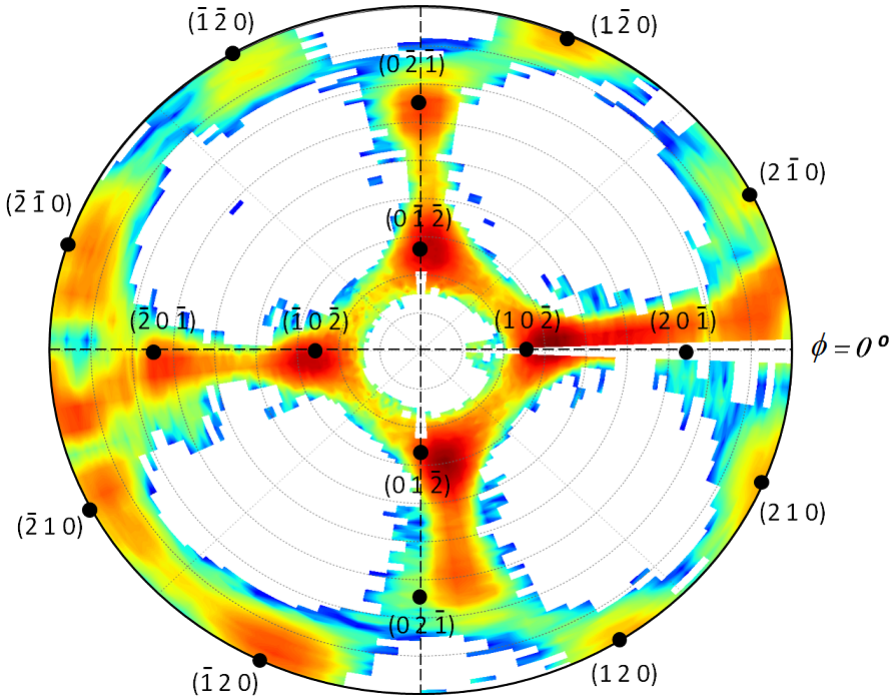

Figure 4.12: Stereographic projection of the points defining the direction of the streaks from the experimental data of particle 1. The theoretical position of the facets are shown in black.

4.3.2 Phase retrieval

After this structural study based on facet determination, iterative phase retrieval algorithms can be used on reciprocal data to reconstruct particle 1 in real space. Besides the morphology of the NP, phase retrieval allows to access the strain field within the particle.

The preparation of the data before applying the phase retrieval algorithms consists of orthonormalising the data (here done with the Python library *xrayutilities*[209]), then taking a 3-dimensional array with 2^n pixels on each side because of memory issues - the choice of the grid size is convenient to reduce the computing time when dealing with such a number of FFTs on multiple 3D arrays (input intensity, support constraints, current iterates...). The 3D raw data used as input in the case presented in this section was an array of $256 \times 256 \times 512$ pixels. After that, the data has to be centered in the array, $i.e.$ the center of the Bragg peak must be in the central position of the 3D array (data far from the center may wrap on the other sides of the array). This step is required by the symmetry of the FFT; an asymmetry on the data induces a non-physical phase gradient in the retrieved object that can be easily identified.

A cube whose length side is slightly larger than the particle dimensions estimated from the thickness fringes in the corresponding directions was chosen as initial support. The reciprocal space resolution being of $\delta q = 2 \times 10^{-4}$ Å^{-1} in the detector plane, a cube of 80 pixels length per side should be tight enough for the algorithm to refine the shape ($i.e.$ a cube of equivalent length size of $\frac{2\pi}{80 \cdot \delta q} \approx 393\ nm$).

A routine using the algorithms described in Chapter 2 was employed to retrieve the lost phase. The routine to find the “correct support" consists in applying 10 times the SW algorithm after every 5 cycles of 50 ER algorithm followed by 100 iterations of the HIO algorithm. Then 50 ER iterations are performed on the new object, thus with the modified support, and this complete routine is repeated. After about 50 iterations, the support gets the expected size and shape, and

the support does not change anymore .

Once the support has been determined, a new series of 50 cycles of {50 ER + 100 HIO} is applied to the measured intensity with different random initial guesses of the phase. All of them converge to the same solution, with a error metric of the order of 10^{-2}.

As the FFT routine works in reciprocal units, a conversion taking into account the sampling and extent has to be applied so that the axis of the object and its dimensions are in direct space as well. For this, the following Fourier conjugation relation can be used:

$$r_i = 2\pi \frac{q_j \times q_k}{V} \tag{4.5}$$

where *V* is the volume defined by $V = q_i \cdot q_j \times q_k$ and {*i, j, k*} indexes are given by the circular permutation of the {*x,y,z*} indexes. The relation is only valid if the q_i vectors define an orthogonal basis. The calculation of the real space coordinates yields to a voxel size of $4 \times 8 \times 6\ nm^3$. The 3D reconstruction of the density in the real space coordinates is shown in Figure 4.13: the different facets of the nanoparticle are well-defined, evidencing the pyramidal shape on the sides, the structure is comparable with SEM measurements. Note that terraces are artifacts due to the isocontours and not real crystal terraces. Also a flat damaged face is revealed by the reconstruction, which corresponds to the side lying on the glassy carbon surface. During the electrochemical process, the bottom phase in contact with the substrate did not react to form faceted planes.

Given the dimensions of the particle, the path of the scattered beam in the sample is much longer than the X-ray wavelength. Thus, an additional phase due to the refraction along this path may contribute to the total phase and hide weak strain in the sample and the retrieved phase has to be corrected[210]. Refraction effects are due to the real part of the refractive index of matter ($n = 1 - \delta + i\beta$), which is slightly smaller than the one of air or vacuum; refraction causes the waves traveling inside the crystal to have a different wavelength from those traveling in the vacuum. The correction can be done by subtracting to the retrieved phase the cumulated phase shift induced by the beam through its path within the sample. This phase shift is spatially dependent and is given by:

$$\phi = k \cdot \delta(OPL) \tag{4.6}$$

where *k* is the modulus of the wavevector of the incoming X-ray beam, OPL the optical path length difference between the wave travelling within the particle and the one in air or vacuum, and $\delta = 4.11 \cdot 10^{-5}$ in the case of Pt at 9 keV[211]. For a Pt particle of maximal width of 400 nm and a beam of 9 keV impinging on the particle under an incident angle of $\theta_{Bragg} = 20.55°$, the maximum path length of the wave through the sample is $\frac{400 \times 10^{-9}}{\sin(20.55°)} = 1.14\ \mu m$. According to Equation 4.6, this corresponds to a maximum phase shift of 4.27 rad. Hence, it is necessary to take into account the refraction effect.

The corrected phase of the retrieved crystal is shown in Figure 4.14. The 2D slices show an inhomogeneous phase inside the particle, as well as its damaged basis.

The calculation of the 3D displacement field u_{002} in the nanoparticle from the reconstructed phase (using Equation 4.3), $i.e.$ in the z direction (see Figure 4.15) yield values that can be compared to the FEM simulated ones. The displacement field is in the order of tenths of Angstroms, so much smaller than the lattice distance through the propagation vector in the Q_{002} direction ($i.e., d_{002} = 1.96$ Å). The center of the particle shows a different displacement field (pink-colored) than its border (blue-colored).

The out-of-plane strain (ϵ_{002} or ϵ_{zz}) can be deduced from the gradient of the displacement field ($\epsilon_{zz} = \frac{\partial u_{zz}}{\partial z}$). Figure 4.16 shows the ϵ_{zz} component of the strain tensor. The core of the particle has a different strain state than the edges: core shows a negative strain compared to the edge (compressive strain). A maximum strain of 0.35% is observed. The difference of strain between the core and the edges of the particle can arise from the potential effects of the electrodeposition process, which introduce a pulse potential responsible of the formed high index facets.

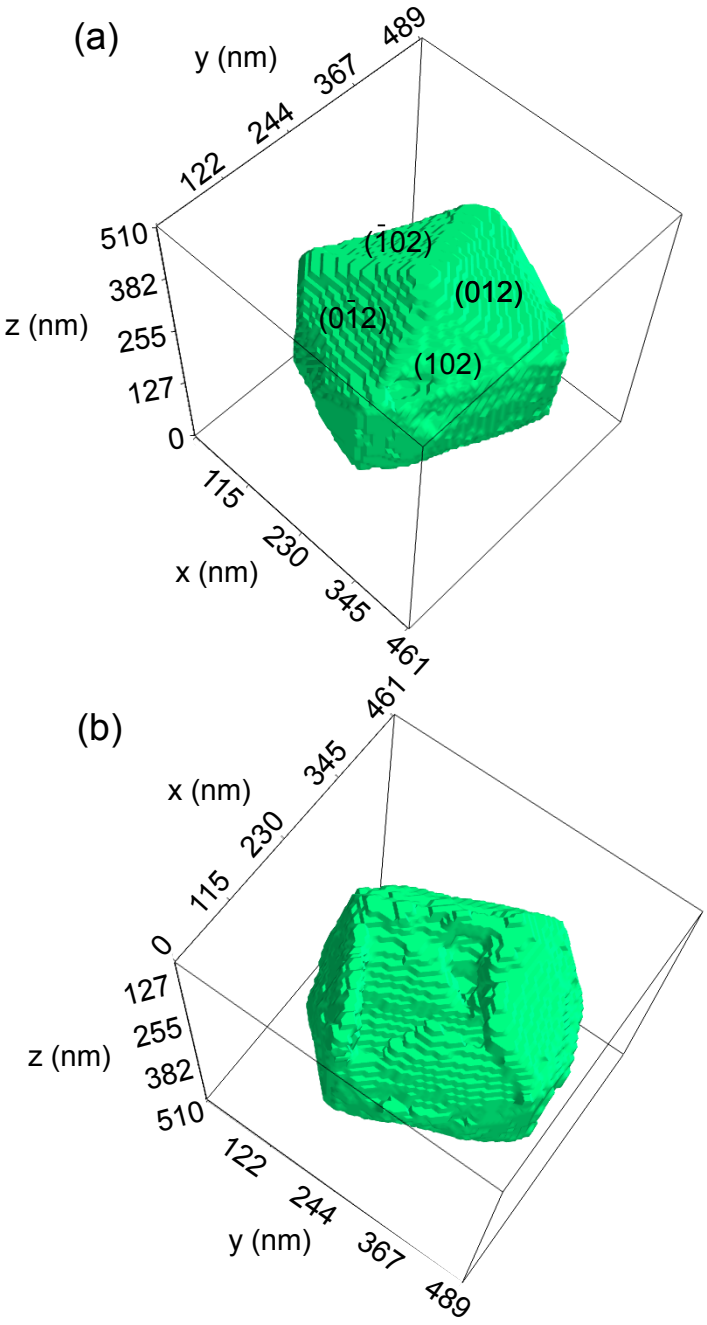

Figure 4.13: Top (a) and bottom (b) views of the 3D reconstructed support of Particle 1. Crystal dimensions are estimated to be $330 \times 400 \times 310$ nm^3.

A similar strain field distribution, which was linked to surface strain, was found in a single gold nanocrystal measured in presence of propane thiol[98]. The authors attributed the compression of the flat facets of the crystal to thiol adsorption. Also in our case, the contact with any gas could explain the strain at the surface of the crystal.

In summary, during the experiment diffraction patterns of different individual Pt THH particles were recorded. The in-depth study of a particle shows an inhomogeneous strain field.

The analysis of the reciprocal raw data allowed us to determine the (hkl) Miller indices of the facets of the nanocrystals and their average out-of-plane strain with respect to bulk Pt. Then, the object was retrieved from the experimental data. A highly crystalline Pt NP with a THH shape was characterised in real space (resolution of about 30 nm) and revealed its structure at the nanometer scale. The strain map demonstrates how particle shape, size, and environment can shape the strain distribution, which will influence catalytic performance. The shape of the electrochemically prepared Pt THH NCs together with the detailed structural information from CDI make this approach suitable to derive structure-performance relationships of individual catalyst particles. This study proves the ability of CDI to image single nanocrystals and opens pathways to investigate in situ the internal structural evolution of nanoparticles in various gaseous and liquid environments during reaction.

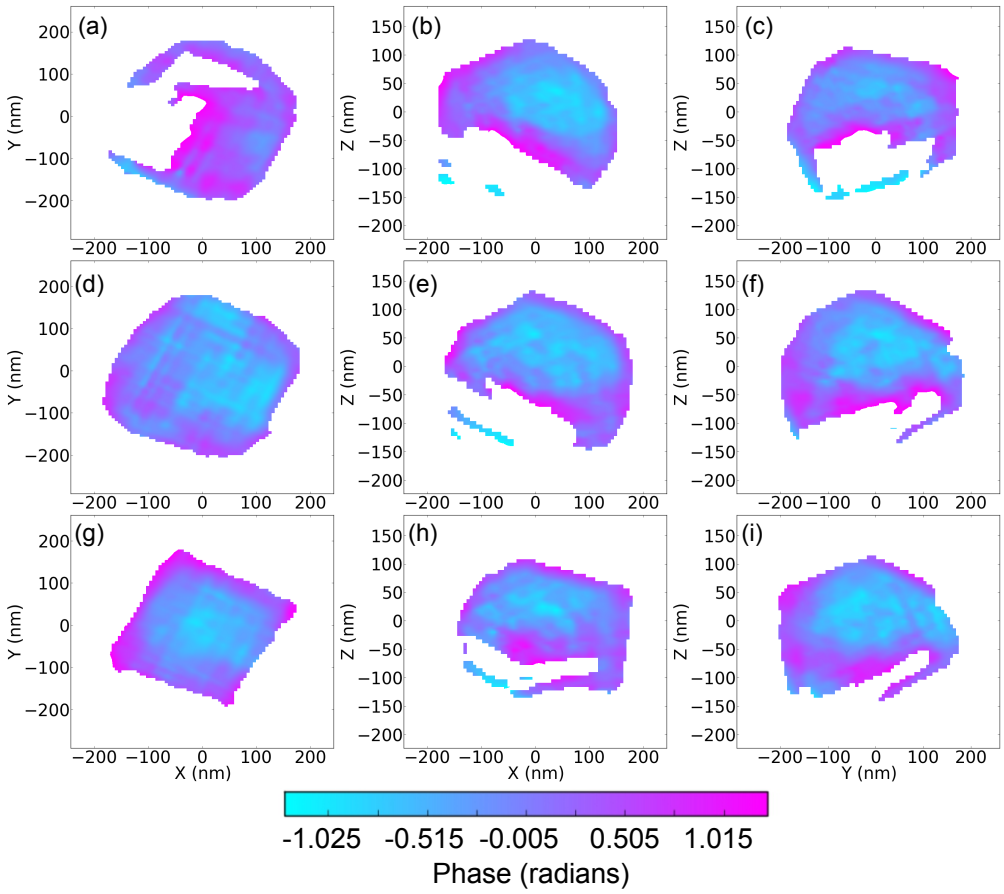

Figure 4.14: In the central row, 2D slices of the retrieved phase after refraction correction at the middle of the particle. In the upper and lower rows, the cross-sections are taken at -60 and +60 nm of distance from the center respectively and for the indicated directions. The colour scale shows the relative phase shift with respect to the non-strained region.

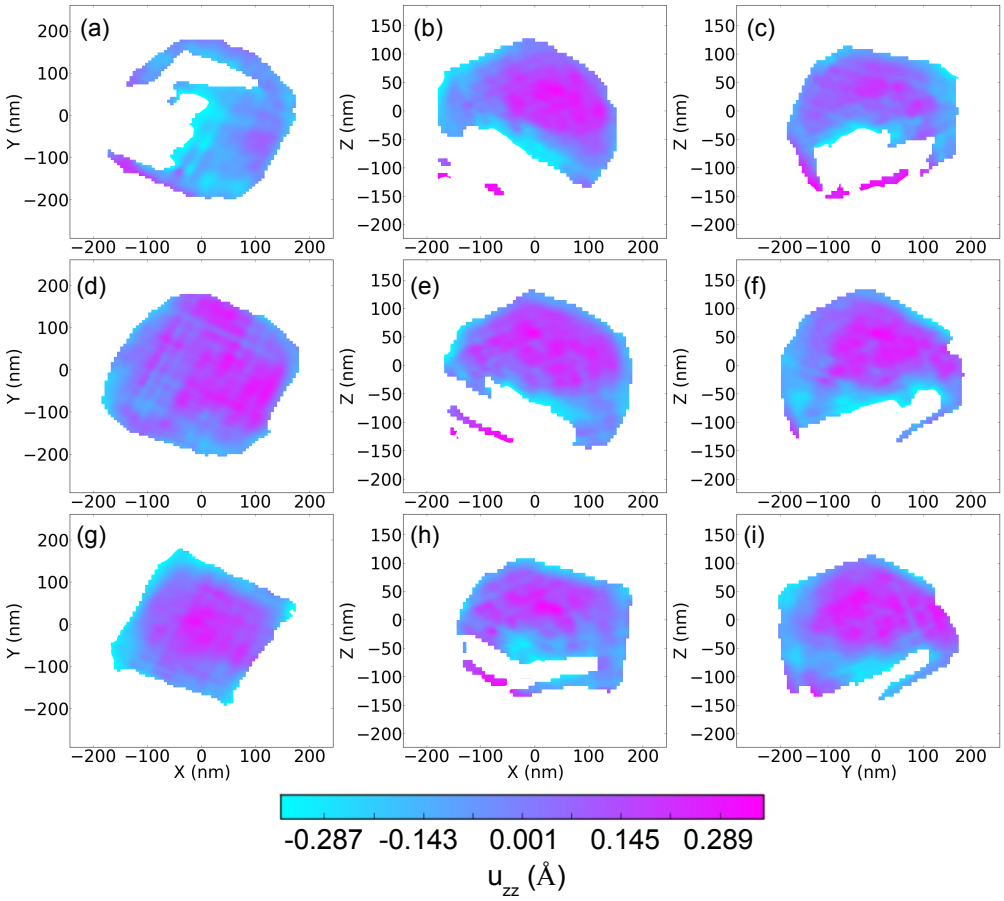

Figure 4.15: 2D cuts of the calculated atomic displacement, corresponding to the cut-planes of the phase shown in 4.14.

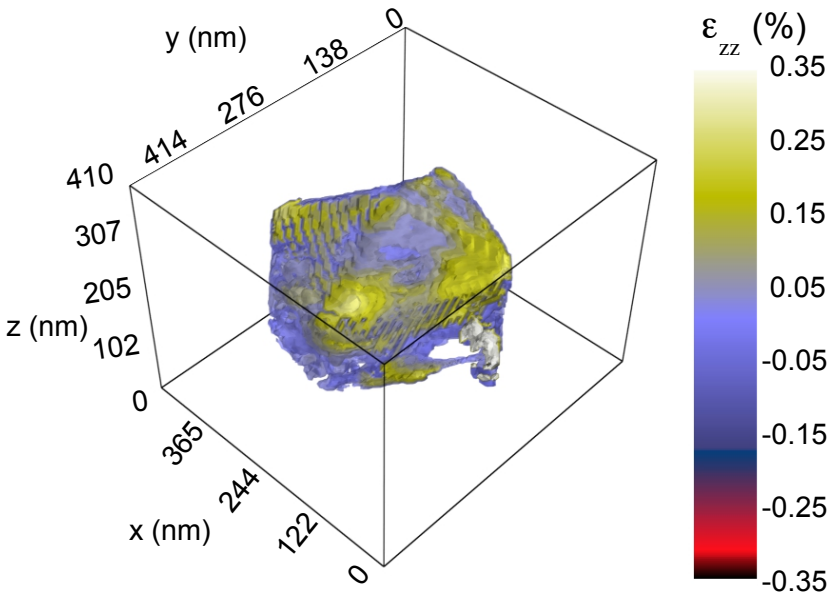

Figure 4.16: Isosurface showing the strain distribution inside the particle

4.4 *In situ* study at ID03 in controlled gas-phase environment

In the previous section it has been shown how it is possible to do a complete characterisation of single Pt NPs using BCDI. The characterised THH Pt NPs exhibit high-index facets whose interest is to enhance their catalytic performances (with respect to conventional particles-based catalysts). Indeed, surface structure and reactivity are coupled to reaction conditions, so that detailed characterisations of single NPs *during* the reactions themselves are necessary to identify favourable structure or strain properties, as NPs can respond differently to changes in the environment (gas composition). Here, the CO oxidation on single Pt NPs is studied using BCDI at ID03 beamline. The sample is the one measured in inert atmosphere at ID01 (see Section 4.3). Note that structural changes are expected during reactions using real catalysts, $i.e.$, catalysts consisting of NPs in the range of $3-10$ nm, but here I will focus on much larger particles in order to have a sufficiently large scattered intensity from a single nanocrystal.

The set-up during the experiment at ID03 beamline is a bit different from the previous one (see ID01 beamline description in Chapter 2). The catalysis experiment was performed in the first experimental hutch of ID03, where a 6-circle diffractometer that supports heavy and big set-ups, such as the flow reactor, is installed. The distance between the sample mounted on the diffractometer and the X-ray generator is 44 m, so that the transverse coherence length ξ_T at $\lambda = 1$ Å is estimated to $34\ (H) \times 22\ (V)\ \mu m^2$.

The sample was mounted horizontally in the center of rotation of the diffractometer with the help of a hexapod (*Symmetrie*) that allows translations in a range of ± 10 mm in the x, y and z directions with a resolution of $0.5\ \mu m$. Sample rotations are called θ and μ while γ and δ place the 2D MAXIPIX detector[157] at the *in-plane* and *out-of-plane* scattering angles respectively. An equivalent χ rotation can be obtained by rotating the hexapod, in a maximal range of $\pm 10^\circ$ with a resolution of 0.001°. The schema of the experimental set-up and rotation angles can be seen in Figure 4.17.

For the presented experiment the ultra-high vacuum (UHV) flow reactor developed for *in situ* catalysis studies at ID03 was mounted on the hexapod as shown in Fig. 4.17. The chamber consists of two separated parts allowing to work either in UHV conditions or at atmospheric (or close to atmospheric) pressure regime as required for catalysis. In this second regime, the sample is isolated from the UHV part and gas can flow in the reactor volume defined by the Be dome. Technical details of the chamber can be found in[212]. The sample was mounted directly onto the heater, held with Boron Nitride paste. The temperature of the sample can be measured and monitored thanks to a thermocouple of type C (thus a Tungsten/Rhenium thermocouple to avoid that the Pt contained in regular thermocouples reacts with the CO). A schematic view of the sample holder is shown in Figure 4.18. The gas entry line is connected to four mass-flow controllers to tune the gas composition in the reactor. The whole gas system can be remote controlled, so that changing gas composition during X-ray data acquisition is possible. During the experiment reported here, only three of the mass-flow controllers were used: $i.e.$, CO and O_2 for CO oxydation and Ar as inert gas to keep constant the total pressure and flow inside the reactor. The total pressure in the reactor was kept to 200 mbar when opening the gap between the two reactor chambers.

A Si(111) monochromator was used to select an incident 12.4 keV ($\sim$1 Å) X-ray beam. A schematic view of the set-up and the diffraction geometry is shown in Figure 4.19. The coherent part of the beam was selected by closing the slits to $30\ (H) \times 100\ (V)\ \mu m^2$ and the coherent beam was focused using Kirkpatrick-Baez (KB) mirrors that yield a minimum focus spot of $5 \times 5\ \mu m^2$ on the sample. The detector was placed at 1.14 m from the sample and moved to the **002** Pt Bragg angle ($2\theta_{Bragg} = 29.7^\circ$). The large beam is used to illuminate the sample in such a way that only the NPs oriented in the (002) direction are detected. As the particles are randomly oriented on the glassy carbon substrate and the density of particles over the sample is not very high, the so-called Debye-Scherrer ring consists of individual intensity distributions coming from single

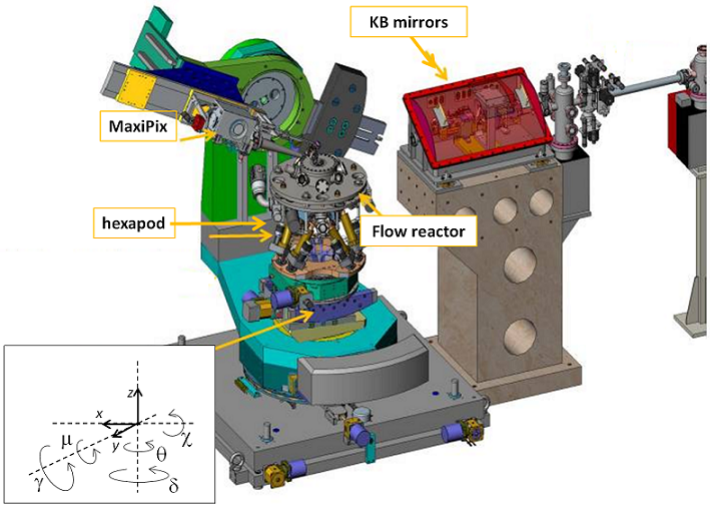

Figure 4.17: Set-up at ID03. The flow reactor is mounted on a hexapod that allows positioning the sample in the center of rotation of the 4+2 diffractometer. KB mirrors are used to focus the incident X-ray beam (coming from right to left in the $x-$direction).

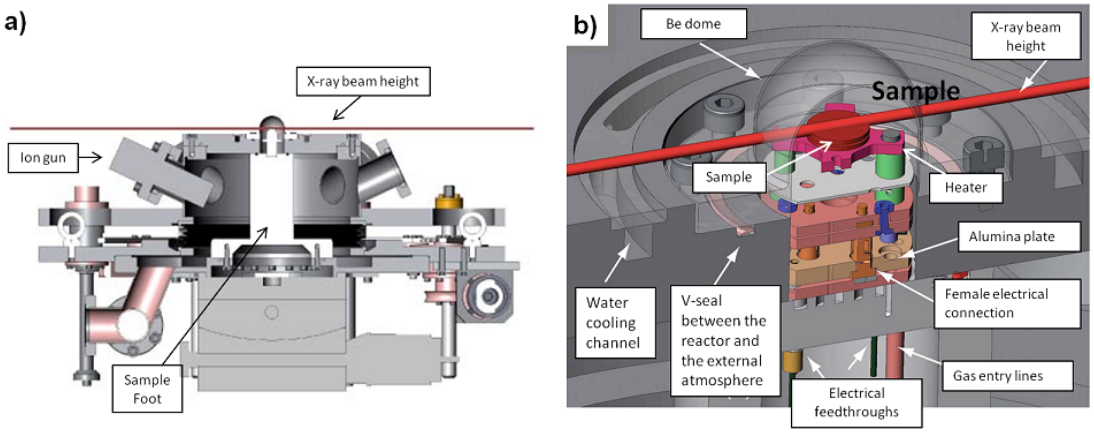

Figure 4.18: Schematic overview of the flow reactor (a) and the implemented sample holder (b) in reaction conditions, adapted from[212]. The sample (in red) is held on the heater and completely isolated from the UHV part when the sample foot is compressed. The water channel cools the reactor walls to prevent reactant gases from reacting on and/or with the reactor walls at high temperatures.

particles that can be afterwards isolated and measured by rotating the sample in the surface plane.

The measured 2D diffraction patterns for two different THH particles in the initial state, *i.e.* at room temperature (RT) and under inert atmosphere are shown in the first row of Figure 4.20 (labelled a) and b)). The detector distance allows to achieve a resolution in reciprocal space of $\delta q = 3 \cdot 10^{-4}$ Å^{-1}. For both particles fringes are visible only in some directions. The line profiles of the modulated streaks allow to calculate the size of the crystals in the given directions, which values are in the range of 75 to 150 nm. Therefore, measuring in these conditions the minimum sampling rate of 2 pixels per fringe cannot be achieved for larger crystals and phase retrieval

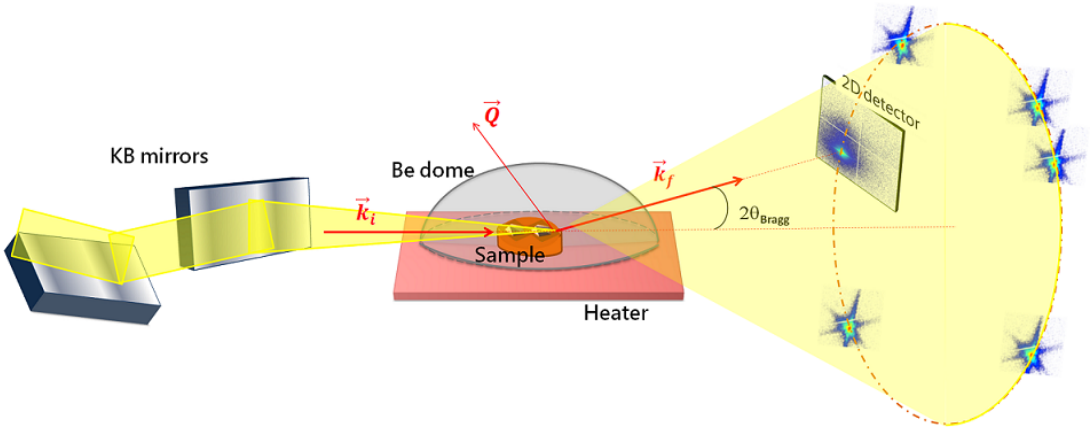

Figure 4.19: The KB focused X-ray beam illuminates the sample surface. The ensemble of particles diffracting in the **002** direction yields to a 3D cone of radius $2\theta_{Bragg}$ that is intersected by the 2D detector. Thus, the $2\theta_{Bragg}$ angle is defined by the position of the detector, $i.e.$, single particles can be selected by adjusting γ and δ to explore the ring.

cannot be done on the recorded data (the MAXIPIX being already in the limit of the detector arm of the diffractometer). Hence hereafter I limit the study of the THH particles in catalysis conditions to a structural study, focusing on the evolution of the shape of the two particles during the reaction.

Let us first study the particle shown in Figure 4.20 a). In this image the sum of the raw data during a rocking curve of 300 points with a counting time of 1 s around the particle **002** Bragg peak is shown, the particle staying in inert conditions and at RT. A second set of data under catalytic CO oxidation reaction conditions of the same particle is shown in Figure 4.20 c). The introduction of reacting gases in the chamber is followed by *in situ* mass spectrometry; the complete 3D reciprocal map was measured under constant partial flows of 8 ml/min of CO, 4 ml/min of O_2 and 35 ml/min of Ar. Data were recorded with the detector placed further with respect to the measurement at the initial state (Fig. 4.20 a)) - in the limit of the detector arm of the diffractometer, which explains the larger size of the particle in reciprocal space ($i.e.$ the increased size of the region of interest (ROI) of the detector). The increased intensity along the streaks is due to a larger number of 2D recorded images during the scan around the same Bragg reflection.

The CO/O_2 flow was kept constant in the mentioned stoichiometric mixture (partial pressure ratio $P_{CO}/P_{O_2} = 2$) for 2 hours. The gas flow composition in the reactor during 2 hours is shown in Figure 4.21. The CO_2 flow graph stays constant, whereas O_2 flow shows a progressive increase during the first 10 minutes before becoming constant at the set value. This would mean that O_2 is adsorbed on the surface of the Pt particles but due to the low temperature - which decreases the efficiency of the catalyts -, there is no consumption of CO, hence no conversion in CO_2.

Even if it is known that low temperature decreases the efficiency of the catalysts and there is no conversion of CO in CO_2 on the residual gas analyser (RGA), the structure of the measured Pt nanoparticle might have changed between the recorded reciprocal space maps shown in Fig. 4.20 a) and c) because of the presence of gas in the chamber. To check any facet change induced by the interaction with gases, the stereographic projection method explained in Section 4.2 was used and results are shown in Figure 4.22. Broad peaks coming from the rods in reciprocal space can be identified in both figures but indexing the directions is challenging because of the multiple possible orientations ($i.e.$, rotations around the axis defining the equator plane),

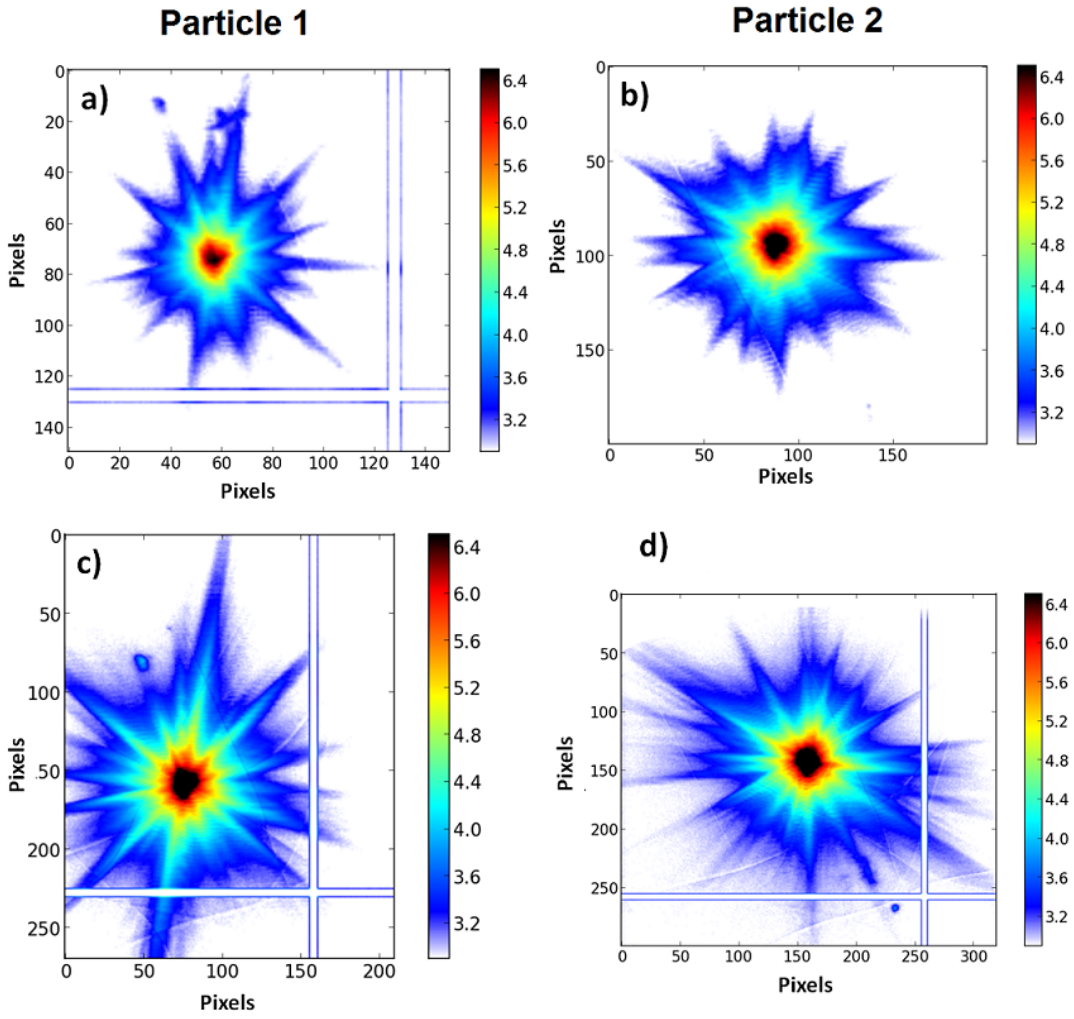

Figure 4.20: Sum of the measured intensity of two different single particles at RT in the initial state (a) and (b), and after introducing CO and O_2 in the reactor chamber at RT (c) and (d). Measurements of particle 1 in a) and c) were taken at different detector distances: a) at 0.95 m and c) at 1.14 m. Only a selected region of the detector is shown. The non-zero intensity lines are due to the junction of the four chips of the MAXIPIX.

without any evident 4 fold symmetry due to the diffraction experimental geometry. However, a simple indexation of the peaks in polar coordinates can be done on both figures, to compare the direction of the streaks of the particle in both states. It can be observed that most peaks are at the same position (taking the center of the peaks as reference) while others have shifted. The last ones have been numbered and their polar coordinates are given in Table 4.2. Shifts in ϕ angle evidence facet changes induced by the presence of gas mixture between both measurements that could be translated in changes of the catalytic activity of the particles.

After the gas exposure, CO and O_2 flows were stopped and rocking curves were performed on the same particle during about 6 hours. Morphology changes are not visible in the recorded diffraction patterns so that reversibility towards the initial state is not observed; the positions

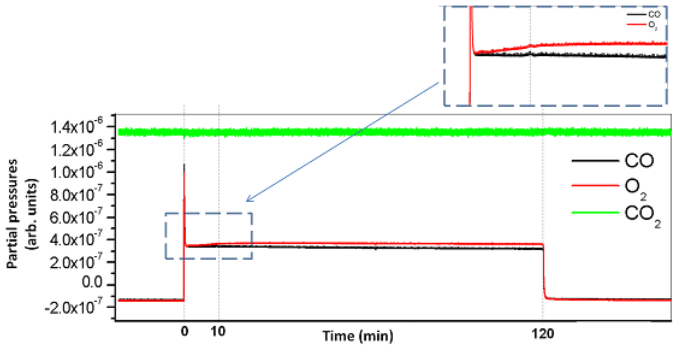

Figure 4.21: Partial pressures of CO, O_2 and CO_2 as measured by the mass spectrometer while measuring the first particle, as a function of time. The sample is measured at RT. Dashed vertical lines evidence the opening and closing of the valves. An adsorption of O_2 can be observed in the first 10 minutes, as shown in the zoom, before becoming constant. The arrows point small oscillations due to gas composition changes.

Peak number	Under inert atmosphere (ψ, ϕ)	Under stoichiometric mixture (ψ, ϕ)
1	$(54.1, 40.1°)$	$(42.7, 45°)$
2	$(58.9, 16.3°)$	$(47.7, 14.3°)$
3	$(66.0, 256.5°)$	$(61.4, 315.0°)$
4	$(63.9, 320°)$	$(64.9, 266.5°)$

Table 4.2: Polar coordinates of the labeled peaks in Fig. 4.22 before and after introduction of gas in the reactor.

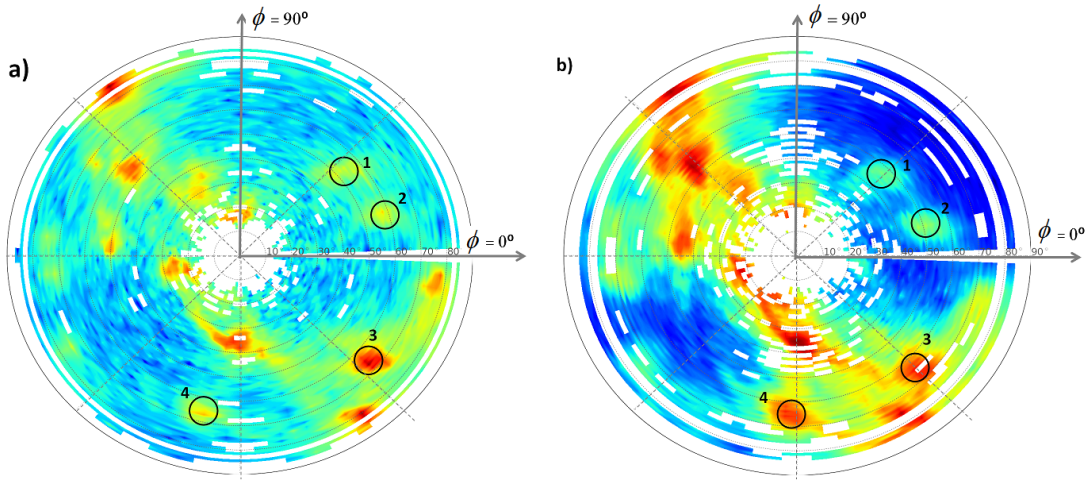

Figure 4.22: Stereographic projection of the 3D Bragg peak of particle 1 in the initial state (a), and under high activity conditions (b). Labeled peaks have shifted, while other remains in the same position after reaction. For clarity in the peaks indexation, circles at $\psi = 10°$ intervals and dashed lines at $\phi = 0°, 90°, 270°$ and $360°$ have been drawn.

of the poles on the stereographic projections of the recorded 3D Bragg peaks stay on the same position.

The oxidation of metallic catalysts under CO/O_2 exposure has been observed on Pd catalysts[213] in similar conditions. However THH Pt NPs are stable during oxygen adsorption and even if an oxide layer is formed on the Pt surface, the ordered high index surfaces are in principle preserved[72]. Furthermore, Han *et al.*[214] found through Density Functional Calculations that Pt NPs with low coordinated surface atoms (such as the ones from {210} facets considered here) significantly increases the adsorption energy of oxygen, hence the higher catalytic activity exhibited by THH NPs would be justified by the faster adsorption of oxygen. However, temperature might not be high enough to activate the reaction - Pt-based catalysts require about 170° C. Moreover, THH NPs may undergo oxidation at different conditions as compared to bulk or other Pt surfaces, $i.e.$, studies as a function of pressure and temperature must be done. Determining the temperature at which the CO conversion takes place is the next step of this study.

Therefore tracking the second particle (Figure 4.20 b)) during oxidation reaction at different temperatures under fixed pressure (200 mbar) is the second part of the study. In Fig. 4.20 d), this second particle after exposure to CO and O_2 at room temperature is shown. After removing gas while measuring the previous particle, the sample was exposed again to the same $P_{CO}/P_{O_2} = 2$ mixture of carbon monoxide and oxygen. Partial pressures were monitored by the mass spectrometer, as shown in Figure 4.23. After filling the chamber with the reactants, still at room temperature, the oxygen slowly increases, as previously observed, until it starts to behave similarly to CO. To successfully measure the particle while increasing temperature, an important factor to take into account is the thermal expansion of the glassy carbon substrate (thermal expansion coefficient $\alpha \sim 3.2 \times 10^{-6}$ K^{-1}). The thermal expansion coefficient increases linearly in the explored temperature range (up to 650°C), but the low stability of the particle makes mandatory to realign the particle at each small temperature step, and wait until the temperature stabilises before measuring the particle at every given temperature. The particle was observed to rotate when temperature changes. Reciprocal space maps around the particle at temperature steps of about 50° C were carefully recorded, without evident induced changes on the diffraction patterns. None of the stereographic projections are conclusive since small changes can be related to particle rotations due to temperature effects.

By heating the sample up to 600° C a decreasing amount of CO and O_2 was observed, together with a refacetting of the particle. Note that the length of the electrode was about 1 cm, so that the temperature measured by the thermocouple is not the sample's one. Figure 4.24 shows the raw data at room and high temperatures under gas exposure. The difference map (Fig. 4.24 c)) displays the intensity difference $\Delta I = \frac{I_{HT} - I_0}{I_0}$ (where I_{HT} is the recorded 3D intensity at high temperature under gas and I_0, the measured intensity at room temperature). In this representation the increase of intensity arises from the new directions of the streaks, which should be induced by the facet changes. Facets changed are pointed by red arrows in Fig. 4.24 a).

Increasing even more the temperature makes the particle rotate so fast that measurements comparable with previous ones (in terms of counting time) could not be performed, despite changes were observed. Figure 4.25 a) shows the recorded intensity for a rocking scan of 20 points with a counting time of 0.5 seconds, at 600° C. An asymmetry as well as some missing facets can be observed. As this might be attributed to the lower scattered intensity, a scan of 600 points (1 s/point), on the final state of the nanoparticle is shown in 4.25 b) for comparison. This last reciprocal map was recorded after cooling down to room temperature and once gas was removed. The peak consists of few streaks, meaning that the particle became more rounded. Nevertheless, some streaks can still be recognised and have slightly changed in direction.

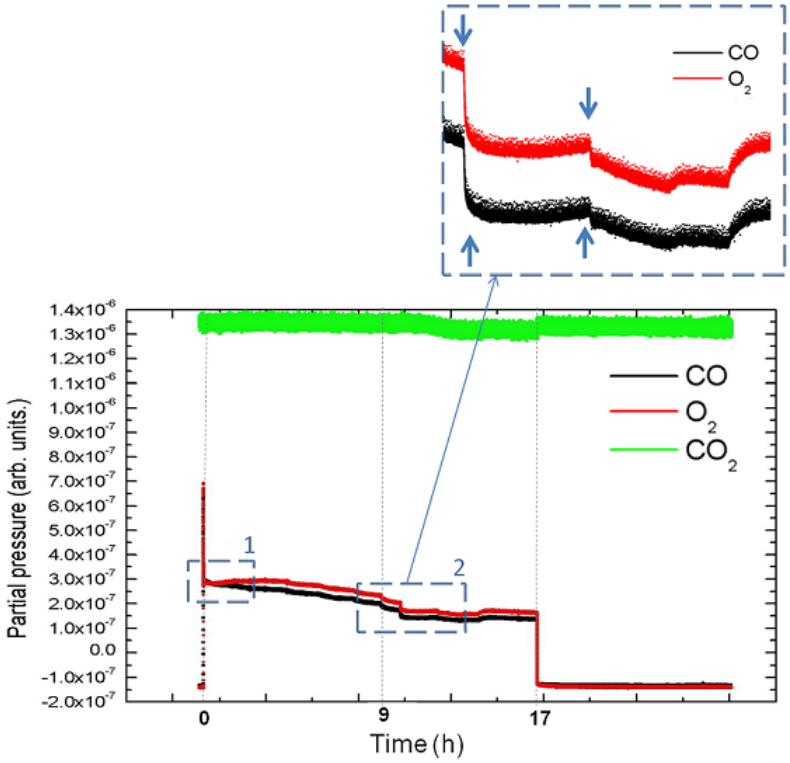

Figure 4.23: Residual gas analyser while tracking the second particle during the increase of temperature and under CO/O_2 exposure. After opening the valves, a first regime (*square 1*) where oxygen is adsorbed is observed. In the inset (*square 2*), simultaneous consumption of CO and O_2 is observed. Oscillations in between are related to the background and temperature changes.

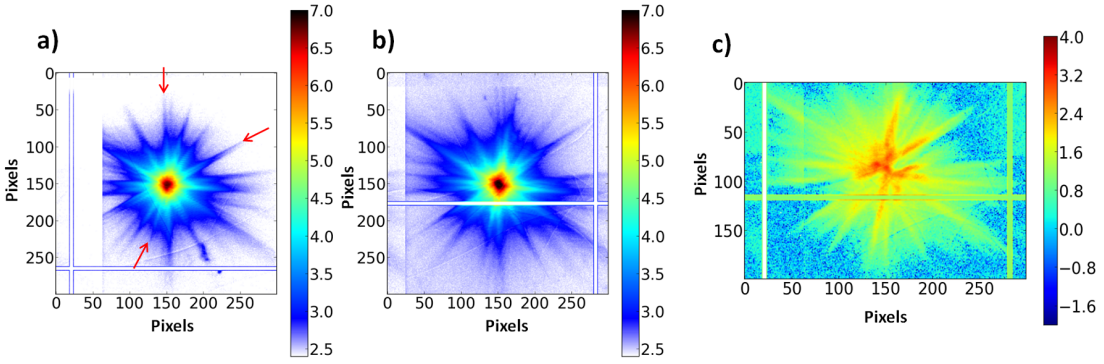

Figure 4.24: Experimental data recorded around the **002** Pt Bragg reflection of the second particle at Room Temperature (a) and at 600° C (b) under gas exposure. Bragg peaks have been centered on the ROI. The difference map in (c) shows an increase of intensity of the streaks whose directions have changed, corresponding to the rods pointed by arrows in (a).

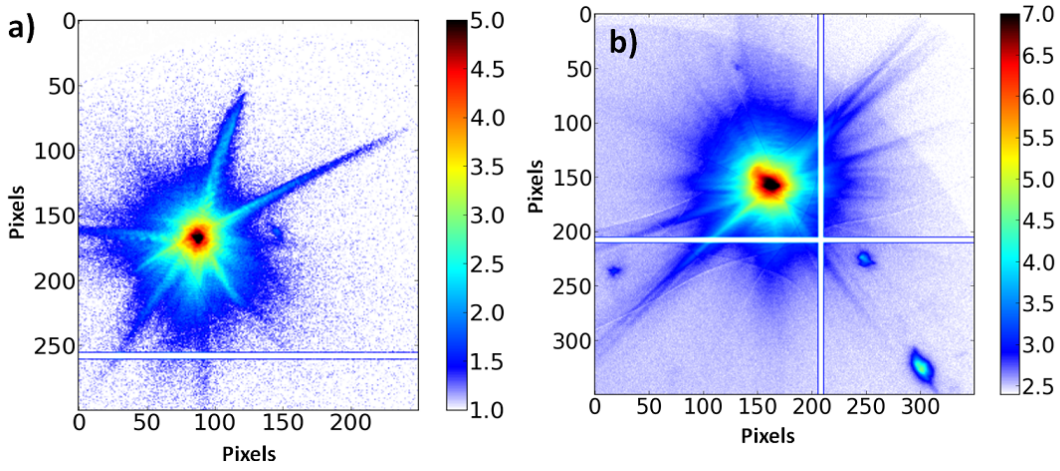

Figure 4.25: Experimental data recorded around the **002** Pt Bragg reflection of the second particle at Room Temperature (a) and at 600° C (b) under gas exposure. Bragg peaks have been centered on the ROI. The difference map in (c) shows an increase of intensity of the streaks whose directions have changed, corresponding to the rods pointed by arrows in (a).

4.5 *In situ* study at ID01 in controlled gas-phase environment

Real catalyst particle sizes are around few nanometers and CO oxidation is obtained in presence of a large amount of NPs. Moreover size cannot be decoupled from morphology: how particle size affects adsorption of O_2 and CO strongly depends on the position in which the adsorption takes place in the catalyst surface[214]. Besides, particles exhibit a certain shape and size distribution, that can yield to different catalytic activity. Hereafter I present an experiment performed on smaller THH particles (size around 100 nm).

The experimental set-up and the experimental strategy to localise and measure isolated NPs have been presented in Section 4.3. The working energy being this time of 8 keV, the nanoreactor described in Chapter 2 was installed on the hexapod, with three gas inlets for CO, O_2 and He bottles. A constant He flowed in the reactor during the whole experiment (20 ml/min), unless specified. The beam size was estimated to $170\ (V) \times 465\ (H)\ nm^2$. Stability turned out to be a big issue during this experiment, small particles rotated under the nanofocused beam, maybe due to the smaller surface in contact with the glassy carbon substrate. Rocking curves had to be performed with very short counting times, between 0.5 and 1 seconds per point. This short exposure of the particles does not allow to get well resolved fringes and the recorded 3D reciprocal space maps often present artifacts due to particle movements. The poorly resolved fringes make impossible the phase retrieval procedure.

A first particle *Particle A* in its initial state in inert atmosphere was measured at room temperature under a constant flow of pure CO of 5 ml/min. Recorded reciprocal space maps (RSMs) around the **002** Bragg reflection can be seen as a function of time in Figure 4.26. The intensity profile along the vertical streak yields to a size of about 65 nm; significative size changes after gas exposure are not observed. In the RSMs, 12 streaks are observed, proving the THH shape of the illuminated particle. Some streaks seem to appear and disappear in consecutive scans but these changes are rather attributed to experiment dynamics so that morphology changes cannot be determined without ambiguity. However, these 3D data sets give enough information to retrieve *out-of-plane* strain information in the particle during its exposure to CO.

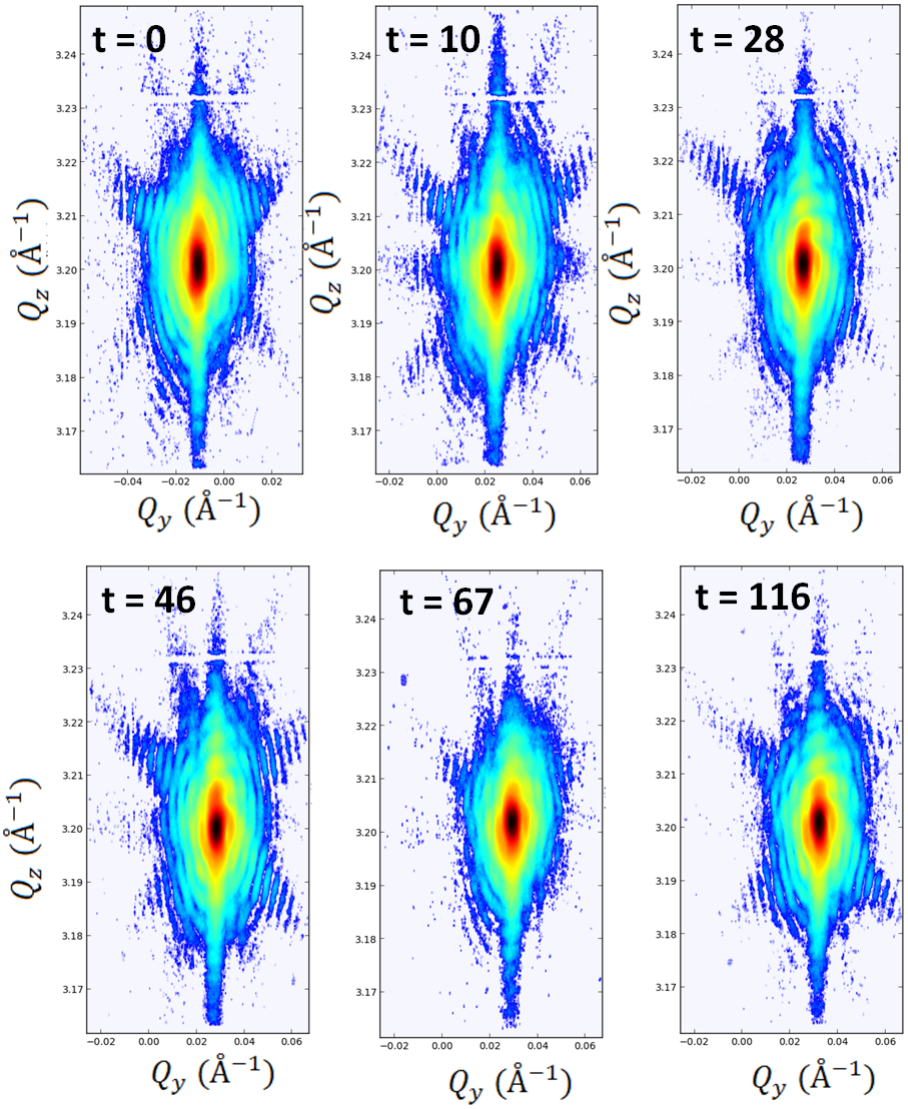

Figure 4.26: Rocking curves around the **002** Pt Bragg reflection of *Particle A* as function of time during CO injection. Time is in minutes.

Strain, ϵ, is defined as the variation of the lattice parameter a with respect to a reference value a_{ref} as follows:

$$\epsilon\ (\%) = \frac{a - a_{ref}}{a_{ref}} \times 100 \tag{4.7}$$

where the strain is expressed in percent. It can be equivalently defined in terms of the distance between lattice planes d:

$$\epsilon(\%) = \frac{d - d_{ref}}{d_{ref}} \times 100 \tag{4.8}$$

where $d = \frac{2\pi}{|\vec{Q}|}$ and $|\vec{Q}| = \sqrt{Q_x^2 + Q_y^2 + Q_z^2}$. Therefore, homogeneous strain in the crystal

results in a peak shift in reciprocal space, whose origin can be simply experimentally defined by the position of the direct beam in the detector. In this way, the fit of the 3D Bragg positions as a function of time determines the *out-of-plane* strain ϵ_{002} induced on *particle A* by the presence of CO in the reactor chamber. Gaussian fits were performed on the shown intensity around the Bragg peaks (Fig. 4.26) and on additional alignment scans with shorter exposure times. Previous conversion of pixels into $Q-$coordinates was done using the *xrayutilites* package of Python[209]. Applying Equation 4.8 with the lattice parameter of the particle measured just before injection of CO in the reactor taken as reference value, one gets the strain evolution shown in Figure 4.27. Strain oscillates as function of time between a maximum tensile strain of 0.01 % and a minimum compression of -0.06 %. The CO flow was stopped after about 2 hours. A significant compression, of about -0.05 %, takes place after 40 minutes exposure, and again after 80 minutes, perhaps exhibiting a periodic behavior.

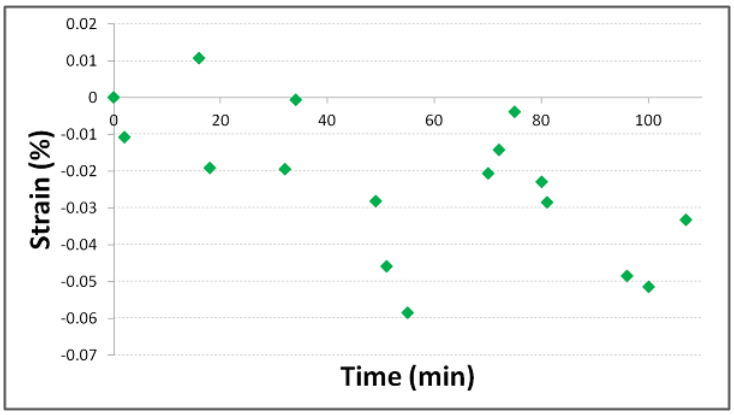

Figure 4.27: Evolution of the *out-of-plane* strain as a function of time of Particle A in CO atmosphere. Reference value ($\epsilon = 0$) is the measured lattice parameter before injection of CO in the chamber. The error bars estimated from the thermal expansion of Pt are smaller than the corresponding symbols.

A second particle, *Particle B*, was investigated under CO and O_2. The sample growth conditions are the same as the previous ones, but the sample was annealed up to 100$^{\circ}C$ in order to get the particles attached to the glassy carbon substrate and improve the stability under the X-ray beam. The annealing process preserves the THH shape, as observed by SEM measurements and diffraction patterns did not show significant differences with respect to unannealed samples.
Particle B was followed from RT to 200 $^{\circ}C$, while recording short 3D RSMs around the **002** Bragg reflection. Once the temperature got stable at 200 $^{\circ}C$ (temperature read by the thermocouple), the following partial flows were set successively to:

1. $f_{O_2} = 5\ ml/min$
2. $f_{CO} = 2.5\ ml/min, f_{O_2} = 2.5\ ml/min$
3. $f_{CO} = 4\ ml/min, f_{O_2} = 1\ ml/min$

Fitting the Bragg peak and applying Equation 4.7 yields the strain evolution shown in Figure 4.28, where the different regimes enumerated here above are separated by dashed lines. As these measurements were performed at high temperature, both thermal strain ($\epsilon_{Thermal}$) of Pt and substrate must be taken into account. In a first approximation, as response to the temperature change ΔT, both materials are expected to linearly expand, yielding a thermal strain that depends on the linear coefficient of thermal expansion (α_L) as $\epsilon_{Thermal} = \alpha_L \Delta T$. The maximum difference in temperature between the recorded strains is $\Delta T = 4^{\circ}C$ (see Fig. 4.28). Taking the

tabulated values $\alpha_{GC} \sim 3.2 \times 10^{-6}\ K^{-1}$ and $\alpha_{Pt} \sim 8.8 \times 10^{-6}\ K^{-1}$, a first estimation of the thermal strain yields to $\epsilon_{Thermal_{Pt}} = 0.00352\%$ in the case of Pt, and to $\epsilon_{Thermal_{GC}} = 0.0013\%$. Hence, larger shifts of the peak with respect to the reference value (first measurement at $200°\ C$ before gas injection) are attributed to variations of lattice parameter in the particle. Exposure to O_2 induces a tensile expansion in the nanoparticle, reaching a 0.13 % strain after 3 hours exposure. In a second step, CO was introduced in the reactor. Once temperature is stable, small changes in the lattice parameter are observed, oscillating in a strain range of 0.007 %. When the CO/O_2 mixture was changed to higher reactivity conditions, a significative compression takes place and after 20 minutes, strain increases again. The whole cycle lasts 30 minutes - before being stopped, and the lattice expansion took place after 20 minutes. CO atmosphere seems to be responsible of the oscillatory behaviour of the strain evolution in the particle, perhaps arising from morphology changes: facetted Pt nanoparticles shape in CO/O_2 mixture has been recently reported to show an oscillatory behaviour, evolving from facetted to rounded shapes according to oxidation or reduction reversible cycles that take place every 10-20 seconds[76]. Recording the 3D intensity takes longer and such accurate measurements cannot be performed, but this strain evolution may be related to morphology changes, even if the samples measured here yield different behaviours because of the particular THH shape. Note that it is supposed here that the particles are not attached to the substrate, so that the Poisson effect is not taken into account, which would affect the apparent dilation coefficient.

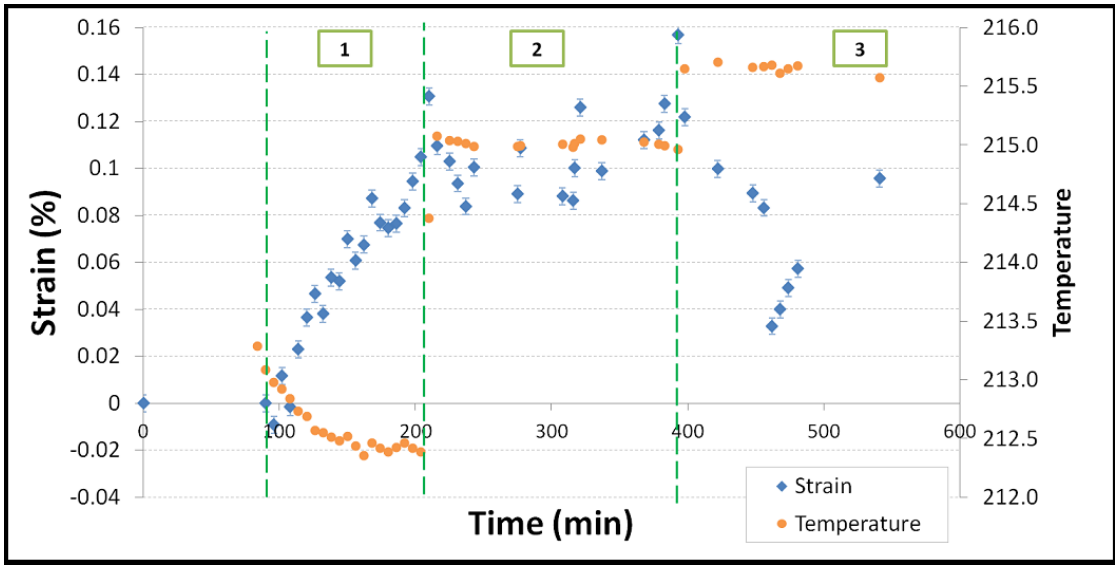

Figure 4.28: *Out-of-plane* strain evolution as a function of time of Particle B at 200°C in three different regimes: 1) in O_2 atmosphere; 2) in CO and O_2 and 3) in a different mixture of CO and O_2. Error bars correspond to calculated Pt thermal strain. Temperature changes are observed simultaneously with gas injection.

After the experiment, SEM measurements were performed on the measured samples (see Fig. 4.29). Images show that some particles, probably the ones that have been subjected to long X-ray exposures, have rotated: the surface initially in contact with the substrate is visible, as well as the "hole" retrieved using the phase retrieval algorithms (Sec. 4.3). These measurements prove the instability of the particles under the beam and ask for solutions regarding upcoming experiments.

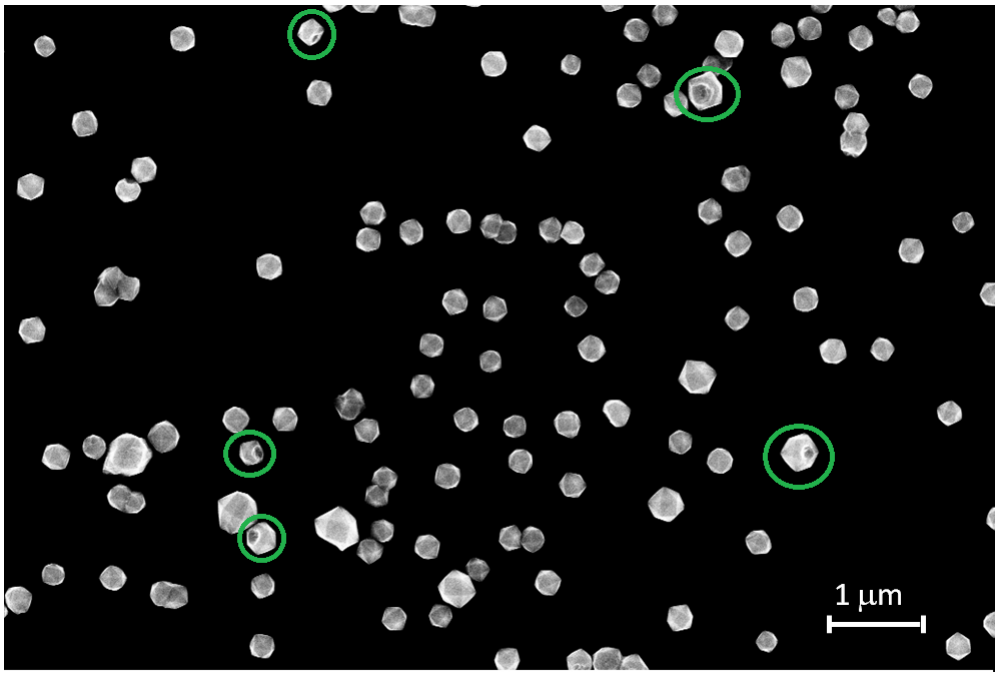

Figure 4.29: SEM image of Pt nanoparticles after CDI experiments at ID01 beamline. The hole of the face initially in contact with the substrate is visible, due to the rotation of the particles under the X-ray beam (circled in green).

4.6 Conclusions

Finite Element Modelling were used to simulate strain in a single THH NP and simulate its coherent diffraction pattern. This model is not adapted to the real system since particles are not fixed to the substrate and they were seen not to be stable enough during last experiments. Nevertheless, experimental results from phase retrieval seems to be in agreement with simulations: particles are significantly strained at the edges between flat facets (ϵ_{zz} component). Such a strain pattern is similar to the one observed by Watari *et al.*[98] in Au NPs with thiol adsorption.

Nanoparticles-based catalysts strongly depend on the shape of the particles, so that characterisation of such nanostructures requires new approaches. Two different methods to characterise faceted objects were presented here taking THH NPs as model: the first one consists in measuring the angle between the streaks of the Bragg peak, and the second one, in projecting the directions of the streaks onto a reference plane. The use of diffraction patterns significantly improves the precision and rapidity compared to other geometrical methods based on angles measurement such as SEM or TEM, that require several projections. Then the real shape of the particle was checked by phase retrieval methods, while retrieving the phase of the object, thus the strain.

Operando and *in situ* experiments were afterwards performed in catalytic conditions. At the ID03 beamline, shape changes were observed in CO oxidation conditions. The strain evolution of a single particle in different gas atmospheres was calculated from data recorded during a later experiment at the ID01 beamline. The oscillatory strain may be related to morphology changes, due themselves to oxidation or reduction states during the reaction. Stability of THH particles under nanofocused beams constitutes an important issue for CDI experiments, as one would like to decrease the size of particles to approach real catalytic processes. However, CDI remains a powerful tool to study single particles during chemical reactions, as it allows to access simultaneously density and 3D strain fields. Besides, understanding how shape and strain

changes of single particles affect the activation or deactivation of the reaction, is the first step to understand reaction of ensembles. The experiments presented in this chapter, together with the very recent results from Ulvestad and co-workers[215], prove the feasibility of CDI experiments in catalytic envrionments. Preparation of the samples by transfer of the particles to different supports after growth, such as graphene or Si_3N_4 membranes, can be the key for next experiments; however special care must be taken when choosing the support, since the choice may alter the catalytic performances of the particles[75]. Also improvements should be performed in the ID01 mini-reactor. Reducing the volume under the Be dome will allow, for instance, a faster reaction in the proximity of the sample surface. Developing automated systems will ensure faster and higher resolution methods and kinetic artifacts could be avoided.

Managing the shape of the particles leads to surface catalytic activity control, $i.e.$ to the possibility of increasing the chemical reactivity while decreasing the production cost. Apart from tuning the shape of particles, composition changes have been proposed as an alternative to increase the catalytic activity of metallic particles (see Chapter 1). A preliminary study on bimetallic Cu-Pt THH NPs was performed during this PhD work. The particles were measured at ID01 beamline and behaviors similar to the ones presented here were observed. New measurements on more stable particles are required and need to be reviewed, as alloying the particles can significantly reduce the production cost with respect to pure Pt catalysts.

Conclusions and outlook

The main goal of the work presented in this manuscript was the experimental characterisation of the lattice displacement and strain of single nanostructures by coherent X-ray diffraction imaging in Bragg condition under thermal treatment and in catalytic conditions. The technique has been applied to the particular case of core/shell nanowires and single Pt nanoparticles. A first approach was to use local X-ray diffraction with a nano-focused beam to characterise the strain of the sample ($e.g.$ single nanowires), but to achieve this goal special attention must be payed to the sample characteristics (such as the density of wires or particles over the sample) and the experimental geometry (the X-ray wings of the beam in high-angle diffraction may rise wrong conclusions about the recorded scattered signal). Hence, special care must be taken to prepare samples for coherent diffraction imaging experiments, which is a suitable technique to probe the morphology but also strain inhomogeneities within the structures. Several strategies in order to isolate nanostructures to perform CDI experiments have been demonstrated: scratching the structures from the original growth substrate (or using an ultrasonic bath to transfer them to a grid), manipulating the structures with a SEM/FIB, or taking advantage of the random orientation of the nano-objects in the case of a non epitaxial growth.
The experimental results have been supported by analytical elastic and finite element analysis of the studied systems, as well as calculations of the diffraction patterns of the modeled objects.

The motivation to study core/shell Ge/Si NWs was their multiple applications as components of new devices. However, the stability of the interface between the core and the shell and how it evolves under thermal treatment are points that have to be considered. In particular, the intermixing problem at the nanoscale raises fundamental questions. Preliminary studies at room temperature were performed by means of CDI and TEM, which allowed to determine the intrinsic strain of the NWs. Coherent diffraction experiments were carried out to investigate the *out-of-plane* strain of the NWs (*i.e.* along the length direction): the Ge core of the NWs was found completely relaxed whereas the Si shell presented an axial strain dependent on the Ge core diameter (the strain being measured with respect to Ge and Si bulk respectively). HRTEM was afterwards used to measure the radial strain, which resulted to be zero for both, core and shell.
CDI was then used to determine the strain field within the Ge core, what is possible by inversion of the recorded coherent diffraction patterns around four different reflections of the same NW. The retrieved phase revealed the possible presence of defects in the NW, whose origin could be related to the sample preparation.

The most interesting result rises from the annealing experiments. It would seem that the Ge atoms from the core and the Si ones from the shell do not interdiffuse; when the temperature is high enough, the Ge-core melts yielding Si(C) nanotubes, as it was observed through environmental TEM. On the other hand, *in situ* CDI experiments showed that the NW bents after annealing, the lattice tilt being as high as 2° over a length of 4 μm.
The remarkable stability of Si/Ge NWs at high temperature and the absence of interdiffusion may be related to the presence of a passivation layer at the interface between the core and the shell, since the EDX profile of the NWs at high temperature proved the abscence of carbon in the Si

shell, and HCl has been excluded as a responsible of the interdiffusion inhibition through *ex situ* CDI experiments. Further investigations are necessary in order to understand the mechanisms yielding the strain relaxation and this lack of interdiffusion. Indeed, an exhaustive characterisation of the core/shell interface must be performed: misfit dislocations and composition should be the subject of future experiments. If strain plays a key role in the intermixing as it is suspected, Ge/SiGe core/shell nanowires with different chemical compositions of the shell - and different levels of epitaxy - may be worth to investigate. Moreover, strain is present in most SiGe systems of technological interest.

Next steps of this research project include as well the analysis of pure-Ge nanowires to investigate the actual effect of the Si-shell. Ge NWs are prone to oxidation and then more difficult to measure compared to Ge-Si core-shell NWs.
Also a different method to isolate the NWs may be considered, or refinements in the phase retrieval treatment, as parasitic signals in the diffraction patterns decrease the spatial resolution of the reconstructions and make difficult the choice of the support in the algorithms.

The second experimental part of the manuscript deals with Pt nanoparticles and their behavior under chemical reactions. The study here reported looked for answers concerning faceting and strain changes in gas atmosphere, the goal being to determine the relationship between these properties. Hence, the first step in this research involves the complete characterisation of the catalysts under ambient conditions, what was performed through coherent diffraction imaging. Also different methods to determine the crystallographic facets were developed during this work, that were shown to be useful to identify the morphological changes of the particles after reaction using the *in situ* recorded reciprocal space maps.
Preliminary *operando* experiments were performed on model THH particles, to study their behavior during the CO oxidation reaction. Phase retrieval allowed to determine the strain distribution within a single particle: the core and the edges of the particle exhibit different strain states. The orientation of the crystallographic facets forming the crystal was also determined at room temperature, which resulted to be $\{210\}$ facets. The importance of this result lays on the enhanced chemical reactivity that high-index facets exhibit. Faceting changes during chemical reaction were observed, despite facets indexation was not possible.
The big issue of *operando* experiments was the stability of the nanoparticles under the focused beam. It was also observed that the average strain of the particles changes under reaction. CDI is expected to resolve the inhomogeneous phase also within the particles, which would affect (together with the morphology) the activity of the individual particles. The shape changes deserve further investigations, with efforts in the improvement of the experimental set-ups and towards the decrease of the size of the particles to approach the real catalyst process usually employed in industry.

The predicted increase of flux after the ESRF upgrade (scheduled in January 2019 for 18 months) is expected to make the task of measuring in catalytic conditions a bit easier by the increase of coherent flux, $i.e.$, shorter counting times during the measurements. Indeed, faster 3D acquisitions would allow to study much faster chemical processes.
In this regard it is also suitable to optimise the current phase retrieval algorithms, which often require a large number of iterations and are computationally intensive. Improvements towards analysis during the data acquisition are needed for real imaging during *in situ* experiments.

It could be also useful to take into account the X-ray probe effects in the measurements, as its phase may affect the retrieved one from the object, and this is the case for both systems, *i.e.* catalyst nanoparticles and core/shell NWs. In this regard, ptychography may be applied but the algorithms used in this work still need some improvement (stagnation was observed in the case of experimental data from the SiGe nanowires). In addition, recording 3D data sets suitable for ptychographic reconstructions need high stability, as measurements must be longer. Hence, the technique is less appropriate for *in situ* or *operando* experiments but they could be complementary with a first characterisation of the nanostructures, as the robustness of

ptychography algorithms improve the convergence and would lead to better understanding of defects or/and strain in the initial (*as-growth*) studied objects.

Bibliography

1. Thomas, O., Loubens, A., Gergaud, P., and Labat, S. *Applied Surface Science* **253**(1), 182–187 October (2006).
2. orange book, T. *ESRF Upgrade programme Phase II (2015-2022)*. Technical design study.
3. Einstein, T. L. *arXiv:1501.02213 [cond-mat]* , 215–264 (2015). arXiv: 1501.02213.
4. De Caro, L. and Tapfer, L. *Physical Review B* **48**(4), 2298–2303 July (1993).
5. Thelander, C., Agarwal, P., Brongersma, S., Eymery, J., Feiner, L. F., Forchel, A., Scheffler, M., Riess, W., Ohlsson, B. J., Gösele, U., and Samuelson, L. *Materials Today* **9**(10), 28–35 October (2006).
6. Li, Y., Tan, B., and Wu, Y. *Nano Letters* **8**(1), 265–270 January (2008).
7. Garnett, E. C., Brongersma, M. L., Cui, Y., and McGehee, M. D. *Annual Review of Materials Research* **41**(1), 269–295 (2011).
8. Patolsky, F. and Lieber, C. M. *Materials Today* **8**(4), 20–28 April (2005).
9. Wolfsteller, A., Geyer, N., Nguyen-Duc, T. K., Das Kanungo, P., Zakharov, N. D., Reiche, M., Erfurth, W., Blumtritt, H., Kalem, S., Werner, P., and Gösele, U. *Thin Solid Films* **518**(9), 2555–2561 February (2010).
10. Xia, Y., Yang, P., Sun, Y., Wu, Y., Mayers, B., Gates, B., Yin, Y., Kim, F., and Yan, H. *Advanced Materials* **15**(5), 353–389 March (2003).
11. Kodambaka, S., Tersoff, J., Reuter, M. C., and Ross, F. M. *Science* **316**(5825), 729–732 May (2007).
12. Dayeh, S. A. and Picraux, S. T. *Nano Letters* **10**(10), 4032–4039 October (2010).
13. Schmidt, V., Wittemann, J. V., and Gosele, U. *Chemical reviews* **110**(1), 361–388 (2010).
14. Lauhon, L. J., Gudiksen, M. S., Wang, D., and Lieber, C. M. *Nature* **420**(6911), 57–61 November (2002).
15. Amato, M., Palummo, M., Rurali, R., and Ossicini, S. *Chemical Reviews* **114**(2), 1371–1412 January (2014).
16. Hochbaum, A. I. and Yang, P. *Chemical Reviews* **110**(1), 527–546 January (2010).
17. Zhang, G., Tateno, K., Gotoh, H., and Sogawa, T. *NTT Technical Review* **8**(8) August (2010).
18. Kagimura, R., Nunes, R. W., and Chacham, H. *Physical Review Letters* **98**(2), 026801 January (2007).

19. Goldthorpe, I. A., Marshall, A. F., and McIntyre, P. C. *Nano Letters* **8**(11), 4081–4086 November (2008).

20. Amato, M., Palummo, M., and Ossicini, S. *Physical Review B* **80**(23), 235333 December (2009).

21. Musin, R. N. and Wang, X.-Q. *Physical Review B* **74**(16), 165308 October (2006).

22. Amato, M., Rurali, R., and Ossicini, S. *Journal of Computational Electronics* **11**(3), 272–279 February (2012).

23. Huang, S. and Yang, L. *Applied Physics Letters* **98**(9), 093114 February (2011).

24. Peng, X. and Logan, P. *Applied Physics Letters* **96**(14), 143119 April (2010).

25. Migas, D. B. and Borisenko, V. E. *Physical Review B* **76**(3), 035440 July (2007).

26. Musin, R. N. and Wang, X.-Q. *Physical Review B* **71**(15), 155318 April (2005).

27. Grönqvist, J., Søndergaard, N., Boxberg, F., Guhr, T., Åberg, S., and Xu, H. Q. *Journal of Applied Physics* **106**(5), 053508 September (2009).

28. Ferrand, D. and Cibert, J. *European Physical Journal: Applied Physics* **67**, 30403 August (2014).

29. Raychaudhuri, S. and Yu, E. T. *Journal of Applied Physics* **99**(11), 114308 June (2006).

30. Kavanagh, K. L. *Semiconductor Science and Technology* **25**(2), 024006 (2010).

31. Trammell, T. E., Zhang, X., Li, Y., Chen, L.-Q., and Dickey, E. C. *Journal of Crystal Growth* **310**(12), 3084–3092 June (2008).

32. Liang, Y., Nix, W. D., Griffin, P. B., and Plummer, J. D. *Journal of Applied Physics* **97**(4), 043519 February (2005).

33. Schmidt, V., McIntyre, P. C., and Gösele, U. *Physical Review B* **77**(23), 235302 June (2008).

34. Pan, L., Lew, K.-K., Redwing, J. M., and Dickey, E. C. *Nano Letters* **5**(6), 1081–1085 June (2005).

35. Ertekin, E., Greaney, P. A., Chrzan, D. C., and Sands, T. D. *Journal of Applied Physics* **97**(11), 114325 June (2005).

36. Goldthorpe, Marshall, and McIntyre. *Nano Letters* **9**(11), 3715–3719 (2009).

37. Dillen, D. C., Kim, K., Liu, E.-S., and Tutuc, E. *Nature Nanotechnology* **9**(2), 116–120 February (2014).

38. Fukata, Mitome, Sekiguchi, Bando, Kirkham, Hong, Wang, and Synder. *ACS nano* November (2014).

39. Dayeh, S. A., Tang, W., Boioli, F., Kavanagh, K. L., Zheng, H., Wang, J., Mack, N. H., Swadener, G., Huang, J. Y., Miglio, L., Tu, K.-N., and Picraux, S. T. *Nano Letters* **13**(5), 1869–1876 May (2013).

40. Taraci, J. L., Hÿtch, M. J., Clement, T., Peralta, P., McCartney, M. R., Drucker, J., and Picraux, S. T. *Nanotechnology* **16**(10), 2365–2371 October (2005).

41. Lu, W., Xiang, J., Timko, B. P., Wu, Y., and Lieber, C. M. *Proceedings of the National Academy of Sciences of the United States of America* **102**(29), 10046–10051 July (2005).

42. Dayeh, S. A., Mack, N. H., Huang, J. Y., and Picraux, S. T. *Applied Physics Letters* **99**(2), 023102 July (2011).

43. Silvestri, H. H., Bracht, H., Hansen, J. L., Larsen, A. N., and Haller, E. E. *Semiconductor Science and Technology* **21**(6), 758 (2006).

44. Lide, D. R. *CRC handbook of chemistry and physics*, volume 85. CRC press, (2004).

45. Wen, C.-Y., Reuter, M. C., Bruley, J., Tersoff, J., Kodambaka, S., Stach, E. A., and Ross, F. M. *Science (New York, N.Y.)* **326**(5957), 1247–1250 November (2009).

46. Clark, T. E., Nimmatoori, P., Lew, K.-K., Pan, L., Redwing, J. M., and Dickey, E. C. *Nano Letters* **8**(4), 1246–1252 April (2008).

47. Geaney, H., Mullane, E., Ramasse, Q. M., and Ryan, K. M. *Nano Letters* **13**(4), 1675–1680 April (2013).

48. Perea, D. E., Li, N., Dickerson, R. M., Misra, A., and Picraux, S. T. *Nano Letters* **11**(8), 3117–3122 August (2011).

49. Grützmacher, D. A., Sedgwick, T. O., Powell, A., Tejwani, M., Iyer, S. S., Cotte, J., and Cardone, F. *Applied Physics Letters* **63**(18), 2531–2533 November (1993).

50. Dupré, L., Buttard, D., Leclere, C., Renevier, H., and Gentile, P. *Chemistry of Materials* **24**(23), 4511–4516 December (2012).

51. Allen, J. E., Hemesath, E. R., Perea, D. E., Lensch-Falk, J. L., Li, Z. Y., Yin, F., Gass, M. H., Wang, P., Bleloch, A. L., Palmer, R. E., and Lauhon, L. J. *Nature Nanotechnology* **3**(3), 168–173 March (2008).

52. Holmberg, V. C. *Semiconductor nanowires : from a nanoscale system to a macroscopic material*. Thesis, December (2011).

53. Schorer, R., Friess, E., Eberl, K., and Abstreiter, G. *Physical Review B* **44**(4), 1772–1781 July (1991).

54. Friess, E., Schorer, R., Eberl, K., and Abstreiter, G. *Journal of Vacuum Science & Technology B* **9**(4), 2045–2047 July (1991).

55. Cowern, N. E. B., Zalm, P. C., van der Sluis, P., Gravesteijn, D. J., and de Boer, W. B. *Physical Review Letters* **72**(16), 2585–2588 April (1994).

56. Zaumseil, P., Fischer, G. G., Quick, C., and Misiuk, A. *physica status solidi (a)* **153**(2), 401–408 February (1996).

57. Aubertine, D. B. and McIntyre, P. C. *Journal of Applied Physics* **97**(1), 013531 January (2005).

58. Persson, A. I., Larsson, M. W., Stenström, S., Ohlsson, B. J., Samuelson, L., and Wallenberg, L. R. *Nature Materials* **3**(10), 677–681 October (2004).

59. Tian, B., Zheng, X., Kempa, T. J., Fang, Y., Yu, N., Yu, G., Huang, J., and Lieber, C. M. *Nature* **449**(7164), 885–889 October (2007).

60. Lewis, N. S. *Science (New York, N.Y.)* **315**(5813), 798–801 February (2007).

61. Singh, A. K., Tiwari, J., Yadav, A., Jha, R. K., Singh, A. K., Tiwari, J., Yadav, A., and Jha, R. K. *Journal of Energy, Journal of Energy* **2014, 2014**, e946406 July (2014).

62. Duan, H. L., Weissmüller, J., and Wang, Y. *Journal of the Mechanics and Physics of Solids* **56**(5), 1831–1851 May (2008).

63. Das, S., Moitra, A., Bhattacharya, M., and Dutta, A. *Beilstein Journal of Nanotechnology* **6**, 1970–1977 October (2015).

64. Zhou, T. *Etude in situ par RX synchrotron de nanofils SiGe: croissance, contrainte et courbure*. PhD thesis, December (2015).

65. Roduner, E. *Chemical Society Reviews* **35**(7), 583–592 June (2006).

66. Kamat, P. V. *The Journal of Physical Chemistry B* **106**(32), 7729–7744 August (2002).

67. Xia, Y., Xiong, Y., Lim, B., and Skrabalak, S. E. *Angewandte Chemie International Edition* **48**(1), 60–103 (2009).

68. Stepanov, A. L., Golubev, A. N., Nikitin, S. I., and Osin, Y. N. *Rev. Adv. Mater. Sci* **38**, 160–175 (2014).

69. Haruta, M. *Catalysis Today* **36**(1), 153–166 April (1997).

70. Narayanan, R. and El-Sayed, M. *The Journal of Physical Chemistry B* **109**(26), 12663–12676 July (2005).

71. Falicov, L. M. and Somorjai, G. A. *Proceedings of the National Academy of Sciences of the United States of America* **82**(8), 2207–2211 April (1985).

72. Tian, N., Zhou, Z.-Y., Sun, S.-G., Ding, Y., and Wang, Z. L. *Science (New York, N.Y.)* **316**(5825), 732–735 May (2007).

73. Sneed, B. T., Young, A. P., and Tsung, C.-K. *Nanoscale* **7**, 12248–12265 (2015).

74. Lee, K., Kim, M., and Kim, H. *Journal of Materials Chemistry* **20**(19), 3791–3798 (2010).

75. Daio, T., Staykov, A., Guo, L., Liu, J., Tanaka, M., Matthew Lyth, S., and Sasaki, K. *Scientific Reports* **5**, 13126 August (2015).

76. Vendelbo, S. B., Elkjær, C. F., Falsig, H., Puspitasari, I., Dona, P., Mele, L., Morana, B., Nelissen, B. J., van Rijn, R., Creemer, J. F., Kooyman, P. J., and Helveg, S. *Nature Materials* **13**(9), 884–890 September (2014).

77. Hejral, U., Müller, P., Balmes, O., Pontoni, D., and Stierle, A. *Nature Communications* **7**, 10964 March (2016).

78. Leonardi, A., Leoni, M., Siboni, S., and Scardi, P. *Journal of Applied Crystallography* **45**(6), 1162–1172 December (2012).

79. Scardi, P., Leonardi, A., Gelisio, L., Suchomel, M. R., Sneed, B. T., Sheehan, M. K., and Tsung, C.-K. *Physical Review B* **91**(15), 155414 (2015).

80. Cha, Jeong, Song, Park, Pham, T., Harder, Robinson, and Kim. *Nature Materials* **12**, 729–734 (2013).

81. Kim, J. W., Manna, S., Dietze, S. H., Ulvestad, A., Harder, R., Fohtung, E., Fullerton, E. E., and Shpyrko, O. G. *Applied Physics Letters* **105**(17), 173108 October (2014).

82. Robinson, I. *Journal of the Physical Society of Japan* **82**(2), 021012 (2012).

83. Favre-Nicolin, V., Eymery, J., Koester, R., and Gentile, P. *Physical Review B* **79**(19), 195401 (2009).

84. Cabié, M., Giorgio, S., Henry, C. R., Axet, M. R., Philippot, K., and Chaudret, B. *The Journal of Physical Chemistry C* **114**(5), 2160–2163 February (2010).

85. Cerezo, A., Clifton, P. H., Galtrey, M. J., Humphreys, C. J., Kelly, T. F., Larson, D. J., Lozano-Perez, S., Marquis, E. A., Oliver, R. A., Sha, G., Thompson, K., Zandbergen, M., and Alvis, R. L. *Materials Today* **10**(12), 36–42 December (2007).

86. Miao, J., Ishikawa, T., Robinson, I. K., and Murnane, M. M. *Science (New York, N.Y.)* **348**(6234), 530–535 May (2015).

87. Miao, J., Charalambous, P., Kirz, J., and Sayre, D. *Nature* **400**(6742), 342–344 July (1999).

88. Robinson, I. K., Vartanyants, I. A., Williams, G. J., Pfeifer, M. A., and Pitney, J. A. *Physical review letters* **87**(19), 195505 (2001).

89. Pfeifer, M. A., Williams, G. J., Vartanyants, I. A., Harder, R., and Robinson, I. K. *Nature* **442**(7098), 63–66 July (2006).

90. Newton, M. C., Leake, S. J., Harder, R., and Robinson, I. K. *Nature materials* **9**(2), 120–124 (2010).

91. Diaz, A., Mocuta, C., Stangl, J., Mandl, B., David, C., Vila-Comamala, J., Chamard, V., Metzger, T. H., and Bauer, G. *Physical Review B* **79**(12), 125324 March (2009).

92. Vaxelaire, N., Proudhon, H., Labat, S., Kirchlechner, C., Keckes, J., Jacques, V., Ravy, S., Forest, S., and Thomas, O. *New Journal of Physics* **12**(3), 035018 (2010).

93. Yang, W., Huang, X., Harder, R., Clark, J. N., Robinson, I. K., and Mao, H.-k. *Nature Communications* **4**, 1680 April (2013).

94. Cha, Jeong, Song, Park, Pham, T., Harder, Robinson, and Kim. *Nature Materials* **12**, 729–734 (2013).

95. Vaxelaire, N., Labat, S., Cornelius, T. W., Kirchlechner, C., Keckes, J., Schulli, T., and Thomas, O. *Acta Materialia* **78**, 46–55 October (2014).

96. Liu, X., Aranda, M. A. G., Chen, B., Wang, P., Harder, R., and Robinson, I. *Crystal Growth & Design* **15**(7), 3087–3091 July (2015).

97. Ulvestad, A., Clark, J. N., Harder, R., Robinson, I. K., and Shpyrko, O. G. *Nano Letters* **15**(6), 4066–4070 June (2015).

98. Watari, M., McKendry, R. A., Vögtli, M., Aeppli, G., Soh, Y.-A., Shi, X., Xiong, G., Huang, X., Harder, R., and Robinson, I. K. *Nature Materials* **10**(11), 862–866 November (2011).

99. Ulvestad, A., Welland, M. J., Collins, S. S. E., Harder, R., Maxey, E., Wingert, J., Singer, A., Hy, S., Mulvaney, P., Zapol, P., and Shpyrko, O. G. *Nature Communications* **6**, 10092 December (2015).

100. Xiong, G., Clark, J. N., Nicklin, C., Rawle, J., and Robinson, I. K. *Scientific Reports* **4**, 6765 October (2014).

101. Haag, S. T., Richard, M.-I., Welzel, U., Favre-Nicolin, V., Balmes, O., Richter, G., Mittemeijer, E. J., and Thomas, O. *Nano Letters* **13**(5), 1883–1889 May (2013).

102. Ulvestad, A., Welland, M. J., Collins, S. S. E., Harder, R., Maxey, E., Wingert, J., Singer, A., Hy, S., Mulvaney, P., Zapol, P., and Shpyrko, O. G. *Nature Communications* **6**, 10092 December (2015).

103. Ulvestad, A., Singer, A., Clark, J. N., Cho, H. M., Kim, J. W., Harder, R., Maser, J., Meng, Y. S., and Shpyrko, O. G. *Science* **348**(6241), 1344–1347 June (2015).

104. Minkevich, A. A., Gailhanou, M., Micha, J.-S., Charlet, B., Chamard, V., and Thomas, O. *Physical Review B* **76**(10), 104106 September (2007).

105. Minkevich, A. A., Baumbach, T., Gailhanou, M., and Thomas, O. *Physical Review B* **78**(17), 174110 November (2008).

106. Diaz, A., Chamard, V., Mocuta, C., Magalhães-Paniago, R., Stangl, J., Carbone, D., Metzger, T. H., and Bauer, G. *New Journal of Physics* **12**(3), 035006 March (2010).

107. Favre-Nicolin, V., Mastropietro, F., Eymery, J., Camacho, D., Niquet, Y. M., Borg, B. M., Messing, M. E., Wernersson, L.-E., Algra, R. E., Bakkers, E. P. A. M., Metzger, T. H., Harder, R., and Robinson, I. K. *New Journal of Physics* **12**(3), 035013 (2010).

108. Beutier, G., Verdier, M., Parry, G., Gilles, B., Labat, S., Richard, M. I., Cornelius, T., Lory, P. F., Vu Hoang, S., Livet, F., Thomas, O., and de Boissieu, M. *Thin Solid Films* **530**, 120–124 March (2013).

109. Jacques, V. L. R., Carbone, D., Ghisleni, R., and Thilly, L. *Physical Review Letters* **111**(6), 065503 August (2013).

110. Dupraz, M., Beutier, G., Rodney, D., Mordehai, D., and Verdier, M. *Journal of Applied Crystallography* **48**(Pt 3), 621–644 April (2015).

111. Labat, S., Richard, M.-I., Dupraz, M., Gailhanou, M., Beutier, G., Verdier, M., Mastropietro, F., Cornelius, T. W., Schülli, T. U., Eymery, J., and Thomas, O. *ACS Nano* August (2015).

112. Ulvestad, A., Clark, J. N., Harder, R., Robinson, I. K., and Shpyrko, O. G. *Nano Letters* **15**(6), 4066–4070 June (2015).

113. Takahashi, Y., Suzuki, A., Furutaku, S., Yamauchi, K., Kohmura, Y., and Ishikawa, T. *Physical Review B* **87**(12), 121201 March (2013).

114. Clark, J. N., Ihli, J., Schenk, A. S., Kim, Y.-Y., Kulak, A. N., Campbell, J. M., Nisbet, G., Meldrum, F. C., and Robinson, I. K. *Nature Materials* **14**(8), 780–784 August (2015).

115. Ihli, J., Clark, J. N., Côté, A. S., Kim, Y.-Y., Schenk, A. S., Kulak, A. N., Comyn, T. P., Chammas, O., Harder, R. J., Duffy, D. M., Robinson, I. K., and Meldrum, F. C. *Nature Communications* **7**, 11878 June (2016).

116. Thompson, A. C. and Vaughan, D. *X-ray Data Booklet*. Lawrence Berkeley Laboratory, (2001).

117. Couprie, M. E. *Journal of Electron Spectroscopy and Related Phenomena* **196**, 3–13 October (2014).

118. Winick, H. *Journal of synchrotron radiation* **5**(3), 168–175 (1998).

119. Als-Nielsen, J. and McMorrow, D. *Elements of Modern X-ray Physics*. John Wiley & Sons, April (2011).

120. Paganin, D. *Coherent X-Ray Optics*. OUP Oxford, August (2013).

121. Van der Veen, F. and Pfeiffer, F. *Journal of Physics: Condensed Matter* **16**(28), 5003 (2004).

122. Leake, S. J., Newton, M. C., Harder, R., and Robinson, I. K. *Optics Express* **17**(18), 15853–15859 August (2009).

123. Emma, P., Akre, R., Arthur, J., Bionta, R., Bostedt, C., Bozek, J., Brachmann, A., Bucksbaum, P., Coffee, R., Decker, F.-J., Ding, Y., Dowell, D., Edstrom, S., Fisher, A., Frisch, J., Gilevich, S., Hastings, J., Hays, G., Hering, P., Huang, Z., Iverson, R., Loos, H., Messerschmidt, M., Miahnahri, A., Moeller, S., Nuhn, H.-D., Pile, G., Ratner, D., Rzepiela, J., Schultz, D., Smith, T., Stefan, P., Tompkins, H., Turner, J., Welch, J., White, W., Wu, J., Yocky, G., and Galayda, J. *Nature Photonics* **4**(9), 641–647 September (2010).

124. Lehmkühler, F., Gutt, C., Fischer, B., Schroer, M. A., Sikorski, M., Song, S., Roseker, W., Glownia, J., Chollet, M., Nelson, S., Tono, K., Katayama, T., Yabashi, M., Ishikawa, T., Robert, A., and Grübel, G. *Scientific Reports* **4** June (2014).

125. Hauptman, H. A. *Reports on Progress in Physics* **54**(11), 1427 (1991).

126. Gabor, D. *Nature* **161**, 777–778 (1948).

127. Faigel, G. and Tegze, M. *Reports on Progress in Physics* **62**(3), 355 (1999).

128. Chamard, V., Stangl, J., Carbone, G., Diaz, A., Chen, G., Alfonso, C., Mocuta, C., and Metzger, T. H. *Physical Review Letters* **104**(16), 165501 April (2010).

129. Eisebitt, S., Lüning, J., Schlotter, W. F., Lörgen, M., Hellwig, O., Eberhardt, W., and Stöhr, J. *Nature* **432**(7019), 885–888 December (2004).

130. Zhu, D., Guizar-Sicairos, M., Wu, B., Scherz, A., Acremann, Y., Tyliszczak, T., Fischer, P., Friedenberger, N., Ollefs, K., Farle, M., and others. *Physical review letters* **105**(4), 043901 (2010).

131. Duckworth, T. A., Ogrin, F., Dhesi, S. S., Langridge, S., Whiteside, A., Moore, T., Beutier, G., and van der Laan, G. *Optics Express* **19**(17), 16223 August (2011).

132. Wang, Y., Li, T., Gao, Q., Zhang, S., and Shi, Y. *Optical Engineering* **52**(9), 091720–091720 (2013).

133. Faulkner, H. M. L. and Rodenburg, J. M. *Physical review letters* **93**(2), 023903 (2004).

134. Thibault, P., Dierolf, M., Bunk, O., Menzel, A., and Pfeiffer, F. *Ultramicroscopy* **109**(4), 338–343 (2009).

135. Maiden, A. M., Humphry, M. J., Zhang, F., and Rodenburg, J. M. *JOSA A* **28**(4), 604–612 (2011).

136. Guizar-Sicairos, M., Johnson, I., Diaz, A., Holler, M., Karvinen, P., Stadler, H.-C., Dinapoli, R., Bunk, O., and Menzel, A. *Optics Express* **22**(12), 14859 June (2014).

137. Nellist, P. D. and Rodenburg, J. M. *Acta Crystallographica Section A Foundations of Crystallography* **54**(1), 49–60 January (1998).

138. Schropp, A., Boye, P., Goldschmidt, A., Hönig, S., Hoppe, R., Patommel, J., Rakete, C., Samberg, D., Stephan, S., Schöder, S., Burghammer, M., and Schroer, C. *Journal of Microscopy* **241**(1), 9–12 January (2011).

139. Dierolf, M., Thibault, P., Menzel, A., Kewish, C. M., Jefimovs, K., Schlichting, I., Von Koenig, K., Bunk, O., and Pfeiffer, F. *New Journal of Physics* **12**(3), 035017 (2010).

140. Howells, M. R., Beetz, T., Chapman, H. N., Cui, C., Holton, J. M., Jacobsen, C. J., Kirz, J., Lima, E., Marchesini, S., Miao, H., Sayre, D., Shapiro, D. A., Spence, J. C. H., and Starodub, D. *Journal of Electron Spectroscopy and Related Phenomena* **170**(1–3), 4–12 March (2009).

141. Le Bolloc'h, D., Livet, F., Bley, F., Schulli, T., Veron, M., and Metzger, T. H. *Journal of Synchrotron Radiation* **9**(4), 258–265 Jul (2002).

142. Jacques, V. L. R., Le Bolloc'h, D., Pinsolle, E., Picca, F.-E., and Ravy, S. *Physical Review B* **86**(14), 144117 October (2012).

143. Xiong, G., Moutanabbir, O., Reiche, M., Harder, R., and Robinson, I. *Advanced Materials* **26**(46), 7747–7763 December (2014).

144. Shannon, C. E. *Proceedings of the IRE* **37**(1), 10–21 (1949).

145. Miao, J., Kirz, J., and Sayre, D. *Acta Crystallographica Section D Biological Crystallography* **56**(10), 1312–1315 October (2000).

146. Miao, J, Sayre, D., and Chapman, H.N. *Journal of Optical Society of America A* **15**(6), 1662–1669 (1998).

147. Andreas Schropp. *Experimental coherent X-ray diffraction imaging: capabilities and limitations of the technique*. PhD thesis, Universität Hamburg, Hamburg, (2008).

148. Miao, J. and Sayre, D. *Acta Crystallographica Section A Foundations of Crystallography* **56**(6), 596–605 November (2000).

149. Gerchberg, R. and Saxton, W. *Optik (Jena)* **35**, 237 (1972).

150. Marchesini, S. *Review of scientific instruments* **78**(011301), 1–10 (2007).

151. Fienup, J. R. *Applied Optics* **21**(15), 2758–2769 August (1982).

152. Marchesini, S., He, H., Chapman, H. N., Hau-Riege, S. P., Noy, A., Howells, M. R., Weierstall, U., and Spence, J. C. *Physical Review B* **68**(14), 140101 (2003).

153. Fienup, J. R. *Frontiers in Optics* , ThI3 (2003).

154. Fienup, J. R. *Applied Optics* **52**(1), 45 January (2013).

155. Oszlányi, G. and Sütő, A. *Acta Crystallographica Section A Foundations of Crystallography* **60**(2), 134–141 March (2004).

156. Mastropietro, F. *Imagerie de nanofils uniques par diffraction cohérente des rayons X*. PhD thesis, Université de Grenoble, October (2011).

157. Ponchut, C., Rigal, J. M., Clément, J., Papillon, E., Homs, A., and Petitdemange, S. *Journal of Instrumentation* **6**(01), C01069 (2011).

158. Mocuta, C., Stangl, J., Mundboth, K., Metzger, T. H., Bauer, G., Vartanyants, I. A., Schmidbauer, M., and Boeck, T. *Physical Review B* **77**(24), 245425 June (2008).

159. Chahine, G. A., Richard, M.-I., Homs-Regojo, R. A., Tran-Caliste, T. N., Carbone, D., Jacques, V. L. R., Grifone, R., Boesecke, P., Katzer, J., Costina, I., Djazouli, H., Schroeder, T., and Schülli, T. U. *Journal of Applied Crystallography* **47**(2), 762–769 April (2014).

160. Evans, P. G., Chahine, G., Grifone, R., Jacques, V. L. R., Spalenka, J. W., and Schülli, T. U. *The Review of Scientific Instruments* **84**(11), 113903 November (2013).

161. Wagner and Ellis. *Ultramicroscopy* **109**, 338–343 (1964).

162. Adhikari, H., Marshall, A. F., Chidsey, C. E. D., and McIntyre, P. C. *Nano Letters* **6**(2), 318–323 February (2006).

163. Hannon, J. B., Kodambaka, S., Ross, F. M., and Tromp, R. M. *Nature* **440**(7080), 69–71 March (2006).

164. Gentile, P., Solanki, A., Pauc, N., Oehler, F., Salem, B., Rosaz, G., Baron, T., Den Hertog, M., and Calvo, V. *Nanotechnology* **23**(21), 215702 June (2012).

165. Schäfer, C. M. *Internship report: Synthesis and in situ characterization of SiGe core-shell nanowires*. PhD thesis, Grenoble INP Phelma, (2016).

166. Gutkin, M. Y., Ovid'ko, I. A., and Sheinerman, A. G. *Journal of Physics: Condensed Matter* **12**(25), 5391 (2000).

167. M Jamal, S. J. A. *Computational Materials Science* **95**(2014), 592 (2014).

168. Haag, S. T., Richard, M.-I., Labat, S., Gailhanou, M., Welzel, U., Mittemeijer, E. J., and Thomas, O. *Physical Review B* **87**(3), 035408 January (2013).

169. Biermanns, A., Breuer, S., Davydok, A., Geelhaar, L., and Pietsch, U. *Journal of Applied Crystallography* **45**(2), 239–244 April (2012).

170. Oehler, F., Gentile, P., Baron, T., Ferret, P., Den Hertog, M., and Rouvière, J. *Nano Letters* **10**(7), 2335–2341 July (2010).

171. Leclere, C., Cornelius, T. W., Ren, Z., Davydok, A., Micha, J.-S., Robach, O., Richter, G., Belliard, L., and Thomas, O. *Journal of Applied Crystallography* **48**(1), 291–296 February (2015).

172. Fernández, S., Richard, M. I., Floettoto, D., Richter, G., Mandula, O., Aizarna, M. E., Favre-Nicolin, V., Burghammer, M., Schülli, T., and Thomas, O. *Thin Solid Films* (2016).

173. Ponchut, C., Rigal, J. M., Clément, J., Papillon, E., Homs, A., and Petitdemange, S. *Journal of Instrumentation* **6**(01), C01069 (2011).

174. Fertey, P., Berenguer, F., Elkaim, E., Legrand, F., Laulhé, C., and Ravy, S. Technical report, SOLEIL synchrotron, (2008).

175. Dupraz, M. *Diffraction des rayons X cohérents appliquée à la physique du métal*. PhD thesis, Grenoble Alpes, (2015).

176. Varahramyan, K. M., Ferrer, D., Tutuc, E., and Banerjee, S. K. *Applied Physics Letters* **95**(3), 033101 July (2009).

177. Hÿtch, M. J., Snoeck, E., and Kilaas, R. *Ultramicroscopy* **74**(3), 131–146 August (1998).

178. Fewster, P. F. *Critical Reviews in Solid State and Materials Sciences* **22**(2), 69–110 June (1997).

179. Leake, S. J., Newton, M. C., Harder, R., and Robinson, I. K. *Optics Express* **17**(18), 15853–15859 August (2009).

180. Clark, J. N., Huang, X., Harder, R., and Robinson, I. K. *Nature Communications* **3**, 993 August (2012).

181. Newton, M. C., Harder, R., Huang, X., Xiong, G., and Robinson, I. K. *Physical Review B* **82**(16), 165436 October (2010).

182. Herráez, M. A., Burton, D. R., Lalor, M. J., and Gdeisat, M. A. *Applied Optics* **41**(35), 7437–7444 December (2002).

183. Guizar-Sicairos, M., Diaz, A., Holler, M., Lucas, M. S., Menzel, A., Wepf, R. A., and Bunk, O. *Optics Express* **19**(22), 21345–21357 October (2011).

184. Ying, L. In *Wiley Encyclopedia of Biomedical Engineering*. John Wiley & Sons, Inc. (2006).

185. `http://scikit-image.org`.

186. Ding, Y., Kong, X. Y., and Wang, Z. L. *Journal of Applied Physics* **95**(1), 306–310 January (2004).

187. Rieger, T., Luysberg, M., Schäpers, T., Grützmacher, D., and Lepsa, M. I. *Nano Letters* **12**(11), 5559–5564 November (2012).

188. Biermanns, A., Rieger, T., Bussone, G., Pietsch, U., Grützmacher, D., and Lepsa, M. I. *Applied Physics Letters* **102**(4), 043109 January (2013).

189. Den Hertog, M. *Characterization of silicon nanowires by transmission electron microscopy*. PhD thesis, Université Joseph-Fourier, Grenoble, (2009).

190. Potié, A., Baron, T., Latu-Romain, L., Rosaz, G., Salem, B., Montes, L., Gentile, P., Kreisel, J., and Roussel, H. *Journal of Applied Physics* **110**(2), 024311 (2011).

191. Gavelle, M., Bazizi, E. M., Scheid, E., Fazzini, P. F., Cristiano, F., Armand, C., Lerch, W., Paul, S., Campidelli, Y., and Halimaoui, A. *Journal of Applied Physics* **104**, 113524–113524 December (2008).

192. Castrillo, P., Pinacho, R., Jaraiz, M., and Rubio, J. E. *Journal of Applied Physics* **109**(10), 103502 May (2011).

193. Bracht, H., Stolwijk, N. A., and Mehrer, H. *Physical Review B* **43**(18), 14465 (1991).

194. Holmberg, V. C., Panthani, M. G., and Korgel, B. A. *Science* **326**(5951), 405–407 (2009).

195. Wu, Y. and Yang, P. *Advanced Materials* **13**(7), 520–523 (2001).

196. Oehler, F., Gentile, P., Baron, T., and Ferret, P. *Nanotechnology* **20**(47), 475307 (2009).

197. Cressler, J. D. *SiGe and Si Strained-Layer Epitaxy for Silicon Heterostructure Devices*. CRC Press, December (2007).

198. Woodruff, J. H., Ratchford, J. B., Goldthorpe, I. A., McIntyre, P. C., and Chidsey. *Nano Letters* **7**(6), 1637–1642 June (2007).

199. McIntyre, P. C., Adhikari, H., Goldthorpe, I. A., Hu, S., Leu, P. W., Marshall, A. F., and Chidsey, C. E. D. *Semiconductor Science and Technology* **25**(2), 024016 (2010).

200. Meier, J. C., Galeano, C., Katsounaros, I., Witte, J., Bongard, H. J., Topalov, A. A., Baldizzone, C., Mezzavilla, S., Schüth, F., and Mayrhofer, K. J. J. *Beilstein Journal of Nanotechnology* **5**, 44–67 January (2014).

201. Heck, R. M. and Farrauto, R. J. *Applied Catalysis A: General* **221**(1–2), 443–457 November (2001).

202. Cao, S., Zhang, L., Chai, Y., and Yuan, R. *Talanta* **109**, 167–172 May (2013).

203. Tian, Zhou, and Sun. *Journal of Physical Chemistry C* **112**(50), 19801–19817 (2008).

204. Santen, R. A. v., Neurock, M., and Shetty, S. G. *Chemical Reviews* **110**(4), 2005–2048 April (2010).

205. Ding, Y., Gao, Y., Wang, Z. L., Tian, N., Zhou, Z.-Y., and Sun, S.-G. *Applied Physics Letters* **91**(12), 121901 September (2007).

206. M Jamal, S. J. A. *Computational Materials Science* **95**(2014), 592 (2014).

207. Favre-Nicolin, V., Coraux, J., Richard, M.-I., and Renevier, H. *Journal of Applied Crystallography* **44**(3), 635–640 June (2011).

208. Mastropietro, F., Carbone, D., Diaz, A., Eymery, J., Sentenac, A., Metzger, T. H., Chamard, V., and Favre-Nicolin, V. *Optics Express* **19**(20), 19223 September (2011).

209. Kriegner, D., Wintersberger, E., and Stangl, J. *Journal of Applied Crystallography* **46**(4), 1162–1170 August (2013).

210. Harder, R., Pfeifer, M. A., Williams, G. J., Vartaniants, I. A., and Robinson, I. K. *Physical Review B* **76**(11), 115425 September (2007).

211. Thompson, A. C. and Vaughan, D. *X-ray Data Booklet*. Lawrence Berkeley Laboratory, (2001).

212. Rijn, R. v., Ackermann, M. D., Balmes, O., Dufrane, T., Geluk, A., Gonzalez, H., Isern, H., Kuyper, E. d., Petit, L., Sole, V. A., Wermeille, D., Felici, R., and Frenken, J. W. M. *Review of Scientific Instruments* **81**(1), 014101 January (2010).

213. Nolte, P. *In situ oxidation study of supported Rh and Pd nanoparticles*. PhD thesis, University of Stuttgart, (2009).

214. Han, B. C., Miranda, C. R., and Ceder, G. *Physical Review B* **77**(7), 075410 February (2008).

215. Ulvestad, A., Sasikumar, K., Kim, J. W., Harder, R., Maxey, E., Clark, J. N., Narayanan, B., Deshmukh, S. A., Ferrier, N., Mulvaney, P., Sankaranarayanan, S. K. R. S., and Shpyrko, O. G. *The Journal of Physical Chemistry Letters* **7**(15), 3008–3013 August (2016).

List of Figures

1.1 a) Face centered cubic structure of Pt. The minimum distance between the atoms is $a/\sqrt{2}$, with $a_{Pt} = 3.924$ Å. b) Diamond unit cell of Si or Ge. The side of the cube is $a_{Si} = 5.431$ Å and $a_{Ge} = 5.6575$ Å respectively. 17
1.2 Comparison of the resolving power in strain and real space for electron microscopy and X-ray methods, from Ref.[2]. 18
1.3 Schematic representation of an edge dislocation (a) and a screw dislocation (b) in a cubic crystalline material. The Burger vector, $\vec{b}$, represents the magnitude and direction of the lattice distortion. The shaded area represents the slipped plane, and the dashed line, the dislocation line. 19
1.4 Illustration of the atomic structure of two layers before (a) and after epitaxy (b) and (c). In b) a perfect heteroepitaxy is represented, whereas in c) a mismatch defect at the interface induces relaxation in one of the layers. 20
1.5 a) Perfect crystal with FCC structure b) Stacking fault in a FCC crystalline structure. Atom colors, labeled by different letters according to the text, represent different atomic layers. 21
1.6 VLS growth mode from a metallic droplet and nanowires with multiaxial and radial heterostructures. Image taken from Reference[17]. 22
1.7 Strain fields of an infinite GaAs-core GaP- shell nanowire (lattice mismatch $\sim 3.6\%$), from Reference[27]. The hydrostatic strain evidences that the core is compressed while the shell is expanded. 24
1.8 Critical NW radius versus lattice mismatch as a function of Burger's vector magnitude, calculated assuming isotropy and elasticity, from Ref.[35]. The critical radius decreases while increasing the lattice mismatch. 25
1.9 a) High-resolution TEM image of a 18 nm diameter Ge NW with a 2 nm Si shell. The shell is single crystalline and heteroepitaxial with the Ge core. TEM images b), c) and d) show the periodic modulation of the surfaces for a Ge core of 26 nm and shell thickness of 4.5, 6 and 17 nm respectively. From Ref.[19]. 25
1.10 a) Scanning Transmission Electron Microscope (STEM) image of a Si/$Si_{1-x}Ge_x$ NW of 21 nm diameter. b) EDS line profile of Si and Ge through the Si/$Si_{1-x}Ge_x$ junction, as indicated in c). A sharp transition of less than 2 nm from Si to SiGe is observed. Both from Ref.[45]. c) TEM image of a Si-shell, Ge-core NW showing the core/shell structure. d) HRTEM image of a representative NW with a Si amorphous shell. e) EDS profile showing the abruptness of the interface. Scale bars are 5 nm. From Ref.[14] 27
1.11 Effect of post growth annealing on Si-core, Ge-shell NWs, from Ref.[64] 29
1.12 a) Measured activities for CO oxidation at 273 K as a function of the average particle size. The symbols are used to differentiate the support of the Au NPs. From Ref.[69]. b) Electron microscopy images of Au nanocrystals with different shapes, from Ref.[67] 30

1.13 Sources of lattice strain in NPs, from Ref.[73]. a) Surface relaxation due to size. b) Anisotropic strain due to shape. c) Strain at grain boundaries due to twinning and unfilled volume. d) Strain from epitaxy in core-shell structures. e) Strain due to alloying. 31
1.14 Illustration of the complex shapes of high-index faceted Pt NPs achieved by Tian *et al.* in 2007[72]. 32
1.15 a) Reciprocal space maps of the averaged Pt NPs under different CO/O_2 mixtures. The thickness fringes are visible because of the shape homogeneity over the sample and they dissapear while increasing the O_2 flux in the reactor. b) Partial pressures at the different stages of the experiment. c) Average particles shapes and sample morphology before (green) and after (red) reaction. After[77] 33
1.16 Correlation of oscillatory CO oxidation reaction with the morphology of a Pt NP. From Ref.[76] 33
1.17 a) Evolution of the diffraction pattern of a Au nanocrystal during Cu diffusion (from i) to vi)) and the corresponding reconstructions. In b), the projections of the atomic displacement and in c) the reconstructed amplitude. From Ref.[100]. . . 35
1.18 a) Reconstructions of the density of two different calcite crystals (i) and (ii). b) 2D cuts at the positions indicated by the dashed lines showing the projected atomic displacement. The magenta circles show the strained region around the defects in the crystals. From Ref.[115] 35

2.1 Average brilliance of X-ray sources and their evolution over the decades (from Ref.[119]) 40
2.2 Scheme of Young's interferometer. The beam is represented in yellow. Two independent waves and their corresponding fringes are represented in orange, the wave coming from one point in the upper side of the source and in flesh tone, the one coming from one point in the optical axis. 41
2.3 a) Schematic of a Michelson's interferometer. S represents a non monochromatic source. b) Intensity fringes produced by waves of different wavelengths (λ and $\lambda + \delta\lambda$ (dashed line)). 42
2.4 Set-up for Fourier holography[131] a) The object and reference slit are illuminated by the coherent X-ray beam. b) Hologram c) Linear differential filter. 43
2.5 a) Experimental set-up used for ptychography, from[132] b) Example of trajectory followed by the sample while recording the diffraction patterns. The "spiral" trajectory is often chosen to avoid periodicity artifacts. Each point on the spiral corresponds to a detector image. c) Circles represents the position of the beam while scanning the sample, showing the overlapping. 43
2.6 Bragg condition for diffraction in crystals. The incident beam of propagation vector $|\vec{k_i}| = \frac{2\pi}{\lambda}$ impinges on the crystal with an incident angle θ. Only the waves exiting in a specific direction $\vec{k_f}$ will interfere in a constructive way to yield a measurable intensity. 45
2.7 Sketch of three-different regimes in CDI, from[143]. CDI experiments are performed with the detector in the Fraunhofer regime and the sample in the Fresnel regime, considering the slits as second source. 46
2.8 a) When a coherent X-ray beam impinges onto a crystal, its reciprocal space is made by a set of sharp points called speckles. As experimentally it is impossible to measure the continuous diffraction pattern, the crystal has to be *oversampled* on a finer grid. The sampling distance in real space Δx is given by[147] $\Delta x = \frac{\lambda L}{Np}$, where *p* is the pixel size. b) Same diffraction pattern sampled at the Nyquist frequency (above) and at twice the Nyquist frequency (below) and their corresponding reconstructions (from[148]). Oversampling with a ratio $\sigma \geq 2$ confines the object in a region (*"support"*) surrounded by zeros. 47

2.9 Representation of the iterative phase retrieval algorithm. Here, according to the text, $|A| = \sqrt{I}$ and $|A| = \mathscr{F}[\rho(\vec{r})]$. φ is a random value of the phase to initiate the algorithm. 49
2.10 Schema of the different *real space constraints* for the algorithms explained in the text. a) ER b) HIO c) CF d) SW, α represents the threshold and β is the feedback parameter. 50
2.11 Overview of OH1 and OH2. The beam comes from the right to the left ($i.e.$ from OH1 to OH2). Si (111) Bragg monochromators (double crystal geometry/channel cut geometry) 52
2.12 The 3+2-circles diffractometer 53
2.13 a) Optical path shift from different zones of a FZP. b) Schematic of the propagation of the wavefield produced by an illuminated FZP. A central stop and a collimating aperture placed close to the focal point are used to isolate the first order from the others. 54
2.14 Photograph of the reactor installed onto the PI of the beamline. Note that the OSA is very close to the Be dome. 55

3.1 a) SEM image of an assembly of Ge/Si core/shell NW measured at ID01 beamline. NWs grow along the $< 111 >$ directions. b) Tip of a Si NW showing the sidewalls in presence and abscence of HCl flow. The segment where the HCl flow is off (top part) is much rougher and small gold droplets diffusing down from the Au catalyst can be observed. From Ref.[165] 59
3.2 STEM image of a Ge/Si core/shell NW (a) and its corresponding EDX map (b). . 59
3.3 Schematic diagram of the cylindrical Ge-Si nanowire. The $z-$axis denotes the NW growth direction. 60
3.4 Theoretical elastic epitaxial strain components in a Ge-Si core-shell nanowire at its center in the z-direction: a) ϵ_{zz}, b) ϵ_{xx} and c) ϵ_{yy}. 61
3.5 Theoretical elastic epitaxial out-of-plane strain in the shell (a) and in the core (b) of Ge-Si core-shell nanowires as a function of shell thickness for a cylindrical geometry. The diameter of the Ge core is indicated in the legend. 62
3.6 (a) Schematic view of the hexagonal Ge-Si core-shell nanowire. (b)-(c) Three-dimensional diffraction patterns of the **111** Bragg reflection in the case of a coherent (b) or incoherent (c) Ge-Si interface. 63
3.7 Diffraction patterns of the **111** Bragg reflection of an hexagonal Ge-Si core-shell nanowire displayed in the Q_x-Q_y (at the Q_z position of the scattering from the Ge core) and Q_x-Q_z planes in the case of a coherent (a-b) or incoherent (c-d) Ge-Si interface. 63
3.8 Diffraction patterns of the **22**$\bar{4}$ Bragg reflection of an hexagonal Ge-Si core-shell nanowire displayed in the Q_x-Q_y and Q_x-Q_z planes in the case of a coherent (a-b) or incoherent (c-d) Ge-Si interface. 64
3.9 a) Experimental set-up at ID01 for CDI experiments on an assembly of NWs. Recording the scattered intensity from the Ge core of an isolated NW, also the diffracting shell yields to a Bragg peak on the 2D detector. The *out-of-plane* angular distance between the Bragg peaks on the detector depends on the lattice mismatch; radial scans moving the detector along the vertical direction (δ) allows to determine the axial strain of the NW. 66
3.10 Intensity distribution as a function of the x, y and z coordinates of the reciprocal space vector $\vec{Q} = \vec{k_f} - \vec{k_i}$ of two NWs with the same core diameter (100 nm), but different shell thickness: a) 20 nm and b) 50 nm. The signal arising from the NW has been circled. The intense vertical and inclined streaks are due to the substrate CTR and the detector saturation respectively. 68

3.11 2D diffraction patterns of single nanowires from samples 2 (a) and 4 (b). The facets are evidenced in the thicker NW. The missing data are due to the strong CTR from Ge substrate c) Intensity profile from Fig. 3.10) b) and fit of the Ge and Si peaks allowing to calculate the axial strain. Dashed gray lines indicate the **111** Ge and Si bulk Bragg positions. 68
3.12 2D RSMs of a) Sample 1 ($\gamma = 1$) and b) Sample 4 ($\gamma = 0.25$). c) Experimental curves of three different NWs, representatives of each sample of different core diameters. 69
3.13 Measured strain in the Si shell with respect to Si bulk for the samples with different radius $\gamma = \frac{d_s}{d_c}$. The theoretical predictions[32] in the elastic epitaxial case are also plotted. 69
3.14 Summary of different systems of isolated NWs. a) NW deposited on a bridge between two Si trenches. b) Diffraction pattern around the $\bar{2}\bar{2}4$ Ge Bragg reflection of a Ge/Si core shell NW lying on a sapphire substrate. The RSM corresponds to the NW on the right of the inset image. c) SEM image showing the transfer of the NW using a FIB manipulator. 71
3.15 a) 6-circles diffractometer and b) mini-goniometer at CRISTAL beamline, from Ref.[175]. c) Image of the measured sample taken with an optical microscope to localise the NWs before the CDI experiment. The NWs were deposited on the TEM grid by the scratching method, which explains the broken areas. 72
3.16 RSMs around the $\bar{2}\bar{2}4$ Bragg reflection of three different NWs deposited on a TEM grid. The additional streak observed in the 3 imaged NWs has been circled. . . . 74
3.17 TEM micrograph of a core/shell NW showing diameter variations along the length. 75
3.18 a) Model of the NW cross section that best fit the EDX line scans b) Example of an EDX line scan and fit to the truncated triangle configuration model. 75
3.19 a) TEM image showing the cross-section of a Ge/Si core/shell NW. The Pt layer protects the NWs during the TEM preparation. The red square shows the region where the high-resolution micrograph shown in b) has been taken. c) Series of TEM micrographs employed to apply the GPA method to determine the strain in the x and y directions: ϵ_{xx} (d) and ϵ_{yy} in (e). 76
3.20 a) SEM image showing the preparation of the NW using a coupled Focused-Ion-Beam/SEM manipulator. b) SEM image showing the studied NW once glued on the Cu tip. The conical shape is evidenced, exhibiting a diameter difference of 220 nm between the top and the bottom. The roughness of the shell and the Au catalyst (in the top of the wire) are also visible. 77
3.21 Comparison of the SEM image showing the position of the NW on the tip (a) and the quicK map during the CDI experiment (b). The features of the tip allow to identify a lower part of the tip where the NW is located. As the NW is barely visible, it has been circled in (a), and the cross points the approximative expected position in b). 78
3.22 RSMs around the a) **111**, b) **333**, c) **2$\bar{2}$0** and **331** Bragg reflections of a Ge/Si core/shell NW. 80
3.23 a) Number of pixels contained in the support as a function of the iterations during the SW procedure for 4 different initial random values. b) Evolution of the support through the iterations. Note that the support is flat (only ones in the prism) but here the sum of the pixels along the $z - axis$ is represented. 81
3.24 a) View of the isosurfaces of the retrieved nanowire from the **111** Bragg reflection. The support size is $275 \times 300 \times 600\ nm^3$. b) Raw experimental amplitude. c) Reconstructed amplitude from the retrieved object. d) Isocontour of the reconstructed density. e) Wrapped slices of the retrieved phase at the center of the NW, as found by the algorithms. 82

3.25 Illustration of the 1D unwrapping problem. a) Original wrapped phase profile presenting phase jumps. b) Continuous phase after unwrapping. 83
3.26 2D slices of the corrected phase at the center of the NW in the yz (a), xz (b) and xy(c) planes. d) Plot of the phase as a function of the length showing the phase jump for several cuts at $y = 0, y = 70$ and $y = -70$ nm. 84
3.27 Isosurfaces of the calculated strain from the **111** reflection. 85
3.28 a) Sum of the density along the $x-$axis of an hexagonal core/shell NW. b) Illustration of the zone of the NW where a 5 radians phase shift was inserted. c) and d) Simulated diffraction patterns corresponding to the objects in a) and b) respectively. The colorbar corresponds to the logarithmic intensity. e) Intensity profiles along the Q_z direction, showing the effect of the insertion in the width of the Bragg peak. 86
3.29 Simulation of the diffraction patterns of a core/shell NW with a phase shift of 5 radians in a larger region (a) and of one with a stacking fault in the middle (b). . 86
3.30 Phase maps cutting through the crystal at the middle of the reconstructed NW from the a) **333**, b) **2$\bar{2}$0** and c) **331** Ge Bragg reflections. 87
3.31 SEM image of the NW prepared using a FIB micro-manipulator. A large amount of carbon surrounds the bottom of the wire, which was used to glue the NW on the tomography tip. 89
3.32 Coherent X-ray diffraction measurements around the **111** Ge Bragg reflection of a single core/shell Ge/Si NW at RT (a), 91 ° C (b), 253 ° C (c) and after cooling down, at 24 ° C (d). 90
3.33 a) 2D real-space map (step of 0.8 μm) of the integrated intensity at different incident angles with respect to the **111** Ge Bragg reflection. The crosses along the NW indicate the positions where the rocking curves used to calculate the tilt and strain at RT before heating were performed. b) Sum of the 3D recorded raw intensity at the higher and lower positions along the wire (labelled *i)* and *ii)* in a)) with the Be dome. c) *Out-of-plane* strain and d) lattice tilt as a function of position of the beam on the NW at RT before and after annealing the sample. The reference is taken at the top of the NW, where $z = 0$ has been defined by convenience. 91
3.34 SEM image of the NW after annealing during the CDI experiment. It can be observed that the NW is bent, as well as carbon clusters on the surface (some of them are pointed out by the red arrows). 92
3.35 (a) Nano-chip sample carrier for temperature accuracy and sample stability. (b) Core of the nano-chip. 93
3.36 (a-b) TEM and (c) HAADF measurements of one of the NWs deposited on the Silicon Nitride membrane for *in situ* experiments. In (c) a Moiré-like pattern along the NW is observed. 94
3.37 One dimensional EDX profiles (c) at 20°C (a) and 800°C (b) on two different parts of the same nanowire (a-b). 95
3.38 STEM imaging of a Ge-Si core-shell nanowire as a function of temperature and annealing time. A black dashed and green full lines are guide for the eyes and indicate the core-shell and shell-air interfaces, respectively. The dashed lines inside the Ge core highlight some fringes on the Moiré pattern. One pixel corresponds to 0.178 nm. 96
3.39 a) TEM micrograph of the NW at 1200°C showing the position at which the EDX profile in b) was performed. b) One dimensional EDX profile at RT after the annealing of the wire at 1200°C, at the position indicated by the black line in a). 97
3.40 STEM imaging of a Ge-Si core-shell nanowire at 1200°C (a) and after 1 min of annealing at 1200°C (b). 97

3.41 Elemental mapping of a single nanowire 1200°C. (a) The region mapped during EDX is shown by a white square. Ge (b), Au (c) and Si (d) elemental mapping. The dashed white lines are guide for the eyes and indicate the total size of the nanotube. 98
3.42 a) SEM image of an assembly of NWs grown on a (111)Ge substrate without HCl. b) Sample grown in the same conditions than a), with subsequent annealing at 700°C during 1 hour. 99
3.43 $Q_y - Q_z$ RSMs of single NWs grown on a (111)Ge substrate without HCl, as grown (a) and after annealing at 700°C. Dashed lines at the Ge and Si bulk position are guidelines to compare the diffracting signals before and after annealing. The colorbar corresponds to the logarithmic intensity. 100
3.44 a) SEM image of an assembly of NWs grown on a (111)Si substrate without HCl. 100
3.45 $Q_y - Q_z$ RSMs of single NWs grown on a (111)Si substrate without HCl, as grown (a) and after annealing at 700°C. Dashed lines at the Ge and Si bulk position are guidelines to compare the diffracting signals before and after annealing. Alloyed islands on the substrate have interdiffused. The colorbar corresponds to the logarithmic intensity. 101
3.46 $Q_x - Q_y$ RSMs of single NWs grown on a (111)Si substrate without HCl, as grown (a) and after annealing at 700°C during 1 hour. A change of faceting is evidenced due to the annealing. The colorbar corresponds to the logarithmic intensity. . . . 101

4.1 Representation of the different steps in the oxidation of carbon monoxide: 2 CO + $O_2 \rightarrow$ 2 CO_2. The oxygen molecules dissociate into two separate atoms of oxygen that are then adsorbed by the surface of the catalyst. CO molecules are adsorbed as well, then combined with each of the oxygen atoms to form a CO_2 molecule. Finally, the carbon dioxide molecules are desorbed from the surface of the catalyst. 105
4.2 a) Scanning electron microscope image (SEM) of a typical sample after growth. b) Magnified image of one of the NPs, illustrating the THH shape. 106
4.3 a) The THH shape consists in a cube whose faces are bounded by equal pyramids. As the NPs do not have a preferential orientation, the crystallographic orientation is simulated as found for the particles measured during the CDI experiments. The colormap corresponds to the $z - component$ of the atomic displacement $\vec{u}_z(\vec{r})$. b) xy cut of $\vec{u}_z(\vec{r})$ in the middle of the particle, $i.e.$, at $z = 50$ nm c) xy cut of $\vec{u}_z(\vec{r})$ at $x = 50$ nm. 107
4.4 Strain fields calculated in the parallel direction to the scattering vector ϵ_{zz} (a) and (b), and the in-plane component ϵ_{xx} (c) an (d). 2D cuts are taken at the same position as in Figure 4.3). 108
4.5 Scattered intensity calculated from FEM atomic displacement. The 2D cuts show a symmetric Bragg peak centered at $|\vec{Q}| = 3.20$ Å^{-1}. Aliasing artifacts can be observed due to the employed FFT algorithm. 108
4.6 Illustration of the stereographic projection of two poles (P and R) on the equator plane (shaded). The projected poles (P' and R') are the intersection of the line joining the South pole with the corresponding pole. The direction of the streaks defining the poles and the radius of the sphere have been extended for clarity. . . 110
4.7 Stereographic projection of the simulated data (from Fig. 4.5) for $l \leq 0$. This **002** pole figure is equivalent to the projected poles on the reference plane (see Fig. 4.6). The simulated facets of type {210} yield 16 peaks whose (hkl) indices are indexed. Additional peaks and high intensity regions arise from aliasing in the calculation and from extra small facets created during the modelling of the particle. 110
4.8 Ptychographic reconstruction of the x-ray wave field amplitude (a) and phase (b) and line profiles (c) of the horizontal and vertical focus intensities yielding a spot size of $100\ (V) \times 400\ (H)$ nm^2. 111

4.9 Schematic overview of the experimental setup in co-planar diffraction geometry at ID01 beamline. 111
4.10 X-ray reciprocal space maps around the **002** Pt reflection for four different THH NPs. The sum of the measured intensity (logarithmic scale) is displayed as a function of Q_y and Q_z. 112
4.11 X-ray reciprocal space maps around the **002** Pt reflection for particle 1: sum of the measured intensity (logarithmic scale) displayed as a function of (a) Q_x and Q_y, (b) Q_x and Q_z (c) Q_y and Q_z. 113
4.12 Stereographic projection of the points defining the direction of the streaks from the experimental data of particle 1. The theoretical position of the facets are shown in black. 114
4.13 Top (a) and bottom (b) views of the 3D reconstructed support of Particle 1. Crystal dimensions are estimated to be $330 \times 400 \times 310\ nm^3$. 116
4.14 In the central row, 2D slices of the retrieved phase after refraction correction at the middle of the particle. In the upper and lower rows, the cross-sections are taken at -60 and +60 nm of distance from the center respectively and for the indicated directions. The colour scale shows the relative phase shift with respect to the non-strained region. 117
4.15 2D cuts of the calculated atomic displacement, corresponding to the cut-planes of the phase shown in 4.14. 118
4.16 Isosurface showing the strain distribution inside the particle 118
4.17 Set-up at ID03. The flow reactor is mounted on a hexapod that allows positioning the sample in the center of rotation of the 4+2 diffractometer. KB mirrors are used to focus the incident X-ray beam (coming from right to left in the $x-$direction). 120
4.18 Schematic overview of the flow reactor (a) and the implemented sample holder (b) in reaction conditions, adapted from[212]. The sample (in red) is held on the heater and completely isolated from the UHV part when the sample foot is compressed. The water channel cools the reactor walls to prevent reactant gases from reacting on and/or with the reactor walls at high temperatures. 120
4.19 The KB focused X-ray beam illuminates the sample surface. The ensemble of particles diffracting in the **002** direction yields to a 3D cone of radius $2\theta_{Bragg}$ that is intersected by the 2D detector. Thus, the $2\theta_{Bragg}$ angle is defined by the position of the detector, $i.e.$, single particles can be selected by adjusting γ and δ to explore the ring. 121
4.20 Sum of the measured intensity of two different single particles at RT in the initial state (a) and (b), and after introducing CO and O_2 in the reactor chamber at RT (c) and (d). Measurements of particle 1 in a) and c) were taken at different detector distances: a) at 0.95 m and c) at 1.14 m. Only a selected region of the detector is shown. The non-zero intensity lines are due to the junction of the four chips of the MAXIPIX. 122
4.21 Partial pressures of CO, O_2 and CO_2 as measured by the mass spectrometer while measuring the first particle, as a function of time. The sample is measured at RT. Dashed vertical lines evidence the opening and closing of the valves. An adsorption of O_2 can be observed in the first 10 minutes, as shown in the zoom, before becoming constant. The arrows point small oscillations due to gas composition changes. 123
4.22 Stereographic projection of the 3D Bragg peak of particle 1 in the initial state (a), and under high activity conditions (b). Labeled peaks have shifted, while other remains in the same position after reaction. For clarity in the peaks indexation, circles at $\psi = 10°$ intervals and dashed lines at $\phi = 0°, 90°, 270°$ and $360°$ have been drawn. 123

4.23 Residual gas analyser while tracking the second particle during the increase of temperature and under CO/O_2 exposure. After opening the valves, a first regime (*square 1*) where oxygen is adsorbed is observed. In the inset (*square 2*), simultaneous consumption of CO and O_2 is observed. Oscillations in between are related to the background and temperature changes. 125
4.24 Experimental data recorded around the **002** Pt Bragg reflection of the second particle at Room Temperature (a) and at 600° C (b) under gas exposure. Bragg peaks have been centered on the ROI. The difference map in (c) shows an increase of intensity of the streaks whose directions have changed, corresponding to the rods pointed by arrows in (a). 125
4.25 Experimental data recorded around the **002** Pt Bragg reflection of the second particle at Room Temperature (a) and at 600° C (b) under gas exposure. Bragg peaks have been centered on the ROI. The difference map in (c) shows an increase of intensity of the streaks whose directions have changed, corresponding to the rods pointed by arrows in (a). 126
4.26 Rocking curves around the **002** Pt Bragg reflection of *Particle A* as function of time during CO injection. Time is in minutes. 127
4.27 Evolution of the *out-of-plane* strain as a function of time of Particle A in CO atmosphere. Reference value ($\epsilon = 0$) is the measured lattice parameter before injection of CO in the chamber. The error bars estimated from the thermal expansion of Pt are smaller than the corresponding symbols. 128
4.28 *Out-of-plane* strain evolution as a function of time of Particle B at $200°$C in three different regimes: 1) in O_2 atmosphere; 2) in CO and O_2 and 3) in a different mixture of CO and O_2. Error bars correspond to calculated Pt thermal strain. Temperature changes are observed simultaneously with gas injection. 129
4.29 SEM image of Pt nanoparticles after CDI experiments at ID01 beamline. The hole of the face initially in contact with the substrate is visible, due to the rotation of the particles under the X-ray beam (circled in green). 130

List of Tables

1.1 Diffusion data for the system Si-Ge, from Ref.[44]. 26
1.2 Diffusion coefficients of Au in Si and in Ge NWs for comparison with diffusivity in bulk, after[52]. 28

2.1 Transmission test with the available domes at ID01. The number of photons in air being $3.252 \cdot 10^6$, the polystyrene dome is the preferred one 55

3.1 Lattice parameters and elastic constants used in the analytic model[167]. 60
3.2 Summary of the characteristics of the samples measured at ID01; γ = Ratio shell/core. Note that the diameters correspond to the nominal values of the diameter of the gold colloids and are smaller than the ones observed in the SEM images. 65
3.3 Measured strain in the shell of single NWs with different ratio $\gamma = \frac{shell\ diameter}{core\ diameter} = \frac{d_s}{d_c}$. 69
3.4 Melting points of the elements involved in the study 97

4.1 Theoretical angles between planes. 113
4.2 Polar coordinates of the labeled peaks in Fig. 4.22 before and after introduction of gas in the reactor. 123

Author's publications

This project has been presented in scientific meetings and in national and international conferences:

- Oral contributions:
  - XTOP 2016, Brno (Czech Republic)
  - AFC 2016, Marseille (France)
  - Size-strain VII, Oxford (England)
  - EMRS 2015, Lille (France)
  - Core/shell nanostructures workshop, 2015, Toulouse (France)
  - CDM 25, Paris (France)
- Contribution through scientific posters:
  - Coherence 2016, Saint Malo (France) –best poster prize
  - XTOP 2014, Villard de Lans (France)
  - ESRF Users' meeting 2013, Grenoble (France)

Some scientific articles issued from this work:

- **Fernández, S.**, Richard, M-I., Floettoto, D., Richter, G., Mandula, O., Elzo-Aizarna, M., Favre-Nicolin, V., Burghammer, M., Schülli, T., Thomas O., *X-ray nanodiffraction in forward scattering and Bragg geometry of a single isolated Ag–Au nanowire.* Thin Solid Films doi:10.1016/j.tsf.2016.04.039
- David, T., Liu, K., **Fernández, S.**, Richard, M-I., Ronda, A., Favre, L., Abbarchi, M., Benkouider, A., Aqua, J-N., Peters, M., Voorhees, P., Thomas, O., Berbezier, I., *Remarkable Strength Characteristics of Defect-Free SiGe/Si Heterostructures Obtained by Ge Condensation.* J. Phys. Chem. C 120, 20333–20340 (2016).
- **Fernández, S.**, Richard, M-I., Labat, S., Hofmann, J.P., Chahine, G., Leake, S., Gao, L., Goryachev, A., Schülli, T., Thomas O. *Bragg coherent X-ray diffraction imaging on single particle model catalysts*, submitted.

Résumé de thèse

La manipulation des propriétés physiques des nanostructures, telles que leur forme ou leur composition, suscite de plus en plus l'intérêt des recherches à cause des propriétés exceptionnelles des matériaux à cette échelle.
L'ingénierie des contraintes a pour objet d'utiliser la déformation pour contrôler les propriétés. Cela est particulièrement intéressant dans les nano-objets car ils peuvent supporter des déformations élastiques élevées. Dans ce travail, nous étudions la déformation et l'influence de la température dans des nanofils uniques de type cœur/coquille. Ceci est possible en utilisant la diffraction cohérente des rayons X (CDI) en condition de Bragg, une technique d'imagerie qui remplace les lentilles optiques par des algorithmes d'inversion capables de reconstruire l'amplitude (densité électronique) et la phase (projection du champ de déplacement atomique) de l'échantillon à partir des clichés de diffraction. Cette méthode a également été appliquée à des particules facettées de platine qui ont des propriétés catalytiques exceptionnelles. Des expériences CDI *in situ* ont permis d'étudier l'évolution du champ de déformation dans les particules pendant des réactions chimiques et donc de progresser vers le découplage entre leur déformation intrinsèque et leur activité chimique.

Abstract

Manipulating the physical and chemical properties of nanostructures by changing their characteristics (such as shape, strain or composition) is a vivid field of research spurred by the numerous applications that may take advantage of the unique properties that materials offer at this scale.
Strain engineering aims to tune the strain in order to control the properties of materials. This is particularly interesting in nano-objects because they can sustain much higher elastic strains before the occurrence of defects. In this work, we study the strain and the influence of temperature in single core/shell nanowires. This is possible thanks to X-ray coherent diffraction (CDI) in Bragg condition, an imaging technique that replaces the optical lenses by inversion algorithms that are able to reconstruct the amplitude (electronic density) and the phase (projection of the atomic displacement field) of the sample from the experimental diffraction patterns. In addition to nanowires, the method is applied to metallic particles of platinum with exceptional catalytic properties. *In situ* CDI experiments allowed to study the strain evolution within particles during chemical reactions, thereby moving forward in the understanding of important relationships such as the intrinsic strain and chemical activity of the nanoparticles.